UNIVERSIDAD NACIONAL AUTÓNOMA DE MÉXICO
POSGRADO EN CIENCIAS FÍSICAS
INSTITUTO DE CIENCIAS NUCLEARES

NUMERICAL SPACETIMES WITH FUNDAMENTAL FIELD SOURCES

T E S I S

QUE PARA OPTAR POR EL GRADO DE
DOCTOR EN CIENCIAS (FÍSICA)

PRESENTA
VÍCTOR MANUEL JARAMILLO PÉREZ

TUTOR PRINCIPAL
DR. DARÍO NÚÑEZ ZÚÑIGA
INSTITUTO DE CIENCIAS NUCLEARES

MIEMBROS DEL COMITÉ TUTOR

DR. JUAN CARLOS HIDALGO CUÉLLAR
INSTITUTO DE CIENCIAS FÍSICAS

DR. MIGUEL ALCUBIERRE MOYA
INSTITUTO DE CIENCIAS NUCLEARES

CIUDAD UNIVERSITARIA, CD. MX., JUNIO 2023

A mis abuelos Estela y Salvador,

AGRADECIMIENTOS

A mi asesor Dr. Darío Núñez por el incalculable apoyo que he recibido, por las ideas originales que comparte. Por crear un ambiente cordial en el que da gusto estar.

Al Dr. Juan Carlos Degollado por su apoyo en la preparación de mi examen de candidatura y en la discusión (y paciente corrección) de muchos de los resultados contenidos aquí.

Al Dr. Olivier Sarbach, Dra. Argelia Bernal y Dr. Juan Barranco por su gran apoyo. Agradezco las discusiones sobre física.

A los colaboradores y coautores de los trabajos que aquí se presentan. Gracias en particular a Erik Jiménez, por su ayuda técnica con el uso del cluster y sus consejos en temas numéricos.

Agradezco el tiempo de cómputo otorgado en el cluster Tochtli del Instituto de Ciencias Nucleares de la UNAM.

A mis compañeros y compañeras de estudio y trabajo Eréndira Gutiérrez, Brandon Bautista, Laura Villegas, Belen Carvente, Eduardo Ramírez, Laura (K) Meneses, Alejandro Aguilar y Daniel Martínez.

Al Dr. Carlos Herdeiro, Dr. Eugen Radu, Etevaldo Costa, Jianzhi Yang, Sergio Xavier y los demás por su hospitalidad en mi estancia en Portugal.

A mis excompañeros y profesores de la escuela de música y en particular a los maestros Luis Cibrián y Joel Rodríguez Almaguer por sus enseñanzas que llevo a todas partes.

Al Consejo Nacional de Ciencia y Tecnología (Conacyt) por la beca otorgada durante la realización de mi doctorado. De igual manera agradezco el apoyo económico brindado por el proyecto No. 376127 “Sombras, lentes y ondas gravitatorias generadas por objetos compactos astrofísicos” para la presentación de

trabajos y asistencia en congresos.

A la Coordinación General de Estudios de Posgrado por el apoyo recibido para la estancia de investigación.

A Alexandra y José en Tonalco. Gracias por la gran hospitalidad y ayuda en los primeros años del doctorado. A Alexandra G. por su paciencia y dedicación.

A mis ciberamig@s Johann, Abigail y Sofía.

A mis tíos Fabiola y Eric y mis primos por siempre invitarme. Sin esas pausas para comer y jugar cartas muy difícilmente habría salido el doctorado.

Por supuesto a toda mi familia y en particular a mis Padres y a mi hermano. Esta tesis también está dedicada a ellos.

A mis abuelos con todo mi cariño y admiración.

Uno solo es absurdo
uno es como ninguno

Maiakovski

全世界无产者，联合起来！

Resumen

Al día de hoy, las pruebas prácticas y observacionales indican que la Relatividad General continúa siendo la mejor descripción para la interacción gravitatoria. La extrapolación de este modelo físico-matemático a escalas cosmológicas forma una gran parte de la base teórica de varios modelos cosmológicos, incluido el modelo estándar actual. Dentro de dicho modelo la materia oscura y la energía oscura son hipótesis complementarias, necesarias por consistencia y pueden entenderse como predicciones de este paradigma, sin embargo, aún ésta descripción del universo presenta problemas a escalas cosmológicas pequeñas, abriendo la posibilidad para explorar formas hipotéticas diferentes de materia y energía oscuras. En este sentido, los campos clásicos acoplados a la gravedad han resultado una excelente alternativa para modelar una o las dos componentes oscuras.

Esperaríamos que en la evolución del universo ésta forma de sustancia se aglomere y forme configuraciones autogravitantes. Por este motivo presenta interés el estudio de soluciones a las ecuaciones de Einstein con campos escalares como fuente del campo gravitatorio. Dicha tarea puede dividirse en dos partes: La primera, que corresponde a la construcción de soluciones estacionarias, en donde la materia se encuentre en equilibrio o bien en movimiento perpetuo regular. La segunda, constituida por los escenarios dinámicos como por ejemplo las evoluciones cosmológicas, las perturbaciones a las soluciones estacionarias y los choques de objetos compactos. Esta última con aplicaciones en la generación de ondas gravitatorias y su posterior comparación con los datos obtenidos oportunamente por los observatorios de ondas gravitatorias.

En esta tesis se utiliza la potencia de diferentes métodos numéricos para construir soluciones relativistas estacionarias en una dimensión temporal y en una o dos dimensiones espaciales, así como evoluciones temporales completamente no lineales con tres dimensiones espaciales. En particular se presentan configuraciones de estrellas de bosones con forma de cáscara y masas arbitrariamente grandes, soluciones formadas de múltiples campos, estrellas de bosones magnéticas, agujeros de gusano esféricos pero formados por campos con dependencia angular no trivial, soluciones formadas por un campo canónico y un campo fantasma cuya compacidad excede el límite de Buchdahl, perturbaciones genéricas a las estrellas de bosones multicampos y colisiones frontales de las mismas. El desarrollo de códigos propios, así como el manejo de códigos públicos, tales como Cactus y Kadath, abre camino al desarrollo de trabajos futuros.

Palabras clave: Relatividad General, Relatividad Numérica, Teoría Clásica de Campos, Campo Escalar, Objetos Compactos.

Abstract

To date, practical and observational evidence indicates that General Relativity remains the best description for the gravitational interaction. The extrapolation of this mathematical model to cosmological scales forms a large part of the theoretical basis for several cosmological models, including the current standard model. In this model, the dark matter and dark energy are additional hypothesis necessary for consistency and can also be understood as predictions of this paradigm, however even this description of the universe presents problems at small cosmological scales, opening the possibility to explore different hypothetical forms of dark matter and dark energy. In this sense, classical fields coupled to gravity have proved to be an excellent alternative for modeling one or both of the dark components.

We would expect that in the evolution of the universe this form of substance will agglomerate and form self-gravitating configurations. For this reason it is of interest to study solutions to the Einstein equations with scalar fields as the source of the gravitational field. This task can be divided into two parts: The first, which corresponds to the construction of stationary solutions, where matter is either in equilibrium or in regular perpetual motion. The second, constituted by dynamical scenarios such as cosmological evolutions, perturbations to stationary solutions and collisions of compact objects. The latter with applications in the generation of gravitational signals and their subsequent comparison with the data obtained by gravitational wave observatories.

In this thesis the power of different numerical methods is used to construct stationary relativistic solutions in one time dimension and in one or two spatial dimensions as well as fully nonlinear time evolutions with three spatial dimensions. In particular, we present configurations of shell-shaped boson stars with arbitrarily large masses, solutions formed of multiple fields, magnetic boson stars, spherical wormholes but formed by fields with nontrivial angular dependence, solutions formed by a canonical field and a ghost field whose compactness exceeds the Buchdahl limit, generic perturbations to multifield boson stars, and head-on collisions of them. The development of our own codes as well as the usage of public codes, such as Cactus and Kadath, paves the way for the development of future work.

Keywords: General Relativity, Numerical Relativity, Classical Field Theory, Scalar Fields, Compact Objects.

Declaration

I hereby declare that this thesis was composed by myself and without use of others than the indicated sources. I confirm that the work submitted is my own, except where work which has formed part of jointly-authored publications has been included. Where the work was done in collaboration with others, a significant contribution was made by the author, which is explicitly indicated below in the List of Publications. This work has not been submitted for any other degree or professional qualification.

Víctor Manuel Jaramillo Pérez, May 2023

CONTENTS

LIST OF PUBLICATIONS

This doctoral thesis is based on the following publications. After each reference I indicate my particular contribution.

[A] Víctor Jaramillo, Erik Jiménez-Vásquez, Darío Núñez
Confinement of exotic matter. Static solutions
Physical Review D **107**, 064061 (2023)
D.N. and me conceived the project and performed the analytical calculations, I wrote the code. All three authors wrote the manuscript.
This work is presented in Chap. 4.

[B] Víctor Jaramillo and Darío Núñez
Magnetostatic boson stars
Physical Review D **106**, 104023 (2022)
I conceived the project and numerically solved the system of PDEs. Together with D.N. (advisor) performed the analytical calculations and wrote the manuscript.
This work is presented in Chap. 6.

[C] Víctor Jaramillo, Nicolas Sanchis-Gual, Juan Barranco, Argelia Bernal, Juan Carlos Degollado, Carlos Herdeiro, Miguel Megevand, Darío Núñez
Head-on collisions of ℓ-boson stars
Physical Review D **105**, 104057 (2022)
I adapted the Einstein Toolkit thorn to interpolate initial data of two multi-field boson stars, evolved the cases presented in the manuscript. All authors analyzed the data and wrote the manuscript.
This work is presented in Chap. 9.

[D] Miguel Alcubierre, Juan Barranco, Argelia Bernal, Juan Carlos Degollado, Alberto Diez-Tejedor, Víctor Jaramillo, Miguel Megevand, Darío Núñez, Olivier Sarbach
Extreme ℓ-boson stars
Classical and Quantum Gravity, **39**, 094001 (2022)
I wrote the spectral code and constructed all the $25 < \ell < \infty$ solutions. Together with O.S. obtained the effective equations for high ℓ, solved the corresponding equations and wrote section 4 of the manuscript.
This work is presented in Chap. 3.

[E] Eréndira Gutiérrez-Luna, Belen Carvente, Víctor Jaramillo, Juan Barranco, Celia Escamilla-Rivera, Catalina Espinoza, Myriam Mondragón, Darío Núñez
Scalar field dark matter with two components: Combined approach from particle physics and cosmology
Physical Review D **105**, 083533 (2022)
This study was conceived by all the authors. I obtained the evolution equations, wrote the code to solve them, obtained the values for the constraints, wrote section 3, a significant part of section 4 and collaborated in the drafting of the other sections of the paper except for section 2.
This work is presented in Sec. 2.2 of Chap. 2.

[F] Belen Carvente, Víctor Jaramillo, Celia Escamilla-Rivera, Darío Núñez
Observational constrains on complex quintessence with attractive self-interaction
Monthly Notices of the Royal Astronomical Society **503**, 4008-4015 (2021)
This study was conceived by all the authors. I performed the analytical calculations of section 3 of the manuscript and collaborated in the drafting of the entire article, except for section 4.
Part of this work is presented in Sec. 2.3 of Chap. 2.

[G] Víctor Jaramillo, Nicolas Sanchis-Gual, Juan Barranco, Argelia Bernal, Juan Carlos Degollado, Carlos Herdeiro, Darío Núñez
Dynamical ℓ-boson stars: Generic stability and evidence for nonspherical solutions
Physical Review D **101**, 124020 (2020)
This study was conceived originally by N.S.G., J.C.D., D.N. (advisor) and myself. Jointly with N.S. implemented the calculation of global quantities in the evolution code. Together with J.C.D. chose the perturbations and evolved the cases presented in the manuscript. All authors analyzed the data and wrote the manuscript.
This work is presented in Chap. 8.

[H] Belen Carvente, Víctor Jaramillo, Juan Carlos Degollado, Darío Núñez, Olivier Sarbach
Traversable ℓ-wormholes supported by ghost scalar fields
Classical and Quantum Gravity **36**, 235005 (2019)
This study was conceived by all authors. I found the trick to construct spherically symmetric solutions in this self-interacting model and wrote the code. Together with B.C. constructed and analyzed the solutions presented in the manuscript. All authors wrote the manuscript.
This work is presented in Chap. 5.

During my PhD I was also an author of the following works which are not discussed in this thesis:

[I] Alejandro Aguilar-Nieto, Víctor Jaramillo, Juan Barranco, Argelia Bernal, Juan Carlos Degollado, Darío Núñez
Self-interacting scalar field distributions around Schwarzschild black holes
Physical Review D **107**, 044070 (2023)

[J] Víctor Jaramillo, Daniel Martínez-Carvajal, Juan Carlos Degollado, Darío Núñez
Born-Infeld boson stars
JCAP **07**, (2023) 017

[K] Laura O. Villegas, Eduardo Ramirez-Codiz, Víctor Jaramillo, Juan Carlos Degollado, Claudia Moreno, Darío Núñez, Fernando J. Romero-Cruz *Determination of the angular momentum of the Kerr black hole from equatorial geodesic motion*
arXiv:2211.10464 Accepted for publication in JCAP

Introduction to this manuscript

CHAPTER 1

INTRODUCTION

Contents

Gravity is one of the four known to exist fundamental interactions of nature. Different mathematical models have been proposed over the years to describe this interaction and discover its essence. The first mathematical description of gravity, proposed by Newton in 1687 [1], considered that between different elements of nature acts a force of attraction whose magnitude is proportional to the product of the mass of the objects and inversely proportional to the square of the distance that separates them.

In the 17^{th} century this theory was enough to describe the motion of terrestrial and celestial bodies, however at the end of the 20^{th} century some discrepancies in observations were discovered with respect to the Newtonian model of gravity. Together with the appearance of the theory of Special Relativity at that time, which is incompatible with Newton's theory, the urgency of constructing a new theory of gravity arose. The theory of General Relativity proposed by Einstein in 1915 [2] succeeded, beautifully and in a single mathematical model, to reconcile the compatibility of the gravitational interaction model with Special Relativity and at the same time managed to accurately predict the advance of Mercury's perihelion.

In General Relativity, gravity is described by a rank 2 tensor field $g_{\mu\nu}$ which contains the information of the metric properties of a geometric four-dimensional entity, called spacetime. The equations of motion for $g_{\mu\nu}$ are the Einstein equations

$$R_{\mu\nu} - \frac{1}{2}R g_{\mu\nu} + \Lambda g_{\mu\nu} = 8\pi G T_{\mu\nu}, \tag{1.1}$$

with $R_{\mu\nu}$ the Ricci tensor, R the Ricci scalar, Λ the cosmological constant and $T_{\mu\nu}$ the energy momentum tensor. The Einstein equations (1.1) can be derived using

a variational approach from the Einstein-Hilbert action

$$S = \frac{1}{16\pi G}\int \mathrm{d}^4x\sqrt{-g}\,(R-2\Lambda)+S_{\mathrm{matter}}, \tag{1.2}$$

with S_{matter} the action for the matter fields and g the determinant of the tensor field $g_{\mu\nu}$. The energy momentum tensor appearing in Eqs. (1.1) given by the variation of S_{matter} with respect to $g_{\mu\nu}$,

$$T_{\mu\nu} = -2\frac{1}{\sqrt{-g}}\frac{\delta S_{\mathrm{matter}}}{\delta g^{\mu\nu}}. \tag{1.3}$$

To date there is no evidence against the predictions of Einsteinian gravitation. On the contrary, in addition to the accurate description of the orbit of the planet Mercury and the proof of light deflection in the event of an Eclipse [3], gravitational waves, predicted by General Relativity, have recently been detected [4].

Other, no less impressive predictions of General Relativity are the existence of black holes, recently confirmed by the first image of Sagittarius A*, at the center of our Galaxy [5] and the supermassive black hole in the center of the giant elliptical galaxy M87 [6]. However, one must not lose sight of the fact that this theory, however perfect it may be, is still a mathematical model of reality that does not exhaust matter, infinite in extension and depth.

The electron is as inexhaustible as the atom,
nature is infinite, but it exists infinitely.

Lenin, Materialism and Empirio-Criticism
(1908)

The main objective of this thesis is the construction of solutions of compact objects within this theory of gravitation, when the matter component refers neither to barotropic fluids nor to electromagnetism but to other (classical) fields motivated by physical cosmology. Obtaining solutions in the context we are interested, requires (as a rule) the use of numerical methods and only in a few exceptions is it possible to obtain solutions in closed form. Following this line of thought, the introduction consists of brief summary of the basics of Numerical Relativity in Sec. 1.1, followed in Sec. 1.2, by the cosmological motivation of the classical (mainly scalar) fields to be used in the thesis; then in Sec. 1.3 a brief summary on the solutions of compact objects in different field theories and finally, in Sec. 1.4 a summary of the thesis content by chapter.

1.1 Numerical Relativity

The spacetime of Special and General Relativity contains in dialectical unity time and space. However, this unity is partially broken on purpose in order to have

more control over the mathematical modeling and to put the differential equations contained in the tensor equation (1.1) in the form of an initial value problem (Cauchy problem), suitable to describe how the gravity fields evolve from an initial configuration toward the future.

The 3+1 formalism allows to formulate the problem of solving the Einstein equations as an initial value problem. A great achievement from the mathematical point of view was the demonstration of well-posedness (existence and uniqueness) in the Cauchy problem in General Relativity [7–9].

Considering a *space-time* (M,g), i.e. a Lorentzian manifold M endowed with a metric g, it is said to be *globally hyperbolic* if there exists a space-like hypersurface Σ such that the union of the causal future and causal past of Σ coincides with M. If the spacetime under consideration is globally hyperbolic, then it can be shown that it is possible to foliate M into space-like Σ surfaces that are themselves manifolds endowed with a metric. Proper distances on this hyper-surface (with coordinates x^i) are measured precisely by this induced three-dimensional metric γ: $\mathrm{d}l^2 = \gamma_{ij}\,\mathrm{d}x^i\,\mathrm{d}x^j$.

To each of these hyper-surfaces composing spacetime, we associate a constant value to a certain scalar function t: Σ_t. We define (see e.g., [10]) Eulerian observers as those observers moving in the direction normal to Σ_t, and define the lapse function, α, as the proper time span of an Eulerian observer between the hyper-surface Σ_t and Σ_{t+dt}, i.e. $\mathrm{d}\tau = \alpha(t,x^i)\mathrm{d}t$.

There is no reason to expect Eulerian observers to necessarily follow trajectories with constant x^i (coordinate observers), so a third 3-tensor, in this case the shift vector β^i, is needed to specify the foliation of (M,g): $x^i_{t+dt} = x^i_t - \beta^i(t,x^i)dt$. In the adapted Cauchy framework [11], where we make a foliation-adapted choice for the vector basis at each point of the manifold, the unit vector $n^m u$ normal to the hyper-surfaces t = constant has components

$$n^\mu = \left(1/\alpha, -\beta^i/\alpha\right). \tag{1.4}$$

And the metric tensor, symbolically reads

$$\mathrm{d}s^2 = \left(-\alpha^2 + \beta_k\beta^k\right)\mathrm{d}t^2 + 2\beta_i\,\mathrm{d}t\,\mathrm{d}x^i + \gamma_{ij}\,\mathrm{d}x^i\,\mathrm{d}x^j. \tag{1.5}$$

In addition to the curvature induced by g and the foliation in Σ_t, we can also define the curvature, in this case called extrinsic, of the hyper-surfaces when immersed in M,

$$K_{\mu\nu} = -P^\alpha_\mu \nabla_\alpha n_\nu, \tag{1.6}$$

where $P_{\mu\nu}$ is the projection operator into the Σ_t hyper-surface, defined as $P^\lambda_\sigma = \delta^\lambda_\sigma + n^\lambda n_\sigma$. It can be shown that its nontrivial components satisfy an evolution equation for the extrinsic curvature:

$$\partial_t \gamma_{ij} = -2\alpha K_{ij} + D_i\beta_j + D_j\beta_i \tag{1.7}$$

with D_i, the covariant derivative compatible with γ_{ij}.

Now, one can define

$$E = n^\mu n^\nu T_{\mu\nu}, \tag{1.8}$$
$$S^\alpha = -P^{\alpha\mu} n^\nu T_{\mu\nu}, \tag{1.9}$$
$$S_{\alpha\beta} = P^\mu_\alpha P^\nu_\beta T_{\mu\nu}, \tag{1.10}$$

interpreted as the energy density, momentum density and the stress tensor (respectively) as measured by an Eulerian observer.

It can be shown now [11], that in this system of coordinates, using the above definitions together with identities from differential geometry the Einstein equations (1.1) are split into two: a set of equations without time derivatives, called constraints, and another set including time derivatives, called evolution equations. The Cauchy problem in General Relativity then reduces, in principle, to providing an initial data solving the Hamiltonian and momentum constraints

$$^{(3)}R + K^2 - K_{\mu\nu}K^{\mu\nu} = 16\pi G\, E, \tag{1.11}$$
$$D_\mu(K^{\alpha\mu} - \gamma^{\alpha\mu}K) = 8\pi G\, S^\alpha, \tag{1.12}$$

respectively and, evolving using (1.7) and the following evolution equation for the extrinsic curvature,

$$\begin{aligned}\partial_t K_{ij} = {} & \beta^k \partial_k K_{ij} + K_{ki}\partial_j \beta^k + K_{kj}\partial_i \beta^k \\ & - D_i D_j \alpha + \alpha\left[{}^{(3)}R_{ij} + KK_{ij} - 2K_{ik}K^k_j\right] + 4\pi G\alpha[\gamma_{ij}(S-E) - 2S_{ij}].\end{aligned} \tag{1.13}$$

The required equations for evolving the initial data as presented, constitutes a system of equations that turns out to be not strongly hyperbolic, which in practice results in unstable simulations. The reformulation of the above equations (called ADM-York equations) is necessary. In this manuscript we will be interested in the one (initially) made by Nakamura, Oohara and Kojima [12] and refined over the years. An extensive discussion of the details of the 3+1 formalism and its numerical implementation can be found in the books [10, 13].

To date there are some numerical codes and computational infrastructures created to solve the equations of numerical relativity. In the case where no continuous symmetries are assumed in the 3+1 formulation (i.e., solving in its full 3+1 dimensions) we find the code Einstein Toolkit [14, 15] which in turn uses the Cactus infrastructure and therefore is composed of several *thorns* that solve different aspects of the physical problem. For example, some thorns will be in charge of implementing the material part of the Einstein equations and others will take care of the evolution of the metric. For the case of interest in this work, for which classical fields are included, the particular implementation will depend on the

mathematical characteristics of the field and the chosen coupling with gravitational and electromagnetic fields.

For the major part of this manuscript (Sec. I and Sec. II) we will be solving only the constraint equations and for this purpose we will use our own spectral solver for the spherically symmetric problems in section I, and the KADATH library [16,17] for the axially symmetric problems. Finally, the evolutions presented at the final part of this manuscript (Sec. III), will be performed in the EINSTEIN TOOLKIT by implementing different thorns in the chapters for the corresponding problem in turn.

The particular choices of the type of matter that we will consider both to construct global solutions/initial data and to evolve in this manuscript have a motivation from the field of physical cosmology, which we will give in the next section.

1.2 Cosmological motivation

The aforementioned virtues of the modern (and yet classical) theory of gravitation have motivated physicists over the last century to extrapolate this particular, mesoscopic-astronomical laws of physics and apply them to cosmological scales i.e., to systems of the size of the observable Universe. Today, thanks to the appearance on the scene of general relativity, quantum field theory and the new possibilities to obtain observations of cosmic processes with considerable precision, cosmology has emerged from the realm of pseudoscience and has established itself as one of the most active fields of theoretical and observational research.

The standard cosmological model, at the time of writing this thesis, describes a spatially homogeneous and isotropic Universe at large scales, whose main material components are photons, neutrinos, baryonic matter, cold dark matter and a cosmological constant Λ (see Eq. (1.1)) also called dark energy. In this model, called ΛCDM, the curvature of spacetime -not just space- and therefore its expansion are linked to the presence of these types of matter precisely through Einstein equations.

Returning to the discussion on the predictions of the physical theories, one may ask whether the dark components of the Universe are a prediction of General of Relativity rather than simply hypotheses to be added by hand to the model for consistency. At first, it might seem that the extrapolation of local laws to gigantic scales may be a mistake, however the current cosmological paradigm is unexpectedly consistent with itself, at least in most of the model's content[1]. Of course, there are alternative models of gravity that modify some or several prin-

[1]However, on the other hand, this model still has an important set of problems/challenges to be solved. Such are the Hubble tension, the S_8 tension, the lithium problem and others. There are also the problems related to the results carried by the assumptions made for dark matter, which will be discussed below.

ciples at the basis of the theory and that interestingly do not require one or both of the two dark components, but we will not discuss them in this manuscript.

Dark matter

Evidence of the existence of dark matter has accumulated during the last decades by different means, but in all cases via gravitational effects, however there is no information on what this component is in terms of its properties at fundamental level and as a consequence there is a wide variety of models for the concrete type of matter that constitutes cold dark matter. On the other hand some of these models seem to fail in the small-scale description of the cosmos [18, 19], such is the case of the ΛCDM model and other scenarios that do not modify the power spectrum, either primordially or through direct modification of the properties of dark matter [20]. The missing satellites problem [21], the core-cusp problem [22] and the too-big-to-fail problem [23] consist of discrepancies between the results of the ΛCDM model N-body simulations and observations of galaxies.

Although these problems may probably be due to an oversimplification of the baryonic (i.e. non-dark) matter physics, it is unlikely that these multiple discrepancies can be fixed simultaneously by considering more complex baryonic matter models given the existence of galaxies with different compositions and particularly when some of them contain mainly dark matter.

One might then raise the possibility that standard cold dark matter is irreconcilable with these problems and therefore a different model for dark matter need to be proposed. Indeed, there is a solution to these issues in the *scalar field dark matter* model [24–26] also called fuzzy dark matter and ultralight dark matter in other contexts. At the action level the scalar field dark matter model substitutes the ΛCDM dark matter fluid with a scalar field in the S_{matter} part of Eq. (1.2),

$$S_{\text{sfdm}} = -\frac{1}{2}\int \mathrm{d}^4x\sqrt{-g}\,\left(\nabla_\alpha\phi\nabla^\alpha\phi + V(\phi)\right), \tag{1.14}$$

where $\phi \in \mathbb{R}$ and $V(\phi)$ is the scalar potential, which is usually that of a free scalar field, $V = \mu^2\phi^2$. The parameter μ is related to the mass of the proposed dark matter (ultralight) particles, and is considered to be of the order of 10^{-22} eV [27], or in terms of the characteristic (Compton wave) length $\lambda_C \sim 1000$ kpc, which is about the scale at which ΛCDM starts to have trouble.

The equations of motion for the scalar field, the fluid components and for the spacetime are obtained from the variation of the total action S and details (in the homogeneous background case) will be given in Chap. 2.

Dark energy

In ΛCDM the density of dark energy, coming from Λ, constitutes about 70% of the Universe content at present with a constant value over time: $\rho_\Lambda = \frac{\Lambda}{8\pi G} = \rho_{\text{crit}}\Omega_\Lambda$

with ρ_{crit} the critical density and $\Omega_\Lambda \approx 0.7$ [28,29]. Dark energy is responsible for the current accelerated expansion of the Universe, and it is only very recently[2] that it has become the dominant component of the cosmos. Beyond speculation, there is no information on what substance makes up dark energy. When treated as a fluid with pressure p and a constant equation of state $p = wE$, then according to the latest data of the cosmic microwave background obtained from the Planck satellite [29] it is obtained $w = -1.03 \pm 0.3$.

Quintessence [30] on the other hand, is a dynamical model for dark energy consisting of a scalar field coupled to gravity. The beautiful name comes from the fifth element, after matter, dark matter, photons and neutrinos [31]. It is also very interesting that such a form of matter could imply the existence of a fifth fundamental interaction in nature [32].

In the simpler case, when the scalar field is real and the coupling to gravity is minimal the Quintessence action is also of the form in Eq. (1.14) and the associated pressures and densities[3] of the scalar field are $p := S^r{}_r = (d\phi/dt)^2 - V(\phi)$ and $E = (d\phi/dt)^2 + V(\phi)$ in a homogeneous background. Therefore, the equation of state for the quintessence is

$$w = \frac{(d\phi/dt)^2 - V(\phi)}{(d\phi/dt)^2 + V(\phi)}, \tag{1.15}$$

so that a slowly varying ϕ along V (slow-roll) lead to an accelerated expansion of the Universe with w dynamical and close to -1. Different models with different motivations have been appearing in the literature, for example the important tracker solutions are obtained with inverse power-law potentials of the form $V(\phi) \propto \phi^{-q}$ $(q > 0)$. Exponential potentials $V(\phi) \propto e^{-q\phi}$, double exponential potentials, to name a few, have also been considered.

Massive and self-interacting potential of the form $V(\phi) = \mu^2|\phi|^2 + \lambda\,|\phi|^4$, used in many areas of physics, from Bose-Einstein condensates to the Standard Model of particle physics, also lead to quintessence solutions and in particular when $\phi \in \mathscr{C}$. In Chap. 2 we will present closed form solutions to the Friedmann equations and analyses to evaluate the viability of these models in the light of recent cosmological data.

Several models proposed for describing dark energy, even the Λ cosmological constant one, violate the strong energy condition. Some dark energy models other than quintessence fail to satisfy the null energy condition which in turn implies the violation of the weak energy condition [33], meaning that at least some time-like observer measure negative energy densities. The *phantom* models [34], with the simplest cases consisting of a scalar field with a negative kinetic term in the

[2] Cosmologically speaking, since in fact the epoch of matter-energy equality occurred at a redshift of $z = 0.3$ i.e., billions of years ago

[3] As measured by a comoving observer with $n^\mu \partial_\mu = \partial_t$.

Lagrangian, are an example of this. On the other hand, quintessence and scalar field dark matter models described above, which encompass scalar fields with a canonical kinetic term, always satisfy the null energy condition [35].

As can be obtained from Eq. (1.15), in quintessence, w stays above the cosmological constant value, $w \geq -1$, while for the phantom field $w \leq -1$. In describing the dark energy with a dynamical equation of state, cosmological data analyses suggest that the boundary $w = -1$ is crossed in the evolution of the Universe [36,37]. Models with this kind of behaviour, require two scalar field (or fluid) components [36, 38] and are called *quintom*[4] (see Ref. [39] for a review).

Self-gravitating scalar fields that violate the null energy condition, such as the phantom field, are the constituent material from with hypothetical objects called wormholes are constructed. In Chap. 5 we will discuss some of these non-trivial topology solutions to the Einstein equations. On the other hand, to our knowledge, compact objects made of quintom fields are less common in literature and we will review two solutions with this type of matter in Chap. 4.

1.3 Compact objects and fundamental fields

Electrovacuum

Birkhoff theorem states that the more general spherically symmetric *electrovacuum*[5] spacetime is static. This greatly restricts the kind of spherical solutions to the Einstein-Maxwell equations, where the metric is given by the Reissner-Nordström metric [40]

$$g_{\mu\nu}\,\mathrm{d}x^\mu\,\mathrm{d}x^\nu = -N(r)\,\mathrm{d}t^2 + \frac{1}{N(r)}\,\mathrm{d}r^2 + r^2\left(\mathrm{d}\theta^2 + \sin^2\theta\,\mathrm{d}\varphi^2\right), \tag{1.17}$$

$$A_\mu\,\mathrm{d}x^\mu = \frac{Q}{4\pi\epsilon_0 r}\,\mathrm{d}t\,, \tag{1.18}$$

where we defined

$$N(r) = 1 - \frac{r_s}{r} + \frac{r_Q^2}{r^2}\,, \qquad r_s = 2GM\,, \qquad r_Q^2 = \frac{Q^2 G}{4\pi\epsilon_0}\,. \tag{1.19}$$

with $\epsilon_0 = 1/\mu_0$ being the vacuum permittivity, the parameters M and Q are the mass and charge of the solution and the coordinate r takes the values $0 \leq r < \infty$. Together with the spacetime metric solution $g_{\mu\nu}$ the Reisner-Nordström solution

[4] From *quint*essence + phant*om*.

[5] Source-free Einstein-Maxwell equations, i.e., Eq. (1.1) and $\nabla_\nu F^{\mu\nu} = 0$, also obtained from the variation of the action

$$S = \int \mathrm{d}^4x\sqrt{-g}\left(\frac{R}{16\pi G} - \frac{1}{4\mu_0}F_{ab}F^{ab}\right). \tag{1.16}$$

with $F_{ab} = \nabla_a A_b - \nabla_a A_b$, A_a the electromagnetic four-potential and μ_0 the vacuum permeability.

gives an explicit form for the electromagnetic four-potential, as given in Eq. (1.18) in Boyer-Lindquist coordinates. This restriction is somewhat expected as it is similar to what happens in Newtonian gravitation and in the Coulomb solution, however an outstanding result in General Relativity are the (somewhat converse of Birkhoff theorem) *black holes uniqueness theorems* which have no analogy with the classical physics areas mentioned but do have an analogy with thermodynamics in the sense that a small set of parameters fully determine the properties of a physical system.

Also let us remind that there is no analogy of Birkhoff theorem for rotating axisymmetric spacetimes however, on the other hand, the uniqueness theorems strongly restrict the possible solutions if the spacetime contains a black hole.

For electrovacuum (the system presented in footnote 5) the black hole uniqueness theorem states that any, four-dimensional, asymptotically flat, stationary, black hole spacetime[6] with regular horizon has an exterior isometric to the Kerr-Newman spacetime, which in Boyer-Lindquist coordinates reads [40]:

$$\begin{aligned} g_{\mu\nu}\,\mathrm{d}x^\mu\,\mathrm{d}x^\nu &= -\frac{\Delta}{\Sigma}(\mathrm{d}t - a\sin^2\theta\,\mathrm{d}\varphi)^2 \\ &\quad + \frac{\sin^2\theta}{\Sigma}\left[(r^2+a^2)\mathrm{d}\varphi - a\,\mathrm{d}t\right]^2 + \Sigma\left(\frac{\mathrm{d}r^2}{\Delta} + \mathrm{d}\theta^2\right), \end{aligned} \tag{1.20}$$

$$A_\mu\,\mathrm{d}x^\mu = -\frac{rQ}{4\pi\epsilon_0\Sigma}\left(\mathrm{d}t - a\sin^2\theta\,\mathrm{d}\varphi\right), \tag{1.21}$$

with

$$a = \frac{J}{M}, \tag{1.22}$$

$$\Sigma = r^2 + a^2\cos^2\theta, \tag{1.23}$$

$$\Delta = r^2 - r_s r + a^2 + r_Q^2, \tag{1.24}$$

r_s, r_Q defined in Eq. (1.19) and J is the angular momentum of the black hole. Further discussion of the Kerr-Newman spacetime can be found in Appendix A of this manuscript.

The uniqueness theorem as stated above, do not assume axisymmetry or staticity, so it also asserts that (electrovacuum) "black holes have no hair", meaning that the complete mathematical solution is completely determined by a small set of parameters, namely M, J and Q.

Beyond classical electrodynamics coupled to gravity, there are cases that present interesting physical scenarios. In nonlinear electrodynamics for instance there is an exact solution of a *regular black hole* [41].

[6] In the precise mathematical statement, the theorem also requires analyticity of the spacetime (M, g), which is physically difficult to justify.

Other self-gravitating matter fields

The electromagnetic field and the gravitational field are classical field prototypes which successfully describe a wide variety of phenomena in nature. Other hypothetical classical field are the scalar dark matter and quintessence, both presented in the previous section. However, it is also worthwhile to take into consideration other kind of matter -say motivated by quantum field theory or some particle model- and couple them with gravity. For example, the Yang-Mills theory presents a historically important case in the development of the general non-hair conjecture. The first particle-like everywhere regular solution to the Einstein-Yang-Mills equations[7] was obtained in 1988 and today is known as the Bartnik-McKinnon solution [42]. One year later Mikhail S. Volkov and Dimitri V. Gal'tsov in the Soviet Union found a generalization containing a horizon i.e., a non-Abelian Einstein-Yang-Mills black hole [43].

Besides Einstein-Yang-Mills Bartnik-McKinnon spacetime, other particle-like everywhere regular solutions, also called *gravitational solitons* (and this is how we will refer to them from now on) have been found using different types of matter; from the Oppenheimer-Volkoff fluid solutions to wormholes composed of exotic fields. There is no Birkhoff theorem outside electrovacuum and many spherical solutions have been found. A solution of central importance to the purposes of this manuscript are *boson stars* [44, 45]: gravitational solitons made of complex scalar field. These are static configurations with harmonic time dependence,

$$\Phi(t,\mathbf{r}) = \phi(\mathbf{r})e^{i\omega t}. \tag{1.26}$$

Boson stars possess robust dynamical properties [46] and even a formation mechanism from clouds of initially unbound states is known [47]. Furthermore, if the substance that gives body to dark matter is an scalar field, as the fuzzy dark matter model states, boson stars with their wide range of shapes, sizes and masses could model galactic dark matter halos [48–51].

An important role of boson stars is that they are the starting point, in terms of simplicity, to study solutions with other kinds of fields (vector, spinor, etc.) coupled to Einstein's theory of gravity. Recent results on global solutions and dynamical analysis in numerical relativity show similarities between the scalar (spin 0) field and other fields with higher spin. Different to what happens for the electrovacuum case, an example of a vector field which manages to constitute stable regular self-

[7] Described by Einstein-Hilbert action plus $S_{\text{matter}} = \int \mathrm{d}^4x\sqrt{-g}\mathscr{L}_{\text{Yang-Mills}}$, with

$$\mathscr{L}_{\text{Yang-Mills}} = -\frac{1}{2}\text{Tr}\, F^2; \quad \text{and} \quad F = \mathrm{d}A + A\wedge A, \tag{1.25}$$

A being the gauge potential.

gravitating objects, is the Proca field, $S_{\text{matter}} = \int \mathrm{d}^4x\sqrt{-g}\mathscr{L}_{\text{Proca}}$ with,

$$\mathscr{L}_{\text{Proca}} = -\frac{1}{4}\mathscr{F}_{\alpha\beta}\mathscr{F}^{\alpha\beta *} - \frac{1}{2}\mu^2\mathscr{A}_\alpha\mathscr{A}^{\alpha *}, \tag{1.27}$$

μ corresponds to the mass parameter of the Proca field, $\mathscr{F} = \mathrm{d}\mathscr{A}$ and $\mathscr{A}$ being the complex (Proca) four-potential, where, similarly to boson stars a harmonic decomposition (Eq. (1.26)) is implemented in the fields $\mathscr{A}$. The equations of motion derived from the Proca action, imply that the vector field, when $\mu \neq 0$, must satisfy the (Lorentz) condition $\nabla_\alpha A^\alpha = 0$, which breaks gauge invariance. From the quantum field theory point of view, the Proca field is prone to certain problems, among them, the non-renormalizability of the field, however at the classical level, the Proca Lagrangian could be thought of as an effective Lagrangian. In fact, (classical) gravitational solitons made of this type of fields also allows to build a family of solutions called *Proca stars*, introduced in [52]. It is also possible to form solitonic configurations with a Dirac field (spin 1/2) [53], however the quantum fermionic nature of the Dirac field compels the particle number[8] to be equal to 1, which in turn implies a discrete distribution of solutions of microscopic nature, which are not useful if the idea is to form compact objects [54].

The *stability* of "mini" boson stars (scalar potential $V(|\Phi|) = \mu^2|\Phi|^2$), has been extensively studied from different points of view. At first from linear perturbation analysis [55] and later in a complete way through nonlinear evolutions [56]. These studies showed that in the boson star family of solutions there is a stable and an unstable set of solutions which have three final fates: black hole, scattering, and migration to a stable solution, depending on the perturbations and more concretely, on the total mass and binding energy of the configuration. But in essence one has a set of solutions, called a stable branch, where equilibrium configurations neither collapse nor scatter and whose final state is a configuration very close to the unperturbed configuration.

In addition to the question of stability, a central question is that of the dynamical conformation of these self-gravitating configurations. In order to consider seriously the possible existence of such stars in nature, a mechanism for their formation should exist; in the paper [47] they showed the existence of a mechanism (in spherical symmetry) called gravitational cooling, which consists of a dissipation of the "excess" of scalar field and the subsequent collapse to a boson star.

Other studies carried out on the dynamics of boson stars are *frontal collisions* [57] and *orbital collisions* (see e.g., [58] for boson stars with a potential somewhat different from the free field case). Also, of relevance to this work is the article [59] where the frontal and orbital collisions of *dark stars*[9] is studied. Further details

[8] Related to the value of the conserved charge associated with the $U(1)$ symmetry of the field under consideration

[9] Which refer to a case where the interaction between the stars in the binary system, is purely gravitational. This case will be explored in Chap. 9.

on the stability and head-on collisions of boson stars will be given in Sec. III.

Similar results for Proca stars, which are also formed by bosonic but now vector fields, have been obtained recently. We make reference to [60–62] where nonlinear analysis of their stability and a study of their formation and frontal/orbital collisions are performed. An interesting peculiarity of Proca stars is that their rotating configurations, unlike the case of rotating Boson Stars, do not possess a non-axisymmetric instability [63], indicating in fact that Proca-rotating stars are "robust" configurations.

1.4 Thesis outline

The organization of this thesis is as follows. Chap. 2 concerning homogeneous solutions to the Einstein equations with scalar fields is part of the introduction to the manuscript, since the cosmological evolution of complex scalar fields is part of the motivation of this work, this chapter includes results from publications [E] and [F]. Part I concerns the solutions of compact objects in spherical symmetry; In Chap. 3, extracted from publication [D], we construct solutions for ℓ-boson star solutions with $\ell \gg 1$, Chap. 4, extracted from [A], discusses new $\mathscr{E}$-boson star solutions, characterized by an exotic matter core and very high compactness. Chap. 5, based on publication [H], concerns numerical construction of multifield wormhole solutions. Part II concerns the solutions of compact objects in axial symmetry; Chap. 6, extracted from publication [B], deals with solutions with two scalar fields coupled to the electromagnetic field and representing a magnetized boson star, in Chap. 7 we discuss two-boson star solutions that we are currently constructing in a system composed of a canonical complex scalar field and a real field that gives mass to it. Finally, in Part III make numerical evolutions of ℓ-boson stars; a perturbation analysis in Chap. 8, which is extracted from [G] and, head-on collisions in Chap. 9, based on publication [C]. Unless otherwise stated, we will continue to use units such that $c = 1$. Throughout the manuscript we will remain using the metric signature $(-,+,+,+)$.

CHAPTER 2

SPATIALLY-HOMOGENEOUS COSMOLOGICAL SOLUTIONS

Contents

Cosmological scenarios such as the ones presented in Chap. 1 motivate the incorporation of scalar fields as the dark matter and dark energy components. Although the *real* scalar fields are most commonly preferred in quintessence and ultralight dark matter models, *complex* fields in certain cases considerably simplify obtaining spatially homogeneous and isotropic solutions to the Einstein equations [64, 65].

In this chapter we present two of such solutions. The first one corresponding to a global two scalar field model describing dark matter and the second case is a quintessence-like (spintessence) model, which has an exact solution in a region of the parameters of the solutions.

This chapter is organized as follows. In Sec. 2.1 the mathematical framework in which homogeneous and isotropic cosmologies are constructed. Also, we obtain general equations that will apply to the following two scalar fields examples. In Sec. 2.2 we construct solutions of a two scalar-field dark matter model and present a simple constraint in its parameters. In Sec. 2.3 we present solutions using another scalar field cosmological model, this time corresponding to a dark energy.

Regarding the constraints in both models, in the dark matter case the free parameters of the model are constrained by comparison with the observed abundance of light elements from big bang nucleosynthesis, while in the dark energy case, the model is simplified by using an approximation and which lead to an equation of state with two free parameters which are then constrained by statistical methods. The motivations for the scalar potential $V(|\Phi|)$ in both model comes from different areas of physics. We will review briefly the context in which such scalar field description arise.

2.1 Dynamics of the homogeneous and isotropic Universe

The spacetime (M,g) is said to be spatially[1] homogeneous if there exists a particular foliation where the hypersurfaces Σ_t of constant t such that for any points $p,q\in\Sigma_t$, there exist an isometry of g which takes p into q. Isotropy means that it should be impossible to find any preferred vectors on Σ_t. Let u^μ be the tangent vector of the timelike curves followed by the particular observers for which the Universe looks isotropic. In coordinates where Σ_t is labeled by the proper time t measured by the isotropic coordinates and assigning fixed spatial coordinates (ψ,θ,φ) to each of these observers it can be shown (see e.g. [66], etc.) that the metric reduce to one of the three possibilities

$$g_{\mu\nu}^{3-\text{sphere}}\,\mathrm{d}x^\mu\,\mathrm{d}x^\nu = -\mathrm{d}t^2+a^2(t)\left[\mathrm{d}\psi^2+\sin^2\psi\left(\mathrm{d}\theta^2+\sin^2\theta\,\mathrm{d}\varphi^2\right)\right], \quad (2.1)$$

$$g_{\mu\nu}^{\text{spat.}-\text{flat}}\,\mathrm{d}x^\mu\,\mathrm{d}x^\nu = -\mathrm{d}t^2+a^2(t)\left[\mathrm{d}\psi^2+\psi^2\left(\mathrm{d}\theta^2+\sin^2\theta\,\mathrm{d}\varphi^2\right)\right], \quad (2.2)$$

$$g_{\mu\nu}^{\text{hyperboloid}}\,\mathrm{d}x^\mu\,\mathrm{d}x^\nu = -\mathrm{d}t^2+a^2(t)\left[\mathrm{d}\psi^2+\sinh^2\psi\left(\mathrm{d}\theta^2+\sin^2\theta\,\mathrm{d}\varphi^2\right)\right], \quad (2.3)$$

for an arbitrary function $a(t)$.

The Friedmann metric (2.1) can be expressed using the "areal-radius" coordinate r:

$$g_{\mu\nu}\,\mathrm{d}x^\mu\,\mathrm{d}x^\nu = -\mathrm{d}t^2+a^2(t)\left[\frac{\mathrm{d}r^2}{1-kr^2}+r^2\left(\mathrm{d}\theta^2+\sin^2\theta\,\mathrm{d}\varphi^2\right)\right] \quad (2.4)$$

where k, which has units of $(\text{length})^{-2}$, is positive, zero or negative in the 3-sphere, spat.-flat and hyperboloid cases of Eq. (2.1), respectively. In this convention $a(t)$ is unitless. Also, if t_0 is the age of the Universe[2], we choose the convention in which $a(t_0)=1$.

We now make use of the Einstein equations to determine the unique metric coefficient $a(t)$. If the matter and energy are modeled by a barotropic fluid[3] at rest in the comoving r,θ,φ coordinates with $T^\mu{}_\nu=\mathrm{diag}(\rho,p,p,p)$.

Combination of the ${}^\mu{}_\nu={}^t{}_t$ and ${}^r{}_r$ components of the Einstein equations (1.1) lead to the *Friedmann equations* [67]

$$\left(\frac{\dot a}{a}\right)^2=\frac{8\pi G}{3}\rho-\frac{k}{a^2}+\frac{\Lambda}{3} \quad (2.5)$$

and

$$\frac{\ddot a}{a}=-\frac{4\pi G}{3}(\rho+3p)+\frac{\Lambda}{3}, \quad (2.6)$$

[1] There also exist spacetimes which are homogeneous throughout space and time (see e.g. Chap. 12 in Ref. [40]). They are also called maximally symmetric Universes in some other references.

[2] 13.8×10^9 years.

[3] The resulting Friedmann equations will be the same if the energy-momentum tensor is that of a scalar field which in an isotropic background is also of the form $T^\mu{}_\nu=\mathrm{diag}(\rho,p,p,p)$.

where $\dot{} = \mathrm{d}/\mathrm{d}t$ and $\ddot{} = \mathrm{d}^2/\mathrm{d}t^2$.

These equations where first derived by the Soviet physicist and mathematician Alexander Alexandrovich Friedmann in 1922, even before the discovery of Hubble's law (1929).

Knowledge of ρ as a function of a and substitution in Eq. (2.5) would be enough to finish solving Einstein equations. To this end we obtain the zero component of the energy-momentum tensor conservation equation, from which we obtain $\dot{\rho} + 3\dot{a}(\rho + p)/a$. Now, if we assume a constant in time equation of state $\rho = wp$, which obviously will not work for the case of a general scalar field but will work for barotropic fluids relevant in cosmology, we obtain $\ln\dot{\rho} + 3(1+w)\ln\dot{a} = 0$ which can be integrated to obtain

$$\rho \propto a^{-3(1+w)} \qquad (w \text{ constant}). \tag{2.7}$$

Now we define some of the cosmological parameters which will be useful below: First, the Hubble parameter $H := \dot{a}/a$, which characterize the rate of expansion of the Universe. $\rho_\Lambda = \frac{\Lambda}{8\pi G}$ being the (constant) density associated with dark energy, as already defined in Chap.1. The critical density is $\rho_{\text{crit}} := 3H^2/(8\pi G)$. And finally the density parameter of the substance x is defined as $\Omega_x := \rho/\rho_{\text{crit}}$, $x = r, m, \Lambda$ being radiation, total matter (baryionic + dark) and the cosmological constant, respectively. With these definitions in hand and the solutions at Eq. (2.7) the Friedmann equation (2.5) can be written as follows:

$$\frac{H^2}{H_0^2} = \frac{\Omega_r}{a^4} + \frac{\Omega_m}{a^3} + \Omega_\Lambda \qquad (\Lambda\text{CDM model}). \tag{2.8}$$

In the last equation we have not included the curvature parameter. According to the latest results [29], the curvature parameter k is consistent with the spatially flat case and will be considered as such for the remainder of this chapter, however the question of the size and finiteness-infiniteness of the Universe is a fascinating topic worth addressing (for a philosophical discussion from dialectical materialism see e.g. [68, 69]),

$$k = 0\,. \tag{2.9}$$

Let us now turn to the scalar field dark matter/energy models. For the case of a complex scalar field minimally coupled to gravity, with (strictly real) mass term μ and quartic (positive or negative) self-interaction λ, the total action reads

$$S = \int d^4x\sqrt{-g}\left(\frac{1}{16\pi G}R - \frac{1}{2}\nabla^\mu\Phi^*\nabla_\mu\Phi - \frac{1}{2}\mu^2|\Phi|^2 - \frac{\lambda}{4}|\Phi|^4\right) + S_{\text{other-matter}}, \tag{2.10}$$

where the other–matter term includes barotropic fluid contributions. Then the scalar field energy momentum tensor $T^{(\Phi)}_{\mu\nu}$ can be computed from Eq. (1.3), obtaining:

$$T^{(\Phi)\mu}{}_{\nu} = g^{\mu\eta}\partial_{(\eta}\Phi^*\partial_{\nu)}\Phi - \frac{\delta^\mu_\nu}{2}\left(g^{\alpha\beta}\partial_\alpha\Phi^*\partial_\beta\Phi + \mu|\Phi|^2 + \frac{\lambda}{2}|\Phi|^4\right), \tag{2.11}$$

for the mixed components.

Using the background metric (2.4), there are only two independent contribution of $T^{(\Phi)}_{\mu\nu}$; these are the energy density and the "pressure" terms,

$$\rho_\Phi = \frac{1}{2}|\partial_t\Phi|^2 + \frac{1}{2}\mu^2|\Phi|^2 + \frac{1}{4}\lambda|\Phi|^4, \tag{2.12}$$

$$p_\Phi = \frac{1}{2}|\partial_t\Phi|^2 - \frac{1}{2}\mu^2|\Phi|^2 - \frac{1}{4}\lambda|\Phi|^4, \tag{2.13}$$

which enter the Friedman in a fluid type fashion:

$$H^2 = \frac{8\pi G}{3}[\rho_{\text{other-matter}} + \rho_\Phi], \tag{2.14}$$

On the other hand, the conservation equation $\nabla^\mu T^{(\Phi)}_{\mu\nu} = 0$ leads[4] to the equation of motion for the field Φ

$$\Box\Phi - \mu^2\Phi - \lambda|\Phi|^2\Phi = 0, \tag{2.15}$$

also known as the *Klein-Gordon equation*. $\Box := \nabla_\mu\nabla^\mu$ is known as the d'Alembert operator. In particular, applying the Friedmann ansatz for $g_{\mu\nu}$ and the definitions for ρ_Φ and p_Φ, Eq.(2.15) implies that $\partial_t\rho_\Phi + 3H(\rho_\Phi + p_\Phi) = 0$, which is identical to the conservation equation for a cosmological barotropic fluid, however, it is important to remember that this parallelism occurs only for the homogeneous case; in scalar field case we should solve only for the function Φ with the Klein-Gordon equation, without assuming fixed *a priori* values for the equation of state $w_\Phi = p_\Phi/\rho_\Phi$.

2.2 Scalar field dark matter with two components[5]

Bohua Li et al. analyzed in Ref. [64] the hypothesis of dark matter comprised by an ultralight complex and self-interacting scalar field. They found by analyzing only the background equations, without the need to make the step to perturbation theory, some constrains that the complex field ultralight particle should satisfy even at this level in order to be consistent the big bang nucleosynthesis and with the expected equation of state of dark matter at the present time. Interestingly, they found that the free parameters of the model are very well constrained with this method. Specifically, the terms they obtained that if the scalar field mass

[4] Equivalently, can be obtained from the variation of S (Eq. (2.10)) with respect to Φ^*.

[5] This section is partially extracted with minor revisions from Ref. [70], which was written in collaboration with E. Gutiérrez-Luna, B. Carvente, J. Barranco, C. Escamilla-Rivera, C. Espinoza, M. Mondragón and D. Núñez.

parameter and the self-interaction satisfy[6]

$$\mu\hbar \gtrsim 5\times 10^{-21}\ \text{eV}; \tag{2.16}$$

$$8\times 10^{-4}\ \text{eV}^{-4} \lesssim \frac{\lambda}{(\mu\hbar)^4} \lesssim 10^{-2}\ \text{eV}^{-4}, \tag{2.17}$$

then the complex scalar field dark matter will have an equation of state sufficiently close to the dust-type material value $|w| < 0.001$ at the epoch of matter-radiation equality and an effective number of neutrino species within the inferred range from observed primordial light element abundances.

Now, the study made by Li et al. was performed without specifying or restricting to a particular elementary particle model extension. Also, there is no good reason to expect that dark matter should be composed by a single type of matter; ultimately its contribution to the energy density of the Universe (today) is several times greater than that of known ordinary matter. With these two ideas in mind, in [70] we addressed a situation with two scalar fields, one motivated by particle physics and the other (classical) motivated by Li et al. study [64] of the possibility of increasing the number of relativistic degrees of freedom by the correct amount indicated by nucleosynthesis.

At the time of writing this manuscript, there has been no success in experiments to detect any of the most popularly proposed dark matter particles, this has prompted the proposal of other solutions to this problem. An example of this are the scalar field models in which we are interested. The two most popular scalar dark matter candidates are the axion and Higgs-like particles. In section II of Ref. [70] we have reviewed some essential properties of the axion/axion-like particles and the Higgs-like particle consisting of an inert scalar SU(2) doublet. For this manuscript we are interested in the final result of the discussion presented there, which indicates that in both extensions of the standard model of particle physics, there are ways in which at a classical level both the axion Φ_a, which at the quantum level is a real field, and the Higgs-like particle Φ_h, which at the fundamental level is a bicomponent field, can be described by complex scalar fields. It turns out that before coupling the fundamental fields with gravity, a classical limit must be performed in order to be able to introduce the semi-classical energy-momentum tensor in the Einstein equations (see section II in [70]), which looks as follows for the scalar potentials

$$V_h = m_h^2(\Phi_h^\dagger\Phi_h) + \frac{\lambda_h}{2}(\Phi_h^\dagger\Phi_h)^2 \quad \longrightarrow \quad V_h(|\Phi_h|) = m_h^2|\Phi_h|^2 + \frac{\lambda_h}{2}|\Phi_h|^4\,;$$

$$V_a = m_a^2 f_a^2\left[1-\cos\left(\frac{\Phi_a}{f_a}\right)\right] \quad \longrightarrow \quad V_a(|\Phi_a|) = m_a^2|\Phi_a|^2 - \frac{m_a^2}{12 f_a^2}|\Phi_a|^4\,,$$

[6] An update of the obtained constraints was made in Ref. [71]

where f_a is the scale of spontaneous symmetry breaking of the axion field which is related to the (negative) self interaction by means of the relation $\lambda_a/2 = m_a^2/(12 f_a^2)$. In the equations above and in the remainder of this section we will use units in which we also assume $\hbar = 1$. In the two-scalar field models we also considered a classical scalar field with potential $V_c(|\Phi_c|) = m_c^2|\Phi_c|^2 + \frac{\lambda_c}{2}|\Phi_c|^4$. Before moving on to the composite systems, let us note that there are already certain a priori ranges or orders of magnitude of the single field models to be considered. Table 2.1 shows the range of these parameters as well as some representative cases that will be useful below.

Table 2.1: Single scalar field models. Three single scalar field models with their free parameters and the validity intervals of m and λ parameters. The representative cases are the specific values of the parameters explored in the figures within this section. Adapted from [70]

SINGLE MODEL	Free param.	m	λ	Representative cases (m, λ)
Axion (Φ_a)	f_a	$5.7\left(\frac{10^6\,\mathrm{GeV}}{f_a}\right)\mathrm{eV}$	$-m_a^2/(6f_a^2)$	$(6\times10^{-13}\,\mathrm{eV}, -5\times10^{-82})$
Higgs (Φ_h)	m_h, λ_h	$\sim 100\,\mathrm{GeV}$	$(-4\pi, 4\pi)$	$(100\,\mathrm{GeV}, 1)$
Classical (Φ_c)	m_c, λ_c	$\lesssim 1\,\mathrm{eV}$	>0	$(3\times10^{-21}\,\mathrm{eV}, 4\times10^{-86})$

All that remains is to solve the Friedmann (2.14) and Klein-Gordon (2.15) equations for a couple of self-interacting scalar fields. To integrate the equations we follow the procedure presented by Li et al. in [64]. To this end we will only consider cases where the two complex scalar fields behave like dust at the present time, which will be the case if the complex phases ω of both fields satisfy

$$\frac{\omega}{H} \gg 1, \tag{2.18}$$

known as the fast oscillation regime for scalar fields. We also ask the interaction between the two fields to be negligible, then, the scalar field dark matter equations presented in Sec. 2.1 are trivially modified. For example, the energy momentum tensor in Eq. (2.11) will be the sum of two (functionally) equal parts and the same happens for the density and pressure terms, while on the other hand we will have two Klein-Gordon equations (2.15), one for Φ_1 and one for Φ_2.

We introduce the variables $A_1 = \rho_1 - p_1$, $A_2 = \rho_2 - p_2$ and $B_1 = m_1^2\partial_t|\Phi_1|^2$, $B_2 = m_2^2\partial_t|\Phi_2|^2$. Then, the Friedmann equation (2.14) become

$$\dot{a} = aH_0\sqrt{\frac{\Omega_r}{a^4} + \frac{\Omega_b}{a^3} + \Omega_\Lambda + \frac{\rho_1}{\rho_{\mathrm{crit}}} + \frac{\rho_2}{\rho_{\mathrm{crit}}}}, \tag{2.19}$$

and, the Klein-Gordon equation (2.15) for the field Φ_1 splits up into

$$\frac{d\rho_1}{da} = -3\frac{2\rho_1 - A_1}{a}, \tag{2.20}$$

$$\frac{dA_1}{da} = \pm\frac{B_1}{\dot{a}}\sqrt{1+\frac{2\lambda_1}{m_1^4}A_1}, \tag{2.21}$$

$$\frac{dB_1}{da} = -3\frac{B_1}{a} + 2m_1^2\frac{1}{\dot{a}}\left[2(\rho_1 - A_1) - \frac{m_1^4}{2\lambda_1}\left(\sqrt{1+\frac{2\lambda_1}{m_1^4}A_1}\mp 1\right)^2\right]. \tag{2.22}$$

where if $\lambda_1 > 0$ the upper signs are used and, if $\lambda_1 < 0$ both signs are possible. Similar equations hold for the Φ_2 field. The density parameter for dark matter, $\Omega_{\rm DM}$ fixes the total energy density $\rho_1+\rho_2$ at the present, $a = 1$, therefore we write

$$\rho_1(a=1) = \eta\ \Omega_{\rm DM}\rho_{\rm crit}, \tag{2.23}$$

$$\rho_2(a=1) = (1-\eta)\ \Omega_{\rm DM}\rho_{\rm crit}, \tag{2.24}$$

with $0 \le \eta \le 1$ representing the fraction of Φ_1 with respect to Φ_2 as of today.

In order to obtain evolutions in terms of the scale factor, it is only necessary to solve Eqs. (2.20–2.22). To this end we will solve backwards in time the differential equations subject to the conditions (2.23). This might seem as a straightforward task, however, since the complex scalar field must be oscillating fast at $a = 1$, Eq. (2.18), solving the system numerically becomes intractable. To solve this problem, the system of differential equations is solved separately and approximately in the interval in which Eq. (2.18) is valid. As shown in [64, 65], the system (2.20–2.22) reduce to the two equations for the field Φ_1,

$$p_1 = \frac{m_1^4}{9\lambda_1}\left(1\mp\sqrt{1+\frac{3\lambda_1}{m_1^4}\rho_1}\right)^2, \tag{2.25}$$

$$\frac{d\rho_1}{da} = -3\frac{\rho_1+p_1}{a}, \tag{2.26}$$

and similarly for Φ_2, whenever $\omega \gg H$. The same previous rule for signs applies here, however, from now on we will choose a sign, because as showed in [65] only the upper sign give rise to dark matter behavior (the lower signs will be addressed in the next section).

To evaluate when the fast oscillation regime stops to be valid for, say, Φ_1 we use the expression [64]

$$\omega_1 := \frac{d}{dt}\arg(\Phi_1) = m_1\sqrt{\frac{1}{3}-\frac{2}{3}\sqrt{1-\frac{3\lambda_1}{m_1^1}\rho_1}}, \tag{2.27}$$

and make the switch to the full system (2.20–2.22) when ω_1/H is sufficiently big. At this point, $a = a_e$, we must provide a non-trivial matching value for B_1, which

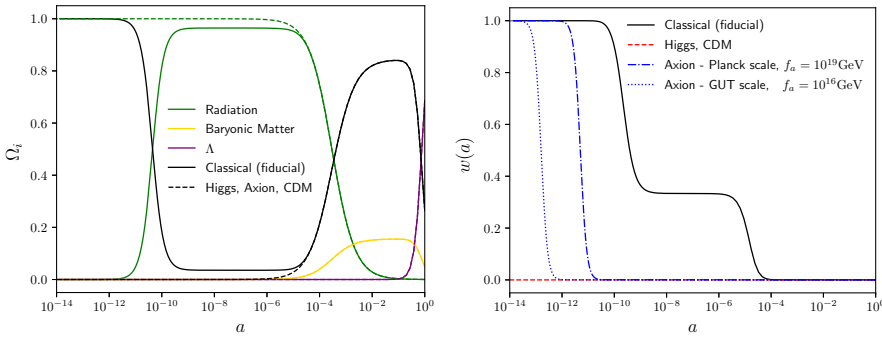

Figure 2.1: Single scalar field representative cases of Table 2.1. Left panel: All solid lines correspond to the classical positive self-interaction fiducial cosmology [64]. The dashed lines are the reference CDM Universe, which happens to coincide in this plot to the Higgs and axion (GUT, Planck) cases. Right panel: Equations of state. While the positive self-interaction classical field undergoes three phases, the negative self-interaction case undergoes two and the Higgs field remains indistinguishable from standard cold dark matter. Adapted from [70].

can be shown to take the value

$$B_1(a_e) = -H(a_e)\frac{\rho_1(a_e)+p_1(a_e)}{\sqrt{1-2\frac{\lambda_1}{m_1^4}(\rho_1(a_e)-p_1(a_e))}}\left[2+\frac{1}{\sqrt{1-3\frac{\lambda_1}{m_1^4}\rho_1(a_e)}}\right]. \tag{2.28}$$

We are now ready to solve the Einstein-Klein-Gordon system by means of numerical integration. To this end we will use a simple implementation of the fourth order Runge-Kutta method. Before proceeding to use this solution and constrain we present typical solutions for the single and double scalar field models. In Fig. 2.1 we show the equation of state for both, the representative single models, shown in the last column of Table 2.1 and the energy fraction parameters $\Omega_x = \rho_x/\rho_{\rm crit}$ for those cosmologies.

In this figure we note in particular that the axion has essentially two stages, a stiff-matter era, with $w = 1$ and then a matterlike dust period $w = 0$, with this transition occurring later in cosmological time as the scale of symmetry breaking f_a increases. On the other hand, the classical field has three characteristic stages: consecutively $w = 1$, then $w = 1/3$ (radiation) and finally $w = 0$, matter-like. Finally, the Higgs-like field have constant $w = 0$ behavior for the considered range of the scale factor.

There are three different types of scalar fields for the two-scalar field model, hence we have taken the three possible combinations and display them in Table 2.2. The analysis of the double model III is an ongoing project and it was not

Table 2.2: Double scalar field models: Three possible two-scalar field models with the corresponding combinations at the description. The η constraint is referred to the minimum fraction of the energy density of the lightest field at the present ($a = 1$) with respect to the total dark matter density. The viability of the models is reported in the last column.

DOUBLE MODEL	Description	η constraint	**Viability**
I	Classical + Higgs	$\gtrsim 0.423$	✓
II	Axion + Higgs	×	×
III	Classical + Axion	-	✓

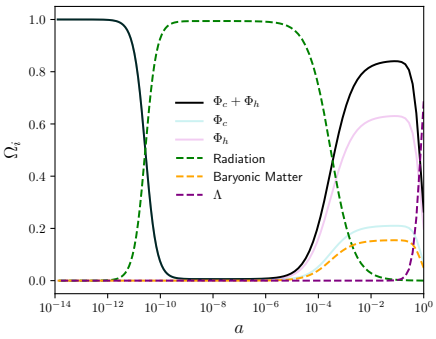

(a) Two scalar field model I. For $\eta = 0.25$

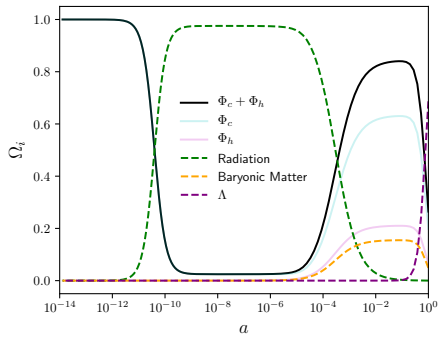

(b) Two scalar field model I. For $\eta = 0.75$

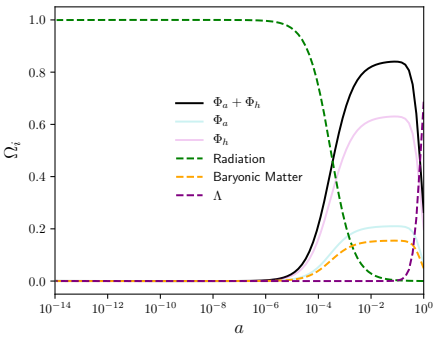

(c) Two scalar field model II. For $\eta = 0.25$

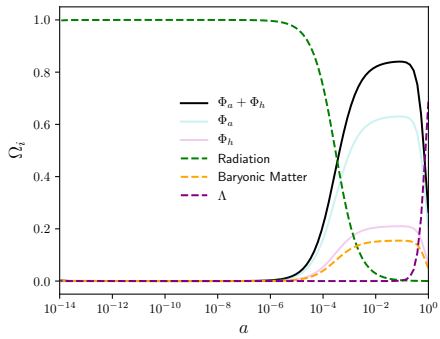

(d) Two scalar field model II. For $\eta = 0.75$

Figure 2.2: Evolution of the density parameters. All solid lines correspond to the scalar field dark matter model with two components and the dashed lines represent the rest of the density contributions. Top panel: Two scalar field model I (Classical + Higgs). Bottom panel: Two scalar field model II (axion+Higgs). Adapted from [70].

presented either in Ref. [70] or in this manuscript. However, we have used the double models I, II in Fig. 2.2 to present the fraction of energy of these scenarios. In the top panels we plot the classical + Higgs case, with the same values for the mass and self-interaction as the ones presented in the single model Table 2.1. In the bottom panels of Fig. 2.2 we show the axion + Higgs case, again with the parameters given by the Table 2.1. Two different values for the fraction η of field 1 with respect to the total dark matter have been selected for each case.

We note that no fully relativistic solutions for a complex axion in a homogeneous background have been reported in the literature before, however cases composed of two (real) dark matter scalar fields have already been reported in other works (see e.g. [72–74]) and new papers continue to appear. We now proceed to explain the last two columns of Table II which are the central result reported in this section and mostly based in Sec. V B in [70].

Constraints from $N_{\rm eff}$ and $z_{\rm eq}$

Among the parameters that determine the production of light elements at BBN we have the expansion rate H. This is a period where every component other than radiation is subdominant, therefore the presence of extra relativistic degrees of freedom, beyond the Standard Model implies a modification to H with respect to its ΛCDM profile. This can be quantified inside the effective number of neutrino species $N_{\rm eff}$ as a contribution to the ΛCDM value $N^0_{\rm eff}$ through a parameter known as number of equivalent neutrinos ΔN_ν, although its source does not necessarily come from a neutrino. It is defined by

$$\Delta N_\nu = \frac{\rho_\xi}{\rho_\nu}, \tag{2.29}$$

where ρ_ν is the energy density of the standard model neutrino (per neutrino specie) and ρ_ξ is the energy density of the additional relativistic fields in consideration, this contribution could correspond to the positive self-interaction (classical) scalar field or to the negative self-interaction axion field for those cases when the energy contribution is important in order to modify H, that is, when they behave as radiation and/or stiff matter during BBN. With the previous definition, the total radiation energy density divided by the photon energy density, ρ_γ, is

$$\frac{\rho_r}{\rho_\gamma} = 1 + \frac{\rho_\nu}{\rho_\gamma}\left(3 + \Delta N_\nu\right). \tag{2.30}$$

If it is assumed that neutrinos are completely decoupled from the electromagnetic plasma at the electron-positron annihilation, then the temperature of the photons increases with respect to that of the neutrinos by $(T_\nu/T_\gamma)^3 = 4/11$. Now, the density ratio $\rho_\nu/\rho_\gamma = 7/8(T_\nu/T_\gamma)^4$, implies that

$$\frac{\rho_r}{\rho_\gamma} = 1 + \frac{7}{8}\left(\frac{4}{11}\right)^{4/3} N_{\rm eff}, \tag{2.31}$$

with

$$N_{\rm eff} = N^0_{\rm eff}\left(1+\frac{\Delta N_\nu}{3}\right);\;\; N^0_{\rm eff} = 3\left[\frac{11}{4}\left(\frac{T_\nu}{T_\gamma}\right)^3\right]^{4/3}. \tag{2.32}$$

Where in this case $N^0_{\rm eff} = 3$. However, if it is not assumed that the neutrinos are completely decoupled when the electron-positron pairs annihilate, then $N^0_{\rm eff} = 3.046$ [75].

The total $N_{\rm eff}$ enters through H to the equations that determine the primordial light element abundances (solved by BBN codes) and if for example the lepton asymmetry is neglected, then the BBN primordial abundances can be confronted with astronomical observations of the abundances of (mainly) deuterium D [76] and the isotope ^{4}He [77]. These constraints on the observed elements can be traduced in constraints over $N_{\rm eff}$ as well as Ω_b [78, 79].

In 2015 reference [79], obtained $N_{\rm eff} = 3.56 \pm 0.23$ or

$$\Delta N_\nu = 0.5 \pm 0.23. \tag{2.33}$$

This value certainly excludes the possibility of a new neutrino as well as the standard $N^0_{\rm eff}$ case. Nevertheless the parameters of a complex scalar field with positive λ can be constrained to be consistent with this measurement as showed by Li et al. [64, 71] if a time dependent $\Delta N_\nu(a)$ is assumed rather than a relatively late time fixed value. The constraint (2.33) is applied through BBN, between the neutron to proton freeze-out and the first nuclei production, at $a_{\rm n/p}$ and $a_{\rm nuc}$ respectively.

In our numerical analysis, if Φ_1 is not subdominant at BBN, then the constraint (2.33) is implemented with the formula,

$$N_{\rm eff} = \frac{N^0_{\rm eff}}{2}\left(1+\frac{\Omega_1}{\Omega_r}+\sqrt{\left(1+\frac{\Omega_1}{\Omega_r}\right)^2+\frac{\Omega_1}{\Omega_r}\frac{32}{7}\left(\frac{11}{4}\right)^{4/3}\frac{1}{N^0_{\rm eff}}}\right), \tag{2.34}$$

which is a result of inserting ρ_γ from (2.31) into (2.32) along with the definition (2.29) and $\rho_\nu = \Omega_r - \Omega_\gamma$, notice that in this expression, Ω_r contains the γ and ν contributions only, which are evolved separately from Φ in the code.

Additional to the BBN constraints discussed so far, there is a need to make the relativistic and stiff matter scalar field solutions reach a matterlike behavior in w at the latest in the matter-radiation equality $z_{\rm eq} \approx 3365$. This condition is imposed in the code by setting $w(z_{\rm eq}) < 0.001$.

The results of this BBN+$z_{\rm eq}$ analysis for the single $\lambda_1 > 0$ scalar field, was reported first by Li et al. in [64] and later an update was made within their work [71]. We recover their result in Eqs. (2.16) and (2.17).

If we repeat this analysis now including the single scalar axion case, we should be able to obtain a constraint on the single parameter f_a particularly for the cases

with big values of this parameter, which as shown in the previous section, are the models that affect expansion the most. It should be mentioned that the general $\lambda < 0$ case cannot be solved in all the cases, particularly in those where the slow oscillation regime appears closer to $a = 1$ and the square root arguments in (2.21) and (2.22) become negative at certain point a_i which corresponds to a place where the scalar field "turns on" [65]. Luckily, numerical experimentation on solutions for the axion field (where the mass and self-interaction have a specific dependence on f_a) shows that this is never the case and therefore, no discontinuities in the Einstein equations appear.

However, the situation occurs when the stiff matter stage of the axion affects $N_{\text{eff}}(a)$ very drastically, and not in the "stepped" way in which it happens for the $\lambda > 0$ case. If the limits are kept to 1σ in equation (2.33) then there is no value of f_a for which $N_{\text{eff}}(a)$ is kept inside these limits, not even at 2σ. It happens that if the $N_{\text{eff}}(a)$ enters into the limits (2.33) in $a_{\text{n/p}}$ at the beginning of nucleosynthesis, then it no longer enters at the end of it, at a_{nuc}, and vice versa.

Therefore, the single axion model is discarded in relation to this cosmological constraint.

It is possible to repeat this analysis for the two scalar field cases. We are interested in exploring Model I and Model II (Table 2.2). Both of them include the Higgs-like field, which as has been said is similar to CDM fluid regardless of the specific values that m_h and λ_h assume. Therefore, in Model I we have a three parameter model and in Model II we have just two parameters.

- Model I. We fix the value of η, (i.e. the fraction of the energy density of Φ_c at $a = 1$ with respect to total dark matter density, (2.23)), and explore the existence of possible values of m_1 and λ_1 consistent with the 1σ BBN+z_{eq} analysis. The case $\eta = 1$ coincides with the single case constraints in (2.16,2.17). If we begin to decrease the value of η, the range of the parameters consistent with the constraint also decrease in size, as shown in Figure 2.3, until a critical value is reached, after which no value is allowed. This constraint on η, gives

  $$\eta \gtrsim 0.423 \, . \tag{2.35}$$

  That is, an upper bound of $\sim 58\%$ for the Higgs (or $w = 0$ fluid) component can be considered in order to be consistent with these constraints. In the critical case, where η takes values near 0.423, we have that the $(m, \lambda/m^4)$ parameter space narrows to the values $m \gtrsim 2 \times 10^{-21}\text{eV}$ and $\lambda/m^4 \sim 3 \times 10^{-2}\text{eV}^{-1}$.

- Model II. In this simpler case, a joint analysis over η and f_a can be made. We find that no $1 - \eta$ ratio of the Higgs field is capable of smoothing the $N_{\text{eff}}(a)$ evolution dictated by the axion, during BBN. And since the Higgs

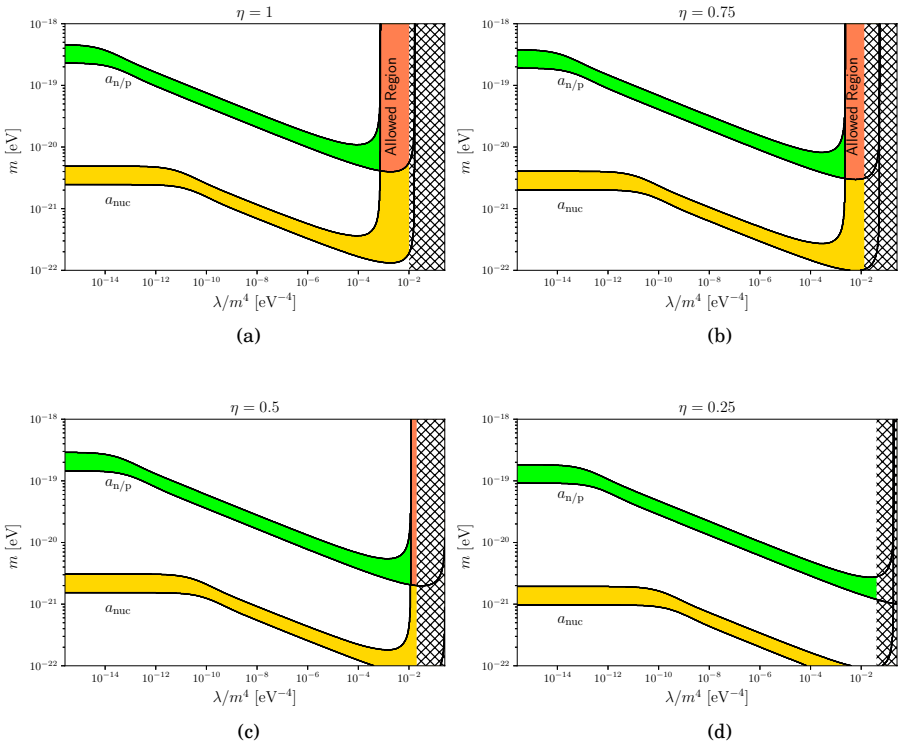

Figure 2.3: Constraints from $z_{\rm eq}$ and $N_{\rm eff}$ within 1σ for the two scalar field Model I. η is the fraction of the classical field with respect to the total dark matter components and its values are (a) $\eta = 1$, (b) $\eta = 0.75$, (c) $\eta = 0.5$, (d) $\eta = 0.25$. The crosshatched region that appears on the right side of all figures, represents the values of the scalar field parameters not allowed by the $z_{\rm eq}$ constraint. The green and yellow bands are the allowed regions from the $N_{\rm eff}$ constraint, (2.33), at $a_{\rm n/p}$ and $a_{\rm nuc}$ respectively. The red band is the region of the parameter space that is consistent with both the $z_{\rm eq}$ and $N_{\rm eff}$, throughout BBN, constraints. Adapted from [70].

field has a contribution to $N_{\rm eff}$ of 0 with respect to $N^0_{\rm eff}$, this two fields case (like the single axion case), is discarded in the sense that there is no set of parameters such that (2.33) is satisfied. Relaxing the constraint to 2σ in (2.33) no allowed values are found either.

- Model III. The classical ($\lambda > 0$) + axion case has 4 relevant free parameters and a higher complexity. It is found that for all axions with $f_a < 10^{19}$GeV, for which the equation of state is 0 before the start of BBN, as showed in Fig. 2.1, the axion scalar field behaves effectively as a $w = 0$ fluid for the purposes of this restriction, and therefore the same restriction as for case I would apply here. A complete analysis of this case will be reported elsewhere.

2.3 Complex quintessence exact solution[7]

Complex scalar fields should be considered since such fields (unlike the real case) have been invoked in many different sectors of particle physics (as discussed in previous section) and interestingly in the scene of ultra cold gases [81]; they can be used to construct static distributions as boson stars, and also configurations surrounding a black hole, the so–called wigs [82]. Furthermore, a real quantized scalar field yields the same field equations as those obtained by using a classical complex scalar field [83]. These reasons motivated us to consider a dark energy model described by a massive quintessence–complex scalar field with attractive self interaction. Such field was formerly studied in [65] and, in the present work, we revisited the idea focusing in the so-called peculiar branch solution of the Einstein-Klein-Gordon equations in order to obtain parameter restrictions of the potential consistent with the current precision observations. Although we are aware of the latest results regarding the possible dynamical behavior of the EoS [37] and the impossibility for a single canonical field to evolve crossing over $w = -1$ because of the no-go theorem [39], it is interesting to explore in detail the properties of the previously mentioned branch and in computing best fit values of their parameters, in order to have a quantitative description of the model and a clearer picture of what the model needs in order to be consistent with such a dynamical behavior of the dark energy. In this section we will use units that recover the speed of light c.

We use the evolution described as a starting point, and introduce a complex scalar field in order to model dark energy. Our proposal is based in the fact that the scalar potential $V(|\Phi|^2)$, has a quartic-form with a negative scattering length

[7] This section is partially extracted with minor revisions from Ref. [80], which was written in collaboration with B. Carvente, C. Escamilla-Rivera and D. Núñez.

as

$$V(|\Phi|^2) = \frac{m^2c^2}{2\hbar^2}|\Phi|^2 - \frac{2\pi A_s m}{\hbar^2}|\Phi|^4, \tag{2.36}$$

where m is the complex scalar field mass, A_s the absolute value of the scattering length and $\hbar$ the reduced Planck constant. This scalar potential describes, for instance, a relativistic Bose-Einstein condensate at zero temperature with attractive self-interaction, and it is also similar to the Higgs potential of particle physics but with an overall opposite sign.

The evolution of this complex scalar field in the cosmological scenario described above is given by the Klein-Gordon equation

$$\frac{1}{c^2}\frac{d^2\Phi}{dt^2} + \frac{3H}{c^2}\frac{d\Phi}{dt} + 2\frac{dV}{d|\Phi|^2}\Phi = 0, \tag{2.37}$$

from where we can express the complex scalar field as

$$\Phi = |\Phi|e^{i\theta}. \tag{2.38}$$

Solutions to the Einstein-Klein-Gordon equations would require in total six parameters related to initial conditions for the real and imaginary parts of Φ and their first time derivative together with the scalar field values for m and A_s. A further simplification can be made within this model when, consistently with dark energy-like behavior, we assume that the field is oscillating rapidly, this leads to a three-parameter model.

In our proposal, we are going to follow the procedure given in [65], of which we summarize some key points. Using (2.38) in (2.37), the Klein-Gordon equation can be divided into a real and an imaginary part, from which the second leads to the equation:

$$Q = -\frac{1}{\hbar c^2}a^3|\Phi|^2\frac{d\theta}{dt}, \tag{2.39}$$

where Q a is constant[8] and a the scale factor.

From the real part, and using the conserved charge Q explicitly in this equation, we obtain

$$\frac{1}{c^2}\left[\frac{d^2|\Phi|}{dt^2} - \frac{Q^2\hbar^2c^4}{a^6|\Phi|^3}\right] + \frac{3H}{c^2}\frac{d|\Phi|}{dt} + 2\frac{dV}{d|\Phi|^2}|\Phi| = 0. \tag{2.40}$$

The term containing Q^2 is usually related to a centrifugal force when making the analogy of this equation with that of fictitious particle with radial coordinate $|\Phi|$, hence the name spintessence for that model [65, 84].

[8] After integration, the imaginary part of the Klein-Gordon equation leads to a conserved quantity, which corresponds to the conserved charge of a complex scalar field, given by $Q = \frac{1}{c^2\hbar}\int dx^3\sqrt{-g}\,\mathrm{Im}(\Phi\partial_t\Phi^*)$.

In the real case, with a quartic potential analogous to (2.36), we have $\theta = 0$, therefore the conserved quantity Q in (2.39) is equal to zero, implying among other things, that the solution must have a rapidly oscillating behavior with an equation of state also oscillating around $w = 0$ [24] and the solutions to the equation of motion must be obtained by numerical integration in an appropriate set of variables. The quartic potential is not the only possibility, for instance taking a massless scalar field ($\mu = 0$, $\lambda = 0$) the equation of state stays trivially at the value $w = 1$. Other (real) scalar fields, describing quintessence potentials, as the ones listed in the introduction, may have dynamical EoS some of which also oscillate in time. In this work we take the opposite approach, namely $Q \gg 0$, leading to an exact solution of the problem which is useful in the implementation of tests for the model with cosmological analyzes. To compute the energy density and pressure of the complex scalar field, we consider the following expressions:

$$\epsilon = \frac{1}{2c^2}\left|\frac{d\Phi}{dt}\right|^2 + V(|\Phi|^2), \tag{2.41}$$

$$P = \frac{1}{2c^2}\left|\frac{d\Phi}{dt}\right|^2 - V(|\Phi|^2). \tag{2.42}$$

Notice how we can connect these equations to the ones presented in Sec.2.1 where the quantity ϵ will replace the ΛCDM quantity $\rho_{\rm crit}\Omega_\Lambda$ in the Fridman equation.

From the equations (2.37), (2.41) and (2.42) we can obtain a useful equation for the energy density that resembles the continuity equation for a barotropic fluid

$$\frac{d\epsilon}{da} + \frac{3}{a}(\epsilon + P) = 0. \tag{2.43}$$

With these equations, now we are ready to study particular solutions of the Einstein-Klein-Gordon system evolving with a complex scalar field mimicking the dark energy component. As mentioned, this particular model in the fast oscillation regime and its homogeneous solution have already been presented previously by [65], and we extend the study in order to obtain analytical expressions for most of the quantities of the solution, including $w(z)$.

Dark Energy Solution in the fast oscillation regime

In [65] was found that in the fast-oscillation regime, i.e., when the oscillation frequency of the scalar field is much larger than the value of the Hubble function, the solution of the Einstein-Klein-Gordon equations for the case of a complex scalar field with an attractive self interaction potential (2.36) has two different solutions. One solution (called normal branch) resembles to a dark matter scalar field, while the other solution (called peculiar branch) corresponds to a quintessence model. This solution only exists in the fast oscillation regime, in which the scalar field suddenly emerges and behaves as dark energy at late times.

Following the same logic, in this paper we propose a deduction of an exact solution for the equation of state of the quintessence field. Once with this equation, we explore their possible constraints by using current observational data.

Peculiar branch solution in the fast oscillation approximation

To establish the fast oscillation regime mentioned above, we consider the following condition which needs to be satisfied during the evolution of the scalar field

$$\omega = \frac{d\theta}{dt} \gg H. \tag{2.44}$$

In addition to the latter condition, we will impose that the magnitude of the scalar field change slowly on time respect to the angular frequency of oscillation ω as:

$$\frac{1}{|\Phi|}\frac{d|\Phi|}{dt} \ll \omega. \tag{2.45}$$

Conditions (2.44)-(2.45) set the so-called fast oscillation regime of the Klein-Gordon equation (2.37). Following this prescription, (2.40) can be reduce to

$$\omega^2 = 2c^2\frac{dV}{d|\Phi|^2}. \tag{2.46}$$

This allows us to write the fast oscillation condition in terms of the charge Q defined in (2.39), which becomes

$$\frac{Q^2\hbar^2c^4}{a^6|\Phi|^4} = 2c^2\frac{dV}{d|\Phi|^2}. \tag{2.47}$$

Using the expression for the scalar field potential (2.36), we can approximate (2.41) using the condition (2.46) as

$$\begin{aligned}\epsilon &= \frac{1}{2c^2}\left[\left(\frac{d|\Phi|}{dt}\right)^2 + \omega^2|\Phi|^2\right] + \frac{m^2c^2}{2\hbar^2}|\Phi|^2 - \frac{2\pi A_s m}{\hbar^2}|\Phi|^4 \\ &\approx \frac{m^2c^2}{\hbar^2}|\Phi|^2 - \frac{6\pi A_s m}{\hbar^2}|\Phi|^4,\end{aligned} \tag{2.48}$$

By a similar approach, the scalar pressure from (2.43) can take the approximate form

$$P \approx -\frac{2\pi A_s m}{\hbar^2}|\Phi|^4. \tag{2.49}$$

Solving (2.48) for $|\Phi|^2$, we obtain two possible branches that correspond to solutions of the Einstein-Klein-Gordon system in the fast oscillation approximation

$$|\Phi|^2 = \frac{c^2 m}{12\pi A_s}\left(1 \pm \sqrt{1 - \frac{24\pi A_s\hbar^2}{m^3c^4}\epsilon}\right). \tag{2.50}$$

Notice that this is a different result in comparison to the repulsive self-interaction case [64], where there is an unique branch in the solution since only the (+) sign of the square root is possible. Furthermore, in [65] was shown that for the attractive self-interaction case (2.50) and when we take the negative sign, the scalar field undergoes a matter-like phase (and even an inflation epoch). While for the positive branch, the solution behaves as dark energy. From this point forward we will take the positive sign, to focus on that particular branch.

Therefore, by using (2.50) in (2.49) we obtain

$$P(\epsilon) = -\frac{m^3c^4}{72\pi A_s\hbar^2}\left(1+\sqrt{1-\frac{24\pi A_s\hbar^2}{m^3c^4}\epsilon}\right)^2. \tag{2.51}$$

Physical solutions of this latter equation correspond to those values of ϵ smaller than a certain ϵ_i:

$$\epsilon_i = \frac{m^3c^4}{24\pi A_s\hbar^2}. \tag{2.52}$$

From the two latter expressions, notice that $P(\epsilon_i) = -\frac{m^3c^4}{72\pi A_s\hbar^2}$, implies that $w_i = \frac{P(\epsilon_i)}{\epsilon_i} = -1/3$.

The scale factor for which the energy density takes the value ϵ_i can be calculated by inserting the value of $|\Phi|^2$ evaluated in ϵ_i, and taking the result on the fast oscillation condition (2.47):

$$a_i = \sqrt[3]{\frac{12\sqrt{3}\pi A_s\hbar^2|Q|}{m^2c^2}}. \tag{2.53}$$

For convenience, we re-define a dimensionless quantity in terms of the differential equation for the energy density as

$$\bar{\epsilon} = \frac{\epsilon}{\epsilon_i}, \tag{2.54}$$

therefore (2.43) can be written as

$$\frac{d\bar{\epsilon}}{da} = -\frac{3}{a}\left[\bar{\epsilon} - \frac{1}{3}\left(1+\sqrt{1-\bar{\epsilon}}\right)^2\right]. \tag{2.55}$$

Evaluating in $\epsilon = \epsilon_i$, we can see that $d\bar{\epsilon}/da$, takes a negative value of $-\frac{2}{a_i}$, therefore for $a < a_i$ the solution is not valid. The value a_i indicates the scale factor at the time when the scalar field turns on. Furthermore, at $a \to \infty$, ϵ approaches to a constant value.

Now, taking the fast oscillation equation (2.47) and inserting $|\Phi|^2$ from (2.50) we obtain

$$\left(\frac{a_i}{a}\right)^6 = 3\left(1+\sqrt{1-\bar{\epsilon}}\right)^2 - 2\left(1+\sqrt{1-\bar{\epsilon}}\right)^3. \tag{2.56}$$

In order to find the asymptotic value of ϵ, when $a \to \infty$, we should consider the fast oscillation equation (2.47), which for potential (2.36) takes the form

$$\frac{Q\hbar c^2}{a^3} = \sqrt{2}c\left|\Phi\right|^2\sqrt{\frac{m^2c^2}{2\hbar^2} - \frac{4\pi A_s m}{\hbar^2}\left|\Phi\right|^2}. \tag{2.57}$$

Since ϵ decreases with a, then $\left|\Phi\right|^2$ increases as $a \to \infty$ as we can notice from (2.50), therefore the term inside the square root in (2.57) should vanish as $a \to \infty$, leading to an asymptotic value of

$$\left|\Phi_\Lambda\right|^2 = \frac{mc^2}{8\pi A_s}. \tag{2.58}$$

Using (2.48) and (2.51) we can obtain

$$\epsilon_\Lambda = \frac{m^3c^4}{32\pi A_s\hbar^2} = \frac{3}{4}\epsilon_i, \tag{2.59}$$

$$P(\epsilon_\Lambda) = -\epsilon_\Lambda. \tag{2.60}$$

Notice how in the limit $a \to \infty$, the scalar field has an EoS with a value $w_\Lambda = -1$. Therefore, the EoS interpolates between the values $-1/3$ and -1. This is a result of both the rapidly oscillating behavior of the field and the chosen peculiar branch, although not a general property of a homogeneous complex cosmological scalar field nor a direct consequence of having a non-zero conserved quantity Q. This result is very different from the one that would have been obtained for the other branch of the solution or even for the real case. In those cases we would not have a scalar field solution with $w < 0$ that turns on at a certain scale factor a_i and not before.

Exact solution for the dark energy term

To obtain an expression for ϵ in terms of the scale factor, we have to solve the equation (2.56). This can be obtained making the change of variable

$$\zeta = \sqrt{1-\bar{\epsilon}} + \frac{1}{2}. \tag{2.61}$$

The latter leads to an expression in terms of a cubic equation

$$\zeta^3 - \frac{3}{4}\zeta + \frac{1}{2}\left(\frac{a_i^6}{a^6} - \frac{1}{2}\right) = 0, \tag{2.62}$$

which has three real solutions. However, it must satisfy the conditions $\zeta(a_i) = \frac{1}{2}$ and $\zeta(a \to \infty) = 1$. The only solution that satisfy these conditions is

$$\zeta(a) = \cos\left[\frac{1}{3}\arccos\left(1 - 2\frac{a_i^6}{a^6}\right)\right], \tag{2.63}$$

in terms of this function $\zeta(a)$, the energy density and the EoS parameter are given by the following expressions

$$\epsilon(a) = \left[1 - \left(\zeta(a) - \frac{1}{2}\right)^2\right]\epsilon_i, \qquad w(a) = -\frac{\left(\zeta(a) + \frac{1}{2}\right)^2}{3 - 3\left(\zeta(a) - \frac{1}{2}\right)^2}. \tag{2.64}$$

This is the so-called Complex Scalar Field Dark Energy (CSFDE) model. These solutions should be considered only in certain region $a_i < a < a_e$ of the evolution of the Universe, the upper limit a_e is defined as the scale factor when the fast oscillation regime ceases to be valid, which we will calculate below. This is evident from (2.47), since ω get suppressed by the term a^6, while $|\Phi|$ goes to a constant value. From now on, a will only be referred to this range. First, we must make sure that the solution at a_i satisfy the fast oscillation approximation described in the latter section.

Under these ideas, the fast oscillation condition $\omega \gg H$ is given by

$$\frac{Q^2\hbar^2c^4}{a^6|\Phi|^4} \gg \frac{8\pi G}{3c^2}(\rho_m + \epsilon), \tag{2.65}$$

where $\rho_m = \Omega_m/\rho_{\text{crit}}$. By performing the substitution of $|\Phi|^2$ using (2.50), rewriting it in terms of $\bar{\epsilon}$ and, finally, taking $\epsilon \gg \rho_m$, we can obtain

$$\left(\frac{a_i}{a}\right)^2 \gg \frac{mG}{3c^2A_s}\bar{\epsilon}(1 + \sqrt{1-\bar{\epsilon}})^2. \tag{2.66}$$

This condition will be satisfied initially if

$$\frac{3c^2A_s}{mG} \gg 1. \tag{2.67}$$

In order to compute the value $a_e > a_i$, where the solution is no longer valid, we will consider the end of the fast oscillation regime when $\omega = NH$ (with $N = 200$ analogous to [64]). If $a_e \gg 1$ and also $a_e \gg a_i$, in order to be able to make the approximations $\epsilon \gg \rho_m$ and $a_i/a_e \ll 1$ in (2.66), then the end value of the scale factor will be

$$a_e \approx \sqrt[6]{\frac{\frac{768}{N^2}\pi^2A_s^3\hbar^4Q^2}{Gm^5c^2}}. \tag{2.68}$$

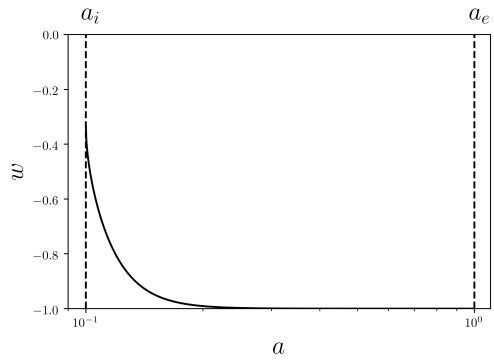

Figure 2.4: Evolution of the w Eq. (2.64) as a function of the scale factor, a, in the quintessence model. Adapter from [80].

In Fig. 2.4 we show an example for the evolution of the equation of state parameter w between the values for the scale factor a_i and a_e, determined by specific values of m, A_s and Q. In this example we take[9] a_i to be the value $a_{\min} = 0.1 < 1/(1+z_{\max})$ where $z_{\max} = 2.26$ corresponds to the maximum redshift used in the multiple data sets within the analysis described in the next section. In this way, we ensure that the scalar field is present throughout the a range of the analysis. We have restricted this example to the case where $a_e = 1$, thus ensuring that the limit of rapid oscillations and therefore the cosmological constant type behaviour continues to be valid today.

[9]This particular choice of a_i and a_e in our example reduces the dimension of the free parameter space from 3 to 2, thus we can put Q and A_s in terms of m:

$$Q = \frac{4a_{\min}^9 mc^4}{27\sqrt{3}\pi NG\hbar^4}, \qquad A_s = \frac{9N^2 G\hbar^2 m}{16a_{\min}^6 c^2}. \tag{2.69}$$

Part I

Spherically-symmetric solutions

CHAPTER 3

EXTREME ℓ-BOSON STARS[1]

Contents

A new class of complex scalar field objects, which generalize the well known boson stars, was recently found as solutions to the Einstein-Klein-Gordon system. The generalization consists in incorporating some of the effects of angular momentum, while still maintaining the spacetime's spherical symmetry. These new solutions depend on an (integer) angular parameter ℓ, and hence were named ℓ-boson stars. Like the standard $\ell = 0$ boson stars these configurations admit a stable branch in the solution space; however, contrary to them they have a morphology that presents a shell-like structure with a "hole" in the internal region. In this chapter we perform a thorough exploration of the parameter space, concentrating particularly on the extreme cases with large values of ℓ. We show that the shells grow in size with the angular parameter, doing so linearly for large values, with the size growing faster than the thickness. Their mass also increases with ℓ, but in such a way that their compactness, while also growing monotonically, converges to a finite value corresponding to about one half of the Buchdahl limit for stable configurations. Furthermore, we show that (the

[1]This chapter is extracted with minor revisions from Ref. [85], which was written in collaboration with M. Alcubierre, J. Barranco, A. Bernal, J. C. Degollado, A. Diez-Tejedor, M. Megevand, D. Núñez and O. Sarbach.

pressure components of the) ℓ-boson stars can be highly anisotropic, with the radial pressure diminishing relative to the tangential pressure for large ℓ, reducing asymptotically to zero, and with the maximum density also approaching zero. We show that these properties can be understood by analyzing the asymptotic limit $\ell \to \infty$ of the field equations and their solutions. We also analyze the existence and characteristics of both timelike and null circular orbits, especially for very compact solutions.

3.1 Introduction

The possibility that dark matter can be described by a scalar field has recently found an increasing interest, either through the study of models with a particle physics motivation [86], or through the description of lighter fields with the potential to alleviate some possible tensions in the standard cosmological scenario on small scales [26, 87–91]. Gravitationally bound bosonic structures appearing as the consequence of these fields may be relevant in astrophysics, as they could develop dark matter halos and/or very compact objects, depending on the particular choice of the parameters of the model. In the high compactness regime, bosonic structures can approach the Buchdahl limit [92] and form objects similar in size and mass to neutron stars or even black holes. Like other compact objects [93], boson stars may form bound binary systems emitting gravitational waves of distinctive features. The dynamics of these systems has been studied for instance in references [58, 59, 94] (see also [95] where the waveforms calculated from the head-on collision between two Proca stars is confronted with gravitational wave observations). On the other hand, in the low compactness regime, gravitationally bound structures can be used to describe dark matter halos, although some controversies have arisen regarding the non-compatibility on the required values of the field mass when combining different data sets. For example, the characteristic masses needed to describe the internal kinematics of the Milky Way dwarf spheroidal satellites are in tension when faced with cosmology [96], and even at local scales the mass density profiles of dwarf spheroidal and ultra-faint dwarf galaxies suggest different values for the field mass. Furthermore, for larger galaxies the dark matter halos could be even more cuspy than the standard cold dark matter Navarro-Frenk-White profiles [97]. These problems emerge when fitting the observations to the dark matter halo profile predicted by a standard boson star, in some cases enlarged with an external Navarro-Frenk-White profile as suggested by numerical cosmological simulations [98]. However, in recent years, it has been argued that more general stable, self-gravitating scalar field objects could exist in nature, and this may affect the previous conclusions.

An interesting example of such configurations are the ℓ-boson stars we have

presented in previous work [99]. Based on similar ideas used previously in the context of gravitational collapse [100], ℓ-boson stars incorporate some effects of the angular momentum into the scalar fields while maintaining the spherical symmetry of the spacetime, which results in a relatively simple model for their description. In the particular case where $\ell = 0$ the standard boson stars by Kaup [44] and Ruffini and Bonazzola [45] are recovered. However, in general, in addition to the parameters that characterize the standard $\ell = 0$ solutions, there is an "angular momentum number" ℓ that provides a model with a richer structure that could potentially be relevant for the description of dark matter halos and compact objects. In particular, and as we further explore in this chapter, boson stars with $\ell > 0$ can be more compact than standard ones. It turns out that the maximum mass of these objects increases greatly with ℓ, giving masses that are orders of magnitude larger than for the $\ell = 0$ case. Even if these configurations are also larger in size than the standard ones, the growth in mass is faster than the growth in size in such a way that the compactness increases.

The stability of ℓ-boson stars under spherical perturbations has first been studied in [101] by performing numerical evolutions of the Einstein-Klein-Gordon equations in spherical symmetry, and later also in [102] based on a more formal study of the linearized system. These analyses have revealed that ℓ-boson stars show stability characteristics that are qualitatively similar to those of the $\ell = 0$ case, where for each value of ℓ there exist a stable and an unstable branch with the transition point given by the solution of maximum total mass. For other studies addressing the stability of ℓ-boson stars which are based on full nonlinear numerical evolutions without symmetries see [103, 104] (see also [105] for a study of the Newtonian regime in axial symmetry). In particular, in [104] it was shown that ℓ-boson stars assume a privileged role among other stationary solutions of the multi-field, multi-frequency scalar field scenario as far as their stability is concerned.

In the present work we perform an exhaustive exploration of the ℓ-boson stars' parameter space, focusing in particular on solutions with very large values of ℓ, including the $\ell \to \infty$ limit. Our analysis covers the stars' morphology, anisotropy and compactness, the characteristics of the circular orbits (including the null ones, also known as light rings), as well as the scaling properties of the fields and relevant physical quantities with respect to ℓ. We start in section 3.2 with a brief review of ℓ-boson stars, presenting the main equations and properties, including the definitions of density, pressure, anisotropy and compactness, and present the equations for geodesic motion, particularly those describing circular causal geodesics. Next, in section 3.3, we present our solutions, analyzing in each case the role played by the angular momentum parameter ℓ on various of their properties, and paying particular attention to the large ℓ regime. We accomplish this by

numerically obtaining and analyzing hundreds of solutions. The observed scaling properties of the fields for large ℓ motivate the in-depth study of section 3.4, where we obtain effective equations which describe the asymptotic behavior of the fields in the limit $\ell \to \infty$. Conclusions and an overview of our results are given in section 3.5. Technical details and tables summarizing our notation and numerical data are included in appendix 3.6.

Throughout this work we use the signature convention $(-,+,+,+)$ for the spacetime metric and Planck units such that $G = c = \hbar = 1$. We present our results in a form that is independent of the scalar field mass μ. The rescaling rules in μ are summarized in table 3.2 of appendix 3.6.

3.2 ℓ-boson stars

In this section we summarize the relevant equations that describe ℓ-boson stars, as well as some of their most significant properties. Additional information can be found in our previous works [99, 101, 102]. ℓ-Boson stars are self-gravitating objects that consist of an odd number $N = 2\ell + 1$ of complex scalar fields $\Phi_{\ell m}$, $m = -\ell, \ldots, \ell$ of equal mass μ and the same radial profile. The dynamics of these fields is described by the following Lagrangian

$$\mathscr{L} = \frac{R}{16\pi} - \frac{1}{2}\sum_{m=-\ell}^{\ell}\left(\nabla_\mu \Phi_{\ell m}\nabla^\mu \Phi^*_{\ell m} + \mu^2|\Phi_{\ell m}|^2\right), \tag{3.1}$$

where R is the Ricci scalar and the scalar fields have the form:

$$\Phi_{\ell m}(t,r,\vartheta,\varphi) = e^{i\omega t}\psi_\ell(r)Y^{\ell m}(\vartheta,\varphi), \tag{3.2}$$

with ω a real frequency and ψ_ℓ a real-valued radial function which is independent of m. As usual, $Y^{\ell m}$ denote the standard spherical harmonics with angular momentum numbers ℓ and m. By applying the addition theorem for spherical harmonics one can see (as shown in [99]) that in the absence of self-interactions, the total stress energy-momentum tensor

$$T_{\mu\nu} = \frac{1}{2}\sum_{m=-\ell}^{\ell}\left[\nabla_\mu \Phi^*_{\ell m}\nabla_\nu \Phi_{\ell m} + \nabla_\mu \Phi_{\ell m}\nabla_\nu \Phi^*_{\ell m} - g_{\mu\nu}\left(\nabla_\alpha \Phi^*_{\ell m}\nabla^\alpha \Phi_{\ell m} + \mu^2 \Phi^*_{\ell m}\Phi_{\ell m}\right)\right] \tag{3.3}$$

is spherically symmetric, even if $\ell > 0$ ($N > 1$) and the individual fields have angular momentum.

The spacetime metric is parameterized according to

$$ds^2 = -\alpha^2(r)dt^2 + \gamma^2(r)dr^2 + r^2 d\Omega^2, \qquad \gamma^2(r) := \frac{1}{1 - \frac{2M(r)}{r}}, \tag{3.4}$$

where α and M denote the lapse and the Misner-Sharp mass functions, respectively, r is the areal radius and $d\Omega^2$ is the standard metric on the unit two-sphere.

The field equations are obtained from the Einstein-Klein-Gordon system and take the form [99]:

$$M' = \frac{\kappa_\ell r^2}{2}\left[\frac{\psi_\ell'^2}{\gamma^2} + \left(\mu^2 + \frac{\omega^2}{\alpha^2} + \frac{\ell(\ell+1)}{r^2}\right)\psi_\ell^2\right] = 4\pi r^2 \rho, \tag{3.5a}$$

$$\frac{(\alpha\gamma)'}{\alpha\gamma^3} = \kappa_\ell r\left[\frac{\psi_\ell'^2}{\gamma^2} + \frac{\omega^2}{\alpha^2}\psi_\ell^2\right] = 4\pi r(\rho + p_r), \tag{3.5b}$$

$$\frac{1}{r^2\alpha\gamma}\left(\frac{r^2\alpha}{\gamma}\psi_\ell'\right)' = \left(\mu^2 - \frac{\omega^2}{\alpha^2} + \frac{\ell(\ell+1)}{r^2}\right)\psi_\ell, \tag{3.5c}$$

whith $\kappa_\ell := 2\ell + 1$, and where we have introduced the energy density, radial pressure and tangential pressure defined as:

$$\rho := -T^t{}_t = \frac{\kappa_\ell}{8\pi}\left[\frac{\psi_\ell'^2}{\gamma^2} + \frac{\omega^2}{\alpha^2}\psi_\ell^2 + \left(\mu^2 + \frac{\ell(\ell+1)}{r^2}\right)\psi_\ell^2\right], \tag{3.6a}$$

$$p_r := T^r{}_r = \frac{\kappa_\ell}{8\pi}\left[\frac{\psi_\ell'^2}{\gamma^2} + \frac{\omega^2}{\alpha^2}\psi_\ell^2 - \left(\mu^2 + \frac{\ell(\ell+1)}{r^2}\right)\psi_\ell^2\right], \tag{3.6b}$$

$$p_T := T^\theta{}_\theta = T^\varphi{}_\varphi = \frac{\kappa_\ell}{8\pi}\left[-\frac{\psi_\ell'^2}{\gamma^2} + \frac{\omega^2}{\alpha^2}\psi_\ell^2 - \mu^2\psi_\ell^2\right]. \tag{3.6c}$$

We denote by M_T the total mass of the object, given by the limit $r \to \infty$ of the function $M(r) = 4\pi\int_0^r \tilde{r}^2\,\rho(\tilde{r})\,\mathrm{d}\tilde{r}$. In the case of our numerical solutions, we approximate M_T by evaluating $M(r)$ a the outer boundary of the numerical domain (after ensuring that the mass variation is negligible near that boundary).

Each ℓ-boson star solution is uniquely determined by a given set of the parameters ℓ, μ, u_0, and a discrete set of values ω, with u_0 given by ψ_ℓ/r^ℓ evaluated at $r = 0$[2]. Given ℓ and μ, u_0 is a free parameter (which reduces to the central scalar field amplitude $\psi_c = \psi(r=0)$ for $\ell = 0$), and the ω's are the frequency eigenvalues obtained by demanding that the field vanishes at infinity and that the solution remains regular at $r = 0$. In this work we only consider the ground state for which ψ_ℓ has no nodes in the open interval $r \in (0,\infty)$, hence fixing ω for each ℓ and u_0. Finally, solutions with different μ are related to each other by a simple rescaling (see table 3.2 in appendix 3.6). Consequently, for each ℓ it is sufficient to study a one-parameter family of solutions, usually parameterized by u_0 or (equivalently) by $\alpha_0 := \alpha(r=0)$.

Since boson stars do not have a well-defined boundary, one usually describes their size by the R_{99} radius, defined as the (areal) radius of the sphere containing

[2]Note that $\psi_\ell = Ar^\ell + \mathcal{O}(r^{\ell+2})$ with constant A, such that ψ_ℓ/r^ℓ is regular at $r = 0$. In practice u_0 is evaluated either by taking the limit $r \to 0$ or by directly evaluating $u_0 = A$.

99% of the total mass M_T. In addition, we use two different measures for the star's compactness:

$$C_{99} := \frac{M_T}{R_{99}}, \tag{3.7a}$$

and

$$C_m := \max_{r>0}\left\{\frac{M(r)}{r}\right\} =: \frac{M_m}{R_m}, \tag{3.7b}$$

where we also defined R_m as the point r of maximum $M(r)/r$, and M_m as $M(r = R_m)$. To help better understand the meaning of these definitions we highlight their differences in the top panel of Fig. 3.1, where some density profiles are shown, together with vertical lines indicating the radii R_{99} and R_m for each star.

As one can appreciate from this figure, some solutions (see for instance the purple and green lines) can be interpreted as having two parts: A very compact "core", located mostly to the left of $r/R_m = 1$, plus a less dense "halo" to the right of that point. Note that the halo is much wider than the central region (a fact that might be unnoticed at a first glance since the horizontal axis is in logarithmic scale). We clearly see that the definition C_{99} is a proper indicator of the whole object's compactness, while the definition C_m is more representative of the central region's compactness. However, as we will see later, the sets of definitions $[R_{99}, M_T, C_{99}]$ and $[R_m, M_m, C_m]$ tend to coincide for larger ℓ's.[3] Although we have found the core-and-halo structure only for configurations lying on the unstable branches, the mentioned differences between these two sets are seen for stable as well as unstable solutions.

The stress tensor of a perfect fluid is isotropic, and pressure is the same in all directions of a fluid star. Even if common for some materials, isotropy is not a natural consequence of the underlying spacetime symmetries, and there exist static and spherical configurations that exhibit fractional anisotropy, defined as the relative difference between the radial and tangential components of the pressure:

$$fa = \frac{p_r - p_T}{p_r}. \tag{3.8}$$

From the right-hand sides of equations (3.6b) and (3.6c) one can see that ℓ-boson stars (including the standard $\ell = 0$ boson stars) are anisotropic. Furthermore, one might suspect that solutions with higher anisotropy will exist for the cases with non-vanishing angular momentum number, due to the presence of the centrifugal term $\ell(\ell+1)/r^2$ in p_r. We will corroborate this assertion in the next sections. This is not just a curious fact, since configurations with larger fractional anisotropy have been identified to be stable up to higher values of the central density [106], hence leading to more compact objects [107]. This enhancement in the

[3] See also Fig. 3.7 for noticeable differences between the two sets of definitions.

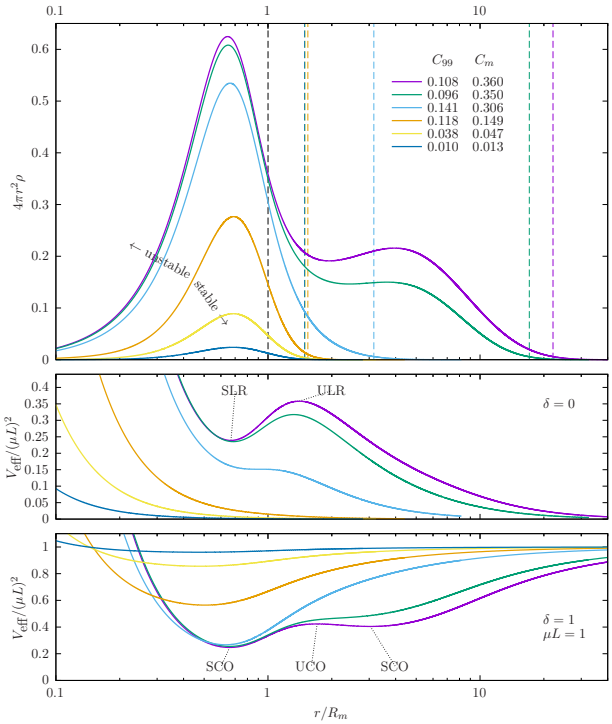

Figure 3.1: *Top panel:* For various configurations with $\ell = 1$, we show the rescaled density profile with respect to the rescaled radial coordinate $r \to r/R_m$. This rescaling provides an easier way to compare the different curves between themselves, while also allowing to easily locate R_m, given by $r/R_m = 1$ (black vertical line), as well as R_{99} (vertical lines with the same color as the corresponding solution). *Middle panel:* Effective potentials for circular null geodesics ($\delta = 0$) for the same solutions as in the top panel, displaying cases without light rings, with a pair of (stable and unstable) light rings, and the transition solution for which the (degenerate) light rings first appear. *Bottom panel:* Effective potentials for circular timelike geodesics ($\delta = 1$) with $\mu L = 1$ for the same solutions as in the other panels. The local extrema correspond to stable (minimum) and unstable (maximum) circular orbits.

allowed compactness within the stable branch is an interesting property that is also satisfied for ℓ-boson stars, as we discuss later.

It will also be helpful to identify some general properties of the motion of test particles propagating in the spacetime associated with the ℓ-boson stars, and in particular to determine whether the solutions admit innermost stable circular orbits (ISCOs) and/or light rings [93] and, if so, to find their location. Given the spacetime symmetries we can obtain the geodesics with the help of conserved quantities using the expression [66]

$$\left(\frac{\mathrm{d}r}{\mathrm{d}\lambda}\right)^2 = \frac{E^2}{\alpha^2\gamma^2} - \frac{1}{\gamma^2}\left(\delta + \frac{L^2}{r^2}\right), \tag{3.9}$$

where E and L are constants of motion (associated with the particle's energy and total angular momentum), and $\delta = 0$ for null geodesics, while $\delta = 1$ for timelike geodesics. It is convenient to introduce the effective potential

$$V_{\rm eff}(r) := \alpha^2\left(\delta + \frac{L^2}{r^2}\right), \tag{3.10}$$

leading to an equation of motion that resembles a point particle moving in a one-dimensional potential.[4] Then, orbiting particles are restricted to the regions where $V_{\rm eff}(r) < E^2$. Circular orbits can be obtained when E^2 equals a local extremum of $V_{\rm eff}$, and those orbits are stable (unstable) if said extremum is a minimum (maximum).

In the null case, the condition for circular orbits is

$$\alpha - r\,\alpha' = 0, \tag{3.11}$$

where the sign of the second derivative of the lapse function evaluated at the light ring radius determines the stability of the orbit: it is stable if α'' is negative and unstable otherwise [108]. In the timelike case the energy and total angular momentum per unit rest mass of a particle in circular motion at radius r must satisfy

$$E = \sqrt{\frac{\alpha^3}{\alpha - r\alpha'}}, \quad L = \sqrt{\frac{r^3\alpha'}{\alpha - r\alpha'}}. \tag{3.12}$$

These orbits are stable wherever $L(r)$ grows with r, whereas they are unstable otherwise [108]. For regular configurations light rings can appear only in pairs,

[4] Defining $x := \int_0^r \alpha(r)\gamma(r)\mathrm{d}r$ we can rewrite equation (3.9) as $\left(\frac{\mathrm{d}x}{\mathrm{d}r}\right)^2 = E^2 - U_{\rm eff}(x)$, where $U_{\rm eff}(x) := V_{\rm eff}[r(x)]$. Hence, in analogy with Classical Mechanics we can infer that the orbits are restricted to the regions where $U_{\rm eff} \leq E^2$, with the equality being satisfied at the turning points. Circular orbits are obtained where E^2 equals an extremum of $U_{\rm eff}$, and their stability depends on whether the extremum is a maximum or a minimum. Given that the transformation $x = x(r)$ is monotonic, the same conditions are satisfied for $V_{\rm eff}(r)$.

one of them being stable and the other unstable. Note, however, that not all stars admit light rings. On the other hand, there always exist stable circular orbits of massive particles. In particular, the existence of stable orbits is guaranteed both at large distances and close enough to the center. However, regions of instability may exist too, being delimited by innermost stable circular orbits (ISCOs) and outermost stable circular orbits (OSCOs). In a similar way, the light ring pairs delimit a region where $\alpha - r\,\alpha'$ is negative and circular orbits are not allowed at all.[5] We will now give more explicit details about these assertions.

The central panel of Fig. 3.1 illustrates distinct cases regarding the existence of light rings, as determined by equation (3.10), all with $\ell = 1$: (i) Potentials without local extrema (besides at $r = 0$). These solutions cannot have light rings. (ii) Potentials with a local minimum at some $r = r_{\rm in}$ and with a local maximum at some other $r = r_{\rm out}$, such that $r_{\rm in} < r_{\rm out}$. These solutions have a pair of light rings, a stable one at $r_{\rm in}$ and an unstable one at $r_{\rm out}$. (iii) The transition case, in which the potential have an inflection point, giving rise to degenerate light ring solutions with $r_{\rm in} = r_{\rm out}$. Note that cases (ii) and (iii) only occur for unstable spacetimes [101,102]. In a similar way, in the bottom panel of this figure we illustrate different cases regarding the existence of unstable circular orbits of massive particles with $\mu L = 1$.

Finally, we give an expression for the test particle's speed moving on a circular orbit (more precisely, the magnitude of its three-velocity as measure by a static observer located at the corresponding radius):

$$v(r) := r\frac{\mathrm{d}\phi}{\mathrm{d}t} = \sqrt{\frac{r\alpha'(r)}{\alpha(r)}}, \tag{3.13}$$

which will be used in the next section to show some rotation curves.

3.3 Extreme ℓ-boson stars

In this section we present and analyze our results. For all integer ℓ from 0 to 15, and for $\ell = 20$, 25, 50, 75, 100, 200, 400 and 1600, we constructed solutions, tens of them in some cases, that correspond to different values of the central parameter u_0. The parameters and main properties of some of the most relevant solutions that we have obtained are displayed in table 3.3 of appendix 3.6, which also includes a reference to the figures in which they are used. In addition, in the next section we obtain general expressions that are applicable for the limiting case in which $\ell \to \infty$.

We present some of our solutions in figure 3.2, where we show the rescaled density profiles (defined as $\varrho = 4\pi r^2 \rho$ such that $M = \int \varrho\,\mathrm{d}r$) associated with some

[5] We note that in all the solutions we have found $\alpha'(r) > 0$ for $r > 0$, such that the lapse is monotonously increasing.

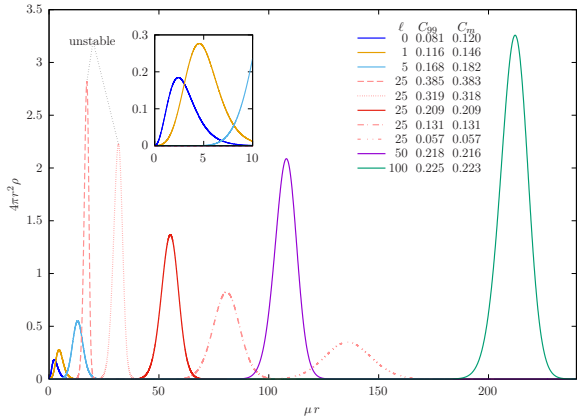

Figure 3.2: Rescaled density profiles, $4\pi r^2\rho(r)$, of solutions with maximum M_T for various values of ℓ (solid lines), and of varying compactness for fixed $\ell = 25$, both in the stable and unstable region (red lines). The inner panel shows a zoom into the small r region for a better reference of the cases with $\ell = 0$ and 1.

of our configurations.[6] Since one needs some criterion in order to compare solutions through different values of ℓ, in this case we chose to display configurations that, for each ℓ, have the maximum total mass, which are also the most compact stable solutions. This is a criterion we will adopt in most of this work. In the same figure we also show some solutions for given ℓ (= 25) and varying compactness, the more compact ones being unstable. The solutions clearly exhibit a shell-like morphology, at least for $\ell > 1$. For bigger ℓ the stars are larger both in size and in total mass. We will see that the compactness also increases with ℓ. In contrast, if one considers stars with fixed ℓ and increasing size, the compactness decreases. We also note that, as is the case for the traditional $\ell = 0$ boson stars, the most compact solutions belong to the unstable branch.

Figure 3.3 shows the dependence of the total mass on the frequency and on the R_{99} radius for $\ell = 0$, 1, 5, 25, 50 and 100. For each ℓ we indicate the maximum of M_T (squares), which we denote $M_{\max}$, and the first appearance of a light rings pair (circles) and of an ISCO-OSCO pair (triangles). We have seen in previous works [101, 102] that the state of maximum mass marks the transition from the stable solutions (to the right in these figures) to the unstable ones (to the left) for ℓ in the interval from 0 to 5. We also corroborated in the present work that this fact is still true for larger values of ℓ.

In the following subsections we analyze various properties of these solutions, including their compactness, anisotropy and causal circular orbits.

[6] Throughout this section we alternate between showing results in terms of ρ and ϱ, depending on what we find more illustrative.

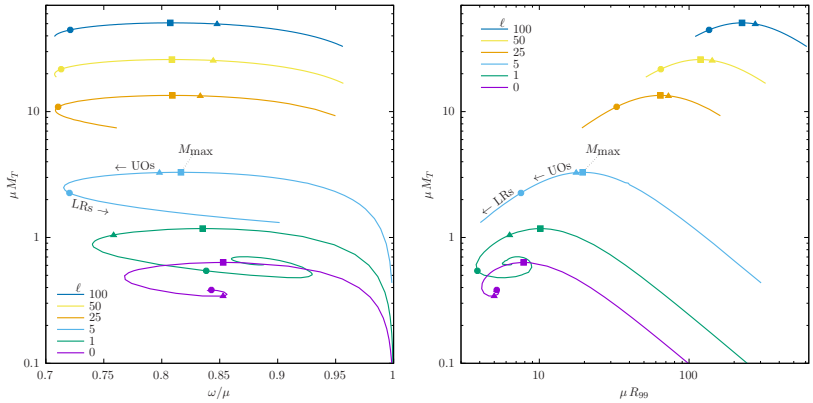

Figure 3.3: M_T vs. ω and vs. R_{99} for $\ell = 0$, 1, 5, 25, 50 and 100. Each point on these curves corresponds to a different solution, including for instance those shown in figure 3.2. The squares denote the maximum of the total mass, which separates the stable and unstable regions. The circles denote the first appearance of light rings, while the triangles denote the first appearance of an ISCO-OSCO pair and, hence, the existence of unstable orbits (UOs).

3.3.1 Compactness

In this section we explore the compactness of our solutions using the definitions of equations (3.7). As can be seen from figure 3.3, larger values of ℓ lead to solutions with higher total mass M_T. On the other hand, considering for instance the solutions of maximum mass, the radius also increases with ℓ, as can be inferred from that same figure and figure 3.2. However, the increase in mass tends to "win" over the increase in radius in such a way that their ratio, the compactness, increases with ℓ. Note that said solutions are the most compact stable ones for each ℓ.

After inspection of our solutions we note that the two mass definitions M_T and M_m from equations (3.7), as well as their associated radii R_{99} and R_m, seem to both show a linear relation with ℓ, at least at large ℓ ($\ell \gtrsim 10$). This can be seen in the first two panels of figure 3.4. Once again, in order to compare configuration with different ℓ's between each other, we have chosen those solutions with maximum total mass $M_{\max}$ for each ℓ.

The apparent linear dependence in ℓ suggests that simple expressions can be obtained by performing linear fits. We show the results of said fits in the figure (continuous lines), together with the fit coefficients (a to d) and their respective errors. Keeping only two significant figures and omitting the errors we can write:

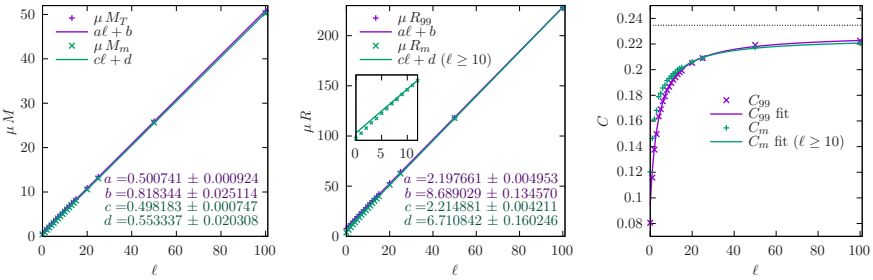

Figure 3.4: We show the dependence on ℓ of the stars' mass, radius and compactness. All quantities shown here correspond to the solution of maximum M_T for each value of ℓ. *Left panel:* M_T and M_m, together with the corresponding linear fits. *Center panel:* R_{99} and R_m, together with their linear fit. In the case of R_m we do the linear fit only to the points with $\ell \geq 10$, which is the region where we actually see a linear dependence. *Right panel:* Compactness C_m and C_{99}, and, in each case, the compactness calculated from the fits of the previous panels. We also indicate the asymptotic value as a dotted line (see section 3.4).

$$\mu M_T \approx 0.50\,\ell + 0.82, \tag{3.14a}$$

$$\mu M_m \approx 0.50\,\ell + 0.55, \tag{3.14b}$$

$$\mu R_{99} \approx 2.2\,\ell + 8.7, \tag{3.14c}$$

$$\mu R_m \approx 2.2\,\ell + 6.7. \tag{3.14d}$$

From here, expressions for our two definitions of compactness can be found by taking the quotient of each M vs. R pair. Said quotients, i.e. C_{99} and C_m, are shown in the last panel of figure 3.4. The point values shown in that panel are obtained by taking individually the quotient of the corresponding data pairs that appear in the first panels, while the continuous line represent the quotient of the linear fit's expressions.

The almost linear relations shown in the first two panels of figure 3.4 suggest that solutions might have simple rescaling properties with ℓ, at least at large enough ℓ. A more detailed analysis of such scaling properties will be given in section 3.4, where we will see that an asymptotic value can be obtained for the compactness at large ℓ. That value is indicated in the right panel of figure 3.4 as a dotted line. Note that initially the compactness increases rapidly with ℓ, and continues to rise monotonically, remaining close to and below the asymptotic value derived in section 3.4.

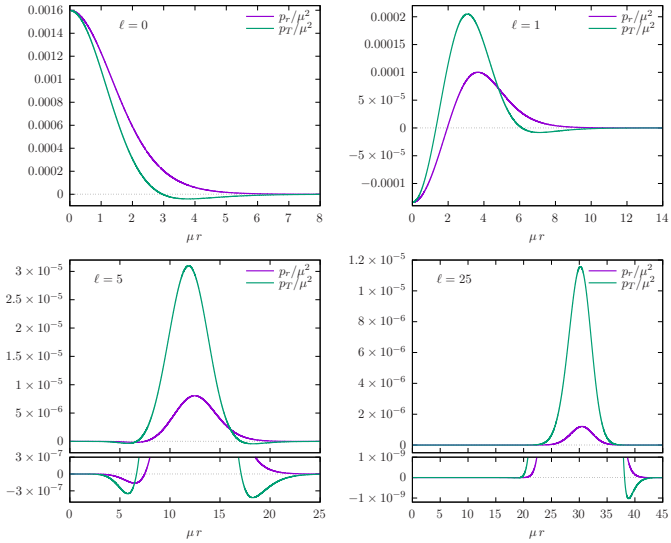

Figure 3.5: Radial and tangential pressures vs. radial coordinate for the solutions of maximum M_T in the cases of $\ell = 0$, 1, 5 and 25. We see that the tangential pressure becomes larger and larger relative to the radial pressure when ℓ increases.

3.3.2 Anisotropy

We move now to the description of the stars' anisotropy. In figure 3.5 we show the pressure profiles for $\ell = 0$, 1, 5 and 25, in all cases for the solution of maximum mass $M_{\max}$. Notice how different the profiles are for $\ell = 0$, $\ell = 1$, and $\ell > 1$. The typical $\ell = 0$ "solid-sphere" star has $p_r > p_T$, while for larger ℓ's the "shell-like" stars have mostly $p_r < p_T$, with this difference becoming more pronounced the higher the value of ℓ. This behavior seems intuitively natural given the stars' morphology. As ℓ increases, the "shells" become larger, as well as thinner relative to their radius, in such a way that the tangential pressure has to become larger relative to the radial one in order to support the configuration.

In figure 3.6 we show parametric plots of $[p_r, p_T]$ vs. r, in which the larger the deviation from the identity $p_r = p_T$ (shown as a dotted line of unit slope), the larger the anisotropy. Additionally, we indicate the density as a color map, as well as the compactness in each case. The differences at the starting points of these curves, which correspond to the pressure values at the origin $r = 0$, are consistent with the stars' shape as seen in our previous work: while they are "empty" at the center when $\ell > 1$, they have maximum density there when $\ell = 0$, as is a well known property of standard boson stars. In the intermediate case, $\ell = 1$, the density is greater than zero at the center, but it does not reach its maximum value at that point. It is also clear from these plots that the anisotropy, as well as

the compactness, grow with ℓ, the tangential pressure becoming larger and larger compared to the radial pressure. In section 3.4 we will see that the limiting case $\ell \to \infty$ would display a vertical line in this type of plot. On the other hand, we see little differences in anisotropy when transitioning between stable and unstable solutions for any given value of ℓ.

3.3.3 Geodesic motion

Given the large compactness that ℓ-boson stars may achieve, one may wonder whether they admit light rings and/or ISCOs/OSCOs. In fact, it is known that even traditional $\ell = 0$ boson stars can have light rings and ISCOs/OSCOs, although this is true only in the case of solutions located very deep into the unstable region[7]. In the remainder of this section we will analyze the appearance of light rings and ISCOs/OSCOs, paying particular attention to their relation with compactness and stability of the underlying spacetime solutions.

In figure 3.3 we indicated with a circle the point corresponding to the first, or less compact, solutions containing a pair of light rings. In all the cases we studied, such solutions are always in the unstable region, although they get closer to the stable region as ℓ increases. It is unclear, however, whether light rings may be found in the stable region for large enough ℓ, although one would expect that this is not the case given that the maximum compactness that a stable ℓ-boson star is able to achieve, $C \approx 0.235$, is far from the expected one for the appearance of light rings, $C = 1/3$. The results presented in [109] seem to indicate that light rings can only exist for unstable solutions. Another matter of astrophysical interest is whether such unstable solutions have a relatively short or a rather long life-time. However, this question goes beyond the scope of the present chapter, so we leave it for future work.

Regarding the existence of ISCOs, we also indicated in figure 3.3 the first appearance of an ISCO-OSCO pair (triangles). We see that for large enough ℓ these pairs can also exist in the case of stable spacetime solutions. In fact, we have found that the smallest ℓ for which stable ℓ-boson stars with ISCO-OSCO pairs exist is $\ell = 9$.

We now go into more detail and analyze the different stability regions in figure 3.7, where we show plots of radius vs. compactness for $\ell = 0$, 1, 5 and 25. Each vertical line in these plots corresponds to a solution, and we can see the transitions through different stability regions as r varies along said line. The green regions are those where the timelike circular orbits are stable (SCOs). The red region is where the circular orbits are unstable (UCOs), and it is delimited by an ISCO at the top and by an OSCO at the bottom. Similarly, the dark gray region is that for which no circular orbitss exist, and it is delimited by a pair of light

[7] Note that the situation may change when non-canonical kinetic terms are considered [108].

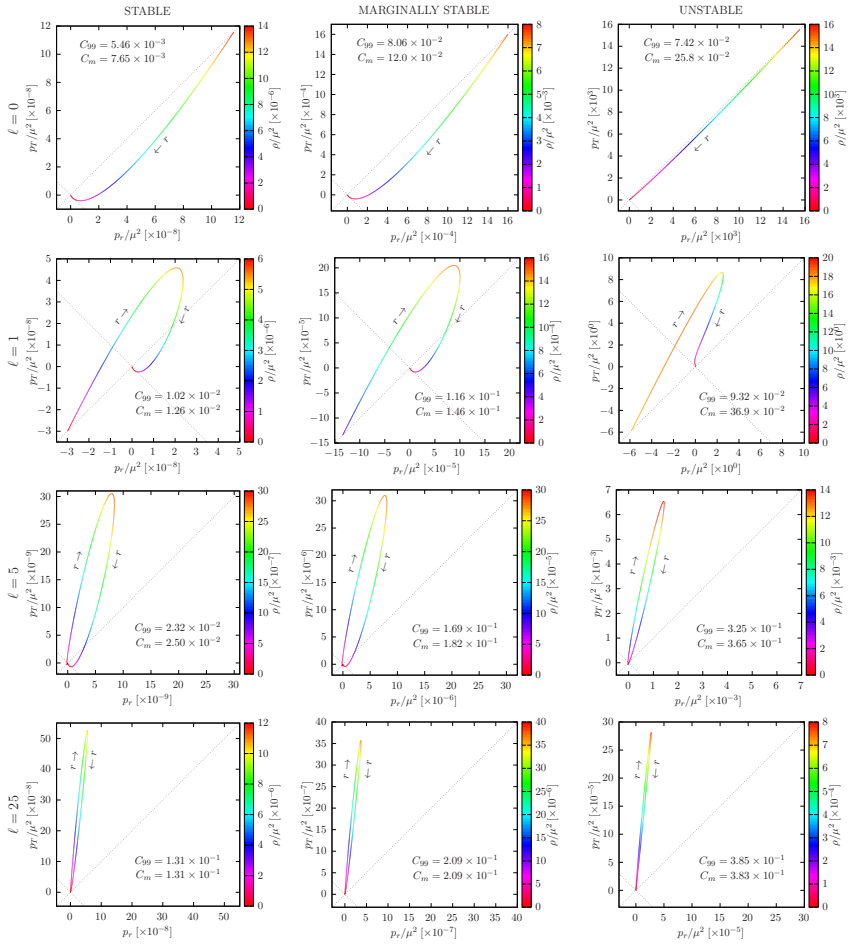

Figure 3.6: Parametric plots of $[p_r, p_T](r)$. Each row corresponds to a value of ℓ, while each column corresponds to a stability type. These figures are particularly well suited for analyzing the pressure anisotropies, measured by the deviation from the identity $p_r = p_T$. The value of the density ρ along the curves is indicated with a color map. The direction of growing r is also indicated. To help guide the eye, the curves $p_r = \pm p_T$ are shown as dotted lines, and the same scale was used in each pair of axes.

rings, indicated with a red line. Since ℓ-boson stars are shell like for $\ell > 1$, with density much smaller than its maximum value and falling quickly towards the center in the interior region –where the spacetime is very close to Minkowski– the circular orbits are almost non-existent there, having speed $v \ll 1$. To make this more apparent we shaded in a darker green the regions in which $v < 10^{-5}$, noting that the rotation curves of these configurations have a maximum in the interval $0.4 \lesssim v < 1$ (see figure 3.8).

Figure 3.7 also indicates the stars' radii, R_{99} and R_m, and also, as a guide, the limit of spacetime stability (vertical dotted line) and the locations of the Schwarzschild ISCO and light ring, given by $r = 6M$ and $r = 3M$, respectively, where for the value of M we used both M_T and M_m. We see that, as the compactness increases, the light rings first appear at or very close to R_m, and soon they move to each side of that location. For small ℓ the definition R_m seems more meaningful than R_{99} when comparing to the location of light rings. On the other hand, both definitions tend to coincide at large ℓ.

Although all the solutions with light rings found in this work are unstable, we see that, for larger values of ℓ, solutions with light rings exist closer and closer to the stable region. However, as mentioned earlier, it is unlikely that stable solutions with light rings exist, even for extremely large ℓ.

Interestingly, the unstable circular orbit regions for large ℓ tend to be delimited almost exactly by the star's radius (from below) and the Schwarzschild ISCO (from above). We can see again in the last panel of figure 3.7 ($\ell = 25$) that regions of instability can exist even for stable ℓ-boson star spacetimes. As already mentioned, this happens for solutions starting at $\ell = 9$. This could constitute an observable feature that might help distinguish some ℓ-boson stars from other dark compact objects.

In figure 3.8 we show the rotation curves for the solutions shown in figure 3.2, that is: solutions of maximum M_T for $\ell = 0$, 1, 5, 25, 50 and 100; and for $\ell = 25$, also some solutions with varying compactness, both in the stable and unstable spacetime branch. The curves have been extended beyond the domain of numerical integration using the Schwarzschild expressions with mass M_T. We can see that this gives and excellent match. The points where the curves reach $v = 1$ correspond to light rings, and no circular orbits exist in the region in between those points (red line and dark gray region of figure 3.7). We also indicate the regions where the circular orbits are unstable (thick gray line).

3.4 Scaling properties for large ℓ

In this section we discuss the scaling properties of the fields in the asymptotic limit $\ell \to \infty$. This is achieved by rescaling the fields $(M, \alpha, \gamma, \psi)$ and by shift-

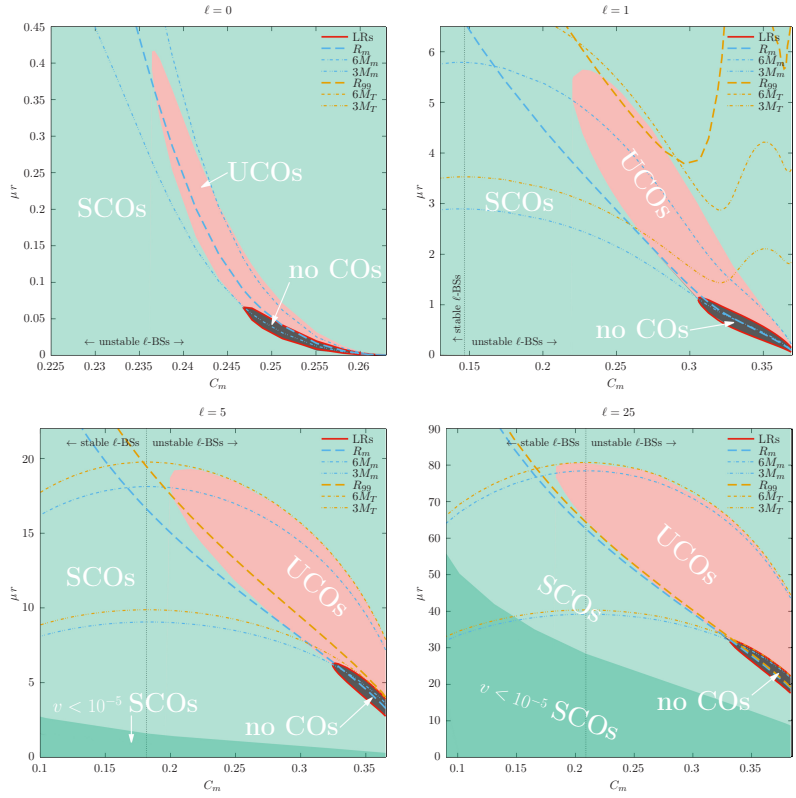

Figure 3.7: For solutions of high compactness we indicate the regions of existence and stability of causal circular orbits (COs). In these plots, each vertical line of constant C_m corresponds to a different solution. The green regions indicate the radii with stable (timelike) circular orbits (SCOs), while the red region indicates those with unstable orbits (UCOs). On the other hand, no COs exist in the dark gray region, which is limited by a pair of light rings (LRs), red line. Finally, the dark green region indicates the "almost empty, almost flat" central region of the $\ell > 1$ "shells", where the circular orbits have speed $v < 10^{-5}$. We also include as a guide R_{99}, R_m, and the corresponding locations of a Schwarzschild LR and ISCO.

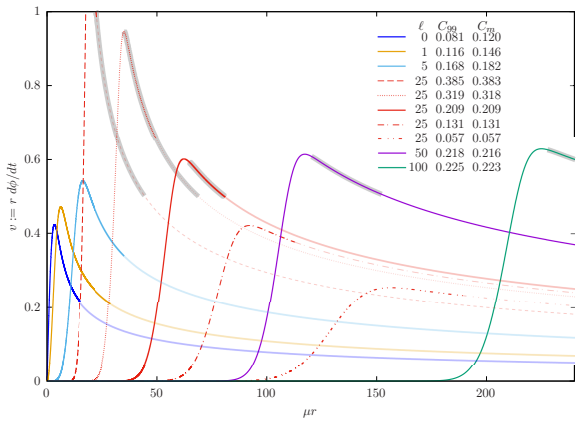

Figure 3.8: Rotation curves as defined by equation (3.13). The solid lines correspond to solutions with maximum M_T for ℓ ranging from 0 to 100. For $\ell = 25$ we also show, in red, some cases with varying compactness around the maximum M_T solution. Beyond the numerical integration region, we extended the curves using the Schwarzschild spacetime with mass M_T. Those parts of the curves are shown in a lighter color. Thick gray lines indicate regions where the circular orbits are unstable. The solutions represented here are the same as those in figure 3.2.

ing and rescaling the radial coordinate r in an appropriate way (which is largely motivated by the empirical numerical data and trial-and-error) such that, when taking the limit $\ell \to \infty$, one obtains a set of effective field equations which can be solved separately. As we show, combining the solution of these effective equations with the aforementioned rescaling, one obtains the correct asymptotic behavior for the fields and related quantities for large values of ℓ. For clarity, we include a summary of these results in the final paragraph of this section.

To describe our scaling method, we consider a family of configurations with increasing value of ℓ and fixed ω. As ℓ becomes large, the numerical data (see figure 3.9) suggests that the fields' profiles depend only on the variable

$$y := \frac{r - \ell x_0}{\ell^a}, \tag{3.15}$$

with x_0 a positive constant that depends on ω but not ℓ, and a a parameter within the range $0 < a < 1$ that will be determined later. This means that the profiles have their center shifted outwards by ℓx_0 and stretched by the factor ℓ^a as $\ell \to \infty$. The fields' amplitudes are rescaled as follows:

$$M_*(y) := \frac{M(r)}{\ell}, \qquad \alpha_*(y) := \alpha(r) \qquad \gamma_*(y) := \gamma(r) \qquad \psi_*(y) := \ell^{1+\frac{a}{2}} \psi_\ell(r), \tag{3.16}$$

the data suggesting that the quantities with a star have finite limits when $\ell \to \infty$. Note that equations (3.15,3.16) and the definition of γ in equation (3.4) imply that

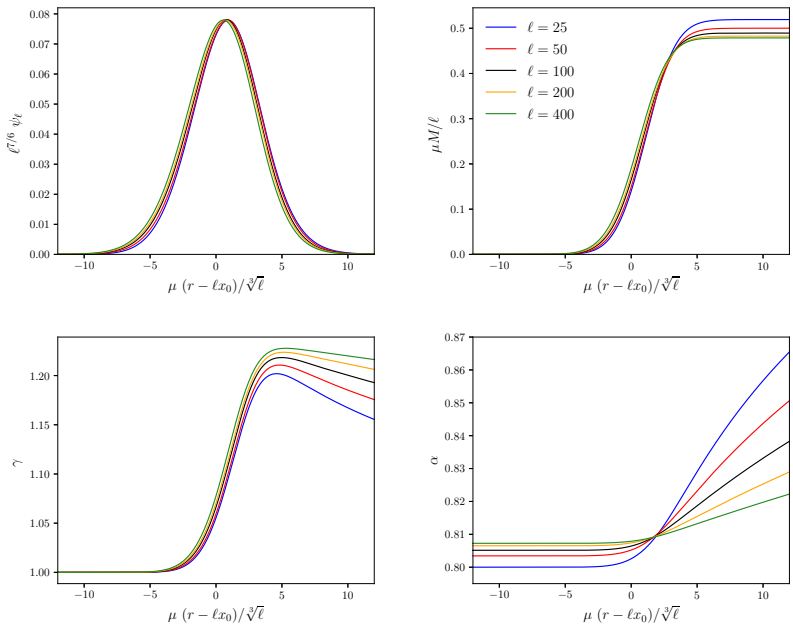

Figure 3.9: Scaling of the solutions with $\omega = 0.8612$, for the quantities ψ_ℓ, $M(r)/\ell$, γ and α. In these plots, the constant x_0 appearing on the horizontal axis has been estimated using as reference the $\ell = 1600$ configuration with the same ω, using the formula $x_0 = r_{1600}/1600$, with r_{1600} defined as the location of the maximum of $\psi_{1600}(r)$. The procedure to determine x_0 without resorting to any particular finite ℓ solution is explained in the text.

$$\gamma_*^{-2}(y) = 1 - \frac{2M_*(y)}{x_0}\frac{1}{1+\ell^{a-1}\frac{y}{x_0}}, \tag{3.17}$$

such that in the limit $\ell \to \infty$ (with fixed y) it follows that $\gamma_*^{-2}(y) = 1 - 2M_*(y)/x_0$. In terms of the rescaled quantities M_*, α_* and ψ_* equations (3.5) can be written as

$$\frac{\mathrm{d}M_*}{\mathrm{d}y} = x_0^2\left(1+\ell^{a-1}\frac{y}{x_0}\right)^2\rho_*, \tag{3.18a}$$

$$\frac{1}{\gamma_*^2\alpha_*}\frac{\mathrm{d}\alpha_*}{\mathrm{d}y} = x_0\left(1+\ell^{a-1}\frac{y}{x_0}\right)p_{r*} + \frac{M_*}{x_0^2}\frac{\ell^{a-1}}{\left(1+\ell^{a-1}\frac{y}{x_0}\right)^2}, \tag{3.18b}$$

$$\frac{1}{\alpha_*\gamma_*}\frac{\mathrm{d}}{\mathrm{d}y}\left(\frac{\alpha_*}{\gamma_*}\frac{\mathrm{d}\psi_*}{\mathrm{d}y}\right) \tag{3.18c}$$

$$+\frac{2}{x_0}\frac{\ell^{a-1}}{1+\ell^{a-1}\frac{y}{x_0}}\frac{1}{\gamma_*^2}\frac{\mathrm{d}\psi_*}{\mathrm{d}y} = -\ell^{2a}\left[\frac{\omega^2}{\alpha_*^2} - \mu^2 - \frac{1}{x_0^2}\frac{1+\frac{1}{\ell}}{\left(1+\ell^{a-1}\frac{y}{x_0}\right)^2}\right]\psi_*,$$

where we have introduced the rescaled energy density and radial pressure

$$\rho_*(y) := 4\pi\ell^{1+a}\rho(r) \tag{3.19a}$$

$$= \left(1+\frac{1}{2\ell}\right)\left[\ell^{-2a}\frac{1}{\gamma_*^2}\left(\frac{\mathrm{d}\psi_*}{\mathrm{d}y}\right)^2 + \left(\frac{\omega^2}{\alpha_*^2} + \mu^2 + \frac{1}{x_0^2}\frac{1+\frac{1}{\ell}}{\left(1+\ell^{a-1}\frac{y}{x_0}\right)^2}\right)\psi_*^2\right],$$

$$p_{r*}(y) := 4\pi\ell^{1+a}p_r(r) \tag{3.19b}$$

$$= \left(1+\frac{1}{2\ell}\right)\left[\ell^{-2a}\frac{1}{\gamma_*^2}\left(\frac{\mathrm{d}\psi_*}{\mathrm{d}y}\right)^2 + \left(\frac{\omega^2}{\alpha_*^2} - \mu^2 - \frac{1}{x_0^2}\frac{1+\frac{1}{\ell}}{\left(1+\ell^{a-1}\frac{y}{x_0}\right)^2}\right)\psi_*^2\right].$$

Let us consider the limiting case $a = 0$ first and take the limit $\ell \to \infty$ in these equations (with y held fixed). In this case, one obtains the effective equations

$$\frac{\mathrm{d}M_\infty}{\mathrm{d}y} = x_0^2\rho_\infty, \qquad \rho_\infty = \frac{1}{\gamma_\infty^2}\left(\frac{\mathrm{d}\psi_\infty}{\mathrm{d}y}\right)^2 + \left(\frac{\omega^2}{\alpha_\infty^2} + \mu_0^2\right)\psi_\infty^2, \tag{3.20a}$$

$$\frac{1}{\gamma_\infty^2\alpha_\infty}\frac{\mathrm{d}\alpha_\infty}{\mathrm{d}y} = x_0 p_{r\infty}, \qquad p_{r\infty} = \frac{1}{\gamma_\infty^2}\left(\frac{\mathrm{d}\psi_\infty}{\mathrm{d}y}\right)^2 + \left(\frac{\omega^2}{\alpha_\infty^2} - \mu_0^2\right)\psi_\infty^2, \tag{3.20b}$$

$$\frac{1}{\alpha_\infty\gamma_\infty}\frac{\mathrm{d}}{\mathrm{d}y}\left(\frac{\alpha_\infty}{\gamma_\infty}\frac{\mathrm{d}\psi_\infty}{\mathrm{d}y}\right) = -\left(\frac{\omega^2}{\alpha_\infty^2} - \mu_0^2\right)\psi_\infty, \tag{3.20c}$$

where the index ∞ refers to the (pointwise) limit for $\ell \to \infty$, i.e. $M_\infty(y) = \lim_{\ell\to\infty} M_*(y)$ and similarly for α_∞, γ_∞ and ψ_∞. We have also introduced the shorthand notation $\mu_0 := \sqrt{\mu^2 + 1/x_0^2}$ in order to abbreviate the notation. Equations (3.20) look

like a nice system of differential equations for $(M_\infty, \alpha_\infty, \psi_\infty)$ which could be integrated numerically and whose solution with the appropriate boundary conditions should approximate the solution of the full system when ℓ is large and $|y| \lesssim \ell$. However, it is not difficult to show that these equations imply that

$$\alpha_\infty \gamma_\infty p_{r\infty} = \text{const}, \tag{3.21}$$

and by virtue of the boundary conditions this constant must be zero. Therefore, $p_{r\infty} = 0$ which implies that α_∞ is constant and $\omega^2/\alpha_\infty^2 - \mu_0^2 < 0$. Then, multiplying both sides of equation (3.20c) with ψ_∞, integrating over y and using integration by parts reveals that $\psi_\infty = 0$ is the only solution which decays to zero as $y \to \pm\infty$. This indicates that the choice $a = 0$ in the rescaling (3.15) is not the correct one.

Therefore, let us assume that $0 < a < 1$ is strictly positive and take again the pointwise limit $\ell \to \infty$ in equations (3.18). This yields

$$\frac{\mathrm{d}M_\infty}{\mathrm{d}y} = x_0^2 \rho_\infty, \qquad \rho_\infty = \left(\frac{\omega^2}{\alpha_\infty^2} + \mu_0^2\right)\psi_\infty^2, \tag{3.22a}$$

$$\frac{1}{\gamma_\infty^2 \alpha_\infty}\frac{\mathrm{d}\alpha_\infty}{\mathrm{d}y} = x_0 p_{r\infty}, \qquad p_{r\infty} = \left(\frac{\omega^2}{\alpha_\infty^2} - \mu_0^2\right)\psi_\infty^2, \tag{3.22b}$$

while the rescaled Klein-Gordon equation (3.18c) implies that $p_{r\infty}$ must vanish in order for the right-hand side to be finite. It follows that

$$\alpha_\infty = \frac{\omega}{\mu_0} \tag{3.23}$$

is constant and that

$$\frac{\mathrm{d}M_\infty}{\mathrm{d}y} = 2x_0^2\mu_0^2\psi_\infty^2 = 2(1+\mu^2 x_0^2)\psi_\infty^2. \tag{3.24}$$

The problem is that (so far) we have no differential equation for ψ_∞. However, a differential equation for ψ_∞ can be obtained by expanding the rescaled fields:

$$\psi_*(y) = \psi_\infty(y) + \varepsilon\psi_1(y) + \mathcal{O}(\varepsilon^2), \tag{3.25}$$

and similarly for M_* and α_* in powers of $\varepsilon = \varepsilon(\ell)$ and looking at the next-order contributions from equations (3.18). For the following, we choose $\varepsilon(\ell) = \ell^{a-1}$ since most of these corrections terms are of this order, and we expand the rescaled lapse in the form

$$\alpha_*(y) = \alpha_\infty\left[1 + \ell^{a-1}\delta(y) + \mathcal{O}(\ell^{-1})\right], \tag{3.26}$$

with the function $\delta(y)$ describing the first-order correction. Using equation (3.23) the right-hand side of equation (3.18c) gives, to leading order in $1/\ell$,

$$2\ell^{3a-1}\left(\mu_0^2\delta - \frac{y}{x_0^3}\right)\psi_\infty, \tag{3.27}$$

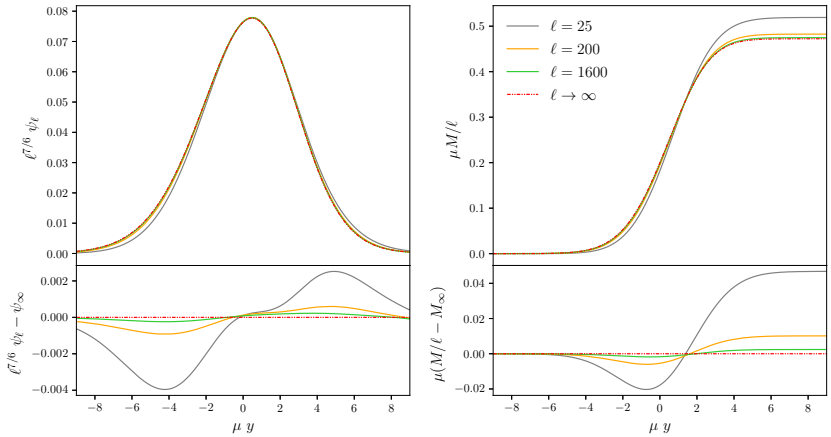

Figure 3.10: Solutions with $\ell \gg 1$ compared to the same $\omega = 0.8612$ solution obtained from the effective ($\ell \to \infty$ limit) equations (3.24,3.28). The asymptotic solution $\ell \to \infty$ yields the value $x_0 = 2.73$. In the bottom panels we show the difference between the finite ℓ configurations and the $\ell \to \infty$ case, which converges to zero.

which yields a finite contribution if $a = 1/3$. Choosing $a = 1/3$ in the expansion (3.26), equations (3.18b,3.18c) yield the two differential equations

$$\frac{1}{\gamma_\infty^2}\frac{\mathrm{d}\delta}{\mathrm{d}y} = x_0\left[\frac{1}{\gamma_\infty^2}\left(\frac{\mathrm{d}\psi_\infty}{\mathrm{d}y}\right)^2 - 2\left(\mu_0^2\delta - \frac{y}{x_0^3}\right)\psi_\infty^2\right] + \frac{M_\infty}{x_0^2}, \tag{3.28a}$$

$$\frac{1}{\gamma_\infty}\frac{\mathrm{d}}{\mathrm{d}y}\left(\frac{1}{\gamma_\infty}\frac{\mathrm{d}\psi_\infty}{\mathrm{d}y}\right) = 2\left(\mu_0^2\delta - \frac{y}{x_0^3}\right)\psi_\infty, \tag{3.28b}$$

which can be integrated along with equation (3.24) and $\gamma_\infty^{-2} = 1 - 2M_\infty/x_0$ in order to find $(M_\infty, \delta, \psi_\infty)$. Note that the expression inside the square parenthesis on the right-hand side of equation (3.28a) is the $\ell^{-2/3}$-contribution to p_{r*}.

The rescaled equations (3.24,3.28) are solved on a finite interval $[y_L, y_R]$ with $y_L < 0 < y_R$, fixing the left boundary conditions $M_* = 0$, $\delta = 0$, $\psi_* = \psi_{*L}$ at $y = y_L$ and the right boundary condition $\psi_* \sim 0$ at $y = y_R$. The integration is carried out by means of a shooting method from left to right, where ψ_* is fixed at y_L and the value of x_0 for which the field matches the boundary condition at y_R is searched for. In this procedure, it is necessary to provide the value of $d\psi_*/dy$ at y_L given ψ_{*L}; this can be done by studying the asymptotic behavior $y \to -\infty$ of the rescaled equations. It is obtained that the scalar field takes the form $\psi_* \propto \mathrm{Ai}(z) \approx \exp(-\frac{2}{3}z^{3/2})/z^{1/4}$ with $z = -\sqrt[3]{2}y/x_0$ and Ai the Airy function of the first kind, obtaining $d\psi_*/dy \approx (\sqrt{-2y/x_0^3} - 1/(4y))\psi_*$.

After x_0 is found, the total mass of the solution is obtained by evaluating

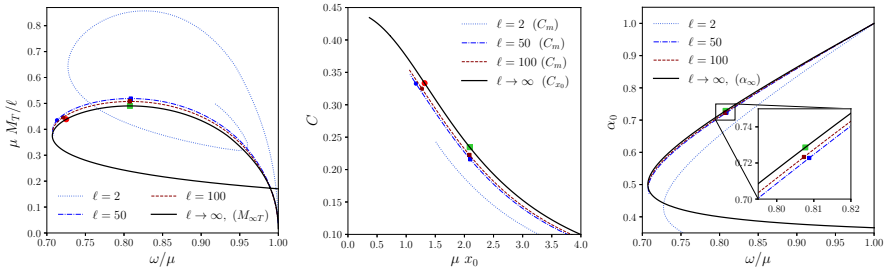

Figure 3.11: Equilibrium $\ell \gg 1$ configurations. Left panel: Total mass *vs.* the frequency ω/μ. Center panel: Compactness C_{x_0} for the $\ell \to \infty$ limit. Right panel: Minimum of the lapse $\alpha_0 = \alpha(r=0)$ *vs.* ω/μ. The green square represents the maximum ($\ell \to \infty$) configuration and the red circle denotes the first appearance of light rings, at $C_{x_0} = 1/3$.

$M_{\infty T} := M_\infty(y = y_R)$. Outside the spherical shell, at $y = y_R$, we evaluate $\alpha_\infty = 1/\gamma_\infty(y_R)$ and calculate ω from equation (3.23). Once the pair (ω, x_0) is obtained from the effective equations, we can compare the fields with those corresponding to the same ω finite ℓ solutions. Notice that there is no loss in generality in choosing $\delta(y_L) = 0$ since the system (3.24,3.28) is invariant under the transformation $(y,\delta) \mapsto (y-\zeta, \delta - \zeta/(\mu_0^2 x_0^3))$ with M_∞ and ψ_∞ unchanged. In fact, as the lower right panel of figure 3.9 shows, the δ correction to α is not zero in the inner shell region. In turn, the previous transformation will translate horizontally the scalar field profile. So there are two ways to calculate ζ, the first is to take a solution with large ℓ and find the value of the δ correction within the shell, the second is to use the scalar field profile and make the maxima of ψ_* of the large ℓ solution and the effective $\ell \to \infty$ solution to overlap; these two forms are equivalent.

We illustrate the fields' rescaling in figure 3.10, showing convergence to the limiting $\ell \to \infty$ case, as expected. We have found that the value of x_0 that corresponds to a solution with the frequency of the previous (stable branch) figure 3.9 configurations, $\omega = 0.8612$, is $x_0 = 2.73$. The estimated value for the α correction in this case is $\zeta = 2.17$. It is found that for this ζ value, the maxima of ψ_* overlap, as expected. Figure 3.11 shows a plot for certain global quantities of the equilibrium solutions of the rescaled $\ell \to \infty$ limit. The left panel shows that a critical mass solution, $M_{\infty T} = 0.49031$, is obtained at $\omega = 0.8077$ (marked with a green square). This solution is obtained for the values $x_0 = 2.0902$ and $\zeta = 1.58$.

Next, we evaluate the anisotropy and compactness of this particular configuration. In contrast to the rescaled radial pressure (3.19b), the rescaled tangential pressure

$$p_{T*}(y) := 4\pi \ell^{1+a} p_T = \left(1 + \frac{1}{2\ell}\right)\left[-\ell^{-2a}\frac{1}{\gamma_*^2}\left(\frac{\mathrm{d}\psi_*}{\mathrm{d}y}\right)^2 + \left(\frac{\omega^2}{\alpha_*^2} - \mu^2\right)\psi_*^2\right], \qquad (3.29)$$

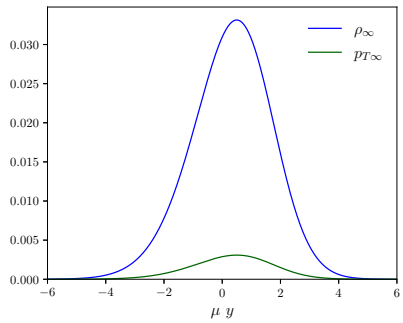

Figure 3.12: Rescaled energy density and tangential pressure for the $\ell \to \infty$ maximum mass solution. Notice that p_T is always positive, while p_r is strictly zero in this limit.

does not vanish in the pointwise $\ell \to \infty$ limit:

$$p_{T\infty} = \left(\frac{\omega^2}{a_\infty^2} - \mu^2\right)\psi_\infty^2 = \frac{\psi_\infty^2}{x_0^2}, \tag{3.30}$$

which is consistent with the observations made in section 3.3.2.

We show in figure 3.12 a plot for the tangential pressure as well as the rescaled energy density, equation (3.22a), for the solution of maximum mass. Now, to determine the compactness of these solutions, the easiest way is to note that the quotient $M(r)/r$ in terms of the rescaled quantities in equations (3.15,3.16), reduces to $M_\infty(y)/x_0$ in the $\ell \to \infty$ limit, allowing us to define,

$$C_{x_0} := \frac{M_{\infty T}}{x_0}. \tag{3.31}$$

In the central panel of figure 3.11 we show the x_0 value of the solution as a function of the compactness C_{x_0} (and C_m for the finite ℓ solutions). For the maximum mass solution, the compactness obtained is $C_{x_0} = 0.234554$. Like the finite ℓ solutions, the compactness increases as the value of the boson star radius decreases, approaching the limit value of 0.5. However, the $\ell = \infty$ solutions with compactness exceeding $\simeq 0.433$ have frequencies ω larger than μ, and thus they do not correspond to a limit of solutions with finite ℓ which must have $\omega/\mu < 1$ due to the exponential decay of the scalar field at spatial infinity.

Next, we wonder about the presence of light rings for the $\ell \gg 1$ configurations. As stated above, the existence of these rings is given by the existence of local extrema of V_{eff}. For large ℓ the effective potential for null geodesics is

$$V_{\text{eff}}(r) = L^2\frac{a^2}{r^2} = \frac{L^2}{\ell^2}\frac{a_\infty^2}{x_0^2}\left[1 + \frac{2}{\ell^{2/3}}\left(\delta(y) - \frac{y}{x_0}\right) + \mathcal{O}\left(\frac{1}{\ell}\right)\right]. \tag{3.32}$$

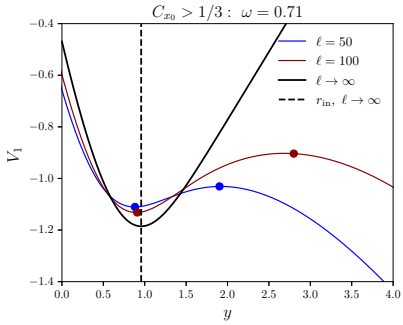

Figure 3.13: Effective rescaled potential V_1 for circular null geodesics for $\ell = 50, 100$ solutions together with the $\ell \to \infty$ case. The circles indicate the position of the light rings.

For the following it is convenient to introduce the rescaled potential V_1, defined as

$$V_1(y) := \ell^{2/3}\left(\frac{x_0^2}{\alpha_\infty^2}\frac{\ell^2}{L^2}V_{\rm eff}(r) - 1\right) = 2\left(\delta(y) - \frac{y}{x_0}\right) + \mathcal{O}\left(\frac{1}{\ell^{1/3}}\right). \tag{3.33}$$

Figure 3.13 shows the function $V_1(y)$ for $\ell = 50$ and $\ell = 100$ along with the $\ell \to \infty$ limit. Starting from the knowledge of $\delta(y)$ we can obtain the approximate location of $r_{\rm in}$, the inner light ring for $\ell \gg 1$ solutions. However, as shown in figure 3.13 at this order one is unable to determine the position of the outer ring which moves away from $y = 0$ as ℓ increases; in fact, it seems that the location of this second light ring diverges to $y \to \infty$ when $\ell \to \infty$. Evaluating the condition $dV_1/dy = 0$ along the $\ell \to \infty$ family of configurations we obtain that the solution closest to the critical mass point satisfying this condition for some value of y, is the one that has compactness $C_{x_0} = 1/3$ (red dot in figure 3.11). This correspond to the solution with $x_0 = 1.32$ and $\omega = 0.7251$.

To close the discussion of this section on the rescaling properties for large ℓ, we list the transformations involving certain relevant quantities mentioned in the previous paragraphs. To do this, suppose the situation in which an ℓ-boson star solution has been obtained for a certain value of ω and sufficiently large $\ell = \ell_1$; then starting from it we can obtain an approximate solution with arbitrarily large $\ell = \ell_2 > \ell_1$ for the same ω in the following way: first, identify the position r of the maximum of ψ_ℓ and estimate[8] $x_0 = r/\ell_1$. Then, apply the transformation $r \mapsto \sqrt[3]{\ell_2/\ell_1}(r - \ell_1 x_0) + \ell_2 x_0$. As function of this redefined coordinate r, the amplitude of the scalar field becomes smaller according to $\psi_{\ell_1}(r) \mapsto \psi_{\ell_2}(r) = (\ell_1/\ell_2)^{7/6}\psi_{\ell_1}(r)$ while the mass function grows as $M(r) \mapsto (\ell_2/\ell_1)M(r)$. The energy density and the

[8]The error induced by this estimation as well as the following ones presented in this paragraph is of the order $\ell_1^{-2/3}$.

tangential pressure both decrease according to $\rho(r) \mapsto (\ell_1/\ell_2)^{4/3}\rho(r)$ and $p_T(r) \mapsto (\ell_1/\ell_2)^{4/3}p_T(r)$. On the other hand, the mass, radius and compactness parameters rescale as follows: $(M_T, R_{99}, C_{99}) \mapsto (\ell_2/\ell_1 M_T, \ell_2/\ell_1 R_{99}, C_{99})$ and $(M_m, R_m, C_m) \mapsto (\ell_2/\ell_1 M_m, \ell_2/\ell_1 R_m, C_m)$. Let this example above serve as an illustration of the rescaling properties; certainly a better way to obtain a solution with $\ell = \ell_2$ is to solve the effective equations and then obtain the quantities with finite ℓ by inverting the definitions of the rescaled variables. In this case the error would be of order $\ell_2^{-2/3}$ or even smaller for some of the quantities.

3.5 Conclusions

We have studied various properties of the recently introduced ℓ-boson stars [99], analyzing in each case the role played by the angular momentum parameter ℓ, and paying particular attention to the large ℓ regime. These objects are composed of $2\ell+1$ massive complex scalar fields and present notable characteristics which single them out from the standard $\ell = 0$ boson stars, while still sharing with them several common features [99, 101–104]. Among these features are the fact that both are formed with complex scalar fields on a spherically symmetric spacetime; they both admit diluted and compact solutions; and they possess stable and unstable branches separated by the solution of maximum mass for a given ℓ. On the other hand, we had previously [99, 101, 102] observed some characteristics related to the ℓ parameter: an increase in the compactness and size of the maximum mass configurations and the fact that their morphology tends to form a hollow-like central region (even in the $\ell = 1$ boson star case), with the position of the maximum of density moving away from $r = 0$. The purpose of the present work was to take a step forward and perform a thorough examination of how these features change with ℓ. In particular, using different numerical methods, we were able to increase notably the magnitude of the parameter ℓ and finally, with the information of $\ell \gg 1$ solutions and a careful analysis of the system of equations, we were able to study the limiting case when the parameter ℓ goes to infinity.

One of the interesting features that can be observed is the fact that for $\ell > 1$ the density in the central region is much smaller than in the shell region. We have shown in this work that, as ℓ grows, so does the object and also the almost empty central region, tending to form shells of scalar fields where the size of the almost empty central region is much larger than the size of the region where the scalar field is mainly distributed. This tendency in the behavior goes all the way to infinity, making the objects look like larger and larger shells. We have shown that, when $\ell \gg 1$ the scalar field profile is shifted outwards proportionally to ℓ while its width grows as $\sqrt[3]{\ell}$. Furthermore, the spatial components of the stress energy-momentum tensor tend to be highly anisotropic as ℓ increases. Indeed,

as ℓ grows the radial pressure tends to zero, while the tangential one remains finite. In this way, for large values of ℓ, the shells tend to have no radial pressure and are supported solely by the tangential ones, analogous to the way in which a Roman arch supports its own weight. This increase in the anisotropy seems related to an increase in the compactness [107] of the ℓ-boson star. The mass of the solutions that divide the stable and the unstable branches, as well as their size, grows with ℓ, but in such a way that the compactness tends to a finite value. We have proven that in the $\ell \to \infty$ limit the compactness tends to about 0.23 for the maximum mass configuration; that is, about half the Buchdahl limit. However, unstable configurations may be much more compact, reaching a compactness of about 0.433 in the large ℓ limit. In this regard, it is interesting to point out that (single and multiple) shell-type configurations have also been found when analyzing the spherically symmetric steady-state solutions of the Einstein-Vlasov system [110]. In particular, it has been proven that such shells satisfy the Buchdahl inequality and that static shells of Vlasov matter can have $M(r)/r$ arbitrarily close to 4/9 [111].

Regarding orbiting particles, the high compactness that ℓ-boson stars can achieve while remaining stable gives rise to new features, which differentiate them from standard boson stars and also from black holes. Schwarzschild black holes have an ISCO located at $6M$, with no stable circular orbits below that value. Consequently, accretion disks around non-rotating black holes typically have an inner boundary and "end" at $r = 6M$. *Stable* standard boson stars do not have ISCOs, meaning that they could in principle possess an accretion disk extending all the way to the star's center. On the other hand, *stable* ℓ-boson stars exist with an ISCO-OSCO pair. In this case, accretion disks could show a "gap" between the ISCO and OSCO, to then again extend all the way to the center. These differences could constitute an important observable feature.

Besides causal circular orbits, we studied null ones, also known as light rings. We found that, for each ℓ, a pair of light rings appears at high enough compactness, the exterior one beeing unstable and the interior one stable. These light rings are always in the unstable spacetime regions, although they begin appearing closer and closer to the stable region as ℓ increases, which seems reasonable given that more compact stable solutions exist for larger ℓ. Our findings are consistent with the results of [109]: if a regular compact object has a light ring, it must have at least two[9], one of them being stable; and the presence of the stable light ring is expected to lead to nonlinear spacetime instabilities.

In our vast parameter exploration we have not included excited modes (higher frequency solutions containing one or more nodes of ψ_ℓ), which would be unstable if results for standard boson stars also hold here [112]. However, solutions

[9] Except, of course, for the degenerate case in which the two light rings coincide.

Table 3.1: Summary of the main definitions used in this chapter.

Symbol	Definition	Depends on
M	Mass function, also $M(r)$	ℓ, u_0, r
M_T	Total mass (or mass function at outer boundary)	ℓ, u_0
R_{99}	Areal radius containing 99% of the total mass	ℓ, u_0
C_{99}	M_T/R_{99}	ℓ, u_0
C_m	Maximum of $M(r)/r$ over $r>0$	ℓ, u_0
R_m	Location of maximum $M(r)/r$	ℓ, u_0
M_m	Mass function evaluated at R_m	ℓ, u_0
$r_{\rm in}$	Location of the inner light ring	ℓ, u_0
$r_{\rm out}$	Location of the outer light ring	ℓ, u_0
$r_{\rm osco}$	Location of the OSCO	ℓ, u_0
$r_{\rm isco}$	Location of the ISCO	ℓ, u_0
$M_{\rm max}$	Maximum of M_T (for a given ℓ)	ℓ

that combine a stable ground state solution with excited ones might again be stable [113]. We expect to address these questions in future works.

Apart from the properties discussed in this chapter, ℓ-boson stars open up the possibility to consider a larger landscape of solutions such as the ones described in [104]. These results along with the existence of a stable branch for the ℓ-boson stars [101–103] make us conclude that such localized bosonic systems may play an important role in modeling astrophysical objects, such as galactic halos or black hole mimickers with potential observable consequences. Further work along these lines is underway and will be presented in the near future.

3.6 Appendices of Chap. 3

Appendix: Definitions and rescaling in μ

We include tables that provide summarized information in a single place, aiding in the reading of this chapter. A summary of the main definitions used in this work is shown in Table 3.1. Rescaling rules in μ, which allows one to obtain solutions for arbitrary μ from the solution of any given μ_0, are shown in Table 3.2.

Appendix 3.B: Numerical methods

We obtain solutions of the eigenvalue problem in equations (3.5) numerically using two different methods, implemented in independent codes. For $\ell \lesssim 25$ we use a shooting method similar to the one described in our previous work [99], but with some improvements. For larger ℓ it becomes more and more difficult for this code

Table 3.2: Solutions for arbitrary values of μ can be obtained from those of a given value by performing a rescaling as shown in this table.

μ	$\mapsto$	$\lambda\,\mu$
$(\alpha,\,\gamma,\,\psi_\ell)$	$\mapsto$	$(\alpha,\,\gamma,\,\psi_\ell)$
u_0	$\mapsto$	$\lambda^\ell\,u_0$
ω	$\mapsto$	$\lambda\,\omega$
$(r,\,M)$	$\mapsto$	$\lambda^{-1}\,(r,\,M)$
$(\rho,\,p_r,\,p_T)$	$\mapsto$	$\lambda^2\,(\rho,\,p_r,\,p_T)$

to converge to a given mode. In those cases we switch instead to a spectral method. These methods, which are described in the following subsections, give the same results in the parameter region where both are able to obtain solutions.

Shooting Method To obtain solutions for $\ell \lesssim 25$ we use a "shooting to a fitting point method" based on [114], implemented in a code which is described in [115]. It consist of doing a direct numerical integration of the ordinary differential equations starting both from the left and right boundaries, at which one imposes either appropriate physical conditions or guesses when those are undetermined, with the goal of matching both the fields and their first derivatives at some intermediate point. This defines a function of the mentioned guesses, plus an additional guess, the eigenvalue ω^2, whose roots correspond to the fitting condition being satisfied. In order to find such roots, a Newton-Raphson method is used. The fitting point method is particularly useful when one has a system with a pair of solutions, one rapidly growing and the other rapidly decreasing at each boundary, and one wants to obtain the (physical) solution that decays to zero at both boundaries, as in the large ℓ cases. For the numerical integration, instead of the algorithm described in [114], we use a more sophisticated step adaptive method provided by the LSODE routines. For the particular applications of this work, it was also helpful in a few cases to modify the left boundary conditions in order to be able to set them at locations quite a bit to the right of $r = 0$. This is due to the shell-like shape of the stars for large enough ℓ. The details are given below. Finally, even though the solutions for a given value of μ can be trivially obtained from a rescaling of the $\mu = 1$ case (see appendix 3.6), which is the value we fixed in most situations, sometimes it helped the numerical code to easily find solutions to vary μ depending on the particular region of the parameter space. This is because some fields may become many orders of magnitude different when one restricts oneself to the $\mu = 1$ case. Nevertheless, we present all our results in a μ independent form.

Approximate solutions for low density As mentioned throughout the chapter, for large values of ℓ the scalar field distribution is shell-like, with very low density (as compared to its maximum value) in an interior region with $r < r_1$ and in an exterior region with $r_2 < r$ for certain values $r_1 < r_2$. In the interior region the solutions can be approximated by those of a scalar field on a flat spacetime, while in the exterior region they can be approximated by solutions of a scalar field on a Schwarzschild spacetime with mass M_T.

In the interior region ($r < r_1$) we can assume $\alpha = \gamma = 1$. Then, from equation (3.5c), we get

$$\frac{1}{r^2}\left(r^2\psi_{\rm in}'\right)' = \left(\mu^2 - \omega^2 + \frac{\ell(\ell+1)}{r^2}\right)\psi_{\rm in}, \tag{3.34}$$

with solutions

$$\psi_{\rm in}(r) = C_1 \frac{J_{\ell+\frac{1}{2}}\left(\sqrt{\omega^2-\mu^2}\,r\right)}{\sqrt{r}} + C_2 \frac{Y_{\ell+\frac{1}{2}}\left(\sqrt{\omega^2-\mu^2}\,r\right)}{\sqrt{r}}, \tag{3.35}$$

where $J_\nu(x)$ and $Y_\nu(x)$ are the Bessel functions of the first and second kind, respectively. Keeping only the solution with the proper behavior at $r = 0$ and writing the arbitrary amplitude in terms of u_0 we obtain

$$\psi_{\rm in}(r) = u_0 \frac{2^{\left(\ell+\frac{1}{2}\right)}\,\Gamma\left(\ell+\frac{3}{2}\right)}{\left(\sqrt{\omega^2-\mu^2}\right)^{\ell+\frac{1}{2}}} \frac{J_{\ell+\frac{1}{2}}\left(\sqrt{\omega^2-\mu^2}\,r\right)}{\sqrt{r}}. \tag{3.36}$$

In order to transform to the gauge used in the remainder of this work, in which $\alpha = 1$ at $r = \infty$, rather than at $r = 0$, one just needs to replace ω with $\gamma_\infty \alpha_\infty \omega$ in equation (3.36). We show an example of this approximation in figure 3.14. We see a very good agreement between the scalar field and its approximation even well beyond $\mu r = \mu r_1 \approx 40$.

Finally, we note that in the exterior region one can assume the metric is given by a Schwarzschild solution with mass M_T. Then, the scalar field can be expressed in terms of the confluent Heun functions. However, we did not use the external region approximations in this chapter, hence we will not present any details here.

Spectral Method An independent code was built based on a multidomain spectral method. Specifically, a collocation method has been used with Chebyshev polynomials as the basis functions. Details of the code described in the following paragraphs were essentially implemented based on [116] which is a review on spectral methods in numerical relativity. The Einstein-Klein-Gordon equations were solved in isotropic coordinates, where the differential operators in the resulting equations in the system are similar to each other and therefore easier to implement in this particular method.

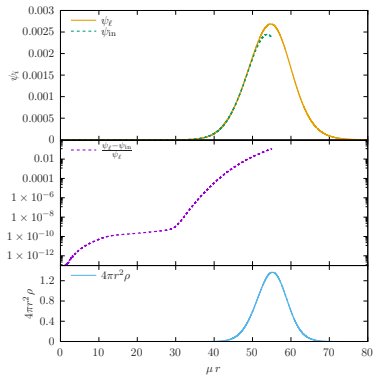

Figure 3.14: Solution ψ_ℓ and approximation $\psi_{\rm in}$ for the case with $\ell = 25$ and maximum mass $M_T = 13.45$ (top panel). The middle panel shows the relative error. For reference we also include the density profile in the bottom panel.

The physical domain, parameterized by the radial coordinate is decomposed into 5 carefully placed domains depending on what range of solutions we want to obtain in a single run, given ℓ. For the outer domain a compactification is carried out so that the external boundary conditions can be imposed at spatial infinity. On the other hand, in the domain that contains the origin, an even base of Chebyshev polynomials is used for the lapse and the conformal factor Ψ, while an even (odd) base is used for the field if ℓ is even (odd), which guarantee the solution is regular at the origin. The non-linear system of equations that results for the coefficients of the expansion is solved iteratively using a Newton scheme, the extra variable ω is compensated with an extra equation $\alpha(r = 0) = \alpha_0 > 0$, which ensures that the code does not converge to the trivial solution.

An initial guess is required in the Newton scheme for the coefficients of the expansion in all the functions (as well as the frequency), this is equivalent to provide an initial guess for the functions. Given certain value of ℓ, the first solution is obtained from reasonable choices for the three parameters, σ, r_0 and ϕ_0, which control the properties of the following simple initial guess

$$\psi_\ell = \left(\frac{\bar{r}}{r_0}\right)^\ell \phi_0 \exp\left(-\frac{\bar{r}^2 - r_0^2}{\sigma^2}\right), \tag{3.37}$$

$$\alpha = -(1-\alpha_0)\exp(-\bar{r}^2) + 1, \tag{3.38}$$

$$\Psi = 1. \tag{3.39}$$

Here $\bar{r}$ refers to the isotropic radial coordinate. The solutions are easier to find in the Newtonian regime where the frequency is close to one. For example, in the $\ell = 50,\ 100$ cases presented here we start with an initial guess of $\omega = 0.95$ and once the first solution is obtained we slightly decrease the value of α_0 and take as

the new initial guess the previous solution.

We have checked that in the spectral code, as in the convergence test performed in [117] for the $\ell = 0$ case, the error indicators, as for example the frequency and the difference of the ADM and Komar masses converge exponentially to a fixed value and to zero respectively, as we increase the number of Chebyshev basis polynomials, as expected for a spectral method.

Appendix 3.C: Summary of numerical data

Table 3.3 shows information regarding most of the solutions analyzed in this chapter.

Table 3.3: Properties of some of the solutions obtained in this work. For each ℓ, the ground state solution is uniquely determined by fixing u_0. In the column titled "stable", "m.s." stands for marginally stable, corresponding to solutions of maximum total mass. In the $\ell = \infty$ case (marked with †), m.s. simply indicates the maximum mass solution. Also in the $\ell = \infty$ case, the total mass values (indicated with *) correspond to the mass rescaled with ℓ as in section 3.4.

ℓ	u_0/μ^ℓ	ω/μ	μM_T	μM_m	μR_{99}	μR_m	C_{99}	C_m	μr_{in}	μr_{out}	μr_{osco}	μr_{isco}	stable	Figure
0	1.30e-2	0.9911	0.229	0.1707	41.908	22.332	0.0055	0.0076	–	–	–	–	yes	3.6
0	2.71e-1	0.8530	0.633	0.4587	7.855	3.815	0.0806	0.1202	–	–	–	–	m.s.	3.2,3.4,3.5,3.6,3.8
0	2.20e+0	0.8428	0.374	0.0016	5.043	0.006	0.0742	0.2581	0.0031	0.0082	0.0031	0.013	no	3.6
1	5.00e-4	0.9864	0.489	0.4041	47.763	32.090	0.0102	0.0126	–	–	–	–	yes	3.1, 3.6
1	4.00e-3	0.9487	0.875	0.7233	23.115	15.460	0.0379	0.0468	–	–	–	–	yes	3.1
1	3.35e-2	0.8353	1.176	0.9650	10.157	6.590	0.1158	0.1464	–	–	–	–	m.s.	3.1,3.2,3.4,3.5,3.6,3.8
1	5.01e-1	0.8384	0.543	0.3739	3.860	1.224	0.1407	0.3056	1.1057	1.1191	1.1057	2.99	no	3.1
1	1.60e+0	0.8742	0.702	0.1504	7.333	0.430	0.0958	0.3500	0.2947	0.5691	0.2947	0.952	no	3.1
1	2.50e+0	0.8603	0.670	0.1008	6.183	0.280	0.1084	0.3596	0.1875	0.3936	0.1875	0.603	no	3.1
1	7.00e+0	0.8883	0.613	0.0376	6.579	0.102	0.0932	0.3690	0.0666	0.1542	0.0666	0.213	no	3.6
5	1.00e-10	0.9757	1.686	1.5377	72.612	61.560	0.0232	0.0250	–	–	–	–	yes	3.6
5	5.00e-7	0.8165	3.293	3.0197	19.470	16.628	0.1691	0.1816	–	–	–	–	m.s.	3.2,3.4,3.5,3.6,3.8
5	3.40e-3	0.9016	1.314	1.1984	4.037	3.282	0.3255	0.3651	2.76	3.90	2.76	7.87	no	3.6
25	4.67e-53	0.9499	9.265	8.9616	162.304	156.420	0.0571	0.0573	–	–	–	–	yes	3.2, 3.8
25	4.67e-47	0.8826	12.490	12.1047	95.484	92.363	0.1308	0.1311	–	–	–	–	yes	3.2, 3.6,3.8
25	1.03e-42	0.8091	13.451	13.0691	64.363	62.556	0.2090	0.2089	–	–	64.8	80.55	m.s.	3.2,3.4,3.5,3.6,3.8, 3.14
25	1.87e-36	0.7167	11.488	11.2098	35.994	35.251	0.3192	0.3180	–	–	35.055	68.85	no	3.2, 3.8
25	9.35e-30	0.7608	7.425	7.2693	19.263	18.969	0.3855	0.3832	17.601	22.275	17.601	44.55	no	3.2, 3.6,3.8
25	1.08e-45	0.8612	12.980	12.5892	84.434	81.799	0.1537	0.1539	–	–	–	–	yes	3.9,3.10
50	1.00e-94	0.8088	25.942	25.5042	119.187	118.120	0.2177	0.2159	–	–	120.1	152.0	m.s.	3.2,3.4, 3.8
50	1.00e-99	0.8612	25.004	24.5308	156.170	154.380	0.1601	0.1589	–	–	–	–	yes	3.9, 3.11
100	1.00e-216	0.8073	50.756	50.2279	225.660	225.660	0.2249	0.2226	–	–	227.1	298.0	m.s.	3.2,3.4, 3.8
100	1.00e-220	0.8612	48.911	48.8731	296.630	296.630	0.1648	0.1631	–	–	–	–	yes	3.9, 3.11
200		0.8612	96.510	95.8531	575.580	577.070	1.6767	0.1661	–	–	–	–	yes	3.9,3.10
400		0.8612	191.452	190.6695	1128.450	1132.820	0.1697	0.1683	–	–	–	–	yes	3.9
1600		0.8612	759.695	758.6214	4422.320	4437.550	0.1718	0.1710	–	–	–	–	yes	3.10
∞		0.8612	$0.472^\star$				0.1730							3.10,3.11
∞		0.8077	$0.490^\star$				0.2346						m.s.†	3.11,3.12
∞		0.7251	$0.439^\star$				0.3333							3.11

CHAPTER 4

CONFINED GHOST[1]

Contents

We present the *$\mathscr{E}$-boson star*: A novel configuration of a boson star with an exotic matter nucleus; the exotic matter being described by a real massive scalar field with self-interaction term and kinetic term of the opposite sign. The other scalar field is canonical, so that the system is similar to the material component of the quintom cosmological scenario. Considering the static spherical symmetric case, we obtain cases where both fields are distributed as concentric spheres, and others with the remarkable feature that the canonical matter is pushed outwards and obtain a shell like distribution of the canonical field, with a nucleus of exotic matter at the center. We present global properties of such $\mathscr{E}$-boson stars and stress the differences that these configurations have with respect to the usual boson stars. In particular, we obtain cases where the compactness goes beyond the Buchdahl limit.

[1]This chapter is extracted with minor revisions from Ref. [118], which was written in collaboration with E. Jiménez-Vázquez and D. Núñez.

4.1 Introduction

The study of the dynamics of matter different to the usual gas or fluid, is an academic subject by itself. Such studies acquire more relevance once that matter is related to possible models describing the dark components of the Universe. Indeed, several models proposed for describing the dark matter, and all the ones proposed to describe the dark energy, even including the cosmological constant one, violate the strong energy condition. Some particular models, specially those concerning dark energy fail to satisfy the null energy condition (NEC) which in turn implies the violation of the weak energy condition, meaning that at least some time-like observer with four-velocity u^μ measures negative energy densities $\rho = T_{\mu\nu}\, u^\mu\, u^\nu$. An example of this are the phantom models [34], whose simplest cases consist of a scalar field with a negative kinetic term in the Lagrangian. On the other hand, quintessence and scalar field dark matter models, which encompass scalar fields with a canonical kinetic term, always satisfy the NEC [35], nevertheless typical cosmological solutions with this type of matter within General Relativity, lead to periods in time with negative pressures $T^i{}_j$, as measured by an static observer, in an analogy with the fluid description [30].

In the Cosmological models the matter is characterized by their equation of state[2] , the ratio of the pressure to the density, $p/\rho = w$. For instance in quintessence, w stays above the cosmological constant value $w \geq -1$, while for the phantom field $w \leq -1$. In describing the dark energy with a dynamical equation of state, cosmological data analyses interestingly suggest that the boundary $w = -1$ is crossed in the evolution of the Universe [36, 37]. Models that can achieve this, require two scalar field (or fluid) components [36, 38] and are called quintom (see Ref. [39] for a review).

Self-gravitating scalar fields that violate the NEC, such as the phantom field, are the constituent material from which hypothetical objects called wormholes are constructed [119–123]. On the other hand, canonical (complex) scalar fields build up dynamically robust gravitational solitons called boson stars [44], which are regular solutions in Euclidean topology and exist in a variety of different models, reaching compactness values comparable to those of the neutron stars. Also solutions to the Einstein-Klein-Gordon equations with phantom fields exist in Euclidean topology [124] which could well be thought of as phantom boson stars. Along the lines of the latter solutions and boson stars in this work we construct objects that combine properties of both. Indeed, in this manuscript, we present solutions to a boson star model, consisting of a canonical complex scalar field and

[2]Perhaps this is not a fortunate definition, as long as it applies directly to fluids and as mentioned above, for some models of matter the concepts of density or pressure are very peculiar and do not fit with the usual ones related to the fluid. In any case, the matter is characterized in such a way and several models have a negative w.

a phantom real scalar field, both minimally coupled to Einstein gravity, where the ghost matter is confined within a bounded object made of a canonical scalar field. We call these objects $\mathscr{E}$-boson stars.

We are able to capture ghost matter in two different ways: with a small distribution inside a bigger soliton of canonical scalar field; and we have also found distribution where the ghost field is present and the canonical field profile tends to zero, with a maximum located away from the center, forming a shell surrounding the ghost matter. In both cases, these solutions can be thought of as boson stars with a phantom matter core that repels (via gravity) the positive density scalar field, allowing more massive and compact solutions compared to standard boson stars.

As mentioned in several works, for instance [125], the scalar field is not a kind of fluid and care should be made when trying to understand it as a kind of fluid. It is interesting that the dynamics described in this manuscript due to the presence of both types of fields, involves in an effective manner a kind of gravitational repulsive interaction which has no analogy to the gradients of pressure of the Archimedes' principle regarding a body submerge in a liquid.

The paper is organized as follows. In Sec. 4.2 we present the action, specify the metric and scalar fields ansatz, derive the static spherically symmetric field equations and define various physical quantities that will be used in the analysis. Numerical solutions of are presented in Sec. 4.3, starting from the known boson star and ghost field soliton solutions and then constructing composite solutions, describing global properties of the configuartions, as well as concrete individual examples. Finally we present a review of our findings and give some final remarks in Sec. 4.4. We use geometrized units, in which $G = 1 = c$, and the convention $(-,+,+,+)$ for the metric signature.

4.2 Theoretical setting

4.2.1 Action and equations of motion

We consider a canonical complex scalar field φ and a ghost real scalar field χ, minimally coupled to Einstein gravity. The system is represented by the action,

$$S = \int \mathrm{d}^4x\sqrt{-g}\left(\frac{1}{16\pi}R + \mathscr{L}_\varphi + \mathscr{L}_\chi\right), \tag{4.1}$$

which contains the Einstein-Hilbert action, R is the Ricci scalar, g the determinant of the metric, and the canonical scalar field φ contribution with Lagrangian,

$$\mathscr{L}_\varphi = -\frac{1}{2}\nabla_\mu\varphi\nabla^\mu\varphi^* - \frac{1}{2}V_\varphi \tag{4.2}$$

as well as the phantom field contribution whose Lagrangian has the following form

$$\mathscr{L}_\chi = \frac{1}{2}\nabla_\mu\chi\nabla^\mu\chi - \frac{1}{2}V_\chi. \tag{4.3}$$

The functions V_φ and V_χ denote scalar potentials given by

$$V_\varphi(|\varphi|) = \mu_\varphi|\varphi|^2; \quad V_\chi(\chi) = -\mu_\chi\chi^2 + \lambda\chi^4\,. \tag{4.4}$$

μ_φ and μ_χ are the mass parameters and λ is a (positive) self-interaction parameter. When $\chi = 0$ the system described by Eq. (4.1) contains the necessary ingredients to construct a mini-boson star [44] and on the other hand, when $\varphi = 0$ the system reduce to the action used for the phantom non-singular spherical solution [124]

Variation of the action with respect to $g_{\mu\nu}$, φ and χ lead to the Einstein equations

$$R_{\mu\nu} - \frac{1}{2}g_{\mu\nu}R = 8\pi T_{\mu\nu}, \tag{4.5a}$$

$$T_{\mu\nu} = g_{\mu\nu}(\mathscr{L}_\varphi + \mathscr{L}_\chi) - 2\frac{\partial(\mathscr{L}_\varphi + \mathscr{L}_\varphi)}{\partial g^{\mu\nu}}, \tag{4.5b}$$

and the Klein-Gordon equations

$$\nabla_\mu\nabla^\mu\varphi = \mu_\varphi^2\varphi\,; \tag{4.6a}$$

$$\nabla_\mu\nabla^\mu\chi = \mu_\chi^2\chi - 2\lambda\chi^3\,. \tag{4.6b}$$

We look for static spherically symmetric solutions and thus employ the following line element,

$$\mathrm{d}s^2 = -N^2\,\mathrm{d}t^2 + \Psi^4\left(\mathrm{d}r^2 + r^2\,\mathrm{d}\Omega^2\right)\,, \tag{4.7}$$

with N, Ψ functions of r only and $0 \le r < \infty$. For the scalar fields we assume that $\chi = \chi(r)$ and for the canonical one we take the anzatz:

$$\varphi = \phi(r)e^{i\omega t}. \tag{4.8}$$

4.2.2 Field equations

Substitution of the metric form (4.7) and the ansatz of the field (4.8), into Einstein Equations (4.5) yield

$$\begin{aligned}
&\Delta_3\Psi + \pi\Psi^5\left[\left(\frac{\omega\phi}{N}\right)^2 + \frac{\partial\phi^2}{\Psi^4} + \mu_\varphi^2\phi^2 - \frac{\partial\chi^2}{\Psi^4} - \left(\mu_\chi^2 - \lambda\chi^2\right)\chi^2\right] = 0,\\
&\Delta_3 N + \frac{2\partial N\partial\Psi}{\Psi} - 4\pi N\Psi^4\left[2\left(\frac{\omega\phi}{N}\right)^2 - \mu_\varphi^2\phi^2 + \left(\mu_\chi^2 - \lambda\chi^2\right)\chi^2\right] = 0,
\end{aligned} \tag{4.9}$$

where $\partial f := \frac{\mathrm{d}f}{\mathrm{d}r}$ and $\Delta_3 f := \partial^2 f + \frac{2}{r}\partial f$. The Klein Gordon equation for the canonical field is

$$\Delta_3\phi + \frac{\partial\phi\partial N}{N} + 2\frac{\partial\phi\partial\Psi}{\Psi} - \Psi^4\left[\mu_\varphi^2 - \left(\frac{\omega}{N}\right)^2\right]\phi = 0\,, \tag{4.10}$$

and the equation for the ghost field is

$$\Delta_3\chi + \frac{\partial\chi\partial N}{N} + 2\frac{\partial\chi\partial\Psi}{\Psi} - \Psi^4\left(\mu_\chi^2 - 2\lambda\chi^2\right)\chi = 0\,, \tag{4.11}$$

To solve the Einstein-Klein-Gordon system of equations (4.5)-(4.11), we demand regularity at the origin $r = 0$ and asymptotical flatness at $r \to \infty$. We apply these boundary condition to ϕ, χ, N, Ψ:

$$\partial\phi|_{r=0} = \partial\chi|_{r=0} = \partial N|_{r=0} = \partial\Psi|_{r=0} = 0\,; \tag{4.12}$$

$$\phi|_{r\to\infty} = \chi|_{r\to\infty} = 0, \quad N|_{r\to\infty} = \Psi|_{r\to\infty} = 1\,. \tag{4.13}$$

Also asymptotically flat equilibrium solutions exists only if $\omega < \mu_\varphi$. Both ω and λ are eigenvalues to be determined iteratively together with the integration of the differential equations.

4.2.3 Quantities of interest

The Komar expression which gives the gravitational mass of the star is given by the following expression

$$M = \frac{1}{4\pi}\int_{\Sigma_t} R_{\mu\nu}n^\mu\xi^\nu\,\mathrm{d}V, \tag{4.14}$$

where Σ_t is an hypersurface of constant t, $\xi = \partial/\partial_t$ is the Killing vector associated with stationarity, n^μ the future-directed unit vector normal to Σ_t. Using the ansatz (4.7) we arrive at the formula $M = r^2\lim_{r\to\infty}\partial N$, for the Komar mass of the present model.

We are also interested in evaluating the compactness of the obtained solutions and for this reason we use the quantity R_{99}, defined as the areal radius ($\Psi^2 r$) that encompasses 99 percent of the total mass of the star. We then define the compactness as

$$C = \frac{M}{R_{99}}, \tag{4.15}$$

which is an important quantity in describing the properties of several compact objects and will be dealt with bellow.

The presence of light rings in horizonless compact objects (ultracompact objects) has been deeply discussed in [109, 126, 127] and are a clear signal of the (in)stability of the space time under study. These results and theorems have the NEC as a requirement for the implications of the existence of such light rings on

the (in)stability of the spacetime. We will see that $\mathscr{E}$-boson stars not always satisfy this energy conditions. With these facts in mind, we have searched for the presence of light-rings in the solutions that we construct, by means of the determination of the light-ring radius $r_{\rm lr}$ using the procedure described in [85], which impose a condition on the lapse-function:

$$N(r_{\rm lr}) - r_{\rm lr}\left(1 + 2r_{\rm lr}\left.\frac{\mathrm{d}\ln\Psi}{\mathrm{d}r}\right|_{r_{\rm lr}}\right)^{-1}\left.\frac{\mathrm{d}N}{\mathrm{d}r}\right|_{r_{\rm lr}} = 0. \tag{4.16}$$

In this way, the energy density as measured by the Eulerian static observer with four-velocity, u^μ, which coincides with the vector normal to the hypersurfaces, n^μ, is an important feature of the solutions and the corresponding expression for both fields are obtained directly from the projection of the stress energy tensors on such velocity:

$$\rho = T_{\mu\nu}\, n^\mu n^\nu = \rho_\varphi + \rho_\chi, \tag{4.17}$$

with

$$\rho_\varphi = \frac{1}{2}\left[\frac{\omega^2\phi^2}{N^2} + \frac{\partial\phi^2}{\Psi^4} + \mu_\varphi^2\phi^2\right], \tag{4.18}$$

$$\rho_\chi = -\frac{1}{2}\left[\frac{\partial\chi^2}{\Psi^4} + \left(\mu_\chi^2 - \lambda\chi^2\right)\chi^2\right], \tag{4.19}$$

Finally, the geometric scalars are also useful for characterizing the solutions, analyzing the curvature of the spacetime and asses its regularity. From the line element Eq. (4.7) we obtain the following expressions for the 4D-scalar of curvature:

$$R = -\frac{2}{\Psi^4}\left(\frac{\Delta_3 N}{N} + 4\frac{\Delta_3\Psi}{\Psi} + 2\frac{\partial N}{N}\frac{\partial\Psi}{\Psi}\right), \tag{4.20}$$

for the Weyl scalar

$$W = \frac{4}{3\Psi^8}\left(\frac{\partial^2 N - \frac{\partial N}{r}}{N} - \frac{2}{\Psi}\left(\partial^2\Psi - \frac{\partial\Psi}{r} - 3\frac{(\partial\Psi)^2}{\Psi}\right) - 4\frac{\partial N}{N}\frac{\partial\Psi}{\Psi}\right)^2, \tag{4.21}$$

and for the Kretschmann scalar:

$$K = -\frac{4}{\Psi^8}\left(\frac{\left(\partial^2 N\right)^2 - 4\partial^2 N\,\partial N\,\partial\ln\Psi}{N^2} + \frac{8}{\Psi^2}\left(\left(\partial^2\Psi\right)^2 + 2\partial^2\Psi\,\partial\Psi\left(\frac{1}{r} - \frac{\partial\Psi}{\Psi}\right)\right)\right.$$
$$\left. + \frac{2\left(\partial N\right)^2}{N^2}\left(\frac{6\left(\partial\Psi\right)^2}{\Psi^2} + \frac{4\partial\ln\Psi + 1/r}{r}\right) + \frac{8\left(\partial\Psi\right)^2}{\Psi^2}\left(\frac{3\left(\partial\Psi\right)^2}{\Psi^2} + \frac{2\partial\Psi}{r\Psi} + \frac{3}{r^2}\right)\right). \tag{4.22}$$

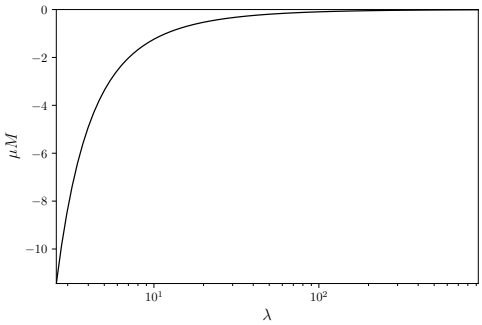

Figure 4.1: Non-singular solutions to Einstein-Klein-Gordon equations with a phantom scalar field [124]. Plot of the (dimensionless) total mass of the exotic configuration, as a function of the self interaction parameter. Notice that this mass is negative for all values of λ. Such plot was originally presented in [124].

As mentioned in [122], the canonical matter generates wells in the geometry, whereas the exotic matter produces bumps, so that the plot of the geometric scalar quantities is also useful to characterize the effects on the different types of matter on the geometry.

4.3 Equilibrium solutions

Before reporting numerical results for the full system (4.1) we first discuss and review, in Sec. 4.3.1, some of the general properties of the cases with $\chi = 0$ and then with $\varphi = 0$. Next, in Sec. 4.3.2 we take into account both canonical and exotic fields to construct a new type of configuration.

In all the configurations presented in this section, we have taken $\mu_\varphi = \mu_\chi$ and named this quantity simply μ. In the Appendix we present some cases where the masses are different $\mu_\varphi \neq \mu_\chi$.

4.3.1 Boson stars and phantom solitons

Boson stars and the non-singular solutions with a phantom scalar field presented in [124] are very similar solutions in the sense that they both are static spherical and regular solutions of the Einstein-Klein-Gordon system in Euclidean topology. However, the latter only exists for $\lambda > 0$ and have a total mass that is always negative as can be seen in Fig. 4.1. Another difference is that these ghost solitons are known to be unstable.

Boson stars on the other hand are stable in a region of the parameter space. Given certain model, they are parameterized by the value of the scalar field at

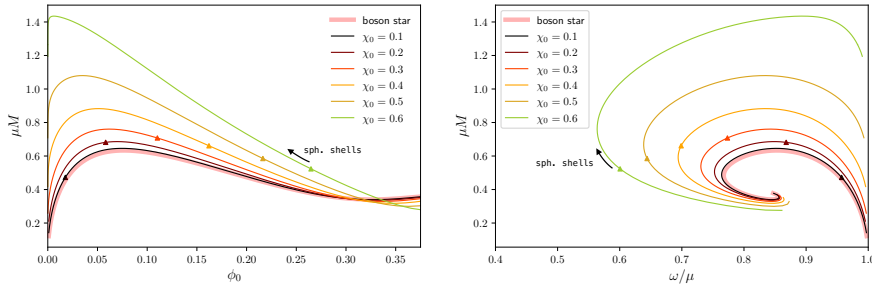

Figure 4.2: Left panel: Value of the canonical scalar field ϕ at $r = 0$ *vs*. total mass. Right panel: Total mass *vs*. frequency. Triangles locate the transition point between $r_{\max(\phi)} = 0$ (concentric spheres) and $r_{\max(\phi)} \neq 0$ (shell distribution of the canonical field). The regions that connect the triangles with the corresponding $\phi_0 = 0$ solutions ($\omega/\mu \to 1$) correspond to the sell-like $\mathscr{E}$-boson stars.

the center of the star, $\phi_0 := \phi|_{r=0}$, the family of solutions is separated by certain configuration that maximizes the value of the mass as can be seen from the thick red line at the left panel of Fig. 4.2. In the right panel of this same figure it can be seen how mini-boson stars, which are recovered when $\chi = 0$ in (4.1), spiral to a limit solution when mass is plotted versus frequency.

It is worth mentioning that interesting multi-field solutions for boson stars have been reported in the literature using a complex and a real scalar field (see also [99, 104, 128] for other boson star solutions with multiple complex scalar fields). Such is the case of Boson Stars in the Friedberg-Lee-Sirlin model [129], in which both fields are coupled (the mass of the complex field is given by its interaction with the real field) and possess a canonical kinetic term. In this FLS-model it has even been possible to construct rotating and black hole solutions with hair. Another example are the boson stars in non-trivial topology [130], in which a massless real field is included, giving rise to solitonic configurations with a wormhole in the core of the star. This solutions happen to inherit the Bronnikov-Ellis wormhole instability inside the star, although the authors show that in a region of parameter space the instability can be very weak.

4.3.2 $\mathscr{E}$-boson stars

In generating the solutions presented in this paper, we consider dimensionless quantities constructed from re-scaling with the mass of the canonical scalar field, μ_φ. For example $r \to \mu_\varphi r$, $\omega \to \omega/\mu_\varphi$, $\mu_\chi \to \mu_\chi/\mu_\varphi$, $M \to \mu_\varphi M$, etc. so that the solutions are obtained for arbitrary μ_φ. Then the set of four coupled non-linear ordinary differential equations for ϕ, χ, N and Ψ (4.5)-(4.11) is solved numerically

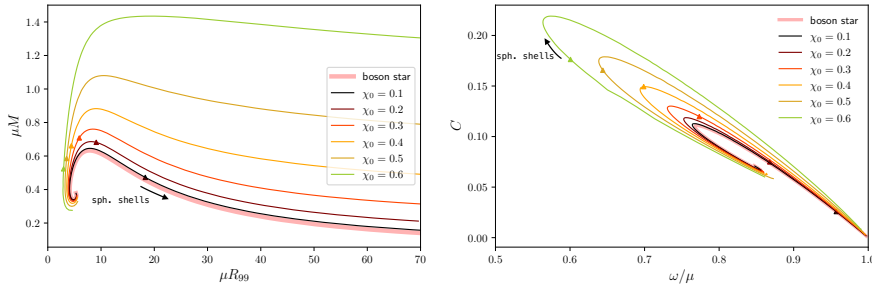

Figure 4.3: First panel: Radius R_{99} *vs.* total mass. Second panel: Frequency *vs.* compactness.

subject to the boundary conditions at (4.12) and (4.13).

We have used a Chebyshev spectral method with the collocation approach using 24 spectral coefficients in all solutions as well as 5 radial domains with boundaries at $\mu r = \{0.1, 2.5, 5, 25\}$. The last domain is compactified and comprises μr from 25 to ∞. The resulting nonlinear algebraic system of equations is solved using a Newton-Raphson iteration.

The composite solutions ($\mathscr{E}$-boson stars), consisting of non-zero ϕ and χ fields, are uniquely determined by the value ϕ_0 (defined above) and $\chi_0 := \chi|_{r=0}$, as long as we restrict ourselves to the solutions in the base state (no nodes), for all the configurations presented in the manuscript. A first solution for the composite system has been obtained by fixing small values for ϕ_0 and χ_0 and taking as initial guess a superposition of a boson star solution $\{\phi_{\rm BS}, N_{\rm BS}, \Psi_{\rm BS}; \omega\}$ and a phantom soliton solution $\{\chi_{\rm Ph}, N_{\rm Ph}, \Psi_{\rm Ph}; \lambda\}$ in the following form;

$$\phi = \phi_{\rm BS}, \quad \chi = \chi_{\rm Ph}\ ; \tag{4.23}$$

$$N^2 = N_{\rm BS}^2 + N_{\rm Ph}^2 - 1, \quad \Psi^4 = \Psi_{\rm BS}^4 + \Psi_{\rm Ph}^4 - 1\ . \tag{4.24}$$

Clearly this superposition introduce constraint violations, however the initial guess leads to configurations close to the true solution of Einstein equations, to which the code converges after a small number of steps. Then, sequence of constant χ_0 solutions are obtained by slowly varying ϕ_0. Different global quantities obtained for this families of boson star solutions are displayed in Fig. 4.2 and 4.3, where we present the total mass of the stars vs ϕ_0, ω and R_{99}. Also in the right panel of Fig. 4.3 we show the compactness as function of the frequency ω. We observe that the mass and even the compactness grow notably by including a larger component of ghost matter, which, as we will see below, is stored in the core of the star.

The first and second column of Fig. 4.4 show solutions with $\chi_0 = 0.5$ and three different values for ϕ_0. We observe an interesting feature: As the value of ϕ_0/χ_0

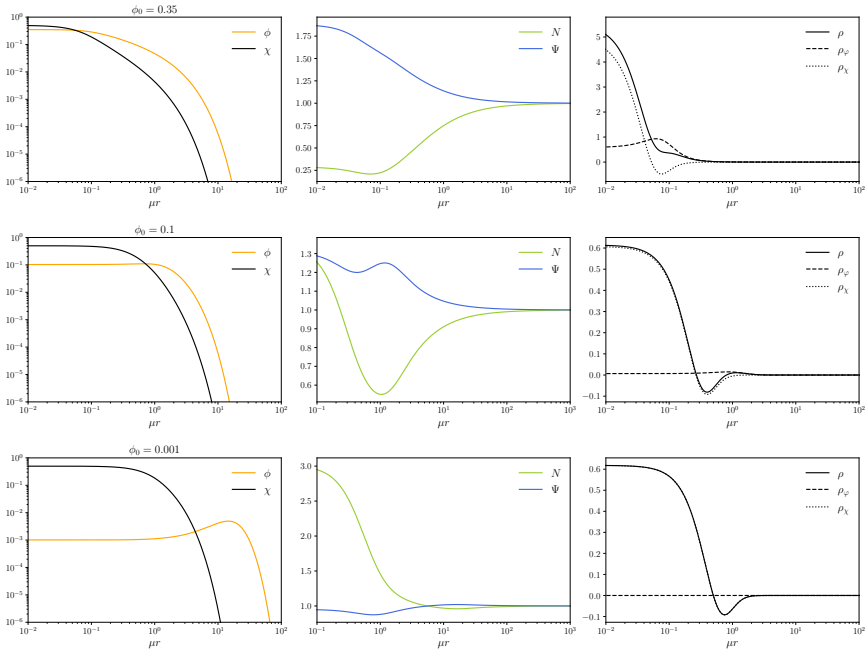

Figure 4.4: $\mathscr{E}$-boson star solutions with $\chi_0 = 0.5$ and $\phi_0 = 0.35$ (upper row), 0.1 (middle row) and 0.001 (bottom row). In the first column the fields are plotted; in the second column, the metric coefficients and in the third column the individual and total densities, all as a function of the distance to center. We notice that the energy density in the lower panel is difficult to be appreciate for the canonical field, since it is four orders of magnitude smaller.

decreases (in fact, for a whole region near $\omega/\mu = 1$) the ϕ field profile shifts its maximum away from the origin. It is also observed that for small values of ϕ_0, the metric factors undergo qualitative changes. They go from having a monotonically increasing (decreasing) behavior for N (Ψ) of the standard boson star, to having local maxima and/or minima. In the third column, we present the densities, the individual corresponding to each field, and the total one, Eqs. (4.19, 4.18, 4.17); as expected [122], the exotic density has regions with negative values and we see that there are configuration such that the total density is positive, while others where the total density has regions with negative values; this features are also related to the distribution being concentric spheres or shells with a nucleus. Fig. 4.5 illustrate the different morphologies of the $\mathscr{E}$-boson stars as 3D plots.

The left panel of Fig. 4.6 shows the outward shift of the maximum of ϕ for a set of solution families. The right panel illustrates how the minimum of N ceases to be located at $r = 0$, as happens in the case of the standard boson stars, $\chi_0 = 0$. In Figs. 4.2, 4.3 we have indicated with a triangle the transition point from which

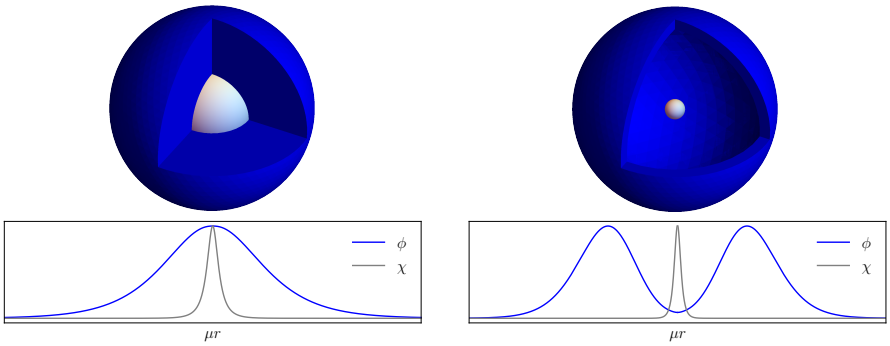

Figure 4.5: Left figure: Concentric solid spheres configuration ($\chi_0 = 0.1$, $\phi_0 = 4 \times 10^{-2}$). Left figure: Shell-like configuration ($\chi_0 = 0.6$, $\phi_0 = 3 \times 10^{-4}$). The field profiles in the lower plots have been normalized and reflected for $-r$. Notice that the scalar fields, do not interact with one another except gravitationally and yet give rise to this type of morphologies.

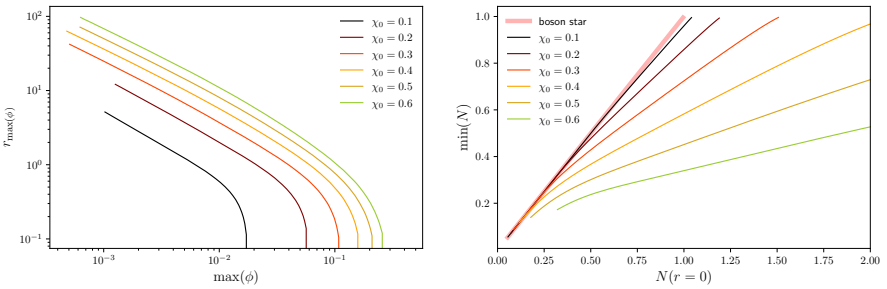

Figure 4.6: Left panel: Maximum of the canonical scalar field ϕ *vs.* position at which this maximum is found. Right panel: Value of the metric function $\sqrt{-g_{tt}}$ at $r = 0$ *vs.* its global minimum.

we have solutions with the maximum of ϕ at $r \neq 0$, *i.e.*, where the canonical field changes its morphology, from a shell distribution to a solid sphere.

The transition to the solutions in the limit $\chi_0 \to 0$ (standard boson star) occurs in a simple way: the ghost field χ, vanishes keeping its center at $r = 0$ while the associated back-reaction of the spacetime also vanishes. However, the limit $\phi_0 \to 0$ is not equally straightforward as the reader can probably already anticipate from the presented results. As already mentioned, the maximum of ϕ moves away from the origin and the value of the absolute maximum of ϕ decreases (Fig. 4.6). Also, as seen in Fig. 4.7, when $\omega/\mu \to 1$ the λ eigenvalue tends asymptotically to the value that the Dzhunushaliev *et al.* solution would have with the corresponding χ_0. Although the canonical field energy density decreases as it approaches to

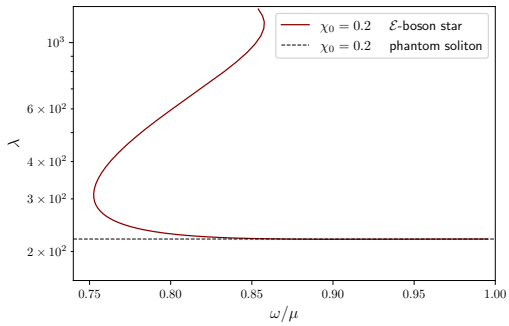

Figure 4.7: Eigenvalues ω and λ for a sequence of solutions with χ_0 constant.

this limit, the shell is of larger size and therefore contributes enough to obtain solutions whose total mass is positive. With the numerical resolution to which we have access we have not been able to find solutions with small $\phi_0 \neq 0$ transiting to the negative mass region, which we believe should be the case for $\omega/\mu \to 1$ in order to have a continuous transition to the phantom solitonic solution.

With respect to the energy conditions, the $\mathscr{E}$-boson stars have a remarkable behavior as well. Indeed, the null energy condition states: $T_{\mu\nu}k^\mu k^\nu \geq 0$, for all null vectors k^μ. If the energy momentum tensor is of the form $T_{\hat{\mu}\hat{\nu}} = \mathrm{diag}(\tau, p_1, p_2, p_3)$ with respect to an orthonormal basis (first Segrè type), then the NEC is satisfied if and only if $\tau + p_i \geq 0$ $(i = 1,2,3)$ [35, 131]. For the orthonormal components of the energy-momentum tensor of the present model (4.1) and spacetime (4.7) we have

$$\tau + p_1 = \left(\frac{\omega\phi}{N}\right)^2 + \left(\frac{1}{\Psi^2}\frac{d\phi}{dr}\right)^2 - \left(\frac{1}{\Psi^2}\frac{d\chi}{dr}\right)^2; \tag{4.25}$$

$$\tau + p_2 = \tau + p_3 = \left(\frac{\omega\phi}{N}\right)^2. \tag{4.26}$$

From these relations it can be seen that, for the Dzhunushaliev *et al.* soliton [124]. when $\phi = 0$, the NEC is always violated (in particular Eq. (4.25)), however with respect to the $\mathscr{E}$-boson stars, it can be seen that there are configurations which abide the energy conditions at all points. In Table 4.1 we include data for a selection of the solutions obtained. We present two cases corresponding to boson stars, another two corresponding to the Phantom configuration and six cases of the $\mathscr{E}$-boson star. Fig. 4.8 evaluates the NEC by plotting the quantity $\tau + p_1$ for the $\mathscr{E}$-boson star configuration in Table 4.1. We note that among the configurations with $\chi_0 = 0.1$ (A, B, C) all of them violate the energy condition; the configuration A even for all r. On the other hand, for the configurations with $\chi_0 = 0.01$ (D, E, F) only D violates the NEC in a small part of the domain while E and F satisfy it at

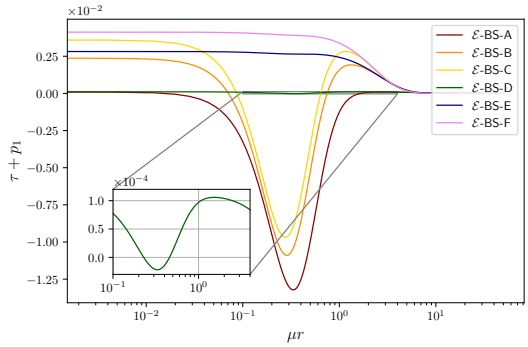

Figure 4.8: Null energy condition for $\mathscr{E}$-boson star configurations described in table 4.1.

all points.

Related to the NEC violation, the high compactness obtained by the solutions (as will be seen below) and the recent results on compact objects and circular photon orbits, we wonder if the appearance of light rings happens before the critical value of the mass, in the branch that in standard boson stars corresponds to the family of stable solutions. However, what we obtain when we evaluate the condition in Eq. (4.16) across fixed χ_0 families of solutions, is that although the light ring "climbs" to the critical mass configuration as we increase the value of χ_0, it never passes to the so-called stable branch.

The $\mathscr{E}$-boson stars have also the remarkable property that the compactness of the configurations can easily rise above the Buchdahl limit as seen in Fig. 4.9. Indeed, the interplay of both scalars field, the exotic pushing away the canonical one, and the canonical exercising a larger pressure, provokes that the matter could be compressed to very high values[3] As shown in Fig. 4.9 and in the Appendix, increasing values of χ_0 or μ_χ/μ_φ points to the fact that the black hole limit could be reached. There was already experience with the ℓ-boson stars, [85] where the maximum compactness tends to the Buchdahl limit as the parameter ℓ grows, but they never rose above such limit. The $\mathscr{C}$-stars, presented in [133] are solutions which describe anisotropic fluid stars with compactness above the Buchdahl limit, due to anisotropic pressures. Gravastars are also an example of compact object solutions within general relativity with compactness above the Buchdahl limit [134]. See [135] for a discussion on the conditions needed to rise above such limit, and it is presented the case for a collection of non-interactive particles, the

[3]This is similar to the effect on the compactness and total mass of self-interacting boson stars [132], where the repulsive (positive) self-interaction allows to accumulate more scalar field within the star, except that in the case presented in this manuscript, the repulsion is driven by the gravitational interaction.

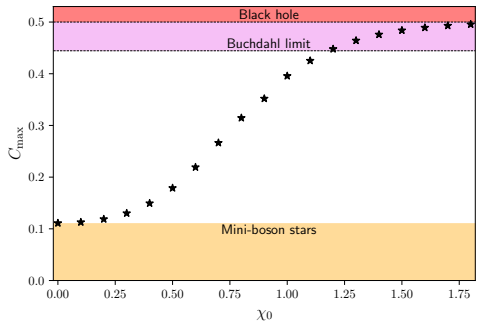

Figure 4.9: Maximum compactness for $\mathscr{E}$-boson stars with fixed values of χ_0.

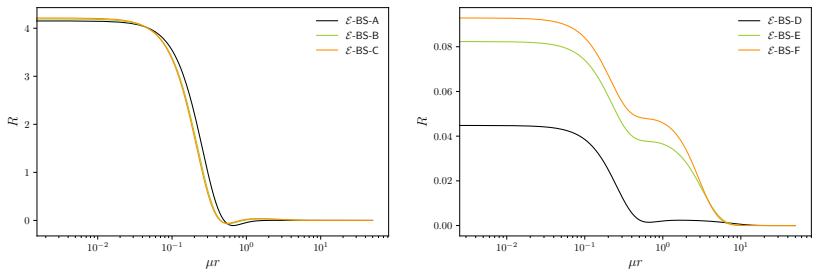

Figure 4.10: 4D curvature scalar for $\mathscr{E}$-boson star configurations described in Table 4.1.

Vlasov gas, where the Buchdahl limit is not surpassed. See Ref. [136] for interesting discussions on the maximum compactness of horizonless compact objects and [137] for case of bosonic fields.

Regarding the geometric scalars, we present their behavior for the six cases of the Table 4.1 labeled as cases $\mathscr{E}$-BS. Several of them describe concentric spheres and one of them (solution $\mathscr{E}$-BS-A) describe a shell-like configuration. In all cases the scalar of curvature (which follows the total density), the Kretschmann and Weyl scalars are well-behaved Fig. 4.10, 4.11, 4.12. For cases A-C, all curvature scalars behave in a similar manner given that we have similar quantities of exotic and canonical matter, not so for the D-F cases that shown differences in their maximum (or minimum) values. Central values ϕ_0 and χ_0 are similar in magnitude, but the curvature behavior is affected by the content of canonical scalar field, smaller values for ϕ_0 results in flatter spaces.

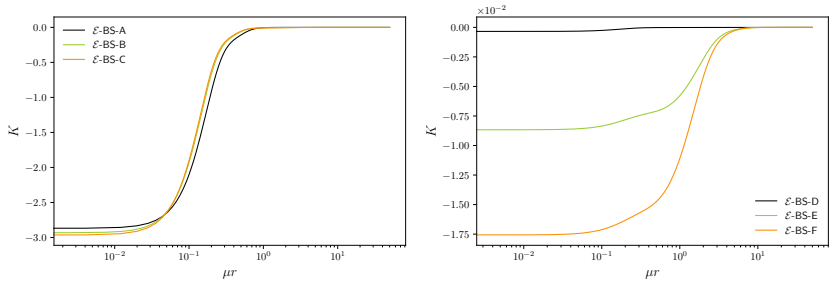

Figure 4.11: Kretschmann scalar for $\mathscr{E}$-boson star configurations described in table 4.1.

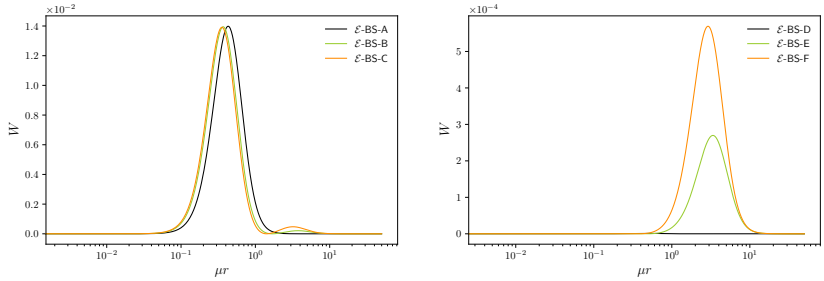

Figure 4.12: Weyl scalar for $\mathscr{E}$-boson star configurations described in table 4.1.

	$\mu_\varphi = \mu_\chi = \mu$						
Solution	ϕ_0	χ_0	ω/μ	λ	μM	μR_{99}	C
BS-A	1.057×10^{-2}	0	0.975	-	0.3696	24.27	1.523×10^{-2}
BS-B	4.650×10^{-2}	0	0.901	-	0.6027	10.68	5.645×10^{-2}
Ph-A	0	0.1	-	925.8	-0.0102	2.903	-3.519×10^{-3}
Ph-B	0	1.0	-	2.559	-11.44	6.665	-1.743
$\mathscr{E}$-BS-A	9.951×10^{-3}	0.1	0.975	925.6	0.3793	24.80	1.530×10^{-2}
$\mathscr{E}$-BS-B	4.512×10^{-2}	0.1	0.901	925.6	0.6148	10.81	5.688×10^{-2}
$\mathscr{E}$-BS-C	5.409×10^{-2}	0.1	0.885	927.2	0.6322	9.687	6.526×10^{-2}
$\mathscr{E}$-BS-D	1.033×10^{-2}	0.01	0.975	9.403×10^4	0.3662	24.57	1.491×10^{-2}
$\mathscr{E}$-BS-E	4.698×10^{-2}	0.01	0.901	9.411×10^4	0.6040	10.62	5.689×10^{-2}
$\mathscr{E}$-BS-F	5.539×10^{-2}	0.01	0.886	9.430×10^4	0.6196	9.614	6.445×10^{-2}

Table 4.1

4.4 Final remarks

We have designed a configuration such that the exotic matter, described by a real massive scalar field with self-interaction and such that the corresponding stress energy tensor has a global sign opposite to the one corresponding to a canonical scalar field, is distributed inside a usual, canonical boson star configuration described by a massive complex scalar field.

We have been able to solve the corresponding differential equations considering that the configuration is static and has spherical symmetry, using an integration method based on the spectral solver procedure and demanding regularity at the origin and asymptotic flatness. We obtain several examples of configurations based on three free parameters, namely the central amplitudes of both scalar fields and the ratio between the exotic scalar mass μ_χ and the canonical one μ_φ.

From the configurations obtained, several interesting features were deduced. First of all, the static spherical configurations inherit a part of the properties of boson stars and phantom solitons, however the gravitational (repulsive) interaction between the fields creates new global features of the configurations, such as an appreciable increase in compactness and also different morphologies, with the phantom field always within the canonical field. As in boson stars, it is obtained that in the plots of the total mass of the configuration versus the frequency, have the usual snail-like plot, with the possible implication that the maximum of each plot separates a region with stable total configurations from the unstable ones.

We also found another interesting feature regarding the ratio of the central amplitudes of the exotic scalar field, χ_0, to the corresponding of the canonical one, ϕ_0; when the ratio is much smaller than one, both distributions, the exotic and the canonical one, are concentric spheres, however, as the ratio grows, the canonical distribution seems to be pushed outwards form the center, forming a shell-like distribution containing in the center the exotic field.

We obtained the scalars of curvature which are regular at all points and describe the characteristic features of the different types of matter on the geometry. An eloquent feature of $\mathscr{E}$-boson stars is that it is possible to tune the amplitudes of the fields in such a way that the NEC is always satisfied and stable numerical implementation could be obtained even with a phantom scalar field. Further information will be given in the forthcoming part II of our work.

We have thus designed and obtained interesting configurations with two types of scalar fields. Clearly, the dynamics of such configurations, with some possible stable or stationary states, is a most pressing question which will be dealt with in a forthcoming work. Preliminary results show that some of these configurations remain bounded.

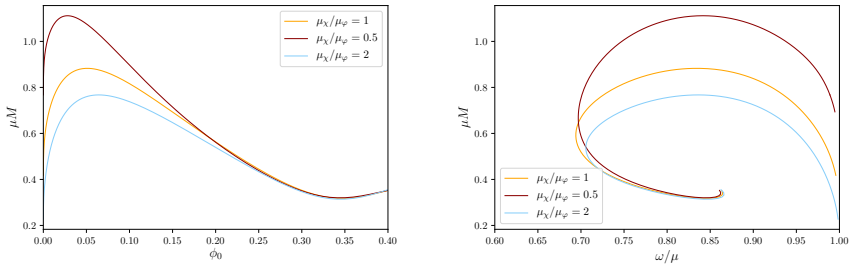

Figure 4.13: $\chi_0 = 0.4$ configurations with three different values for the ratio μ_χ/μ_φ. Left panel: Value of the canonical scalar field ϕ at $r = 0$ *vs.* total mass. Right panel: Total mass *vs.* frequency.

4.5 Appendix of Chap. 4. Solutions with $\mu_\varphi \neq \mu_\chi$

The ratio between the mass parameter of χ and φ is also a free parameter in the model and cannot be absorbed by any simple rescaling. Nevertheless the implication of modifying this parameter are relatively simpler than the effects of the χ_0 parameter.

In Figs. 4.13 and 4.14 we show some global quantities of solutions for fixed value $\chi_0 = 0.4$ and three different values of the quotient μ_χ/μ_φ. The conclusions regarding the mass and compactness are straightforward: as μ_χ/μ_φ increases, the effects of the phantom field are more present and bigger values for the total mass of the distribution and for the compactness are obtained. We have verified that similar effects are obtained for other values of χ_0, in addition to those presented in the above figures. For example, we have configurations with $\mu_\chi/\mu_\varphi = 1$ which do not exceed the Buchdahl limit, but it is possible to modulate the value of the quotient to obtain configurations with compactnesses as close to 0.5 as desired.

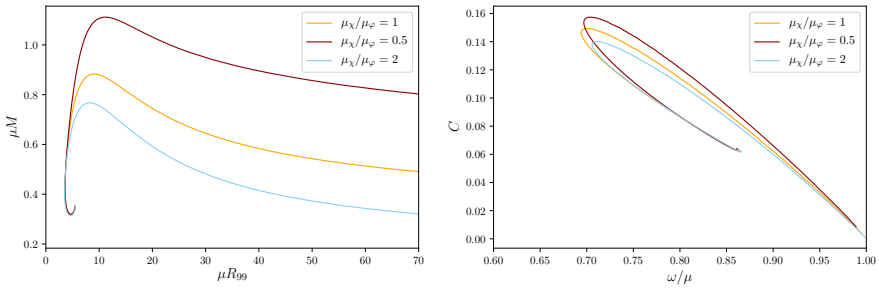

Figure 4.14: $\chi_0 = 0.4$ configurations with three different values for the ratio μ_χ/μ_φ. First panel: Radius R_{99} *vs.* total mass. Second panel: Frequency *vs.* compactness.

CHAPTER 5

TRAVERSABLE ℓ-WORMHOLES[1]

Contents

We present new, asymptotically flat, static, spherically symmetric and traversable wormhole solutions in General Relativity which are supported by a family of ghost scalar fields with quartic potential. This family consists of a particular composition of the scalar field modes, in which each mode is characterized by the same value of the angular momentum number ℓ, yet the composition yields a spherically symmetric stress-energy-momentum and metric tensor. For $\ell = 0$ our solutions reduce to wormhole configurations which had been reported previously in the literature. We discuss the effects of the new parameter ℓ on the wormhole geometry including the motion of free-falling test particles.

[1]This chapter is extracted with minor revisions from Ref. [122], which was written in collaboration with B. Carvente, J. C. Degollado, D. Núñez and O. Sarbach.

5.1 Introduction

The essential property of General Relativity, namely, that matter determines the geometry of the spacetime, acquires a new light when the matter is such that it violates the energy conditions [138–142]. In particular, the violation of the null energy condition opens the possibility for the existence of globally hyperbolic, asymptotically flat spacetimes with non-trivial topological structures [143]. Such matter, usually referred to as *exotic* in the literature, generates peculiar responses in the properties of the spacetime curvature with important consequences on the effective gravitational potential, producing potential "bumps" instead of the usual potential wells. To provide an explicit example, in Fig. 5.1, we present the gravitational effective potentials for a massive, radially infalling test particle for two cases: the first one is due to the presence of a point mass which generates the usual gravitational well, whereas the second one is generated by a distribution of exotic matter (as the one discussed later in this work) in which case the potential exhibits a different type of convexity corresponding to a gravitational potential bump.

Figure 5.1: Gravitational potential produced by a point mass $\sim -1/r$ (left panel) and by the exotic distribution presented in this work (right panel), see section 5.5.1. In both cases a test particle with vanishing angular momentum is considered.

Moreover, under specific circumstances, the *bump* could be such that it connects two separated regions of spacetime. The resulting configuration is dubbed *wormhole*, and it offers challenges and opportunities to better understand the relation between matter and geometry, aside from the fact that, being bona fide solutions to Einstein's equations, it could potentially describe an astrophysical scenario if exotic matter turns out to actually being present in our Universe.

In cosmology, matter with negative pressure can be used to describe the observed accelerated expansion of the Universe [144–147] and seems to be favored by several observational constraints [29, 148, 149]. Additionally, modeling the dark energy with an equation of state of the form $p = \omega\rho$, the observations suggest a

value of ω close to -1 or even smaller, in which case the existence of astrophysical or cosmological wormholes becomes plausible.

The studies of traversable wormholes have their origin with Ellis' work [150], where the author presented a black hole like solution to Einstein's equations, and in order to remove the singularity, used a scalar field and *drain the hole*. Actually, the same solution, based on a different approach was obtained almost at the same time by Bronnikov [119]. It turned out that the solution represented a bridge between two regions of the spacetime. Over the years, the idea was further developed, and the best known example of a traversable wormhole appeared in 1988, in the work of Morris and Thorne [151]. Since then, a plethora of literature has arisen and the complexity of the models has increased, see for example [152, 153] and references therein.

In order to obtain a wormhole solution to the Einstein equations, some works use generation procedures, such as the Newman-Janis algorithm, which allows to obtain a Kerr black hole solution starting from a Schwarzschild one; in this way, a rotating (although not asymptotically flat) solution was obtained starting from one of the original Ellis models [120]. There is also a technique which uses the thin shell approach, which assumes that the matter is concentrated in a three-dimensional submanifold. However, a common practice is to analyze the geometry describing a putative wormhole without mentioning the possible matter that could generate it, artificially producing general forms of such wormholes which might even include rotation; in the words of Morris and Thorne: fixed the geometry... *"and let the builders of a wormhole synthesize, or search throughout the universe for, materials or fields with whatever stress-energy tensor might be required"* [151].

In the present work, we prefer to avoid this "reversed engineering approach" and assume the specification of a suitable matter model which allows for a large class of static, spherically symmetric and traversable wormhole solutions. In particular, following the recent approach in [99] to construct a generalized class of static and spherically symmetric boson stars, we consider a family of massive, complex and self-interacting ghost scalar fields similar to the one considered in Dzhunushaliev *et al.* [121, 124], but which includes an extra parameter ℓ mimicking the effects of the angular momentum. In this way, new spherical and traversable wormhole solutions can be constructed which generalize those of Refs. [121, 124] to $\ell > 0$. Accordingly, and following the terminology of the ℓ-boson stars, we dub these solutions ℓ-wormholes.

While Ellis' original solutions use a massless, time-independent real scalar field without self-interaction, in this work we consider massive, complex and self-interacting scalar fields with a harmonic time-dependency *à la* Dzhunushaliev *et al.* [121, 124], but instead of considering just a single field we consider a fam-

ily of fields with angular momentum number ℓm with ℓ fixed and $m = -\ell, \ldots, \ell$. Assuming like in [99] that each of these fields has exactly the same radial dependency, we obtain static, spherically symmetric wormhole solutions. When $\ell = 0$, the mass of the scalar field, its self-interaction and the time-frequency vanish one recovers Ellis' wormhole solutions.

The new wormholes have several interesting characteristics, such as curvature scalars and effective potentials which smooth out the features of the corresponding 0-wormholes. The geodesic motion helps us to understand the role played by the ℓ–parameter in the spacetime configuration. Finally, the presence of a new parameter gives rise to the possibility that this wormhole might be stable, a feature that will be discussed in a followup work.

The paper is organized as follows. In Section 5.2, we specify our metric ansatz describing static, spherical symmetric and traversable wormhole spacetimes and introduce the matter model. In Section 5.3, we derive the static field equations in spherically symmetry, discuss some qualitative properties of the wormhole solutions and then construct numerical solutions to the field equations whose main properties are discussed next in Section 5.4. In Section 5.5, we discuss the embedding diagrams visualizing the spatial geometry of the solutions, derive the geodesic equations for massive or massless test particles propagating in the wormhole metric and analyze the motion under several conditions determined by the wormhole parameters. Finally, we discuss and summarize our results in Section 5.6.

5.2 Foundations

The determination of the stress-energy-momentum tensor that supports a wormhole geometry is of the utmost importance to understand its physical properties and structure. As already mentioned in the introduction, an asymptotically flat wormhole geometry in general relativity requires the matter to be *exotic*, that is, matter that does not fulfill the regular properties of the usual matter we deal with everyday.[2] More specifically, the matter must violate the null energy condition, $T_{\mu\nu}k^\mu k^\nu \geq 0$, where $T_{\mu\nu}$ is the stress-energy-momentum tensor and k^μ any null vector [151, 153]. Incidentally, this is also the fundamental ingredient of the so-called ghost energy, a model not excluded by observations to be a candidate for dark energy. For instance, constraints from the Supernovae Ia Hubble diagram [156] favor the existence of an equation of state for such dark fluid, $p = \omega\rho$ with $\omega < -1$, a model consistent with ghost energy [141].

[2] However, it should be mentioned that there are examples of traversable wormholes without exotic matter in modified theories of gravity [154] or in general relativity when the asymptotic flatness condition is replaced by adS-asymptotics [155].

In practice, violation of the null energy condition is accomplished by changing the global sign in the stress-energy-momentum tensor in Einstein's equations. Ellis called this the *other polarity of the equations* [150]. This change in sign in the equations is attributed to the type of matter, and has multiple implications which might lead to misunderstandings. A global change in sign to the stress-energy-momentum tensor implies that the usual definition of density also has the opposite sign and is thus negative.

In this work we interpret the physical properties of the wormhole directly in terms of the theory of general relativity and Einstein's field equations, so that the exotic matter produces a different reaction in the curvature of the spacetime, particularly in the effective potential in which the test particles move, generating bumps instead of wells, so that a particle has to spend potential energy in order to get closer to the source, while it gains kinetic energy and accelerates when getting away from it; like when climbing a mountain to reach the summit and then going down.

In particular, we stress that when talking about test particles we assume the validity of the weak equivalence principle, which assumes that the inertial and gravitational masses are equal to each other. Therefore, free-falling test particles or photons always follow causal geodesics of the underlying spacetime, regardless of the sign of their mass. The "bump interpretation" mentioned so far will become evident when analyzing the geodesic motion of test particles in Section 5.5.

5.2.1 Metric ansatz

We will consider a static spherically symmetric spacetime with a line element of the form:

$$\mathrm{d}s^2 = -a(r)\,c^2\,\mathrm{d}t^2 + a(r)^{-1}\,\mathrm{d}r^2 + R^2(r)\,\mathrm{d}\Omega^2, \tag{5.1}$$

where R and a are positive functions only of the radial coordinate r, and $\mathrm{d}\Omega^2 = \mathrm{d}\theta^2 + \sin^2\theta\,\mathrm{d}\varphi^2$. Notice that for $R^2 = r^2 + b^2$, with b a positive constant, and $a = 1$, the reflection-symmetric Ellis wormhole metric is recovered [150] and, from it, with a suitable redefinition of the radial coordinate, one obtains the usual form of the Morris–Thorne like wormhole [151]. Also note that the coordinate r our work is based on extends from $-\infty$ to $+\infty$, and we will demand that R be regular at the throat $r = 0$, which corresponds to a minimum of the area $4\pi R^2$ of the invariant two-spheres.

5.2.2 Matter content

In the present work, we consider a set of several massive scalar fields with a self-interaction term. Our configurations are constructed in such a way that the sum of the fields preserves the spherical symmetry of the stress-energy-momentum

tensor and includes an extra parameter associated with the angular momentum number ℓ. This approach was introduced in [100] in the context of critical collapse, and recently used in [99] to construct ℓ-boson stars.

We start with the Lagrangian density for N complex massive scalar fields

$$\mathscr{L}_\Phi = -\frac{1}{2\kappa}\left[\sum_{i=1}^{N}\eta\nabla_\mu\Phi_i\nabla^\mu\Phi_i^* + V(\left|\Phi\right|^2)\right], \tag{5.2}$$

with a quartic potential

$$V(\left|\Phi\right|^2) = \sum_{i=1}^{N}V^{(i)} = \sum_{i=1}^{N}\left(\eta_\mu\frac{m_\Phi^2c^2}{\hbar^2}|\Phi_i|^2 + \eta_\lambda\frac{\lambda}{2\hbar^2}\left|\Phi_i\right|^2\sum_{j=1}^{N}\left|\Phi_j\right|^2\right) \tag{5.3}$$

where $\kappa = 8\pi G/c^4$, $\hbar$ is the reduced Planck constant, m_Φ is the mass of the scalar field particle and λ is the parameter measuring the strength of the quartic interaction term. The values $\eta = \eta_\mu = \eta_\lambda = 1$ represent the canonical scalar fields while $\eta = \eta_\mu = -\eta_\lambda = -1$ describe the type of ghost fields in which we will be interested in, and from now on we fix the latter choice. In the following, for convenience, we will work with the rescaled quantities $\mu = m_\Phi c/\hbar$ and $\Lambda = \lambda/2\hbar^2$ instead of m_Φ and λ.

The stress-energy-momentum tensor associated with the scalar field Φ_i is thus given by

$$T_{\mu\nu}^{(i)} = \frac{c^4}{16\pi G}\left[-\left(\nabla_\nu\Phi_i\,\nabla_\mu\Phi_i^* + \nabla_\nu\Phi_i\,\nabla_\mu\Phi_i^*\right) - g_{\mu\nu}\left(-\nabla_\alpha\Phi_i\nabla^\alpha\Phi_i^* + V^{(i)}\right)\right], \tag{5.4}$$

while the total stress-energy-momentum tensor that we plug into Einstein's field equations is

$$T_{\mu\nu} = \sum_{i=1}^{N}T_{\mu\nu}^{(i)}. \tag{5.5}$$

In [100], for the case of real scalar fields, and in the appendix of [99], for complex ones, it was shown that for an appropriate superposition, a stress-energy-momentum tensor of the form (5.5) with $\Lambda = 0$ may be spherically symmetric, even though the individual fields Φ_i have non-vanishing angular momentum. Here, we generalize this result further to include the self-interaction of the field. The procedure is as follows.

Each scalar field Φ_i has the form

$$\Phi_i(t,r,\theta,\varphi) = \phi_\ell(t,r)Y^{\ell m}(\theta,\varphi), \qquad i = \ell+1+m, \tag{5.6}$$

where m varies over $-\ell, -\ell+1, \ldots, \ell$ (such that i varies from 1 to $N = 2\ell+1$) and $Y^{\ell m}(\theta,\varphi)$ denote the standard spherical harmonics. Here, the parameter ℓ is kept fixed and the amplitudes $\phi_\ell(t,r)$ are equal to each other for all m. Using the addition theorem for the spherical harmonics, one can show that the resulting

stress-energy-momentum tensor in Eq. (5.5) for the $N = 2\ell+1$ fields is spherically symmetric.

Next, one considers a stationary state with harmonic time dependence for the scalar field

$$\phi_\ell(t,r) = e^{i\omega t}\,\chi_\ell(r), \tag{5.7}$$

where χ_ℓ is function of r and ω is a real constant. Once such procedure is carried out, the following non-trivial components of the stress-energy-momentum tensor are obtained:

$$T^t{}_t = \frac{c^4}{8\pi G}\frac{2\ell+1}{8\pi}\left\{a\left(\frac{\mathrm{d}\chi_\ell}{\mathrm{d}r}\right)^2+\left[\frac{\ell\left(\ell+1\right)}{R^2}+\mu^2-\frac{2\ell+1}{4\pi}\Lambda\chi_\ell^2+\frac{\omega^2}{a}\right]{\chi_\ell}^2\right\}, \tag{5.8}$$

$$T^r{}_r = \frac{c^4}{8\pi G}\frac{2\ell+1}{8\pi}\left\{-a\left(\frac{\mathrm{d}\chi_\ell}{\mathrm{d}r}\right)^2+\left[\frac{\ell\left(\ell+1\right)}{R^2}+\mu^2-\frac{2\ell+1}{4\pi}\Lambda\chi_\ell^2-\frac{\omega^2}{a}\right]{\chi_\ell}^2\right\}, \tag{5.9}$$

$$T^\theta{}_\theta = T^\varphi{}_\varphi = \frac{c^4}{8\pi G}\frac{2\ell+1}{8\pi}\left\{a\left(\frac{\mathrm{d}\chi_\ell}{\mathrm{d}r}\right)^2+\left[\mu^2-\frac{2\ell+1}{4\pi}\Lambda\chi_\ell^2-\frac{\omega^2}{a}\right]{\chi_\ell}^2\right\}. \tag{5.10}$$

Notice how the procedure of adding individual stress-energy-momentum tensors maintains the spherical symmetry and yields a result that depends on the angular momentum number ℓ through the centrifugal-like terms $\ell(\ell+1)/R^2$. As expected and shown below, this dependency plays a nontrivial role in the solutions of Einstein's equations. The mixed components $T^t{}_r$, $T^t{}_\theta$ and $T^t{}_\varphi$ vanish; indicating that there are no fluxes of matter in this case, which is compatible with the assumption of staticity of the metric.

Notice also that the stress-energy-momentum tensor (5.8–5.10) violates the null energy condition everywhere; for instance, the null vector field $k = a^{-1/2}c^{-1}\partial_t + a^{1/2}\partial_r$ gives

$$T_{\mu\nu}k^\mu k^\nu = -T^t{}_t + T^r{}_r = -\frac{c^4}{8\pi G}\frac{2\ell+1}{4\pi}\left[a\left(\frac{\mathrm{d}\chi_\ell}{\mathrm{d}r}\right)^2+\frac{\omega^2}{a}\chi_\ell^2\right], \tag{5.11}$$

which is negative unless the scalar field vanishes.

Now, one can compute the equation of motion for each individual field, *i. e.* the Klein-Gordon equation, using the fact that the divergence of the total stress-energy-momentum tensor is zero. Each amplitude obeys the identical equation:

$$\frac{\mathrm{d}}{\mathrm{d}r}\left[aR^2\frac{\mathrm{d}\chi_\ell}{\mathrm{d}r}\right]+R^2\left(\frac{\omega^2}{a}-\frac{\ell\left(\ell+1\right)}{R^2}-\mu^2+\frac{2\ell+1}{2\pi}\Lambda\chi_\ell^2\right)\chi_\ell = 0, \tag{5.12}$$

where we have used the fact that spherical harmonics are eigenfunctions of the Laplace-Beltrami operator

$$\Delta_{S^2}Y^{\ell m} = \left(\frac{\partial^2}{\partial\theta^2}+\cot\theta\frac{\partial}{\partial\theta}+\frac{1}{\sin^2\theta}\frac{\partial^2}{\partial\varphi^2}\right)Y^{\ell m} = -\ell\left(\ell+1\right)Y^{\ell m}\,. \tag{5.13}$$

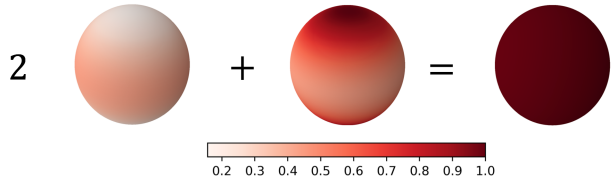

Figure 5.2: Normalized density at the throat for a $\ell = 1$ wormhole. The first sphere represents the $m = \pm 1$ contribution while the center sphere corresponds to the $m = 0$ contribution.

As an example of the construction of the $\ell-$wormhole by the contribution of individual non-spherical scalar fields, in Fig. 5.2 we show the distribution of the density at the throat for the fields $(\phi_1 Y^{1-1}, \phi_1 Y^{10}, \phi_1 Y^{11})$. The values are given by Eq. (5.5) for the $T^t{}_t \propto \rho$ component. This is the case for $\ell = 1$ wormhole, so that there are three values for m. The first sphere represents the sum of the $m = -1$ and $m = 1$ contributions, the second one represents the $m = 0$ field, and the combination is given in such a way that the total density (the third sphere) is spherically symmetric.

5.3 Stationary Wormhole equations

In order to obtain the remaining field equations, it is helpful to notice that with the stress-energy-momentum tensor components given by Eqs. (5.8, 5.9, 5.10) the following equation is satisfied

$$\frac{T^t{}_t - T^r{}_r}{2} - T^\theta{}_\theta = -\frac{c^4}{8\pi G}\frac{2\ell+1}{8\pi}\left(\mu^2 - \frac{2\ell+1}{4\pi}\Lambda\chi_\ell^2 - \frac{2}{a}\omega^2\right)\chi_\ell^2. \tag{5.14}$$

On the other hand, from the line element Eq. (5.1), we obtain the Bianchi-Einstein tensor, $G^\mu{}_\nu$, and the same linear combination of the components gives:

$$\frac{G^t{}_t - G^r{}_r}{2} - G^\theta{}_\theta = -\frac{1}{2R^2}\frac{\mathrm{d}}{\mathrm{d}r}\left[R^2\frac{\mathrm{d}a}{\mathrm{d}r}\right]. \tag{5.15}$$

Thus, with the aid of Einstein's equations:

$$G^\mu{}_\nu = \frac{8\pi G}{c^4}T^\mu{}_\nu, \tag{5.16}$$

we obtain our next field equation:

$$\frac{1}{2R^2}\frac{\mathrm{d}}{\mathrm{d}r}\left[R^2\frac{\mathrm{d}a}{\mathrm{d}r}\right] = \frac{2\ell+1}{8\pi}\left(\mu^2 - \frac{2\ell+1}{4\pi}\Lambda\chi_\ell^2 - \frac{2}{a}\omega^2\right)\chi_\ell^2. \tag{5.17}$$

Notice that when a static, massless scalar field (regular or exotic) without interaction is considered, then a particular solution is obtained in which the metric function a is constant.

A further field equation comes from the combination of the $G^t{}_t$ component plus the $G^r{}_r$ one, and the corresponding $T^\mu{}_\nu$ components:

$$\frac{\mathrm{d}R^2}{\mathrm{d}r}\frac{\mathrm{d}a}{\mathrm{d}r}+a\frac{\mathrm{d}^2R^2}{\mathrm{d}r^2}-2=\frac{2\ell+1}{4\pi}\left[R^2\left(\mu^2-\frac{2\ell+1}{4\pi}\Lambda\chi_\ell^2\right)+\ell(\ell+1)\right]\chi_\ell^2. \tag{5.18}$$

As mentioned above, for the first independent field equation, we consider the Klein-Gordon equation, Eq. (5.12). In this way we obtain a system of equations in which each function $\chi_\ell(r)$, $a(r)$ and $R^2(r)$ appears as the only second derivative:

$$\chi_\ell''=-\left(\frac{R^{2\prime}}{R^2}+\frac{a'}{a}\right)\chi_\ell'+\frac{1}{a}\left[\mu^2-\frac{\omega^2}{a}+\frac{\ell(\ell+1)}{R^2}-\frac{2\ell+1}{2\pi}\Lambda\chi_\ell^2\right]\chi_\ell, \tag{5.19}$$

$$a''=-\frac{R^{2\prime}}{R^2}a'+\frac{2\ell+1}{4\pi}\left(\mu^2-\frac{2}{a}\omega^2-\frac{2\ell+1}{4\pi}\Lambda\chi_\ell^2\right)\chi_\ell^2, \tag{5.20}$$

$$R^{2\prime\prime}=\frac{1}{a}\left\{-a'R^{2\prime}+2+\frac{2\ell+1}{4\pi}\left[\left(\mu^2-\frac{2\ell+1}{4\pi}\Lambda\chi_\ell^2\right)R^2+\ell(\ell+1)\right]\chi_\ell^2\right\} \tag{5.21}$$

where a prime denotes derivative with respect to r. The remaining field equation is the rr-component of Eq. (5.16) which yields

$$\frac{R^{2\prime}}{2R^2}\left(a'+\frac{aR^{2\prime}}{2R^2}\right)-\frac{1}{R^2}=\frac{2\ell+1}{8\pi}\left[-a\,{\chi_\ell}^{2\prime}+\left(\mu^2-\frac{2\ell+1}{4\pi}\Lambda\,{\chi_\ell}^2-\frac{\omega^2}{a}+\frac{\ell\,(\ell+1)}{R^2}\right){\chi_\ell}^2\right], \tag{5.22}$$

which can be interpreted as a constraint since it only involves zeroth and first-order derivatives of the fields. Provided the second-order field equations (5.19, 5.20, 5.21) are satisfied, the twice contracted Bianchi identity $\nabla_\mu G^\mu{}_r=0$ and $\nabla_\mu T^\mu{}_r=0$ imply that

$$\frac{\mathrm{d}}{\mathrm{d}r}\left[aR^4\left(G^r{}_r-\frac{8\pi G}{c^4}T^r{}_r\right)\right]=0, \tag{5.23}$$

such that it is sufficient to solve Eq. (5.22) at one point (the throat, say).

A particular simple solution arises when a static, spherical, massless scalar field (regular or exotic) without interaction is considered. In this case, the parameters ω, μ, and Λ vanish and considering $\ell=0$, the field equations (5.19–5.22) can be integrated explicitly [119, 150], see also [157]. The simplest (but not unique) solution is obtained assuming that the metric function a is constant. This yields the solution

$$a=1,\qquad R^2=b^2+r^2,\qquad \chi_{\mathrm{Ellis}}(r)=\sqrt{8\pi}\arctan\left(\frac{r}{b}\right), \tag{5.24}$$

which has the property that the metric functions a, R^2 and the gradient of χ_{Ellis} are reflection symmetric about the throat $r=0$. In Fig. 5.3, we present the plot of Ellis' ghost field and the corresponding energy density. Although the scalar

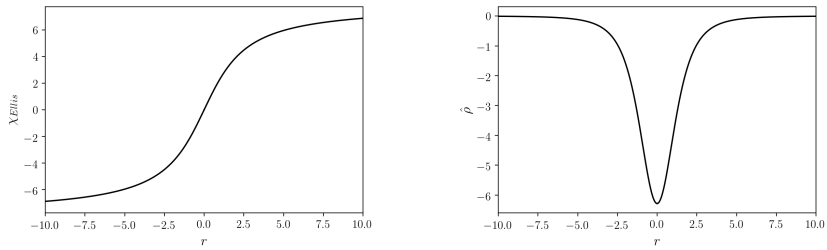

Figure 5.3: Ghost field and the corresponding density for the original Ellis wormhole.

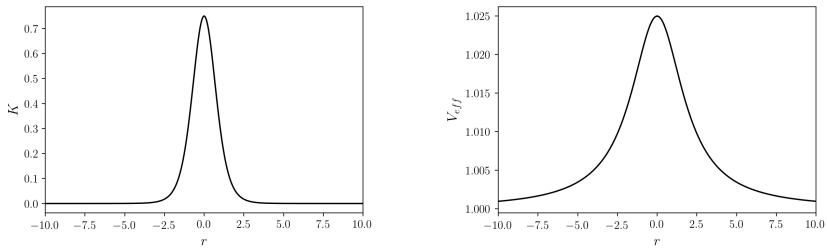

Figure 5.4: Kretschmann scalar and effective potential, $V_{\text{eff}} = L^2/R^2 + \kappa$ for a massive particle propagating on the reflection-symmetric Ellis wormhole.

field itself does not decay to zero simultaneously at both asymptotic ends $r \to \pm\infty$, its gradient does. Since in the massless case the stress-energy-momentum tensor and equations of motion only depend on the gradient of the scalar field, the configuration is localized from a physical point of view. Furthermore, we observe that the density is negative everywhere. The curvature and Kretschmann scalars are given by $R_{s,\text{Ellis}} = -\frac{2b^2}{\left(r^2+b^2\right)^2}$ and $K_{\text{Ellis}} = R^2_{s,\text{Ellis}}$ (see Fig. 5.4), respectively, and like the density, they have a fixed sign.

In the following, we consider much more general wormhole solutions in which the parameters ω, ℓ, μ and Λ do not necessarily vanish. These solutions are obtained by numerically integrating the field equations (5.19, 5.20, 5.21) and taking into account the constraint (5.22). For simplicity, in this article, we restrict ourselves to the reflection-symmetric case (although more general wormhole solutions which are asymmetric about the throat could also be considered). These solutions satisfy the following boundary conditions at the throat, $r = 0$:

$$\chi'_\ell(0) = 0, \tag{5.25}$$

$$a'(0) = 0, \tag{5.26}$$

$$R^{2\prime}(0) = 0. \tag{5.27}$$

Denoting by $b := R(0)$ the areal radius of the throat, the constraint (5.22) yields the following condition at $r = 0$:

$$\left[1 + \frac{(2\ell+1)\ell(\ell+1)}{8\pi}\chi_\ell(0)^2\right] b^{-2} = \frac{2\ell+1}{8\pi}\left(\frac{\omega^2}{a(0)} - \mu^2 + \frac{2\ell+1}{4\pi}\Lambda\chi_\ell(0)^2\right)\chi_\ell(0)^2, \tag{5.28}$$

which fixes the radius b of the throat and requires $a(0)$ and $\chi_\ell(0) \neq 0$ to be chosen such that

$$\frac{\omega^2}{a(0)} + \frac{2\ell+1}{4\pi}\Lambda\chi_\ell(0)^2 > \mu^2. \tag{5.29}$$

Note that this inequality and Eq. (5.20) also imply that a has a local maximum at the throat. Next, Einstein's equation (5.21) together with the conditions (5.25, 5.26, 5.27), implies the relation

$$\frac{1}{2}a(0)(R^2)''(0) = \frac{2\ell+1}{8\pi}\left[b^2\left(\mu^2 - \frac{2\ell+1}{4\pi}\Lambda\chi_\ell(0)^2\right) + \ell(\ell+1)\right]\chi_\ell^2(0) + 1. \tag{5.30}$$

Using Eq. (5.28) this can be simplified considerably,

$$\frac{1}{2}a(0)(R^2)''(0) = \frac{2\ell+1}{8\pi}\frac{b^2\omega^2}{a(0)}\chi_\ell(0)^2, \tag{5.31}$$

which shows that the throat is indeed a local minimum[3] of R^2. For $\ell = 0$ the Eqs. (5.28, 5.31) reduce to the corresponding equations in Ref. [121] (see their equation (18) and the unnumbered equation below it.) Due to Eq. (5.28), one has two free parameters at the throat, given by $\chi_\ell(0) \neq 0$ and $a(0)$, say. As can be checked, the field equations (5.19,5.20, 5.21, 5.22) as well as the conditions (5.28, 5.31) are invariant with respect to the transformations

$$(\omega, t, r, a, R^2, \chi_\ell) \mapsto \left(\frac{\omega}{\sqrt{B}}, \sqrt{B}t, \frac{r}{\sqrt{B}}, \frac{a}{B}, R^2, \pm\chi_\ell\right), \tag{5.32}$$

with $B > 0$ a real parameter. Therefore, one can fix the value of $a(0)$ to one, say, and adjust the value of B such that $a(r) \to 1$ for $r \to \infty$. In this way, one is left with just one shooting parameter ($\chi_\ell(0) > 0$, say) at the throat $r = 0$.

At $r \to \pm\infty$, we require asymptotic flatness,

$$\chi_\ell(r) \to 0, \tag{5.33}$$

$$a(r) \to 1, \tag{5.34}$$

$$\frac{R(r)}{r} \to 1. \tag{5.35}$$

[3] For $\omega \neq 0$ the right-hand side of Eq. (5.31) is positive since χ_ℓ and χ_ℓ' cannot both vanish at $r = 0$; otherwise it would follow from Eq. (5.19) that χ_ℓ vanishes identically. For the special case $\omega = 0$ see the proof of Theorem 2 below.

Under these assumptions, the field equation (5.19) for the scalar field reduces to

$$\chi_\ell''(r) \approx (\mu^2 - \omega^2)\chi_\ell(r), \tag{5.36}$$

which shows that[4]

$$\omega^2 < \mu^2 \tag{5.37}$$

is required to have the exponentially decaying solution $\chi_\ell(r) \approx e^{-\sqrt{\mu^2-\omega^2}r}$. Approximating the (exponentially decaying) right-hand sides of Eqs. (5.17, 5.18) to zero, one obtains the following behavior of the metric coefficients in the asymptotic region:

$$a \approx e^{-\frac{c_0}{r+c_1}}, \qquad R^2 \approx (r+c_1)^2 e^{\frac{c_0}{r+c_1}}, \qquad r \to \infty, \tag{5.38}$$

for some constants c_0 and c_1.

5.3.1 Qualitative analysis of the solutions

Before numerically constructing the wormhole solutions, we make a few general remarks regarding the restrictions on the parameters ω, μ and Λ and the initial condition $\chi_\ell(0)$ and regarding the qualitative properties of the solutions. We assume in the following that $(\chi_\ell(r), a(r), R^2(r))$ is a smooth solution of Eqs. (5.12), (5.17), (5.18) (or, equivalently, of Eqs. (5.19, 5.20, 5.21)) on the interval $[0,\infty)$ which satisfies $a > 0$, $R^2 > 0$, the boundary conditions (5.25, 5.26, 5.27) at $r = 0$ and (5.33, 5.34, 5.35) at $r \to \infty$, and is subject to the conditions (5.28, 5.31) at the throat. We had already observed that an exponentially decaying solution at infinity requires $\omega^2 \leq \mu^2$. Furthermore, at the throat, the inequality (5.29) needs to be satisfied. A first immediate consequence of this last inequality is that the parameters ω and Λ cannot be both zero. In fact, one has the following stronger result which shows that the self-interaction term is needed.

Theorem 1 There are no reflection-symmetric solutions with the above properties if $\Lambda = 0$.

Proof. We prove the theorem by contradiction. If $\Lambda = 0$, the inequality (5.29) implies that

$$\mu^2 < \frac{\omega^2}{a(0)} \leq \frac{\mu^2}{a(0)}, \tag{5.39}$$

which requires $a(0) < 1$ and $\omega^2 > 0$. However, Eq. (5.20) with $\Lambda = 0$ implies that at any point $r = r_c$ where the derivative of a vanishes, the equality

$$a''(r_c) = \frac{2\ell+1}{4\pi}\left(\mu^2 - \frac{2\omega^2}{a(r_c)}\right)\chi_\ell(r_c)^2 \tag{5.40}$$

holds. Since $\mu^2 - 2\omega^2/a(0) < 0$, a has a local maximum at the throat, as already remarked above, such that $a(r)$ decreases for $r > 0$ small enough. Since $a(r) \to 1$ as

[4] The limiting value $\omega^2 = \mu^2$ is discussed in Ref. [121].

$r \to \infty$ there must be a point $r = r_c$ for which a ceases to decrease, corresponding to a (local) minimum of a. At this point, we must have $a(r_c) < a(0)$, $a'(r_c) = 0$ and $a''(r_c) \geq 0$. On the other hand, since

$$\mu^2 - \frac{2\omega^2}{a(r_c)} < \mu^2 - \frac{2\omega^2}{a(0)} < 0, \tag{5.41}$$

Eq. (5.40) implies $a''(r_c) < 0$, provided that $\chi_\ell(r_c) \neq 0$, which leads to a contradiction. If $\chi_\ell(r_c) = 0$, we do not obtain an immediate contradiction since in this case it follows that $a''(r_c) = 0$. However, in this case, we must have $\chi'_\ell(r_c) \neq 0$ since otherwise χ_ℓ (as a solution of the second-order equation (5.19)) would be identically zero. By differentiating Eq. (5.20) twice with respect to r and evaluating at $r = r_c$ one obtains $a'''(r_c) = 0$ and

$$a''''(r_c) = \frac{2\ell+1}{2\pi}\left(\mu^2 - \frac{2\omega^2}{a(r_c)}\right)\chi'(r_c)^2 < 0, \tag{5.42}$$

which shows that $r = r_c$ is a local maximum of a and yields again a contradiction. This concludes the proof of the theorem. □

The next result implies that there cannot be more than one throat.

Theorem 2 Under the assumptions stated at the beginning of this subsection, the function $R^2(r)$ is strictly monotonously increasing and strictly convex on the interval $[0,\infty)$.

Proof. By combining Eqs. (5.21,5.22) one obtains the simple equation

$$\frac{(R^2)''}{R^2} = \frac{1}{2}\left[\frac{(R^2)'}{R^2}\right]^2 + \frac{2\ell+1}{4\pi}\left(\chi_\ell'^2 + \frac{\omega^2}{a^2}\chi_\ell^2\right) \tag{5.43}$$

for R^2, which shows that $(R^2)'' \geq 0$ and hence that R^2 is convex. We show further that the right-hand side of Eq. (5.43) cannot vanish at any point. This is clearly the case if $\omega \neq 0$ since χ'_ℓ and χ_ℓ cannot vanish at the same point (otherwise it would follow from Eq. (5.19) that χ_ℓ is identically zero). Next, we rule out the exceptional case in which $\omega = 0$ and there existed a point $r_0 \geq 0$ where $(R^2)'(r_0) = \chi'_\ell(r_0) = 0$. If this case occurred, successive differentiation of Eq. (5.43) would yield

$$(R^2)'''(r_0) = 0, \qquad \frac{(R^2)''''(r_0)}{R^2(r_0)} = \frac{2\ell+1}{2\pi}[\chi''_\ell(r_0)]^2. \tag{5.44}$$

Further, evaluating Eq. (5.22) at $r = r_0$ one would obtain

$$-\frac{1}{R^2(r_0)} = \frac{2\ell+1}{8\pi}\left(\mu^2 - \frac{2\ell+1}{4\pi}\Lambda\chi_\ell(r_0)^2 + \frac{\ell(\ell+1)}{R^2(r_0)}\right)\chi_\ell(r_0)^2, \tag{5.45}$$

implying that $\chi_\ell(r_0) \neq 0$ and that the expression inside the parenthesis on the right-hand side must be negative. Eq. (5.19) would then imply that

$$a(r_0)\frac{\chi''_\ell(r_0)}{\chi_\ell(r_0)} < -\frac{2\ell+1}{4\pi}\Lambda\chi_\ell(r_0)^2 < 0, \tag{5.46}$$

and hence $\chi_\ell''(r_0) \neq 0$ and $(R^2)''''(r_0) > 0$. It follows that any critical point of R^2 must be a strict minimum of R^2. However, since R^2 is convex there can be only one such critical point which is the one at the throat. Therefore, it follows from Eq. (5.43) that $(R^2)''(r) > 0$ for all $r > 0$ and the theorem is proven. □

5.3.2 Numerical shooting algorithm

Next, we describe a shooting algorithm which allows us to find asymptotically flat wormhole solutions from a given set of initial conditions at the throat by numerically integrating the equations outwards. As discussed above, there is only one free parameter to start the shooting procedure. Such parameter is the value of the scalar field at the throat, $\chi_\ell(0)$.

We are looking for the desired solutions in the same spirit as the boson stars (see for instance [46]), in which the solutions are parametrized by the value of the scalar field at the center of the configuration so that for each solution a set of discrete values for the frequency is found to satisfy the asymptotic flatness conditions, each with different number of nodes for the scalar field profile. Qualitatively, the same happens with the ℓ-wormhole solutions discussed here. All the solutions reported in this article are those corresponding to the ground state, in which the scalar field χ_ℓ has no nodes.

So for given values of $a(0)$, Λ, ℓ, ω, only one particular value of $\chi_\ell(0)$ picks the $\chi_\ell \to 0$ solution at infinity. We can see this in the approximation of the Klein-Gordon equation for large r. If we assume that $a(r)$ tends to unity and $R(r)$ to the coordinate r fast enough, then Eq. (5.36) is satisfied, which is consistent with exponential decay of χ_ℓ for large r as long as $\mu^2 - \omega^2 > 0$. In a similar way we see that if χ_ℓ is exponentially decaying at both infinities then, from (5.20) we obtain $\frac{\mathrm{d}^2 a}{\mathrm{d}r^2} + \frac{2}{r}\frac{\mathrm{d}a}{\mathrm{d}r} \approx 0$, which has solutions:

$$a \approx B + \frac{A}{r}, \tag{5.47}$$

where A and B are constants. This is a particular simplification over Eq. (5.38) that is useful in the numerical procedure. In particular B will enter as a normalization factor, since we will ask for $B = 1$, as required by the asymptotic condition (5.34).

As mentioned previously, $\chi_\ell(0)$ is used as the shooting parameter so the requirements needed to find a solution are those described in the previous paragraphs. Using the Lsoda Fortran solver for initial value problems of ordinary differential equations, we perform the integration of the system (5.19–5.21) starting at the value $r = 0$ using steps of $\Delta r = 1 \times 10^{-6}$ until a final value is reached. This finite value of the asymptotic boundary needs to be sufficiently large for the functions to reach their asymptotic behavior. Once the desired behavior of χ_ℓ is

$\omega = 0$	$\ell = 0$			$\ell = 1$			$\ell = 2$		
	$\chi_\ell(0)$	$R(0)$	$a(0)$	$\chi_\ell(0)$	$R(0)$	$a(0)$	$\chi_\ell(0)$	$R(0)$	$a(0)$
$\Lambda = 0.5$	6.26	1.07	1.40	3.94	1.72	7.43	3.08	2.71	20.21
$\Lambda = 0.7$	4.91	1.75	0.80	3.21	1.97	2.59	2.58	2.81	7.04
$\Lambda = 1.0$	3.90	2.79	0.58	2.48	2.70	1.03	2.08	3.14	2.51
$\Lambda = 4.0$	1.81	13.21	0.41	1.05	13.14	0.42	0.82	13.00	0.44

Table 5.1: Central values of the field χ_ℓ and metric functions R and a for several values of $\Lambda = 0.5, 0.7, 1.0, 4.0$ and $\ell = 0, 1, 2$ with $\omega = 0$.

$\Lambda = 0.7$	$\ell = 0$			$\ell = 1$			$\ell = 2$		
	$\chi_\ell(0)$	$R(0)$	$a(0)$	$\chi_\ell(0)$	$R(0)$	$a(0)$	$\chi_\ell(0)$	$R(0)$	$a(0)$
$\omega = 0.1$	4.88	1.77	0.83	3.18	2.01	2.60	2.56	2.85	7.03
$\omega = 0.2$	4.64	2.01	1.07	2.95	2.34	2.82	2.36	3.28	7.13
$\omega = 0.3$	4.06	3.01	2.25	2.45	3.67	4.49	1.94	5.01	9.77

Table 5.2: Central values of the field χ_ℓ and metric functions R and a for several values of ω and $\ell = 0, 1, 2$ with $\Lambda = 0.7$.

obtained up to a precision of order Δr, the asymptotic values of R and a are adjusted by means of the transformation (5.32) which leaves the system of equations invariant, where the parameter B is chosen equal to the corresponding coefficient in Eq. (5.47).

Examples are shown in Tables 5.1 and 5.2. Their physical implications are shown in section 5.4. The 0-wormhole recovers the wormhole studied by Dzhunushaliev *et al.* in [121] for complex, massive and self-interacting ghost scalar fields. Our results match those of them as can be seen in the $\Lambda = 4.0$ row in Table 5.1 when the following change of variables is performed:

$$r \mapsto \int_0^r \frac{\mathrm{d}r}{\sqrt{a(r)}}, \ \Lambda \mapsto \frac{\Lambda}{4}, \ \chi_\ell \mapsto \sqrt{\frac{8\pi}{2\ell+1}}\chi_\ell, \tag{5.48}$$

which takes into account the differences in the definitions, nondimensionalization and the coordinate election. These authors also studied the case for a real scalar field in a previous work [124], which in fact corresponds to the $\omega = 0$ results in this paper.

5.3.3 Energy density, mass and curvature scalars

In order to help interpreting the solutions presented in the next section, we discuss several scalar quantities, like the energy density ρ of the ghost field measured by static observers, the Misner-Sharp mass function and the scalars related with

the curvature of the spacetime, such as the Ricci scalar R_s and the Kretschmann scalar K. These quantities will turn out to be helpful for understanding the features of the ghost field and its action on the geometry.

Explicitly, the function ρ, associated with the density of the ghost field, is given by

$$\rho = -\frac{T^t{}_t}{c^2} = \left(\frac{c^2}{8\pi G}\right)\hat{\rho}, \tag{5.49}$$

where $\hat{\rho}$ is defined by

$$\hat{\rho} = -(2\ell+1)\left[a\,\chi_\ell'^2 + \left(\frac{\ell(\ell+1)}{R^2} + \mu^2 - \frac{2\ell+1}{4\pi}\Lambda\chi_\ell^2 + \frac{\omega^2}{a}\right)\chi_\ell^2\right]. \tag{5.50}$$

A striking feature of the wormhole solutions is that despite the presence of the exotic matter which violates the null energy condition everywhere, the density may still be *positive* at the throat,[5] as will be shown in the numerical examples discussed in the next section. In fact, using Eq. (5.22) one can obtain the following simple expression for $\hat{\rho}$ at the throat:

$$\hat{\rho}(0) = \frac{8\pi}{b^2} - 2(2\ell+1)\frac{\omega^2}{a(0)}\chi_\ell(0)^2, \tag{5.51}$$

which shows explicitly that for those solutions with $\omega = 0$ the energy density is indeed positive near the throat. The plots in the next section show that this behavior also holds for other solutions with small enough values of ω^2.

The total (ADM) mass of the wormhole configurations can be computed from the asymptotic limit $M_\infty = \lim_{r\to\infty} M(r)$ of the Misner-Sharp mass function $M(r)$, defined by

$$\frac{2GM}{c^2} = R\left[1 - g^{\mu\nu}(\nabla_\mu R)(\nabla_\nu R)\right] = R\left(1 - aR'^2\right). \tag{5.52}$$

From Eqs. (5.38, 5.47) one obtains $GM_\infty/c^2 = c_0/2 = -A/2$. Alternatively, using Eqs. (5.21, 5.22) one also obtains $M' = 4\pi\rho R^2 R'$ which can be integrated to

$$M(r) = \frac{c^2}{2G}\left(b + \int_0^r \hat{\rho}(\bar{r})R^2(\bar{r})R'(\bar{r})d\bar{r}\right), \tag{5.53}$$

with $b = R(0)$ the throat's areal radius. As long as $\hat{\rho}$ is positive near the throat, the mass function increases as one moves away from the throat. However, M decreases as soon as $\hat{\rho}$ becomes negative, so that solutions which have either sign of the total mass are possible. This is shown in Table 5.3, where values of the total mass M_∞ for our wormhole were computed taking several values of ℓ and fixing the values of all other parameters.

[5] Note that the violation of the null energy condition implies the violation of the weak energy condition, which means that there exists at least one observer which measures negative energy density. Our example shows that this observer does not necessarily need to be a static one.

$\omega = 0,\ \Lambda = 1$	$M_\infty\ (m_{\rm pl}^2/m_\Phi)$
$\ell = 0$	0.677
$\ell = 1$	0.224
$\ell = 2$	−1.25
$\ell = 3$	−4.69

Table 5.3: Total mass values for ℓ-wormholes with $\Lambda = 1$, $\omega = 0$ and $\ell = 0, 1, 2, 3$.

The Ricci scalar, $R_s = R^{\mu}{}_{\mu}$, associated with the geometry given by Eq. (5.1) has the form

$$R_s = -a'' - 2a\frac{R^{2\prime\prime}}{R^2} + a\left(\frac{R^{2\prime}}{R^2}\right)^2 + \frac{2}{R^2}\left(1 - a' R^{2\prime}\right). \tag{5.54}$$

A further commonly used curvature measure is the Kretschmann scalar, defined by $K = R^{\mu\nu\sigma\tau} R_{\mu\nu\sigma\tau}$. For the metric under consideration, Eq. (5.1), the Kretschmann scalar has the following explicit form:

$$\begin{aligned} K = a'' &+ 2\left(\frac{aR^{2\prime\prime}}{R^2}\right)^2 + 2a\frac{R^{2\prime\prime}R^{2\prime}}{R^4}\left(a' - \frac{aR^{2\prime}}{R^2}\right) \\ &+ \frac{4}{R^4} + \left[\frac{3}{4}\left(\frac{aR^{2\prime}}{R^2}\right)^2 - \frac{a^{2\prime}R^{2\prime}}{2R^2} + a'^2 - 2\frac{a}{R^2}\right]\left(\frac{R^{2\prime}}{R^2}\right)^2. \end{aligned} \tag{5.55}$$

All these quantities will turn out to be helpful when understanding the role played by the several parameters of the solution in the geometry and in the dynamics of the bodies moving on it.

From Einstein's equations, Eq. (5.16), we have that $R_s = -\frac{8\pi G}{c^4} T$ with T the trace of the stress-energy-momentum tensor. Numerical experiments show that the behavior of the stress-energy-momentum tensor components in the throat region are similar to each other, and thus $R_s \approx \frac{8\pi G}{c^2}\rho$, as seen in the actual solutions. That is, the Ricci scalar goes as the density, irrespective of its character, exotic or usual matter. We will discuss this fact in more detail in the explicit cases that we present below.

5.4 Numerical wormhole solutions

Following the procedure described above, we are able to obtain several solutions to the Einstein-Klein-Gordon system, given the four parameters, namely μ, ω, Λ, and ℓ. We will present the solutions first for trivial values of the angular momentum parameter, $\ell = 0$, and vary the self-interaction parameter Λ, while keeping the oscillation frequency ω fixed and then we explore the properties of the solution

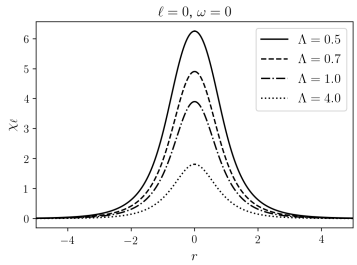

Figure 5.5: Solitonic profile for the 0-wormhole, for $\Lambda \in [0.5, 4.0]$, and $\omega = 0$.

for some values of ω maintaining Λ fixed, as was done in [121, 124]. Next, we repeat the study for different values of ℓ. In all our solutions presented in this work, we keep the mass of the scalar field μ fixed. These experiment allow us to have a better understanding on the role that each parameter plays in determining the geometry of the solutions.

All the solutions presented are asymptotically flat, and are generated by looking for a solution of the ghost scalar field, once the parameters ℓ, Λ and ω are chosen. We fix the value of mass parameter μ to one, and the distance scale of the solution is given by the dimensionless parameter $\hat{r} = \mu r$. Also, from Eq. (5.28) we see that the size of the wormhole throat $R(0)$ is given by

$$R(0) = \left(\frac{\ell(\ell+1) + \frac{8\pi}{(2\ell+1)\chi_\ell^2(0)}}{\frac{2\ell+1}{4\pi}\Lambda\chi_\ell^2(0) + \frac{\omega^2}{a(0)} - \mu^2} \right)^{1/2} . \tag{5.56}$$

In Fig. 5.5, we present this localized solution, for the case $\ell = 0$, $\omega = 0$, for several values of Λ. All the other solutions with $\ell > 0$ are localized as well. Notice how the amplitude of the pulse decreases as the value of the self-interaction parameter Λ increases.

In our experiments, we see that the ghost density, in order to form a wormhole, is distributed in such a way that it has a positive value in the region of the throat, and then it starts to have larger concentrations of negative ghost density on both sides of the throat, as shown in Fig. 5.6. From the geometric perspective, as suggested above, the profile of the Ricci scalar follows the density one and has a convex region at the throat, surrounded by concave zones, see Fig. 5.8.

Also we will show that, in general, as can be seen in Fig. 5.6, the action of the self-interaction parameter, Λ, smooths out this behavior of the exotic density and spacetime interaction. Indeed, the scalar field, at least the massive ghost field, possess a radial pressure that creates the throat and then the spacetime strongly reacts generating regions of negative density; it is the role of the self-interaction term to smooth down such reaction and allows to keep the wormhole throat open

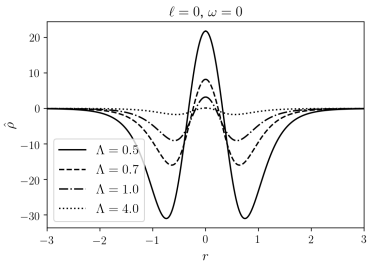

Figure 5.6: Density profile for the 0-wormhole, for $\Lambda \in [0.5, 4.0]$ and $\omega = 0$.

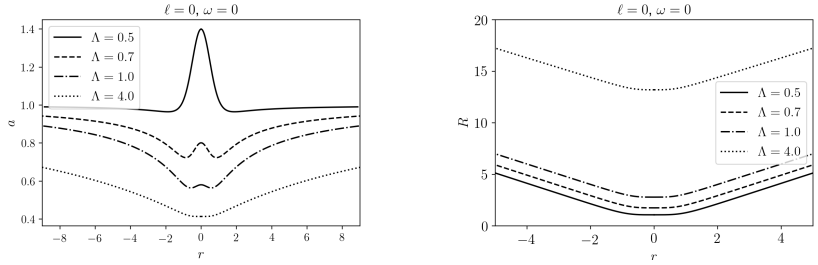

Figure 5.7: Metric coefficients for $\Lambda \in [0.5, 4.0]$ and $\omega = 0$.

with smaller amount of ghost density. Conversely, as the self-interaction parameter Λ becomes smaller, the metric coefficient a, the curvature scalars and density at the throat become more and more localized, an observation which is compatible with the result in Theorem 1 where we have shown that the solutions cease to exist for $\Lambda = 0$.

5.4.1 0-wormhole

We start our discussion for the case with vanishing angular momentum, *i. e.* $\ell = 0$. Setting also ω equal to zero for the moment, we start by sweeping a range of values for the self-interaction parameter, Λ. The corresponding results for the scalar field and the density profile are shown in Figs. 5.5 and 5.6, respectively. As mentioned above, the ghost density has regions of positive magnitude near the throat, and regions with negative density which tend to zero from below in the asymptotic region.

The corresponding metric coefficients, $a(r)$ and $R(r)$ are shown in Fig. 5.7. Notice how the metric coefficient $a(r)$ shows concave regions which will determine a similar behavior in the effective potential of the spacetime, which in turn will imply the existence of particles moving on bound trajectories. Again, the effect of the self-interaction parameter is to smooth out the concavity of the metric functions.

Regarding the curvature scalars, as expected, the Ricci scalar R_s has a be-

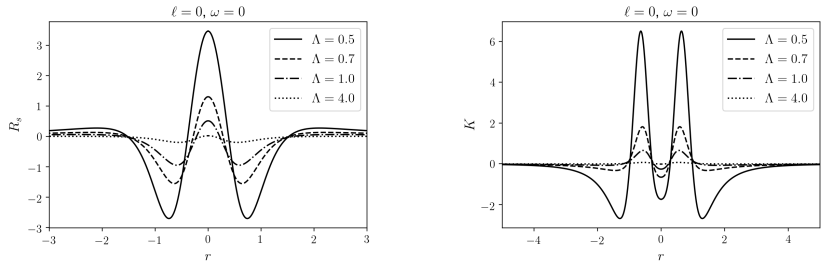

Figure 5.8: Ricci and Kretschmann scalars for $\Lambda \in [0.5, 4.0]$ and $\omega = 0$.

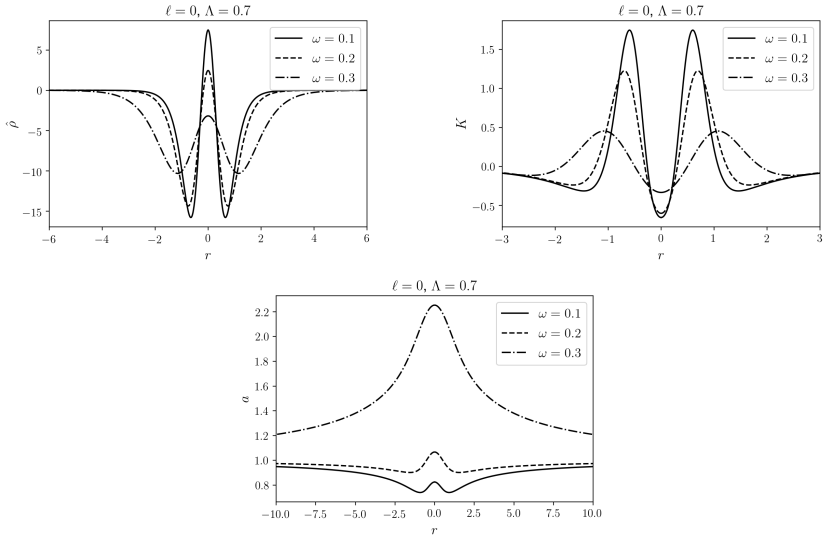

Figure 5.9: Density profile, curvature scalar and metric function a for the 0-wormhole, $\Lambda = 0.7$ and $\omega = 0.1, 0.2, 0.3$.

havior which follows the one of the density, with regions of positive values and then valleys with negative values of the curvature as we can see in Fig. 5.8. The Kretschmann scalar, however, is very different and shows two peaks of positive values and they decrease as the self-interaction parameter grows, and the central one is negative in the region of the throat, surrounded by bumps.

The next step is to increase the parameter ω keeping $\ell = 0$ and the self-interaction parameter $\Lambda = 0.7$ fixed. We show in Fig. 5.9 the corresponding density and Kretschmann scalar for three non-zero values, $\omega = 0.1, 0.3, 0.5$, of the frequency. Notice the difference between the behavior of the Kretschmann scalar, in which a larger value of ω gives the effect of increasing the central value, acting in the same way as the parameter Λ discussed above.

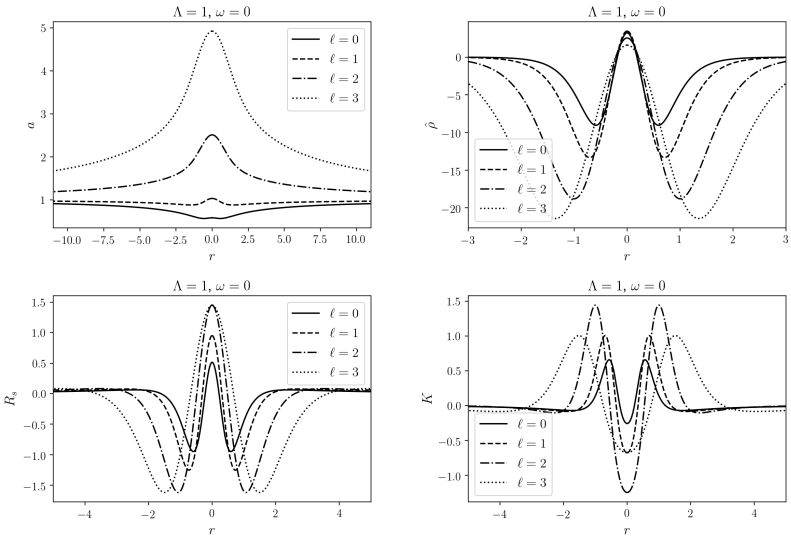

Figure 5.10: Metric function $a(r)$, density profile $\hat{\rho}$ and R_s, K scalars for $\ell \geq 0$, $\Lambda = 1.0$ and $\omega = 0$.

5.4.2 ℓ-wormhole

In this section we present the behavior of the ℓ parameter and the effect on the metric functions and the curvature scalars. For the latest we can see in Fig. 5.10 that an increment on the ℓ parameter increases the central peak for the Ricci scalar and decreases the central bump for the Kretschmann scalar. The case for $a(r)$ is quite different: while for $\ell = 1$ the two minima are still present, for larger values of the ℓ parameter the central peak is increased and the minima disappear. The presence of a minimum (or two in this case) also corresponds to positive total masses as can be verified in Table 5.3 and Fig. 5.11, consequently, its absence corresponds to negative masses. This is a general property of all solutions given the asymptotic behavior of a (see Eq. 5.47).

On the other hand, as is shown in Fig. 5.12, the increment of the ω parameter plays a role quite similar to the one made by the ℓ parameter: an increase on the former elevates the central peak on the metric function $a(r)$.

Moreover, as can be seen from a comparison of Figs. 5.7 and 5.10, the effect of the Λ parameter on the metric coefficient a is opposite to the one generated by the ℓ parameter on that metric coefficient. Indeed, for small values of Λ, the metric coefficient a has a global maximum at the throat, while for large values of this Λ, the metric coefficient a only has a local maximum. Thus, for small values of Λ, the ℓ parameter is not able to change the qualitative behavior of the metric coefficient, while for larger values of Λ, the appearance of the local maximum is

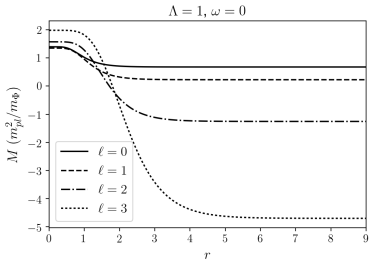

Figure 5.11: Mass function $M(r)$ for the parameters $\ell \geq 0$, $\Lambda = 1$ and $\omega = 0$.

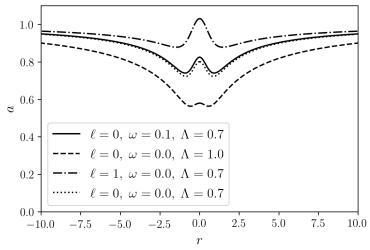

Figure 5.12: Metric function a for different values of the parameters ℓ, ω and Λ.

recovered or enhanced with the parameter ℓ. This fact will have consequences on the effective potential and the geodesic motion of particles, as discussed below.

5.5 Embedding diagrams and geodesic motion

In order to gain a better understanding of the configurations described by the scalar field and the geometry in the vicinity of the throat, in this section we discuss the embedding procedure and geodesic motion. Because the metric (5.1) is static and spherically symmetric, it is sufficient to analyze the induced geometry on a t = constant and $\theta = \pi/2$ slice, described by the two-metric

$$\mathrm{d}\Sigma^2 = a^{-1}\,\mathrm{d}r^2 + R^2\,\mathrm{d}\varphi^2\ . \tag{5.57}$$

In order to visualize this geometry as a two-dimensional surface embedded in three-dimensional flat space we shall employ cylindrical coordinates (ρ, φ, z). The metric for a flat space in these coordinates is

$$\mathrm{d}S^2 = \mathrm{d}\rho^2 + \rho^2\,\mathrm{d}\varphi^2 + \mathrm{d}z^2\ . \tag{5.58}$$

We seek for the functions $\rho(r)$ and $z(r)$, specifying a surface with the same geometry as the one described by the metric (5.57).

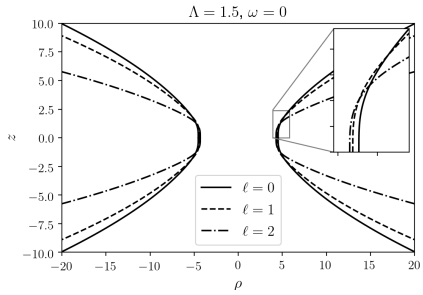

Figure 5.13: Embedding of the different ℓ-wormholes, for $\Lambda = 1.5, \omega = 0$. The complete embedding diagram is obtained by rotating this figure about the z axis. In the enlarged picture we underline the change of the value of the throat radius for the given values of ℓ.

The line element for the embedding surface will be

$$d\Sigma^2 = \left[\left(\frac{\mathrm{d}z}{\mathrm{d}r}\right)^2 + \left(\frac{\mathrm{d}\rho}{\mathrm{d}r}\right)^2\right] dr^2 + \rho^2 d\varphi^2 \,, \tag{5.59}$$

if the following conditions are satisfied:

$$\rho = R \,, \tag{5.60}$$

and

$$\left(\frac{\mathrm{d}z}{\mathrm{d}r}\right)^2 + \left(\frac{\mathrm{d}\rho}{\mathrm{d}r}\right)^2 = \frac{1}{a} \,. \tag{5.61}$$

Using the expression (5.60) to calculate $\frac{\mathrm{d}\rho}{\mathrm{d}r}$, Eq. (5.61) gives the following differential equation for $z(r)$:

$$\frac{\mathrm{d}z}{\mathrm{d}r} = \left[\frac{1}{a} - \frac{1}{4}\frac{(R^{2\prime})^2}{R^2}\right]^{1/2} \,. \tag{5.62}$$

Integrating this equation gives the function $z = z(r)$; in order to plot it in an Euclidean space, we need to find r as a function of ρ. However, it is not possible to express this function $r = r(\rho)$ in closed form because R was found numerically. Nevertheless, one can obtain $r = r(\rho)$ numerically from (5.60) and finally get $z = z(\rho)$.

In Fig. 5.13 we show the visualization of this embedding. It is seen that as ℓ increases from 0 to 2, the profile of of the embedding representing the wormhole's geometry becomes more and more curved (which is analogous to the increase of $|R_s|$ and $|K|$ shown in Fig. 10) , with a slight decrease in the throat's radius.

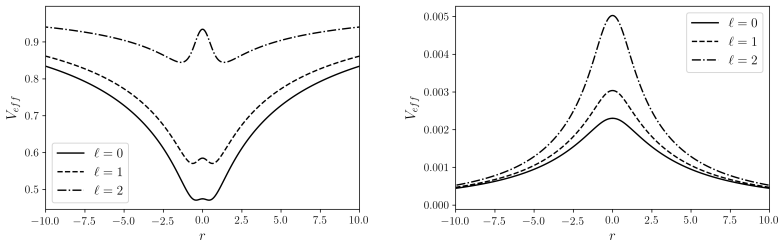

Figure 5.14: Effective potential for time-like (left panel) and null geodesics (right panel) for $L = \sqrt{\frac{1}{10}}$.

5.5.1 Geodesic motion

In order to describe the motion of the particles in the spacetimes described above, we start from the Lagrangian for the metric (5.1),

$$\mathscr{L} = g_{\mu\nu}u^\mu u^\nu + \kappa\, c^2 = -a c^2 (u^0)^2 + a^{-1}(u^r)^2 + R^2[(u^\theta)^2 + \sin^2\theta (u^\varphi)^2] + \kappa\, c^2, \quad (5.63)$$

where $u^\mu = \dot{x}^\mu$ is the four velocity and the parameter κ assumes the values 1 or 0, depending on whether the particle is massive or massless. The line element is spherically symmetric and static, so that the energy, $E = -\frac{\partial \mathscr{L}}{\partial u^0}$, the azimuthal momentum, $L_\varphi = \frac{\partial \mathscr{L}}{\partial u^\varphi}$, and the total angular momentum, $L^2 = \left(\frac{\partial \mathscr{L}}{\partial u^\theta}\right)^2 + \frac{{L_\varphi}^2}{\sin^2\theta}$, are conserved quantities. Explicitly, they have the form:

$$E = -\frac{\partial \mathscr{L}}{\partial u^0} = a c^2 u^0, \quad (5.64)$$

$$L_\varphi = \frac{\partial \mathscr{L}}{\partial u^\varphi} = R^2 \sin^2\theta\, u^\varphi. \quad (5.65)$$

Since we are only interested in the motion of a single particle (as opposed to a swarm of particles) we can choose the angles such that the orbital plane coincides with the equatorial plane $\theta = \pi/2$, in which case $L_\varphi = L$. In this way, we can express the components of the four-velocity in terms of the conserved quantities L and E, and the normalization condition $g_{\mu\nu}\, u^\mu\, u^\nu = -\kappa\, c^2$ yields the radial equation of motion:

$$(u^r)^2 + V_{\text{eff}} = \frac{E^2}{c^2}, \quad (5.66)$$

with the effective potential

$$V_{\text{eff}} = \frac{a\, L^2}{R^2} + a\, \kappa\, c^2. \quad (5.67)$$

In Fig. 5.14 we plot V_{eff} for the parameter choices $L = \sqrt{\frac{1}{10}}$, $\omega = 0$ and $\Lambda = 1.5$ for time-like and a null geodesics. As expected, the term involving L generates

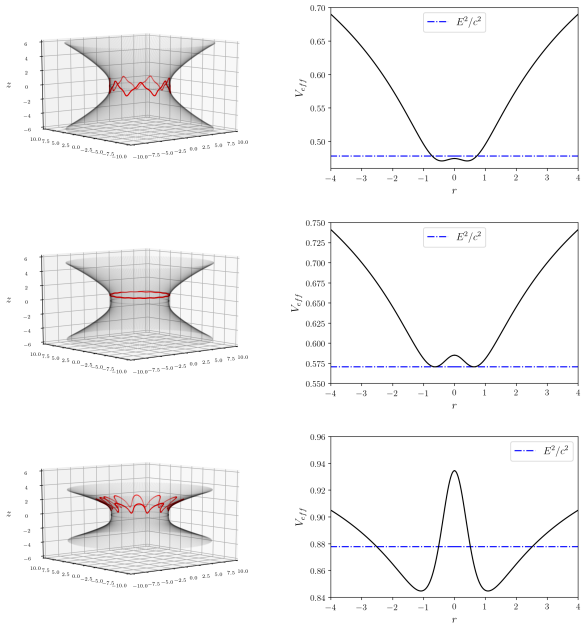

Figure 5.15: Different $\ell = 0$ (top), $\ell = 1$ (middle) and $\ell = 2$ (bottom) geodesics for $\kappa = 1$, $\omega = 0$, $\Lambda = 1.5$, $L = \sqrt{1/10}$. On the left we plot the motion of the particle in the embedding surface of the wormhole and on the right the value of E and V_{eff}.

an angular momentum barrier, corresponding to a local maximum of the effective potential located at the throat $r = 0$. (Recall from Section 5.3 that $a(r)$ has a local maximum while $R^2(r)$ has a local minimum at $r = 0$.) This maximum corresponds to an unstable equilibrium point giving rise to circular unstable particle orbits. For the $\ell = 0$ case, and for this value of L and with $\kappa = 1$, the effective potential also has a minimum at $r \approx \pm 1.34$, which means that bound orbits also exist for this value of L.

In Fig. 5.15 we plot different geodesics for massive particle with $L = \sqrt{1/10}$ and $\Lambda = 1.5$ in the $\ell = 0, 1, 2$ wormholes. Here we picked the same initial conditions in terms of the initial radial velocity $u^r(0) = 0$ and initial position $r(0) = 0.65$, $\varphi(0) = \pi$ ending up with particles with different energies and qualitatively different motion. As stated above, one can assume without loss of generality that the motion is confined to the equatorial plane $\theta = \frac{\pi}{2}$, so that it can be plotted in the embedding surface. As can be noticed from the plots, the motion is quite interesting and can be understood based on the behavior of the effective potential and the energy level of the test particle.

In order to further clarify the behavior of the geodesics, in Fig. 5.16 we plot the trajectory in the embedding diagram and the radial velocity u^r for two dif-

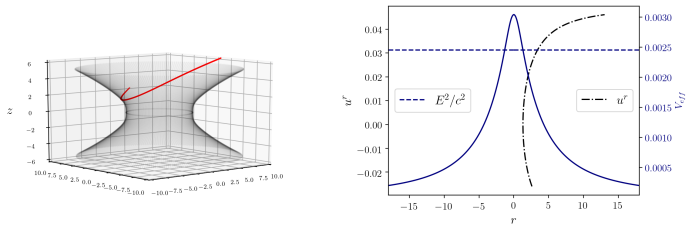

(a) A particle having insufficient energy to pass through the wormhole. The motion starts at $r = 2.6$, the velocity decreases until the particle arrives near the throat after which it returns, moving away with increasing speed. In this case the particle stays on the same side of the wormhole and does not cross the throat.

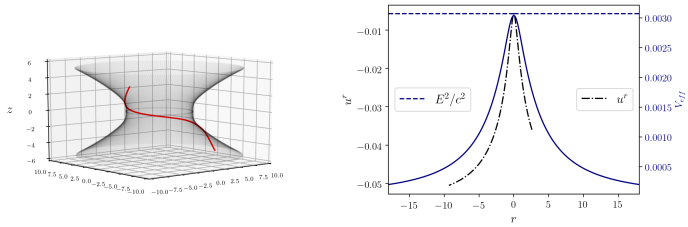

(b) A particle starts its motion at $r = 2.6$, traverses the throat, and continues its motion with a growing absolute value of the velocity.

Figure 5.16: Two different $\ell = 1$ geodesics for $\kappa = 0$, $L = \sqrt{1/10}$, $\omega = 0$, $\Lambda = 1.5$. We plot the motion with their corresponding E (right y-axis) and u^r (left y-axis) values.

ferent null geodesics with angular momentum$L = \sqrt{1/10}$ propagating in the $\ell = 1$ wormhole. In the first case, shown in Fig. 5.16a, the particle does not have sufficient energy to traverse the throat so it starts approaching the throat with a decrement of the velocity, reaches a zero radial velocity and resumes its motion going away from the throat. On the other hand, the second example in Fig. 5.16b shows that, for a particle that has enough energy to pass through the throat, the absolute value of its velocity decreases as it moves towards the throat (from right to left) until it traverses the throat, after which the absolute value of the velocity increases again as the particle moves away from the throat on the other side of the wormhole.

5.6 Discussion and concluding remarks

We have described how to construct new families of traversable wormhole solutions which are parametrized by a parameter ℓ, related to the angular momentum of the ghost fields supporting the throat, and discussed its effects on the shape of

the geometric functions characterizing the solution, and on the geodesic motion of the corresponding spacetime. These families generalize previous wormhole spacetimes discussed in the literature [121, 124] which are recovered from our models by setting $\ell = 0$.

Indeed, we have obtained *bona fide* solutions to the Einstein-Klein-Gordon system and performed a detailed analysis of such solutions, which allowed us to gain a better understanding on the effects of the new parameter ℓ. We have been able to establish that its role on the geometric function a (determining the redshift factor), on the curvature scalars and on the density is quite similar to the role played by the frequency ω characterizing the time-dependency of the field, while its effect on these quantities is opposite to the one generated by the parameter of self-interaction Λ. Moreover, as can be clearly seen in the plot of the effective potential for time-like geodesics shown in Fig. 5.14, as the value of ℓ grows, the positions of the local minima move farther away from the throat, which is similar to the effect of increasing the angular momentum L of the test particles. In this sense, from the point of view of the test particle, the parameter ℓ plays a similar role than its conserved total angular momentum L.

It is interesting to point out that the energy density of some of our solutions – despite of the fact that the stress-energy-momentum violates the null energy condition – is actually positive close to the throat (but changes its sign as one moves away from it and then converges to zero which is consistent with our asymptotic flatness asymptions). In fact, the construction of a wormhole does not necessarily require measurements of a negative energy density made by static observers, as already indicated in [140]. However, the fact that the null energy condition is violated at the throat implies that such observers also measure a “superluminal" energy flux. In general, the wormhole solutions discussed in this article possess a much richer structure than the simple, reflection-symmetric Bronnikov-Ellis wormholes, whose energy density is everywhere negative. In particular, the spacetimes discussed here exhibit a rich profile of bumps and wells in their curvature scalars whose precise shape depends on the values of ℓ as much as it does on the other parameters.

Indeed, we presented a detailed analysis of the role played by the several parameters in our wormhole solutions, namely the self-interaction term Λ, the oscillating frequency, ω, and the angular momentum parameter, ℓ of the scalar fields. Moreover, we have proved that there are no solutions for which the metric and scalar fields are reflection-symmetric about the throat if $\Lambda = 0$ (see Theorem 1). In this sense, the self-interaction term needs to be included in the action in order to extend the solution space. Actually, we have seen that it plays a smoothing role in the geometric reaction to the ghost matter. Also, we have seen that the effects on the geometry of the self-interaction parameter is opposite to the effects due

to the frequency ω. As mentioned previously, the role of the ℓ parameter on the geometry is similar to the one generated by the frequency. This fact can be used to obtain real scalar field wormholes, with a new degree of freedom analogous to the case in which the solution space is extended by permitting the scalar field to be complex and harmonic in time. As shown in Theorem 2, all our wormhole solutions are characterized by a single throat whose areal radius is fixed by the parameters and the value of the scalar field at the throat, see Eq. (5.56).

We also provided a study of the effects of the parameters on the embedding diagrams visualizing the spatial geometry of the solutions, including the shape of the throat for several relevant cases. Finally, we presented a detailed analysis of the effective potential describing the motion of free-falling test particles as a function of the parameters, and we showed how the potential may present a local maximum at the throat which is surrounded by regions with local minima. Accordingly, we obtained several interesting types of trajectories. Depending on the values of the parameters and on those of the constants of motion (namely, the energy and angular momentum of the particle), we displayed trajectories approaching the throat until they reach a turning point and go back, other trajectories which describe bound motion on either side of the throat, and then we even obtained orbits that are bound but cross the throat repeatedly and keep passing from one side of the Universe to the other; a nice property for a space station!

In the plots of Fig. 5.16 we have shown the behavior of the geodesics passing through the throat, we presented the absolute value of the particle's radial velocity and showed that it decreases as the particle approaches the throat until it crosses it after which it increases again as the particle gets further away from the throat. Such behavior is consistent with the interpretation that the reaction of the geometry to the ghost matter is to create bumps in the effective potential, instead of the wells generated by the usual matter. As mentioned at the beginning of Section 5.2, there is no need to invoke negative masses to explain such behavior; it is simpler to imagine that the reaction of the geometry to the ghost matter is to create bumps that the particle have to surmount, consistent with the fact that the absolute value of the velocity decreases as it approaches the throat, and then, goes down the hill.

The new configurations we have found and discussed in this article considerably extend the parameter space describing wormhole solutions of the Einstein-scalar field equations, and they provide a large arena that offers the possibility to further study the intriguing properties of wormhole spacetimes, including the relation between the properties of exotic matter and their geometry. While it has been shown that the solutions $\ell = 0$ are linearly unstable [121, 157, 158], there is hope that such a large arena may contain a set of parameter values with $\ell > 0$ describing stable wormholes or unstable wormholes.

Part II

Axisymmetric solutions

CHAPTER 6

MAGNETOSTATIC BOSON STAR[1]

Contents

We solve the Einstein-Maxwell-Klein-Gordon system of equations and derive a compact, static axially symmetric magnetized object which is electrically neutral and made of two complex massive charged scalar fields. We describe several properties of such solution, including the torus form of the matter density and the expected dipolar distribution of the magnetic field, with some peculiar features in the central regions. The solution shows no divergences in any of the field and metric functions. A discussion is presented on a case where the gravitational and magnetic fields in the external region are similar to those of neutron stars.

6.1 Introduction

Boson stars are self-gravitating solitons made up of complex scalar field. This objects are interesting for various reasons. They serve as simple models for compact

[1]This chapter is extracted with minor revisions from Ref. [128], which was written in collaboration with D. Núñez.

objects in the interplay of Field Theory and General Relativity and are also interesting on their own since they possess important dynamical properties that allow to study them in hypothetical strong gravity astrophysical scenarios, for example, in the gravitational waveform research; see *e.g.* [95]. Bosonic stars have applications also as black hole mimickers [159, 160] and, more generally, scalar fields are relevant in cosmology as quintessence [161], ultralight dark matter [25–27] and as a source of inflation [162].

Static and stationary single field configurations have been presented in the literature in the past years, for instance, the free and massive bosonic field solution of the Einstein-Klein-Gordon equations in spherical symmetry [44] can be generalized gauging the global $U(1)$ symmetry, which leads to the charged version of boson stars [163]. Rotating generalizations of boson stars were obtained in [164] within the Einstein-Klein-Gordon setup and in the Einstein-Klein-Gordon-Maxwell extension, the charged rotating one [165]. In these models the coupling constant parameter is freely specifiable, however, in order to obtain equilibrium solutions, the value of the coupling parameter ranges from zero up to a critical value [163, 165].

Staying within the complex, massive, free scalar field case there are two more characterizations that can be found in the literature up to the present time, these are the multipolar boson stars [166], which are static nonspherical configurations with similar morphologies to the probability density of atomic orbitals and the multifield (ℓ-) boson stars [99, 103, 104], in which the $U(1)$ symmetry is generalized by considering a $U(N)$ symmetry. Of particular interest in this paper is the toroidal static boson star of [104], which can be understood as the superposition of two contrarotating solutions that give rise to a static equilibrium configuration.

The rotating charged boson stars share some properties with the uncharged rotating case, such as the toroidal shape and with the charged (electrostatic) case, such as the critical value of the coupling constant. As one would expect the charged and rotating general solutions include electric charge and magnetic dipole moment with the particularity that the magnetic moment is nonzero only if the electric charge is nonzero, therefore obtaining solutions where both electric and magnetic fields are present in the local inertial frame of zero angular momentum. Until now, no electrically neutral and magnetized self-gravitating bosonic stars have been constructed, which might be relevant models in the study of strong gravity and magnetic fields phenomena.

Magnetic fields play an important role in many astrophysical scenarios. Some of the relativistic applications involve compact, electrically neutral objects and strong magnetic fields where their self-gravitation must be taken into account. Fully relativistic and self-consistent models of neutron stars with magnetic fields where first presented in [167] (see also *e.g.* [168, 169] for poloidal and [170–172] for

toroidal magnetic fields). These are numerical solutions of the Einstein-Maxwell-Euler system in axial symmetry which can possess angular momentum and total electric charge. Even the globally neutral and static cases are deformed by the effect of the magnetic field, changing in consequence the global properties of the equilibrium configurations.

The purpose of this paper is to construct and study magnetostatic solutions of boson stars with zero total electric charge. To do so we obtain a generalization of the toroidal static boson stars by coupling the scalar fields to the electromagnetic field, we shall show that the gauge coupling parameter can exceed the critical value obtained for the electrostatic boson stars. In Sec. 6.2 we present the action for the model, the ansätze for the fields and the conserved quantities. Then, in Sec. 6.3 we describe the numerical procedure and the construct sequence of solutions with different values of the coupling parameter, discussing the physical properties of the configurations. The magnetic field for the constructed solutions and a comparison with strongly magnetized neutron stars is presented Sec. 6.4. We conclude our manuscript and give some perspectives of future works in Sec. 6.5. In Appendix 6.6 we give the complete set of elliptic partial differential equations of our model together with explicit expressions for the $3+1$ decomposition of the energy momentum tensor. We work with $c = G = 1$ and the metric signature is taken to be $(-,+,+,+)$.

6.2 Model

A single electrically charged scalar field in spherical symmetry allows to construct charged boson stars, which are static solutions that give rise to an electric field as measured by an observer at rest [163]. Even the rotating generalization of this configurations, which also generate a magnetic field, possess an electric field that does not vanish [165]. There are no immediate simple models consisting of one scalar field that give rise to magnetostatic self-gravitating solutions, however the multifield approach leads to a natural way of obtaining such boson stars.

On the other hand, although fully relativistic neutron stars with magnetic fields have been constructed, all the solutions (to the best of our knowledge) have been obtained using the free current assumption, i.e., electromagnetic sources J^μ independent to the fluid movement. This means in particular that in the (magneto)static solutions the fluid is at rest while the spatial components of the electric current are nonzero. This is a limiting assumption, and as pointed out in [169], in principle the currents should be derived from a microscopic model which"would require a multifluid approach to model the movements of free protons and electrons".

For boson stars, in the Einstein-Klein-Gordon-Maxwell framework, the free

current assumption cannot be even made since the electric current is determined by the scalar fields, however the multifield approach is feasible. In our approach globally neutral configurations are constructed by superposition of two contrarotating "thick current loops" made of charged scalar fields.

The general framework in which magnetized boson stars are constructed consists of two self-gravitating complex scalar fields minimally coupled to the electromagnetic four-potential with coupling constants of opposite sign. In this section we summarize the basic equations needed to construct the solutions and the conserved quantities that will be useful in the analysis.

6.2.1 Field equations

We consider two massive complex scalar fields, $\Phi_{(1)}$ and $\Phi_{(2)}$, minimally coupled to the Einsteinian gravity and to the electromagnetic field,

$$S = \int d^4x\sqrt{-g}\left[\frac{R}{16\pi} - \frac{1}{2}\sum_{j=1}^{2}\left(g^{\mu\nu}(D_\mu^{(j)}\Phi_{(j)})(D_\nu^{(j)}\Phi_{(j)})^* + \mu^2|\Phi_{(j)}|^2\right) - \frac{F_{\mu\nu}F^{\mu\nu}}{4\mu_0}\right], \tag{6.1}$$

where $F_{\mu\nu} = \partial_\mu A_\nu - \partial_\nu A_\mu$ is the Faraday tensor and the covariant derivative operators, $D_\mu^{(1)} = \nabla_\mu + iqA_\mu$ and $D_\mu^{(2)} = \nabla_\mu - iqA_\mu$ couple both scalar fields with A_μ. Notice that we have chosen equal mass terms for both scalar fields and opposite signs for the electromagnetic coupling constants (boson charges). The scalar fields interact with each other indirectly, through gravity and the electromagnetic field.

Variation of Eq. (6.1), with respect to the different fields leads to the Euler-Lagrange equations of the model (see *e.g.* [173]). Variation with respect to $g_{\mu\nu}$ leads to

$$R_{\mu\nu} - \frac{1}{2}Rg_{\mu\nu} = 8\pi T_{\mu\nu}; \tag{6.2a}$$

$$T_{\mu\nu} = T_{\mu\nu}^{(1)} + T_{\mu\nu}^{(2)} + (T^{\rm EM})_{\mu\nu}, \tag{6.2b}$$

$$T_{\mu\nu}^{(j)} := \frac{1}{2}(D_\mu^{(j)}\Phi_{(j)})(D_\nu^{(j)}\Phi_{(j)})^* + \frac{1}{2}(D_\nu^{(j)}\Phi_{(j)})(D_\mu^{(j)}\Phi_{(j)})^* - \frac{1}{2}g_{\mu\nu}\left(g^{\alpha\beta}(D_\alpha^{(j)}\Phi_{(j)})(D_\beta^{(j)}\Phi_{(j)})^* + \mu^2|\Phi_{(j)}|^2\right), \tag{6.2c}$$

$$(T^{\rm EM})_{\mu\nu} := \frac{1}{\mu_0}F_{\mu\sigma}F_{\nu\lambda}g^{\sigma\lambda} - \frac{1}{4\mu_0}g_{\mu\nu}F_{\alpha\beta}F^{\alpha\beta}. \tag{6.2d}$$

The equation for the fields $\Phi_{(1)}$ and $\Phi_{(2)}$ are the Klein-Gordon equations,

$$g^{\mu\nu}D_\nu^{(j)}D_\mu^{(j)}\Phi_{(j)} = \mu^2\Phi_{(j)}. \tag{6.3}$$

Variation with respect to A_μ leads to the Maxwell equations with source the

charged scalar fields which define a current four-vector J^μ,

$$\nabla_\nu F^{\mu\nu} = \mu_0 J^\mu := \mu_0 (q j_1^\mu - q j_2^\mu); \tag{6.4a}$$

$$j_i^\mu := \frac{i g^{\mu\nu}}{2} (\Phi_{(i)}{}^* D_\nu^{(i)} \Phi_{(i)} - \Phi_{(i)} (D_\nu^{(i)} \Phi_{(i)})^*), \tag{6.4b}$$

here J^μ is the (total) electromagnetic current.

6.2.2 Global quantities

The spacetime we will consider in this work is stationary (static) and axisymmetric. Komar expressions allow to calculate global quantities for each of this isometries; if ξ is the Killing vector associated with stationarity, Σ_t is a spacelike surface and n^μ the unit vector normal to this hypersurface, then the quantity,

$$M = \frac{1}{4\pi} \int_{\Sigma_t} R_{\mu\nu} n^\mu \xi^\nu dV, \tag{6.5}$$

defines the Komar mass. Similarly, if χ is the Killing vector associated with the axial symmetry, the quantity

$$J = \frac{1}{8\pi} \int_{\Sigma_t} R_{\mu\nu} n^\mu \chi^\nu. \tag{6.6}$$

gives the angular momentum of the spacetime.

The quantities j_1^μ and j_2^μ defined in Eq. (6.4) are Noether density currents ($\nabla_\mu j^\mu = 0$) which arise from the invariance of Eq. (6.1) under the $U(1)$ gauge transformation of $\Phi_{(1)}$ and $\Phi_{(2)}$. It follows that integration of the projection onto n^μ of this currents over Σ_t leads to the conserved particle numbers

$$\mathcal{N}_1 = \int_{\Sigma_t} j_1^\mu n_\mu dV, \quad \mathcal{N}_2 = \int_{\Sigma_t} j_2^\mu n_\mu dV; \quad \mathcal{N} := \mathcal{N}_1 + \mathcal{N}_2. \tag{6.7}$$

In the rotating boson stars, it was shown [117, 164, 174] that the angular momentum J takes values that are integer multiples of the particle number, $J = m\mathcal{N}$, with m the winding number (defined below) of the scalar field ansatz, this result is also valid in the charged rotating case [165]. However, in the magnetized solutions obtained in this work this relation does not hold since they are by construction $J = 0$ static, as will be argued in the next section.

The associated total electric charge, related to the sources at the Maxwell equation is given by $Q = \int_{\Sigma_t} J^\mu n_\mu dV = q(\mathcal{N}_1 - \mathcal{N}_2)$. In the single field static and rotating charged boson stars the total charge of the system is related to the particle number by $Q = q\mathcal{N}$ and it was obtained [163] that Q coincides with the asymptotic value extracted from the electric potential and matches the exterior Reissner-Nordström solution. Again, the relation $Q = q\mathcal{N}$ is not valid for our case because, as we will see bellow, the obtained solutions satisfy $Q = 0$.

6.2.3 Static axisymmetric spacetime and Ansätze for the fields

In coordinates adapted to the Killing fields, where $\xi = \partial/\partial t$ and $\chi = \partial/\partial\varphi$, the general static and axially symmetric line element we will consider is in the Lewis-Papetrou form,

$$g_{\mu\nu}dx^\mu dx^\nu = -e^{2F_0}dt^2 + e^{2F_1}(dr^2 + r^2 d\theta^2) + e^{2F_2}r^2\sin^2\theta d\varphi^2, \tag{6.8}$$

where the metric functions F_0, F_1 and F_2 depend only on the coordinates r and θ. We have used the same line element as the one in Ref. [104], where the toroidal static boson star is constructed, however, the $g_{t\varphi}$ term usually written as the function $w(r,\theta)$ or $w(r,\theta)/r$, is not included in (6.8) because we are looking for static configurations with zero total angular momentum J, and in this case it can be seen [40, 175] that $w = 0$ if and only if the spacetime is static.

The contribution of the scalar fields in the energy-momentum tensor, $T^{(1)}_{\mu\nu}$, $T^{(2)}_{\mu\nu}$ will be consistently independent of t and φ if for the scalar fields we use the following ansatz, which is similar to the one used for rotating, multifield, multifrequency boson stars and even for chains [176],

$$\Phi_{(1)} = \phi(r,\theta)e^{i\omega t - im\varphi}; \qquad \Phi_{(2)} = \phi(r,\theta)e^{i\omega t + im\varphi}. \tag{6.9}$$

Here m is and integer called winding number. Moreover, the opposite sign of this parameter for each field in Eq. (6.9) can be interpreted as having contrarotating scalar fields distributions. It is not difficult to obtain that with this election of winding numbers, $T^{(1)}_{t\varphi} = -T^{(2)}_{t\varphi}$, consistent with the Einstein tensor component $G_{t\varphi}$ being zero for the metric in Eq. (6.8).

Again, analyzing the components of the Einstein tensor we can elucidate the anzatz for the field A_μ. Two possibilities for the electromagnetic four-potential are compatible with the spacetime at hand: the purely poloidal ($A_r = A_\theta = 0$) and the purely toroidal ($A_t = A_\varphi = 0$) magnetic fields[2] [170, 171], however only the first possibility can be realized given the ansatz (6.9) chosen for the scalar fields since only the J^φ source of the Maxwell equations is nonzero[3], which additionally implies that $A_t =$ constant, therefore we adopt

$$A_\mu dx^\mu = C(r,\theta)d\varphi. \tag{6.10}$$

The resulting number density currents, given in Eqs. (6.36) and (6.36), imply $Q = 0$ since $J^\mu n_\mu = 0$.

[2] In both cases, the circularity property of spacetime is not broken and the metric tensor takes the form (6.8).

[3] In the single field charged rotating star, also the J^t component is nonzero, in our case however $j^t_1 = j^t_2$, see Appendix 6.6.

6.3 Numerical solutions

6.3.1 Boundary conditions and numerical method

In order to construct magnetostatic solutions of boson stars, the Einstein-Klein-Gordon-Maxwell system is solved. This means solving for the five functions

$$\{\phi, C, F_0, F_1, F_2\}$$

and the unknown parameter ω, imposing the appropriate symmetries and boundary conditions. The full elliptic system of coupled partial differential equations (PDEs) in r and θ is given in the Appendix 6.6.

First, we impose even parity with respect to reflections at the equatorial plane of the five unknown functions which in particular implies that derivatives with respect to θ at $\theta = \pi/2$ vanish and also that the required integration domain reduces to $0 \leq \theta \leq \pi/2$, $0 \leq r < \infty$.

Asymptotic flatness implies that the following outer boundary conditions must be imposed,

$$\begin{aligned} &\phi|_{r\to\infty} = 0, \quad C|_{r\to\infty} = 0; \\ &F_0|_{r\to\infty} = 0, \quad F_1|_{r\to\infty} = 0, \quad F_2|_{r\to\infty} = 0. \end{aligned} \tag{6.11}$$

Also the condition $\omega < \mu$ is necessary in order to have $\phi|_{r\to\infty} = 0$. Regularity of the solution at the origin and on the symmetry axis require,

$$\begin{aligned} &\phi|_{r=0} = 0, \quad C|_{r=0} = 0; \\ &\partial_r F_0|_{r=0} = 0, \quad \partial_r F_1|_{r=0} = 0, \quad \partial_r F_2|_{r=0} = 0, \\ &F_1|_{r=0} = F_2|_{r=0}. \end{aligned} \tag{6.12}$$

$$\begin{aligned} &\phi|_{\theta=0,\pi} = 0, \quad C|_{\theta=0,\pi} = 0; \\ &\partial_\theta F_0|_{\theta=0,\pi} = 0, \quad \partial_\theta F_1|_{\theta=0,\pi} = 0, \quad \partial_\theta F_2|_{\theta=0,\pi} = 0, \\ &F_1|_{\theta=0,\pi} = F_2|_{\theta=0,\pi}. \end{aligned} \tag{6.13}$$

The regularity conditions for ϕ for the case $m = 0$ are different from those of the previous expressions, however this case reduce to the widely studied spherical, nonrotating, neutral boson star, and will not be addressed in this manuscript except for comparison.

The nonlinear PDEs are solved numerically using the spectral solver Kadath [16, 17] which implements a Newton-Raphson iteration. This library, which has been successfully applied to solve a wide variety of PDEs in theoretical physics and in particular in relativity, was also used in the construction of rotating boson stars [117].

Chebyshev polynomials have been used in the spectral method as basis functions for the expansions of the five unknown functions. The spatial domain is divided into 8 spherical shells with boundaries located at $r = \{2,4,8,16,32,64,128\}$. The regularity conditions in Eqs. (6.12) and (6.13) are either imposed by the spectral basis[4] for a given function on the corresponding domain, or checked that they hold up to numerical accuracy. On the other hand the outer boundary conditions in Eq. (6.11) are imposed "exactly" (without the need of a cutoff radius) given the compactification of the radial variable at the outermost spherical shell.

An initial guess for the functions is required in order to start the iteration. For each value of m this needs to be done only once. The expressions

$$N := e^{F_0} = 1-(1-N_0)e^{-r^2/r_0^2}, \quad F_1 = F_2 = 0, \quad C = 0, \tag{6.14}$$

also used in [85], and

$$\phi = \phi_0 (r\sin\theta)^m e^{-(x^2/2+2z^2)m/r_0^2} \tag{6.15}$$

with $x = r\sin\theta$, $z = r\cos\theta$, proposed in Ref. [117], have proven to be good guesses given certain choice of ϕ_0, r_0 fixing the coupling constant $q = 0$ and the lapse at $r = 0$, $N_0 \approx 0.95$. The last condition prevents convergence to the trivial $\phi = 0$ solution and also leads to a Newtonian configuration ($\omega \sim \mu$). Once the first solution is obtained the rest of the solutions are obtained by varying N_0 and increasing q by small steps.

In addition to the Komar expression on Eq. (6.5), the ADM mass definition can be used to obtain the total mass of the star. Both quantities should coincide given the stationarity of the spacetime we are considering [175], therefore the difference between the ADM and the Komar masses can be used as an indicator of the numerical accuracy and provide an estimation of the numerical error of the solution. An expression for the ADM mass suitable for our case is the expression [175],

$$M = -\frac{1}{8\pi}\lim_{S\to\infty}\oint_S \left[\frac{\partial}{\partial r}(F_1+F_2)+\frac{F_2-F_1}{r}\right] r^2\sin\theta d\theta d\varphi, \tag{6.16}$$

where the limit indicates integration over a sphere S of radius $r\to\infty$.

One can also verify that the value of the unknown frequency ω converge exponentially to a finite value with the number of collocation points. This error indicator has been used together with the relative difference of the ADM and Komar masses to monitor accuracy along the sequence of numerical solutions and to carry out convergence tests of the solutions with increasing number of spectral coefficients.

[4] Details on how this is implemented in terms of the Chebyshev spectral basis in the innermost shell and on the symmetry axis for similar problems can be found in [117] and [116].

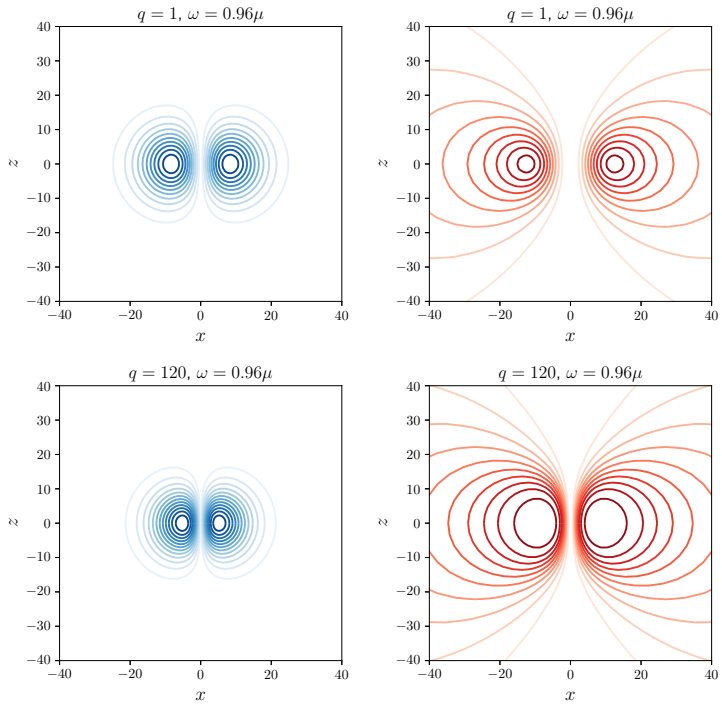

Figure 6.1: Scalar field ϕ isocontours (left) and magnetic field lines (right) in a plane of constant φ with $x = r\sin\theta$ and $z = r\cos\theta$ for $m = 1$ and $\omega = 0.96\mu$ using different values of q.

6.3.2 Structure of the stars

One can use the code to solve for boson stars of several types. The spectral code has been able to reproduce sequences of solutions already presented in the literature such as the single field static and the rotating mini-boson stars, as well as the multifield ℓ-boson stars and the toroidal static boson stars. In this section we present new solutions that correspond to magnetostatic boson stars. These configurations generalize the toroidal static boson stars, incorporating a new parameter, q, in addition to the frequency ω and the winding number m.

Typical solutions for magnetized ($q \neq 0$) boson stars are presented in Fig. 6.1, where isocountours of the scalar field function ϕ and the φ component of A_μ are plotted for $m = 1$. In the first place we can notice from the ϕ contours, that the star has a toroidal structure just like the $q = 0$ case, secondly we observe from the isocontours of C, which can be interpreted as the magnetic field lines (see Sec. 6.4), that the expected poloidal magnetic field distribution preserves as q increases, however, as we will show next in this paragraph, near to the location of maximum

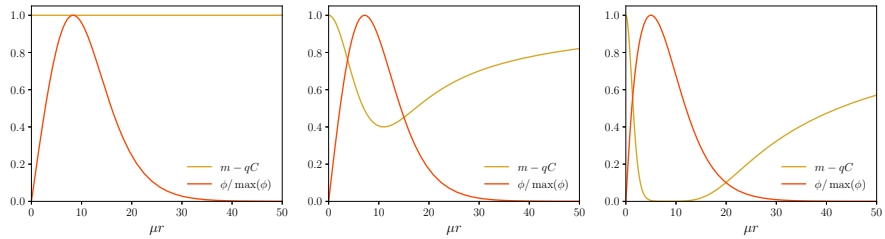

Figure 6.2: Profiles of ϕ and C at the equatorial plane for solutions with $m = 1$ and $\omega = 0.96\mu$. Left panel: Neutral ($q = 0$). Center panel: $q = 25$. Right panel: $q = 140$.

ϕ a region of constant C (zero magnetic field) is formed which grows in size. This effects on the structure of the star and the morphology of the magnetic field can be seen more clearly, plotting the profiles of the scalar field and the electromagnetic potential on the equatorial plane. This is done in Fig. 6.2 where we have plotted $m - qC$ instead of C, to observe an interesting property: Above certain value of q (which in the $\omega = 0.96\mu$ case of Fig. 6.2 is at $q \approx 50$, between the second and third panel), the quantity qC approaches but never exceeds m in a region that grows as q increases. In all of the solutions presented in this paper we have obtained $C(r) < m/q$ for all r.

The sources of gravitational field are also enlightening regarding the structure of the star as well as its global properties, as we will see in the next section. Restricting to the equatorial plane, $\theta = \pi/2$, the complete contributions of the energy momentum tensor (see Appendix. 6.6) are given by,

$$E|_{\theta=\pi/2} = \left[\frac{\omega^2}{e^{2F_0}} + \frac{(m-qC)^2}{e^{2F_2}r^2}\right]\phi^2 + \frac{1}{e^{2F_1}}\left(\frac{\partial\phi}{\partial r}\right)^2 + \mu^2\phi^2 + E_B, \quad (6.17)$$

$$S^r{}_r|_{\theta=\pi/2} = \left[\frac{\omega^2}{e^{2F_0}} - \frac{(m-qC)^2}{e^{2F_2}r^2}\right]\phi^2 + \frac{1}{e^{2F_1}}\left(\frac{\partial\phi}{\partial r}\right)^2 - \mu^2\phi^2 + E_B, \quad (6.18)$$

$$S^\theta{}_\theta|_{\theta=\pi/2} = \left[\frac{\omega^2}{e^{2F_0}} - \frac{(m-qC)^2}{e^{2F_2}r^2}\right]\phi^2 - \frac{1}{e^{2F_1}}\left(\frac{\partial\phi}{\partial r}\right)^2 - \mu^2\phi^2 - E_B \quad (6.19)$$

$$S^\varphi{}_\varphi|_{\theta=\pi/2} = \left[\frac{\omega^2}{e^{2F_0}} + \frac{(m-qC)^2}{e^{2F_2}r^2}\right]\phi^2 - \frac{1}{e^{2F_1}}\left(\frac{\partial\phi}{\partial r}\right)^2 - \mu^2\phi^2 + E_B \quad (6.20)$$

Where we have defined E_B as the purely electromagnetic contribution to the energy density (at the equatorial plane),

$$E_B := \frac{1}{2r^2 e^{2F_1+2F_2}}\left(\frac{\partial C}{\partial r}\right)^2. \quad (6.21)$$

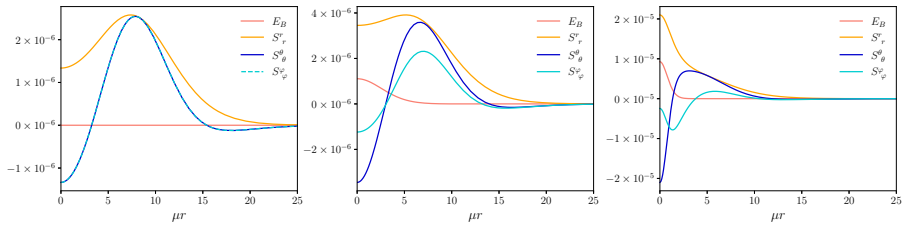

Figure 6.3: Source terms at the equatorial plane for boson stars with $m = 1$ and $\omega = 0.96\mu$. Left panel: Neutral ($q = 0$). Center panel: $q = 25$. Right panel: $q = 140$.

Regarding the stress tensor components, which are usually identified as components of the pressure, the system is completely anisotropic even in the $q = 0$ case, where for instance the difference $S^\theta{}_\theta - S^\varphi{}_\varphi \propto \phi^2 e^{-2F_2}/r^2$ is not zero, although suppressed by r^2. In the left panel of Fig. 6.3 we plot the sources of the $q = 0$ case where in fact the difference between $S^\theta{}_\theta - S^\varphi{}_\varphi$ cannot be appreciated. The middle and right panels of Fig. 6.3 show the magnetized $q = 25$ and $q = 140$ cases respectively. Notice that the extrema of $S^\varphi{}_\varphi$ decrease in magnitude with respect to the extrema of $S^\theta{}_\theta$ and $S^r{}_r$. In particular near $r = 0$, the minimum of $S^\varphi{}_\varphi$ increases due to the E_B contribution. The behavior of the pressure term $S^\varphi{}_\varphi$ is relevant in the analysis of the effect of q on global quantities, as for example the magnetic dipole moment and the total mass. This will be discussed in the next section.

6.3.3 Sequence of magnetic boson stars

For $m = 1, 2$ we obtained a family of configurations by means of slowly varying the parameters of the solution starting from a Newtonian solution, as stated before. First, we have verified that in the case $q = 0$, $m = 1$ we obtain the known sequence of toroidal static boson stars [104]. Thereafter, starting from this set of solutions, we have slowly increased the value of q, generating in this way sequences of magnetized boson stars.

In Fig. 6.4, the global quantity M is shown *vs.* the scalar field frequency ω for $m = 1$ and five chosen values for q. Some interesting aspects arise from these solutions: firstly the mass of the star decreases monotonically with q; this is the opposite behavior to that obtained in models of neutron stars with magnetic fields [167, 168], where their structure begins from spherical morphology at zero magnetic field (for the static case), and flattens, increasing the circumferential radius of the star, as the magnitude of the magnetic fields increase, with a corresponding increase in the mass of the star. The observed structure dependence on q of the magnetized boson stars, is also opposite to the corresponding dependence of charged boson stars as discussed in the previous section. However, such

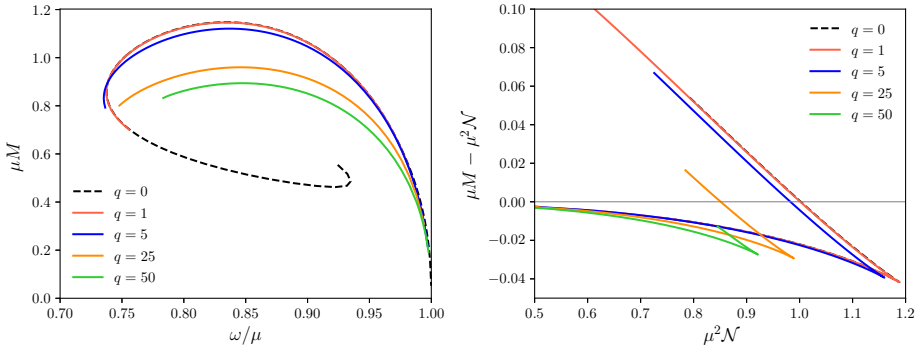

Figure 6.4: Left panel: Frequency *vs.* mass for the $m = 1$ magnetostatic boson star solutions using different values of the coupling constant q. Right panel: Binding energy $M - \mu N$ for $m = 1$.

observed decrease on the size and total mass M as the coupling constant q grows, is also observed in the magnetized Bose-Einstein condensate stars [177].

The second aspect to consider about Fig. 6.4, regards the existence of equilibrium configurations with coupling constant q above the value $q_{\text{crit}} \approx 1/\sqrt{2}$. Indeed, as reported in [165,178], that value was an upper limit for stable charged and stable rotating-charged boson stars. In our model without total charge, that limit is overcome. This interesting result is related to the fact that the Lorentz force,

$$f_\nu := F_{\nu\alpha} J^\alpha = -\nabla_\mu (T^{\text{EM}})^\mu{}_\nu, \tag{6.22}$$

points everywhere outwards for the charged mini-boson stars, while for the magnetostatic boson star it only points outward near the origin and points inward outside the main distribution of scalar field. Therefore, the nonrelativistic argument regarding Coulomb repulsion *vs.* gravitational attraction does not apply here. Instead, it is the stress anisotropy that ultimately determines the structure and global properties of the star, as we will see below in relation to the decrease in the total mass. Numerically we have not obtained any limiting value for the parameter q, the equations are difficult to solve for large values of the coupling constant due to the resolution required at the "edges of the plateau" that forms in the function C (see the right panel of Fig. 6.2).

Anisotropic pressures are essential to obtain equilibrium configurations with high compactness and large values for the mass. In [85] (see [133] for recent discussion on fluid anisotropic stars and [135] for shell-type configurations in the Einstein-Vlasov system) it was shown that for ℓ-boson stars, small radial pressures and big tangential pressures are related to an increase in the mass and radius of the star in a way that resembles the forces on an arch. In our case, to understand the decrease in size of the magnetic boson stars, we start by noticing

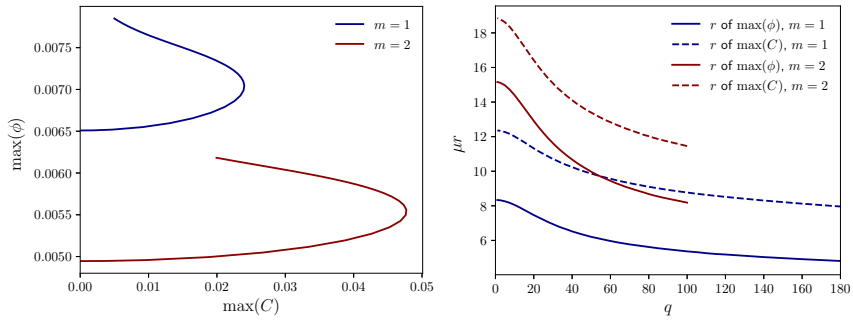

Figure 6.5: Sequence of solutions constant ω and increasing coupling q. Given q we locate in the solution for the maximum of ϕ and C and its location. Left panel: Maximum value of the scalar field with respect to the maximum value of the four potential function C for sequence of solutions with $m = 1$ and $m = 2$ with $\omega = 0.96\mu$. Right panel: Radius at which the maxima of ϕ and C is attained, as a function of the coupling constant q.

that the tangential pressure is composed by two different contributions, $S^{\theta}{}_{\theta}$ and $S^{\varphi}{}_{\varphi}$, which act together with the radial pressure (and with the Lorentz force in some region) against gravity in order to support the configuration. The toroidal shape, which is made possible by the $S^{\varphi}{}_{\varphi}$ contribution, shrinks with increasing q - right panel Fig. 6.5, given that the electromagnetic contribution to the energy-momentum tensor in the region where the scalar field concentrates, is bigger for $S^{r}{}_{r}$ than for the tangential components and in particular with respect to $S^{\varphi}{}_{\varphi}$, as discussed in Sec. 6.3.2. Our results indicate that this reduction in the size of the star is accompanied by a reduction in the total mass that the boson star can support.

Fig. 6.5 shows properties of the scalar field, ϕ and of the electromagnetic one, C *vs.* q. More precisely, the figure shows the maximum of the functions and the coordinate at which the maximum is attained. From the right panel we appreciate the decrease in size of the torus as a function of q for fixed ω. In the left panel we see another important property of the solutions: $\max(C)$ reaches a maximum value and then begins to decrease with q. As a consequence, the magnetic dipole moment $\mathscr{M}$ which can be obtained from the asymptotic behavior of the electromagnetic potential A_μ,

$$A_\mu dx^\mu \sim \frac{\mu_0}{4\pi}\frac{\mathscr{M}\sin^2\theta}{r}d\varphi, \tag{6.23}$$

reaches a maximum and decreases thereafter. This behavior is shown in the right panel of Fig. 6.6 for the sequence of $m = 1$ solutions using four selected values of q and in the same panel can be seen for fixed ω, $m = 1,2$ and several values of q. One can note from these plots that larger values for the maximum of $\mathscr{M}$ are

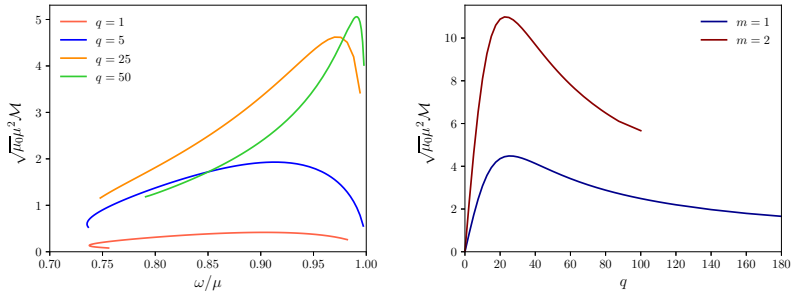

Figure 6.6: Left panel: Frequency vs. magnetic dipole moment $\mathcal{M}$ for the $m = 1$ magnetostatic boson star solutions using different values of the coupling constant q. Right panel: Magnetic dipole moment $\mathcal{M}$ as a function of q for configurations with $m = 1$ and $m = 2$ and a fixed value of ω.

obtained, closer to $\omega = \mu$, as q increases. In Table 6.1 we provide data of the maximum $\mathcal{M}$ configuration for a sample of values for the coupling constant. For the explored $q \gg 1$ configurations, the maximum of $\mathcal{M}$ increases more slowly, for example, the $q = 200$ case, with $\max(\mathcal{M}) = 4.84$, is not far from the value obtained for the $q = 50$ case, plotted in Fig. 6.6, so the maximum dipole moment seems to tend asymptotically to a finite value, however to establish with precision the limit, it would be necessary to solve the equations in the limiting case $q \to \infty$, which is beyond the scope of this paper.

Finally, we wonder about the possibility of determining the magnetic dipole moment from the asymptotic behavior of the metric functions. For example, in the charged mini-boson star, the total electric charge of the configuration can be read off the g_{rr} component by comparing with the Reissner-Nordström solution [163]. Some electrovacuum exact solutions (in General Relativity) for a mass endowed with a magnetic dipole moment have been obtained in the literature, as for example the Gutsunaev-Manko [179] and Bonnor [180] two-parameter family of solutions. However, analyzing our solutions, we obtain that they do not match with neither of those metrics, for instance the lapse function in all of the solutions that we generate has the asymptotic behavior $N^2 = 1 - 2M/r + \alpha/r^2 + \mathcal{O}(1/r^3)$, with α some constant, while according to [179], the lapse of the Gutsunaev-Manko metric goes as $N^2 = 1 - 2M/r + \mathcal{O}(1/r^3)$. On the other hand, comparison with the Bonnor solution, for which $N^2 = 1 - 2M/r + M^2/r^2$, could seem to be a better alternative, however we obtain from the analysis of our solutions that the coefficient α is a function of both of M and $\mathcal{M}$ and in the $\mathcal{M} = 0$ case, it is not proportional to M^2. Therefore the magnetic dipole moment of the star cannot be obtained from the the metric components by comparison with any of the mentioned exact solutions, allowing us to conclude that our solutions differ from those two spacetimes.

Table 6.1: Maximum mass and magnetic dipole configurations.

	q	$\sqrt{\mu_0}\mu^2\mathscr{M}$	ω/μ	μM	$\mu^2\mathscr{N}$	$\max(\phi)$	$\mu r_{\max(\phi)}$
Max. $\mathscr{M}$							
	0.1	0.0418	0.905	1.048	1.077	0.0156	4.66
	1	0.417	0.905	1.047	1.076	0.0156	4.66
	5	1.93	0.911	1.015	1.041	0.0147	4.82
	25	4.62	0.970	0.627	0.633	0.00492	9.08
	50	5.06	0.990	0.363	0.363	0.00154	16.8
	100	5.17	0.997	0.195	0.195	0.000454	30.1
	200	4.84	0.999	0.084	0.085	0.000132	36.0
Max. M							
	0	0	0.840	1.147	1.189	0.0290	2.76
	0.1	0.0368	0.834	1.147	1.189	0.0303	2.65
	1	0.366	0.834	1.146	1.188	0.0303	2.65
	5	1.66	0.839	1.121	1.160	0.0296	2.69
	25	2.46	0.848	0.960	0.989	0.0312	2.22
	50	1.69	0.848	0.894	0.921	0.0337	1.85

6.4 Magnetic field

The electric and magnetic field as measured by an observer whose four-velocity is n^μ (Eulerian observer) are given by the formulas $E_\mu = F_{\mu\nu}n^\nu$ and $B_\mu = -\frac{1}{2}\epsilon_{\mu\nu\alpha\beta}n^\nu F^{\alpha\beta}$. where ϵ is the Levi-Civita tensor. For the metric (6.8) and the electromagnetic four-potential (6.10), we obtain $E_\mu = 0$ as expected and

$$B_\mu dx^\mu = \frac{e^{-F_2}}{\sin\theta}\left(\frac{1}{r^2}\frac{\partial C}{\partial\theta}\,dr - \frac{\partial C}{\partial r}\,d\theta\right). \tag{6.24}$$

Some examples of B^i for configurations with $m = 1$ are given in Fig. 6.7. The distribution of the vector field resemble that of the magnetic field around a finite size current loop. For reference we also plot the isocontour of half the maximum value of the energy density. Rotation of this curve around the z axis generates a torus. The figure also shows the region of zero magnetic field that forms in configurations with high values of q, where $m - qC \approx 0$, see for instance the black line region with $\sqrt{B^iB_i}/(\mu\sqrt{\mu_0}) < 10^{-6}$ inside the torus in the right panel of Fig. 6.7.

We have seen in the previous section that as q get closer to zero, the magnetic moment decreases and the maximum values of ϕ and C are reached at larger radii. This explains why some of the configurations with relative low values of q, as for example the $q = 5$ and $q = 25$ cases (Fig. 6.7, left and central panels), do not have the maximum of B^i at the center of the star but in a toroidal region around the center, while other configurations as for instance the $q = 140$ case (Fig. 6.7, right panel), posses magnetic fields concentrated in a central region with maximum

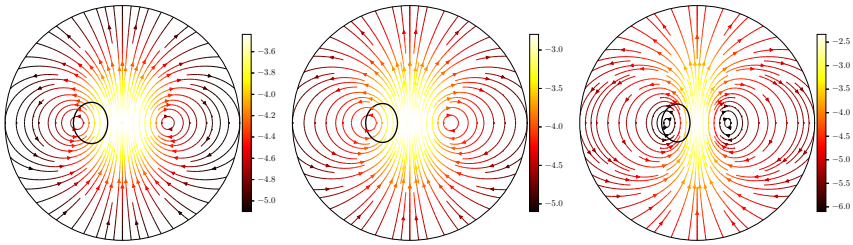

Figure 6.7: Magnetic field in a plane of constant φ for configurations with $m = 1$ and $\omega = 0.96\mu$, for the coupling constant with values (from left to right) $q = 5$, 25 and 140. The thick black line correspond to the density isocountour $E = 0.5\,\mathrm{max}(E)$. The color bar indicates the norm of the quantity $\log_{10}[B^i/(\mu\sqrt{\mu_0})]$ The radius of the circle is $\mu r = 32$.

along $\theta = 0$.

Until now it has not been required to specify the value for the mass parameter of the scalar field given that solutions with different μ are related to each other by rescaling rules. In particular, we have used these rules to construct dimensionless quantities (*e.g.*, μr, ω/μ, μM, $B^\mu/(\mu\sqrt{\mu_0})$, etc.), used in the numerical implementation and in the results reported in previous sections. We now proceed to recover units of different physical quantities in order to compare magnetostatic boson stars with magnetized neutron star solutions. Restoring c and G, the dimensionless quantities related to the total mass of the star and the norm of the magnetic field ($B^2 = B^\mu B_\mu$) are $Gc^{-2}\mu M$ and $Gc^{-4}B^2/(\mu^2\mu_0)$. Furthermore, the product

$$\mathscr{I} := \frac{1}{c^4}\sqrt{\frac{G^3}{\mu_0}}\,MB, \tag{6.25}$$

is dimensionless and, more importantly, do not rescale with μ. Evaluating the magnetic field at the center of the star we define $\mathscr{I}_c = \mathscr{I}|_{r=0}$ and plot it along $m = 1$ sequences in Fig. 6.8.

For a neutron star with mass in the range $1.1M_\odot \lesssim M \lesssim 2.1M_\odot$ and strong magnetic fields at the star's pole within the interval $10^9\mathrm{T} \lesssim B_{\mathrm{pole}} \lesssim 10^{11}\mathrm{T}$ [181], the value of the product of mass and magnetic field is between $10^{-7} \lesssim \mathscr{I}_{\mathrm{pole}} \lesssim 3\times10^{-5}$. Internal magnetic fields in magnetars have been estimated according to simulations to be as high as[5] 10^{14}T. An extended range for $\mathscr{I}$ at the center of strongly magnetized neutron stars would be $10^{-7} \lesssim \mathscr{I}_c \lesssim 3\times10^{-2}$.

[5]Restricting to the Einstein-Maxwell-Euler self-consistent models of neutron stars with equations of state independent of the magnetic field, the maximum magnetic field B_c, which is attained at the center of the star, is approximately only one order of magnitude bigger than B_{pole} (see *e.g.*, [167]).

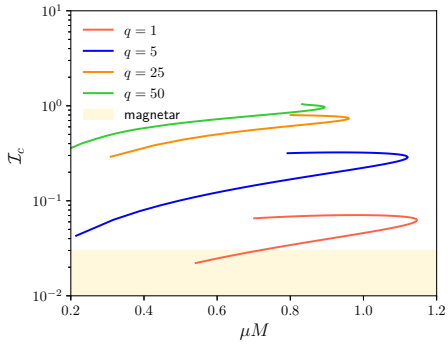

Figure 6.8: Dimensionless quantity $\mathscr{I}$ defined in Eq. (6.25), evaluated at $r = 0$ for configurations with $m = 1$ and different values of q. The yellow region corresponds to the upper region of the interval $\mathscr{I}$ at the center of strongly magnetized neutron stars (see the text for details).

As can be appreciated from Fig. 6.8, some of the individual configurations intersect with the interval $10^{-7} \lesssim \mathscr{I}_c \lesssim 3 \times 10^{-2}$, which means that it is possible to find a value of μ such that B_c and M are within the range of neutron stars. In particular some of the low mass solutions obtained with $q = 1$ are in this region, while typical, compact solutions with $q = 1, 5, 25$ and 50 might have stronger magnetic fields (larger masses) than magnetars if we assume similar values of the mass (magnetic fields) of the boson stars to those of the neutron star models. In order to perform a numerical application we restrict to the configurations with $q = 1$ and $M\mu = 0.7$ and choose $M = 1.5 M_\odot$. This fixes $\mu(c\hbar) = 1.8 \times 10^{-10}$eV which in turn sets the magnitude of all other physical variables, for instance the magnitude of the magnetic field at the center of coordinates takes then the value of $B_c \approx 1 \times 10^{14}$T, which is within the expected values of magnetic fields inside magnetars. Furthermore, the size of this bosonic configuration, which can be estimated from the size of the torus, is of order $r_{\max(\phi)} \approx 9$ km, obtaining a compactness comparable to those of neutron stars.

6.5 Conclusions

In the present work we have constructed magnetized solutions of boson stars, which are static, axisymmetric, everywhere regular and asymptotically flat solutions of the Einstein-Maxwell-Klein-Gordon system characterized by the mass parameter of the scalar field μ, the azimuthal harmonic index (winding number) m and the coupling constant q. The configurations consist of two contrarotating oppositely charged tori, and we have seen that they give rise to an electrically neutral current that generates a poloidal magnetic field, according to the observer at

rest.

Comparing with the $q = 0$ case, which reduces to the toroidal static boson stars found in [104], we obtained that the electromagnetic field affects the structure of the star and can noticeably change their mass and size. Similarly to other boson star models, in the magnetostatic solutions obtained in this work, a maximum mass configuration was found for each q, and in all explored cases the sequence of solutions contain a region of negative binding energy. Regarding the electromagnetic part, the dipole magnetic moment $\mathscr{M}$ has been obtained and an important difference is noted with respect to the rotating charged boson star, namely that the maximum $\mathscr{M}$ configuration does not corresponds with the maximum mass configuration for every q, and is shifted towards the zero mass solution ($\omega = \mu$).

We showed that regions of zero magnetic field form at the inner part of the torus which grow in size as one considers large enough values of the electromagnetic coupling constant q. On the other hand, it has also been found that the electromagnetic contribution to the sources increases in relation to the scalar field corresponding sources. For these reasons and since we have not found any bound for q, it would be interesting to study in a future work, the numerically challenging solutions with $q \gg 1$ and also analyze the asymptotic limit $q \to \infty$.

The magnetic field has been compared to that of strongly magnetized neutron stars, obtaining that for similar values of the total mass of the star, the inner magnetic field is comparable to that of magnetars for $q \lesssim 1$ compact configurations and greater, for larger values of q, making our objects, besides being interesting by their own value, faithful mimickers of neutron stars. Since toroidal static boson stars with $q = 0$ are known to be unstable we expect that the obtained solutions (at least for small values of q) remain unstable, however there is a stabilization (and formation) mechanism for neutral multifield boson stars [104] which might be applied to the charged scalar field case. Starting from the conditions in which these magnetized boson stars are stable, a mechanism for their formation could be devised. Boson stars are useful entities in strong gravity research, in particular in dynamical studies and as toy models of more complex scenarios. In this sense, the compactness and magnetic field magnitudes of magnetostatic boson stars motivates the study of the collapse and the consequent emission in both the gravitational and electromagnetic channels. Such collapse dynamics and multimessenger studies will be presented in future works.

6.6 Appendix of Chap. 6. 3+1 decomposition of $T_{\mu\nu}$ and the elliptic system of PDEs

In terms of energy-momentum tensor decomposed into the 3+1 quantities,

$$E = T_{\mu\nu} n^\mu n^\nu; \quad P_\alpha = -n^\nu T_{\mu\nu} \gamma^\nu_\alpha; \quad S_{\alpha\beta} = T_{\mu\nu} \gamma^\mu_\alpha \gamma^\nu_\beta. \tag{6.26}$$

where $n^\alpha = (1/N, 0, 0, 0)$, $\gamma^\alpha_\beta = \delta^\alpha_\beta + n^\alpha n_\beta$ and $N := e^{F_0}$, the Einstein equations can be written [117, 182] as the following system of elliptic equations for the metric coefficients at Eq.(6.8),

$$\Delta_3 F_0 = 4\pi e^{2F_1}\left(E+S\right) - \partial F_0 \partial\left(F_0+F_2\right), \tag{6.27a}$$

$$\Delta_2\left[\left(Ne^{F_2}-1\right)r\sin\theta\right] = 8\pi N e^{2F_1+F_2} r\sin\theta\left(S^r{}_r + S^\theta{}_\theta\right), \tag{6.27b}$$

$$\Delta_2\left(F_1+F_0\right) = 8\pi e^{2F_1} S^\varphi{}_\varphi - \partial F_0 \partial F_0, \tag{6.27c}$$

where,

$$\Delta_3 := \frac{\partial^2}{\partial r^2} + \frac{2}{r}\frac{\partial}{\partial r} + \frac{1}{r^2}\frac{\partial^2}{\partial\theta^2} + \frac{1}{r^2\tan\theta}\frac{\partial}{\partial\theta}, \tag{6.28}$$

$$\Delta_2 := \frac{\partial^2}{\partial r^2} + \frac{1}{r}\frac{\partial}{\partial r} + \frac{1}{r^2}\frac{\partial^2}{\partial\theta^2}, \tag{6.29}$$

$$\partial f_1 \partial f_2 := \frac{\partial f_1}{\partial r}\frac{\partial f_2}{\partial r} + \frac{1}{r^2}\frac{\partial f_1}{\partial\theta}\frac{\partial f_2}{\partial\theta}. \tag{6.30}$$

The source terms using the ansatz in Eqs. (6.8), (6.9) and (6.10) lead to the following expressions:

$$E+S = \frac{4}{N^2}\omega^2\phi^2 - 2\mu^2\phi^2 + \frac{e^{-2(F_1+F_2)}}{\mu_0 r^2\sin^2\theta}\partial C\partial C, \tag{6.31}$$

$$S^r{}_r + S^\theta{}_\theta = 2\left[\frac{\omega^2}{N^2} - \frac{e^{-2F_2}(m-qC)^2}{r^2\sin^2\theta}\right]\phi^2 - 2\mu^2\phi^2, \tag{6.32}$$

$$S^\varphi{}_\varphi = \left[\frac{\omega^2}{N^2} + \frac{e^{-2F_2}(m-qC)^2}{r^2\sin^2\theta}\right]\phi^2 - e^{-2F_1}\partial\phi\partial\phi - \mu^2\phi^2 + \frac{e^{-2(F_1+F_2)}}{2\mu_0 r^2\sin^2\theta}\partial C\partial C. \tag{6.33}$$

The two Klein Gordon Eqs., (6.3), and the Maxwell Eq., (6.4), reduce to,

$$\Delta_3\phi = e^{2F_1}\left(\mu^2 - \frac{\omega^2}{N^2}\right)\phi - \partial\phi\partial(F_0+F_2) + e^{2F_1-2F_2}\frac{(m-qC)^2\phi}{r^2\sin^2\theta} \tag{6.34}$$

$$(2\Delta_2 - \Delta_3)C = -\partial C\partial(F_0-F_2) - 2\mu_0 q e^{2F_1}(m-qC)\phi^2. \tag{6.35}$$

We have obtained the following number density currents,

$$j^\mu_1 = \left(\omega\frac{\phi^2}{N^2}, 0, 0, \frac{e^{-2F_2}(m-qC)\phi^2}{r^2\sin^2\theta}\right), \tag{6.36}$$

and

$$j^\mu_2 = \left(\omega\frac{\phi^2}{N^2}, 0, 0, -\frac{e^{-2F_2}(m-qC)\phi^2}{r^2\sin^2\theta}\right), \tag{6.37}$$

which have been inserted in Eq. (6.4) to obtain Eq. (6.35), and corresponds to the nontrivial remaining Maxwell equation, $\Box A^{\varphi} - R^{\varphi}_{\ \varphi} = -\mu_0 J^{\varphi}$.

The Eqs. (6.27), (6.34) and (6.35) make up the elliptic system of PDEs for the model (6.1) using the ansatz presented at section 6.2.

CHAPTER 7

TWO BOSON STARS IN EQUILIBRIUM[1]

Contents

In this chapter we construct solutions to the Einstein-Friedberg-Lee-Sirlin system, representing two boson stars in equilibrium made of a complex scalar field whose mass is given to it by a real scalar field with a finite vacuum expectation value generated via a symmetry breaking potential.

Solutions in full General Relativity interpreted as two non-spinning static boson stars in equilibrium where first obtained in [183]. And subsequently the (mini) two boson star system have been obtained as a special case within more complex families, some of them consisting of several more scalar field accumulations [176], some of them out of axial symmetry [166] and some other using multiple scalar fields [104]. The system of two boson stars in equilibrium is also known as a dipolar boson star. The equilibrium obtained for such kind of system is due to the odd symmetry of the complex scalar field with respect to the plane of symmetry that separates both lumps which implies a phase difference between both lumps and consequently a repulsive interaction between them, which together with the gravitational attraction allows obtaining equilibrium solutions.

According to the fully-nonlinear numerical evolutions in 3+1 dimensions performed in [104], the two boson star solutions with the standard massive non-self interacting complex scalar fields, are unstable. In the same Ref. it was also found a stabilization mechanism for the dipolar boson stars, which consists in superpose a sufficient amount of a spherical mode of an extra scalar field (complex,

[1]This chapter will be incorporated into a paper to be published with C. Herdeiro, D. Núñez and E. Radú. The work contained in this chapter as well as the numerical implementation described here is under development.

canonical and of the same mass). Of course, the stable scenarios in this context no longer represent a simple two-star system and therefore the search for stabilization mechanisms for this system has continued[2]. Attempts to use the self-interacting parameters of the scalar field to achieve dynamically robust systems have apparently not been successful, however there is one more possibility at hand to be explored.

7.1 Mathematical background

The Friedberg-Lee-Sirlin model [184] is a composite system which contain a complex scalar field Φ and a real scalar field Ψ. In this model the complex scalar field acquires mass due to a coupling m with the real field. On the other hand, the real scalar field possesses a mass parameter μ and a vacuum expectation value v in such a way that when $\Psi \to v$ the system reduce to the Klein-Gordon case with a complex scalar field of mass mv. Relevant for our work are the solitonic solutions in the Friedberg-Lee-Sirlin model (in Minkowski spacetime), obtained in [185] in the limit $\mu \to 0$.

This system can be minimally coupled to gravity and the full action reads

$$S = \int \mathrm{d}^4x\sqrt{-g}\left[\frac{1}{4\alpha^2}R - g^{\mu\nu}\nabla_\mu\Phi\nabla_\nu\Phi^* \right. \\ \left. -\frac{1}{2}g^{\mu\nu}\nabla_\mu\Psi\nabla_\nu\Psi - m^2\Psi^2|\Phi|^2 - \mu^2\left(\Psi^2 - v^2\right)^2\right], \tag{7.1}$$

please be aware that the references [129, 186, 187] have typos in the Lagrangian of the matter fields or in the ψ Klein-Gordon equation (and sometimes in both) however the action (7.1) is consistent with that originally presented in [184] except for multiplicative factor changes. Here m and μ are the mass parameters of the complex and real scalar fields, respectively. We have used the signature $(-,+,+,+)$, $c = 1$ units and $\alpha^2 = 4\pi G$.

Boson stars and rotating solutions with horizons (hairy black holes) in this theory have already been mentioned in Chap. 4 of this manuscript. This interesting solutions where obtained in Ref. [129]. In this reference are presented rotating solutions of parity-even and parity-odd boson stars[3], we note that the latter have been much less studied in the literature even in the case of mini boson stars. The purpose in this chapter is to address the non-rotating static case with a scalar field in the odd symmetry case.

[2] Carlos Herdeiro, Eugen Radu. Personal communication

[3] This refers to the allowed boundary conditions adopted for Φ in the equatorial plane which maintain the reflection symmetry $\theta \to \pi - \theta$: $\Phi = 0$ for parity-odd and $\partial_\theta\Phi = 0$ for parity-even at $\theta = \pi/2$.

The Einstein equations obtained from (7.1) are:

$$\begin{aligned} &R_{\mu\nu} - \frac{1}{2} R g_{\mu\nu} = 2\alpha^2 T_{\mu\nu}; \\ &T_{\mu\nu} = 2\nabla_{(\mu}\Phi\nabla_{\nu)}\Phi^* + \nabla_\mu\Psi\nabla_\nu\Psi \\ &\quad - g_{\mu\nu}\left(g^{\alpha\beta}\nabla_\alpha\Phi\nabla_\beta\Phi^* + \frac{1}{2}g^{\alpha\beta}\nabla_\alpha\Psi\nabla_\beta\Psi + m^2\Psi^2|\Phi|^2 + \mu^2\left(\Psi^2 - v^2\right)^2\right) \end{aligned} \tag{7.2}$$

The equation of motion for the complex scalar fields Φ and Ψ are

$$g^{\mu\nu}\nabla_\nu\nabla_\mu\Phi = m^2\Psi^2\,\Phi, \qquad g^{\mu\nu}\nabla_\nu\nabla_\mu\Psi = 2\left[m^2|\Phi|^2 + 2\mu^2\left(\Psi^2 - v^2\right)\right]\Psi. \tag{7.3}$$

We are looking for static solutions in axial symmetry:

$$g_{\mu\nu}\,\mathrm{d}x^\mu\,\mathrm{d}x^\nu = -e^{2F_0(r\theta)}\,\mathrm{d}t^2 + e^{2F_1(r,\theta)}(\mathrm{d}r^2 + r^2\,\mathrm{d}\theta^2) + e^{2F_2(r,\theta)}r^2\sin^2\theta\,\mathrm{d}\varphi^2, \tag{7.4}$$

$$\Phi = \phi(r,\theta)e^{-i\omega t}, \quad \Psi = \psi(r,\theta). \tag{7.5}$$

The 3+1 source terms are

$$E = T_{\mu\nu}n^\mu n^\nu; \quad P_\alpha = -n^\nu T_{\mu\nu}\gamma^\nu_\alpha; \quad S_{\alpha\beta} = T_{\mu\nu}\gamma^\mu_\alpha\gamma^\nu_\beta. \tag{7.6}$$

with $n^\alpha = (1/N,0,0,0)$, $\gamma^\alpha_\beta = \delta^\alpha_\beta + n^\alpha n_\beta$. The Einstein equations for the metric (7.4) are the following,

$$\Delta_3 F_0 = \alpha^2 A^2\left(E+S\right) - \partial F_0\partial\left(F_0+F_2\right) \tag{7.7}$$

$$\Delta_2\left[\left(NB-1\right)r\sin\theta\right] = 2\alpha^2 NA^2 Br\sin\theta\left(S^r{}_r + S^\theta{}_\theta\right) \tag{7.8}$$

$$\Delta_2\left(F_1+F_0\right) = 2\alpha^2A^2S^\varphi{}_\varphi - \partial F_0\partial F_0, \tag{7.9}$$

where $N = e^{F_0}$, $A = e^{F_1}$ y $B = e^{F_2}$ and

$$\Delta_3 := \frac{\partial^2}{\partial r^2} + \frac{2}{r}\frac{\partial}{\partial r} + \frac{1}{r^2}\frac{\partial^2}{\partial\theta^2} + \frac{1}{r^2\tan\theta}\frac{\partial}{\partial\theta} \tag{7.10}$$

$$\Delta_2 := \frac{\partial^2}{\partial r^2} + \frac{1}{r}\frac{\partial}{\partial r} + \frac{1}{r^2}\frac{\partial^2}{\partial\theta^2} \tag{7.11}$$

$$\partial f\partial g := \frac{\partial f}{\partial r}\frac{\partial g}{\partial r} + \frac{1}{r^2}\frac{\partial f}{\partial\theta}\frac{\partial g}{\partial\theta}. \tag{7.12}$$

Only the source terms remain to be determined explicitly. Using our ansatz for metric and fields we arrive at the following,

$$E+S = 4\frac{\omega^2}{N^2}\phi^2 - 2m^2\psi^2\phi^2 - 2\mu^2\left(\psi^2-v^2\right)^2 \tag{7.13}$$

$$S^r{}_r + S^\theta{}_\theta = 2\frac{\omega^2}{N^2}\phi^2 - 2m^2\psi^2\phi^2 - 2\mu^2\left(\psi^2-v^2\right)^2 \tag{7.14}$$

$$S^\varphi{}_\varphi = \frac{\omega^2}{N^2}\phi^2 - \frac{1}{A^2}\partial\phi\partial\phi - \frac{1}{2A^2}\partial\psi\partial\psi - m^2\psi^2\phi^2 - \mu^2\left(\psi^2-v^2\right)^2 \tag{7.15}$$

Explicitly,

$$E = \frac{\omega^2}{N^2}\phi^2 + \frac{1}{A^2}\partial\phi\partial\phi + \frac{1}{2A^2}\partial\psi\partial\psi + m^2\psi^2\phi^2 + \mu^2\left(\psi^2 - v^2\right)^2, \quad (7.16)$$

$$S^r{}_r = \frac{\omega^2}{N^2}\phi^2 + Y - m^2\psi^2\phi^2 - \mu^2\left(\psi^2 - v^2\right)^2, \quad (7.17)$$

$$S^\theta{}_\theta = \frac{\omega^2}{N^2}\phi^2 - Y - m^2\psi^2\phi^2 - \mu^2\left(\psi^2 - v^2\right)^2, \quad (7.18)$$

with

$$Y = \frac{1}{A^2}\left[\left(\frac{\partial\phi}{\partial r}\right)^2 - \frac{1}{r^2}\left(\frac{\partial\phi}{\partial\theta}\right)^2 + \frac{1}{2}\left(\frac{\partial\psi}{\partial r}\right)^2 - \frac{1}{2r^2}\left(\frac{\partial\psi}{\partial\theta}\right)^2\right] \quad (7.19)$$

The equation of motion for Φ and Ψ are

$$\Delta_3\phi = A^2\left(m^2\psi^2 - \frac{\omega^2}{N^2}\right)\phi - \partial\phi\partial(F_0 + F_2) \quad (7.20)$$

and

$$\Delta_3\psi = 2A^2\left[m^2\phi^2 + 2\mu^2\left(\psi^2 - v^2\right)\right]\psi - \partial\psi\partial(F_0 + F_2) \quad (7.21)$$

Asymptotic flatness implies that the following outer boundary conditions must be imposed,

$$\begin{aligned} &\phi|_{r\to\infty} = 0, \quad \psi|_{r\to\infty} = v; \\ &F_0|_{r\to\infty} = 0, \quad F_1|_{r\to\infty} = 0, \quad F_2|_{r\to\infty} = 0. \end{aligned} \quad (7.22)$$

Also the condition $\omega < \mu$ is necessary in order to have $\phi|_{r\to\infty} = 0$. Regularity of the solution at the origin and on the symmetry axis require,

$$\begin{aligned} &\phi|_{r=0} = 0, \quad \partial_r\psi|_{r=0} = 0; \\ &\partial_r F_0|_{r=0} = 0, \quad \partial_r F_1|_{r=0} = 0, \quad \partial_r F_2|_{r=0} = 0, \\ &F_1|_{r=0} = F_2|_{r=0}. \end{aligned} \quad (7.23)$$

$$\begin{aligned} &\partial_\theta\phi|_{\theta=0,\pi} = 0, \quad \partial_\theta\psi|_{\theta=0,\pi} = 0; \\ &\partial_\theta F_0|_{\theta=0,\pi} = 0, \quad \partial_\theta F_1|_{\theta=0,\pi} = 0, \quad \partial_\theta F_2|_{\theta=0,\pi} = 0, \\ &F_1|_{\theta=0,\pi} = F_2|_{\theta=0,\pi}. \end{aligned} \quad (7.24)$$

Then, we impose the spacetime to be invariant with respect to a reflection on the $\theta = \pi/2$ plane while on the other hand expect a change of sign in the complex scalar field profile. In particular implies that derivatives with respect to θ at $\theta = \pi/2$ of the metric functions vanish

$$\begin{aligned} &\phi|_{\theta=\pi/2} = 0, \quad \partial_\theta\psi|_{\theta=\pi/2} = 0; \\ &\partial_\theta F_0|_{\theta=\pi/2} = 0, \quad \partial_\theta F_1|_{\theta=\pi/2} = 0, \quad \partial_\theta F_2|_{\theta=\pi/2} = 0, \end{aligned} \quad (7.25)$$

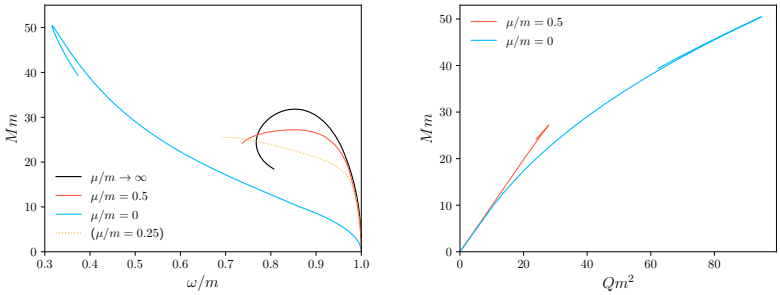

Figure 7.1: Spherical Klein-Gordon and Friedberg-Lee-Sirlin boson stars. Our $\mu/m = 0.25$ solutions do not correspond to the $\mu/m = 0.25$ solutions reported in [129], but the $\mu/m = 0.5$ curve does coincide with the later.

The required integration domain therefore reduces to $0 \leq \theta \leq \pi/2$, $0 \leq r < \infty$.

7.2 Some results

7.2.1 Spherical boson star parenthesis

Before proceeding to obtain the dipolar solutions, we solve the above equations for parity-even Φ, substituting the boundary condition $\phi|_{r=0} = 0$ and $\phi|_{\theta=\pi/2} = 0$ by

$$\partial_r \phi|_{r=0} = 0, \quad \partial_\theta \phi|_{\theta=\pi/2} = 0. \tag{7.26}$$

The two-dimensional solver converges to the spherical symmetric boson star in the Friedberg-Lee-Sirlin model, reported in [129]. We reproduce Fig. 1 of [129]. In Fig. 7.1 we show quick numerical integrations using 11 spectral coefficients in r and θ. Although we use the same conventions and rescalings as they do, the solution curve they report as $\mu/m = 0.25$ and $\alpha = 0.5$, in our case corresponds to the $\mu/m = 0.5$ and $\alpha = 0.5$ solutions.

7.2.2 Solutions

We consider the following initial guess to obtain a Einstein-Klein-Gordon dipolar boson star ($\mu \to \infty$ limit),

$$\phi = r\phi_0 e^{-x^2/\sigma_x^2 - z^2/\sigma_z^2} Y_1^0(\theta,\varphi), \quad N = 1-(1-N_0)e^{r^2}, \quad \omega = 0.965, \tag{7.27}$$

where $\phi_0 = 9.07 \times 10^{-3}$, $\sigma_x = \sqrt{200}$, $\sigma_z = \sqrt{50}$ and $Y_1^0(\theta,\varphi) = \frac{1}{2}\sqrt{\frac{3}{\pi}}\cos\theta$. For a solution with $N_0 = 0.9404$.

After that we construct the equilibrium two-boson star solution family in the Einstein-Klein-Gordon theory, whose resulting mass as function of frequency and

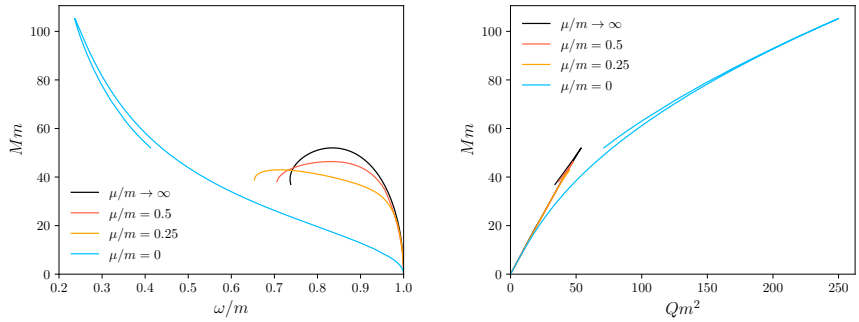

Figure 7.2: Two boson stars in equilibrium in Klein-Gordon and Friedberg-Lee-Sirlin for different values of μ/m and $\alpha = 0.5$.

Noether charge is shown in Figure 7.2 (black line). In this result we have used $\alpha = 0.5$ and that is why the mass looks so large. However in the $\mu/m \to \infty$ limit (and only in that limit) the constant α can be rescaled away. So by rescaling to solutions with $\alpha^2 = 4\pi$ i.e. units where $G = 1$, we have verified that the magnitude reported in [104, 166, 188] for the dipole boson star mass is obtained.

$\alpha = 0.5$ sequence of boson star solutions

Finite μ solutions are obtained using a corresponding equal-frequency Einstein-Klein-Gordon solution as initial guess and slowly decreasing the value of μ. In Figure 7.2 we display the total mass and Noether charge plots for the values $\mu/m = 0.5$ and 0.25, as well as the limit of vanishing scalar potential $\mu = 0$.

We have analyzed the ψ profiles and obtained that the field ψ becomes long-ranged when $\mu = 0$, as expected from the asymptotic behavior of ψ from Eq. (7.21).

$\omega = 0.9$ sequence of solutions varying α

Figure 7.3 shows M as a function of the gravitational coupling for solutions with $\omega/m = 0.9$.

7.2.3 Flat spacetime static equilibria

Figure 7.3 already showed that there are solutions with zero or even negative gravitational coupling constant α^2. In the latter the negative sign could be passed to the $T_{\mu\nu}$ and thus speak of a ghost field soliton [118, 124].

In reference [188] it was argued that the short-range character of the self-interactions that normally allows to obtain Q-balls, does not work to obtain equilibrium solutions composed by distant energy lumps, concluding that gravity, be-

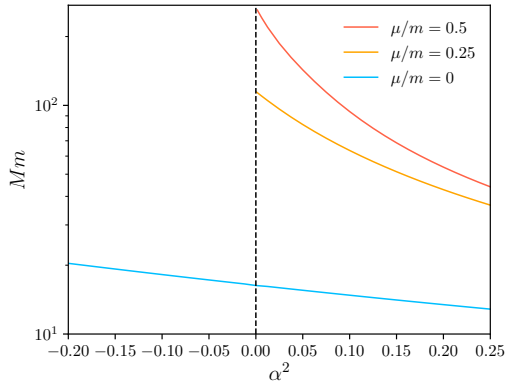

Figure 7.3: $\omega/m = 0.9$ sequence of solutions for different cases of μ/m. For the $\mu/m = 0.5$ and 0.25 cases we have not been able to obtain flat space solutions so far.

ing long-range, is mandatory for configurations of a single scalar field. It is interesting that only in the $\mu = 0$ case we have been able to construct solutions with $\alpha \leq 0$, but precisely this corresponds to the case in which the Ψ field becomes massless and long-ranged, the latter being precisely the fact that allows to balance at a distance the scalar repulsive interaction due to the phase difference of π between the two lumps. Reference [188] also provides a proof of why there are no two energy lumps solutions in Minkowski and we might be interested in finding out exactly where the argument fails. It is possible to follow the steps from equation 5.11 to equation 5.20 of [188] using the total energy-momentum tensor of our system and, using the odd-parity of ϕ and the even parity of ψ we obtain an analogous to equation 5.22 of [188]:

$$\int_0^\infty \rho \left[\phi_1^2 - \frac{1}{2}\psi_{0,\rho}^2 - \mu^2 \left(\psi_0^2 - v^2 \right)^2 \right] d\rho = 0, \tag{7.28}$$

From which we can not conclude anything. We could also try to apply the procedure on a part of the $T_{\mu\nu}$, for example the one associated to Φ:

$$Q_{\mu\nu} = 2\nabla_{(\mu}\Phi\nabla_{\nu)}\Phi^* - g_{\mu\nu}\left(g^{\alpha\beta}\nabla_\alpha\Phi\nabla_\beta\Phi^* + m^2\Psi^2|\Phi|^2 \right), \tag{7.29}$$

however due to the m^2 term, this tensor is not conserved:

$$\nabla_\alpha Q^\alpha{}_\beta = \nabla_\beta\Phi^*(\Box\Phi - m^2\Psi^2\Phi) + \nabla_\beta\Phi(\Box\Phi^* - m^2\Psi^2\Phi^*) - 2m|\Phi|^2\Psi\nabla_\beta\Psi. \tag{7.30}$$

In any case we have obtained the sequence of solutions for $\alpha = 0$ and $\mu = 0$ two static Q-balls in equilibrium. Figure 7.4 shows the Noether charge as a function

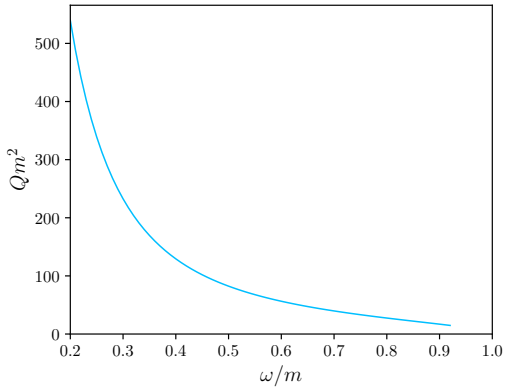

Figure 7.4: $\alpha = 0$, $\mu = 0$ sequence of solutions. (For $\omega > 0.9$ numerical error indicators get large)

of ω. These results are reminiscent of the results obtained for Q-balls in the FLS model in spherical symmetry [189].

Part III

Numerical evolutions

CHAPTER 8

STABILITY[1]

Contents

The ℓ-boson stars are static, spherical, multi-field self-gravitating solitons. They are asymptotically flat, finite energy solutions of Einstein's gravity minimally coupled to an odd number of massive, complex scalar fields. A previous study assessed the stability of ℓ-boson stars under spherical perturbations, finding that there are both stable and unstable branches of solutions, as for single-field boson stars ($\ell = 0$). In this work we probe the stability of ℓ-boson stars against non-spherical perturbations by performing numerical evolutions of the Einstein-Klein-Gordon system, with a 3D code. For the timescales explored, the ℓ-boson stars belonging to the spherical stable branch do not exhibit measurable growing modes. We find, however, evidence of zero modes; that is, non-spherical perturbations that neither grow nor decay. This suggests the branching off towards a larger family of equilibrium solutions: we conjecture that ℓ-boson stars are the enhanced isometry point of a larger family of static (and possibly stationary), non-spherical multi-field self-gravitating solitons.

[1]This chapter is extracted with minor revisions from Ref. [103], which was written in collaboration with N. Sanchis-Gual, J. Barranco, A. Bernal, J. C. Degollado, C. Herdeiro and D. Núñez.

8.1 Introduction

Boson stars [44,45] are remarkable gravitational solitons. These self-gravitating, localised energy lumps of a complex, massive scalar field have appealing theoretical properties. A key one is their dynamical stability. For spherical boson stars there is a stable branch of solutions against perturbations. Indeed, a variety of studies including linear perturbation theory [106, 190, 191], catastrophe theory [192] and numerical simulations [56, 193] agree that boson stars are perturbatively stable, as long as the amplitude of the scalar field is smaller than a critical value. When the latter is attained, boson stars acquire their maximum mass.

Being dynamically stable legitimates inquiring about the possible (astro)physical role of boson stars. Albeit exotic, lacking undisputed observational evidence, boson stars have found important applications in strong gravity and astrophysics. For instance, boson stars provide a common model for a black hole mimicker [49, 159, 194]. Being dynamically tractable, one can then compare dynamical spacetime properties, such as waveforms of binary boson star systems, with those of black holes [57, 58, 195]. This is particularly timely in view of the recently initiated gravitational-wave astronomy era [196, 197], which provides data for both models to be compared with.

A second important application is in relation to a central mystery of contemporary science: the nature of dark matter. An increasing attention has been dedicated to models that consider dark matter as an ultra-light bosonic particle [26, 89–91]. The bosonic nature allows this sort of dark matter to form coherent macroscopic excitations. In this context, bosons stars can model, in particular, the core of dark matter galactic halos [98, 113, 198, 199].

In their original guise, the Einstein-Klein-Gordon (EKG) model contains a massive, free scalar field, and the solitonic solutions are called *mini*-boson stars. A variety of generalisations ensued. Boson stars for scalar field theories with self-interactions have been reported, starting with the case of quartic self-interactions considered by Colpi *et al.* [132]. Spacetime angular momentum was introduced for mini-boson stars in [164], giving rise to stationary (but not static) self-gravitating solitons. A cousin model with a complex, massive vector (rather than scalar) field yields *Proca stars* [52]. These and other examples use single (complex) field models; however, multi-field boson stars have also been reported. One example is given by *multi-state* boson stars [113, 199, 200]. More recently, multi-field boson stars with an arbitrary odd number, $N = 2\ell + 1$, $\ell \in \mathbb{N}_0$, of equal mass, uncoupled (except through gravity) complex scalar fields with harmonic time dependence were introduced [99]; they are dubbed *ℓ-boson stars* and they will be the focus of this paper.

ℓ-boson stars are described by spherically symmetric and static metrics. For

$\ell = 0$ they are simply the usual mini-boson stars. For $\ell \geqslant 1$, the $2\ell+1$ scalar fields have an angular dependence given by the corresponding $2\ell+1$ spherical harmonics $Y^{\ell m}$. Then, if the radial dependence for all fields is the same, corresponding to choosing the amplitude of the spherical harmonics equal at all radial distances, static, spherical configurations are obtained, regardless of the energy-momentum tensor of each individual field being angular dependent. This is an example of *symmetry non-inheritance*: the (spherical) spacetime and the (non-spherical) individual matter fields do not share spherical symmetry. The usual boson stars already have a version of symmetry non-inheritance: the (time oscillating) scalar field and the (static) spacetime do not share time-translation symmetry. Consistency requires only that the spacetime geometry and the total energy-momentum tensor share the same symmetries, not the individual matter fields.

Generic ℓ-boson stars have been shown to exhibit similar properties to those of the standard $\ell = 0$ stars. In particular, ℓ- boson stars have a stable branch of solutions against *spherical* perturbations [101]. The main goal of this paper is to assess the stability of ℓ-boson stars (in this branch) against generic, non-spherical perturbations. As we shall see, our analysis will show that, in this respect, generic ℓ-boson star do not exactly mimic the $\ell = 0$ case. Although no instabilities are observed, the analysis provides a glimpse of a larger landscape of solutions, of which ℓ-boson stars are just the enhanced symmetry point.

Departure from spherical symmetry is physically relevant. Firstly, spherical objects – such as ℓ-boson stars – need to be stable against non-spherical perturbations, in order to be dynamically viable. Secondly, astrophysical bodies are not, typically, perfectly spherical, in particular due to angular momentum. So one must assess if some perturbations actually deform ℓ-boson stars into acquiring new degrees of freedom. In this respect, it was recently proposed that multi-field boson stars, in the *non-relativistic regime*, could have non-spherical stable configurations. This provides an extra motivation to inquire about the behaviour of relativistic ℓ-boson stars under non-spherical perturbations Finally, assessing non-spherical configurations and perturbations often yields a richer phenomenology. As a fruitful example, it was recently found that spinning, single-field mini-boson stars are unstable against non-axisymmetric perturbations, either decaying into a non-rotating boson star or collapsing into a Kerr black hole [58,63]. By contrast, spinning Proca stars do not present instabilities under non-axisymmetric perturbations and furthermore, they can form dynamically [63]. This example shows how the study on non-spherical perturbations unveiled a new relevant dynamical property of boson stars.

We shall investigate the behaviour of ℓ-boson stars under non-spherical perturbations using fully non-linear numerical simulations of the corresponding Einstein-Klein-Gordon system. As initial data, we use configurations found in [99] which

are then perturbed in two different ways. The first type of perturbation tests the stability against non-axially symmetric perturbations, targeting potential bar-mode instabilities. The second type of perturbation tests the stability against a relative change in the amplitude of the internal fields. In none of the two cases measurable growing modes were found, either by perturbing the total mass density or by perturbing each of the constituent fields, as long the ℓ-boson star belongs to the stable branch against spherical perturbations. By following the evolution of distortion parameters (defined below) we found, however, evidence for long-lived perturbations, which we interpret as zero modes. These modes, in turn, are interpreted as evidence for a larger family of equilibrium solutions.

Consider the Schwarzschild black hole of vacuum General Relativity. It has been shown to be mode stable in the renowned works of Regge and Wheeler [201] and Zerilli [202]. No gravitational perturbations grow. However, a perturbation that carries angular momentum yield not decay. The Schwarzschild solution migrates to a small angular momentum Kerr solution and oscillates around this new ground state. Similarly, a perturbation which electric charge will not decay and the spacetime will oscillate around a small charge Reissner-Nordström solution. These special perturbations are zero modes. Such modes are often found when a spacetime is unstable against some sort of perturbations, at the threshold between stable and unstable modes. An example occurs for the superradiant instability of the Kerr spacetime due to a massive bosonic field. The zero modes indicate the bifurcation of the Kerr family towards a new family of black holes with bosonic hair [203]. But zero modes can also occur even if there is no instability, as in the Schwarzschild example, indicating, nonetheless, an enlarged family of solutions (Kerr or Reissner-Nordström), of which the initial spacetime (Schwarzschild) is a special case. Thus, one of the outcomes of our analysis is the conjecture that ℓ-boson stars are the enhanced isometry point of a larger family of static (and possibly stationary), non-spherical multi-field self-gravitating solitons.

In the rest of this work we will focus on configurations with $\ell = 1$. Such ℓ-boson stars are described by $N = 3$ fields, with $m = -1, 0, 1$ respectively. In order to follow the dynamics of the perturbed system a numerical code that solves the Einstein-N-Klein-Gordon system is required. We have used the Einstein Toolkit framework [14, 15, 204] with the Carpet package [205, 206] for mesh-refinement capabilities to achieve our goal.

As a technical step we perform a Cauchy (3+1) decomposition on each scalar field that constitutes the star and solve the full Einstein-N-Klein-Gordon system. This is done implementing an arrangement in the Einstein Toolkit, a *thorn*, to solve N scalar fields using finite differences [63].

This paper is organized as follows: Section 8.2 addresses the construction of

initial data to set up perturbed ℓ-boson stars. Section 8.3 describes the diagnostic tools used to monitor the evolution and some aspects used to decide on whether instabilities are present. The numerical results are described in Section 8.4 and in Section 8.5 our conclusions and final remarks are presented. In this work we use units where $G = 1 = c$.

8.2 Initial Data

Following previous works on ℓ-boson stars [99,101], we consider a set of $N = 2\ell+1$ complex scalar fields, with mass μ and no self-interaction within the Einstein theory of gravity, for which the energy-momentum tensor is given by:

$$T_{\alpha\beta} = \sum_{i=1}^{N} T^{(i)}_{\alpha\beta}\,, \tag{8.1}$$

where the index i labels each field and the stress-energy-momentum for each field is given by

$$\begin{aligned} T^{(i)}_{\alpha\beta} &= \left(\nabla_\alpha\Phi_i\,\nabla_\beta\Phi_i^* + \nabla_\beta\Phi_i\,\nabla_\alpha\Phi_i^*\right) \\ &\quad + g_{\alpha\beta}\left(\nabla_\sigma\Phi_i\nabla^\sigma\Phi_i^* + \frac{1}{2}\mu^2|\Phi_i|^2\right). \end{aligned} \tag{8.2}$$

Complex conjugation is denoted by '*'. Following [99, 100] we propose a set of scalar fields of the form

$$\Phi^{(i)}(t,r,\vartheta,\varphi) = \psi_\ell(r,t)Y^{\ell m}(\vartheta,\varphi)\,, \tag{8.3}$$

where the angular momentum number ℓ is fixed, and m, which plays the role of index i in equation (8.3), takes the values $m = -\ell, -\ell+1, \ldots, \ell$ (hence the total number of fields needed for a fixed value of ℓ will be $2\ell+1$), $Y^{\ell m}$ are the spherical harmonics defined over the unitary 2D-sphere. Then we assume that the amplitudes $\psi_\ell(r,t)$ are the *same* for all m. It was shown in [99] that if the N fields have all the same amplitude ψ_ℓ, the stress-energy tensor (8.1) has spherical symmetry regardless if the fields have angular dependence. See also [100] and for a detailed discussion on the procedure, see [122].

Assuming the harmonic time dependence

$$\psi_\ell(r,t) = \phi_\ell(r)e^{-i\omega t}\,, \tag{8.4}$$

where $\phi_\ell(r)$ and the frequency ω are both real-valued, the stress-energy tensor becomes time independent. Under these assumptions it is possible to find self gravitating static, spherically symmetric equilibrium configurations by solving the EKG system of equations. Those configurations are parametrized by the angular momentum number ℓ, hence the name, ℓ-boson stars.

In order to obtain initial data suitable for numerical evolution, we construct equilibrium ℓ-boson stars, to be subsequently perturbed. Considering a spherically symmetric spacetime with a line element given by:

$$ds^2 = -\alpha(r)^2\,dt^2 + A(r)dr^2 + r^2(d\vartheta^2 + \sin^2\vartheta\, d\varphi^2)\,, \tag{8.5}$$

where α and A, are functions of r, and the assumptions mentioned above for ψ_ℓ, the EKG system yields

$$\partial_r^2\phi_\ell = -\partial_r\phi_\ell\left(\frac{2}{r} + \frac{\partial_r\alpha}{\alpha} - \frac{\partial_r A}{2A}\right) + A\phi_\ell\left(\mu^2 + \frac{\ell(\ell+1)}{r^2} - \frac{\omega^2}{\alpha^2}\right), \tag{8.6}$$

$$\partial_r A = A\left\{\frac{(1-A)}{r} + 4\pi r A\left[\frac{(\partial_r\phi_\ell)^2}{A} + \phi_\ell^2\left(\mu^2 + \frac{\ell(\ell+1)}{r^2} + \frac{\omega^2}{\alpha^2}\right)\right]\right\}, \tag{8.7}$$

$$\partial_r\alpha = \alpha\left[\frac{(A-1)}{r} + \frac{\partial_r A}{2A} - 4\pi r A\phi_\ell^2\left(\mu^2 + \frac{\ell(\ell+1)}{r^2}\right)\right]. \tag{8.8}$$

By studying the Klein-Gordon equation in the vicinity of $r = 0$ one finds that the scalar field behaves as $\phi \sim \phi_0 r^\ell$ in that region. For a fixed value of the angular momentum number ℓ, a given value of the parameter ϕ_0, and the boundary condition at infinity requesting that ϕ_ℓ decays exponentially, the system of equations (8.6-8.8) becomes a nonlinear eigenvalue problem for the frequency ω. We solve this set of equations in a finite size grid by means of a shooting method using the frequency ω as the shooting parameter. For numerical purposes we take the mass parameter $\mu = 1$.

Fig. 8.1 shows a plot of the Arnowitt-Deser-Misner (ADM) mass M versus the frequency ω for the ℓ-boson stars. In Ref. [99] it was shown that ℓ-boson stars with $\ell > 0$ have similar properties to those of single-field mini-boson stars, *i.e.* the $\ell = 0$ case. For instance, given a value of ℓ, the mass M of the equilibrium configurations as a function of ω has a maximum, which gets larger as ℓ increases, yielding more compact stars. Furthermore, as in the case of 0-boson stars, the maximum value of the mass separates the space of solutions into two branches. These branches correspond to stable and unstable configurations against spherical perturbations, as shown in [101].

As mentioned above, the hypothesis that all the fields must have the same amplitude is essential to keep the spherical symmetry of the configuration. If one wants to consider different amplitudes of each constituent field, the assumption of spherical symmetry has to be relaxed. However, hitherto there has been no evidence that the resulting states may be equilibrium solutions of the Einstein-N-Klein-Gordon system. In this work we will show that deviations from spherical symmetry may indeed lead to new equilibrium solutions.

To proceed further with our non-spherical analysis we transform the solutions of the previous system of equations to Cartesian coordinates, $x^\mu = (t, r, \vartheta, \varphi) \rightarrow$

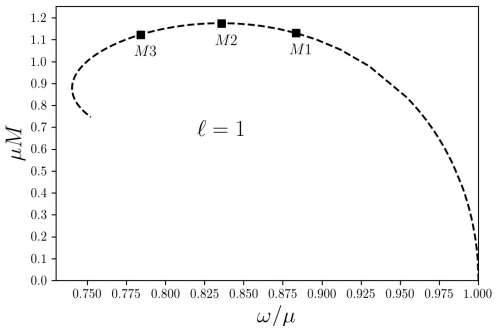

Figure 8.1: ADM mass vs. frequency for static ℓ-boson stars. The properties of models $M1$, $M2$ and $M3$ are listed in Table 8.1.

$x^\mu = (t, x, y, z)$. Then we perform a full non-linear numerical evolution of the perturbed stationary solutions.

8.3 Diagnostics

In order to test the stability of the static solutions we perform two different types of perturbations:

(i) The first type consists in perturbing the energy density of the star given by $\rho = n^\alpha n^\beta T_{\alpha\beta}$, where n^α is the four velocity of Eulerian observers in the 3+1 space time decomposition. The perturbed energy density is obtained by adding a non spherically symmetric small amplitude term to the homogeneous density in the following way [207]:

$$\rho = \rho_0 \left[1 + \kappa \left(\frac{x^2 - y^2}{R_{99}^2} \right) \right] \tag{8.9}$$

where ρ_0 is the energy density of the equilibrium configuration, obtained from the solution of Eqs. (8.6)-(8.8), and R_{99} is the radius enclosing 99% of the configuration's mass. In our simulations we choose $\kappa = 0.1$. This type of perturbations could trigger a potential bar-mode instability because it only affects the I_{xx} and I_{yy} components of the quadrupole moment defined as

$$I_{xx} = \int \rho(y^2 + z^2) dV \ , \qquad I_{yy} = \int \rho(x^2 + z^2) dV \ . \tag{8.10}$$

Since the value of κ is small $\kappa \ll 1$, this perturbation can be considered linear, initially; more importantly, it breaks the spherical symmetry of the original solution.

(ii) The second type of perturbations consist in varying separately the amplitude of each field. With these perturbations it is possible to study the stability of

the stars against variations on each mode m and break the spherical symmetry. We choose the following form

$$\phi_{\ell,m} = (1+\epsilon)\phi_\ell, \tag{8.11}$$

where ϕ_ℓ is the unperturbed solution of the system of Eqs. (8.6)-(8.8). This perturbation introduces an additional constraint violation, besides the well known numerical error, but its magnitude is controlled by choosing a small ϵ, which, in general, depends on the ℓ, m-mode. Note that if ϵ is the same for all m, the perturbation is spherical.

In order to assess the stability properties of the stars during the numerical simulation, we monitor the mass of the star, its angular momentum, and its density. We also follow the change in the quadrupole moment of the star, as shown below. Following the technique described in [207, 208] to examine the stability of rotating neutron stars, we monitor the behaviour of the distortion parameter defined as

$$\eta_z := \frac{I_{xx} - I_{yy}}{I_{xx} + I_{yy}}\,, \tag{8.12}$$

which is a good measure of the magnitude of the bar-mode instability for perturbation (i). This parameter has been used to study the stability of rapidly, differentially rotating stars [207]. It has been observed that when the star is dynamically unstable, η_z grows exponentially up to a maximum value; then the maximum value of η_z remains constant on dynamical timescales. For stable stars, on the other hand, the maximum initial value of η_z remains constant throughout the evolution. Thus the monitoring of η_z provides a good tool to determine the properties of the star against bar-mode perturbations. In this work we also use

$$\eta_y := \frac{I_{xx} - I_{zz}}{I_{xx} + I_{zz}}\,, \tag{8.13}$$

as a measure of the deformation of the star.

As further diagonostics, the maximum of the density and the lapse function are used to determine whether the configuration disperses or is undergoing a collapse. We have used the thorn AHFinder [209] to follow the formation of an apparent horizon (AH) during the evolution. We have also computed the Hamiltonian constraint [13] to check the fourth order convergence of the implementation - see the Appendix for details on this procedure.

8.4 Time evolution and numerical results

In this section we present the results from dynamical spacetime simulations from the perturbed ℓ-boson stars. We have compared the evolution of the equilibrium ℓ-boson stars with the perturbed stars.

Model	ℓ	ω/μ	μR_{99}	$\mu M_{\rm ADM}$
$M1$	1	0.882	13.45	1.133
$M2$	1	0.836	12.75	1.176 (maximum)
$M3$	1	0.783	7.53	1.122

Table 8.1: Frequency, radius and ADM mass for the configurations analysed.

We numerically integrate the EKG system using fourth-order spatial discretization within the Einstein Toolkit framework. The Einstein Toolkit solves the Einstein equations within the ADM 3+1 framework and evolves the spacetime using the Baumgarte-Shapiro-Shibata-Nakamura (BSSN) formulation of the Einstein equations [210] through the McLachlan thorn [211]. All the evolutions were made using the 1+log time slicing condition for the lapse α, and the *Gamma-driver* condition for the shift β^i [10].

We use the Method of Lines thorn to solve the equations in time by using a fourth order Runge-Kutta scheme. The equations for the scalar fields are solved using a finite difference scheme of fourth order. We also employ the mesh refinement capabilities provided by the Carpet arrangements. The fixed mesh refinement grid hierarchy used consists of nested cubes with 3 levels of refinement. The finest is set in such a way that it covers the entire star.

We set the spatial resolution on the finest level to $\{{\rm d}x, {\rm d}y, {\rm d}z\} = 0.8$ (and the coarsest to $\{{\rm d}x, {\rm d}y, {\rm d}z\} = 3.2$) in order to fully capture the properties of the star. We follow the formation of an AH after the collapse of unstable stars.

More details on the resolution, as well as numerical convergence are given in the Appendix.

The three stationary configurations we chose to illustrate the general behaviour of the stars are represented with a square over the curve in Fig. 8.1 denoted as $(M1, M2, M3)$. Some of the properties of these stars are summarized in Table 8.1.

Both spherical and non-spherical perturbations to the stationary solutions are induced by increasing or decreasing the amplitude of the different constituent fields, see Eq. (8.11). In our case of study, $\ell = 1$ and thus, for each configuration $M1, M2, M3$ there are three fields $\phi_{\ell,m}$: $\{\phi_{1,-1}, \phi_{1,0}, \phi_{1,1}\}$. We use the position of sub-index in the models $(M1_{m=-1,m=0,m=1})$ to label the mode (field) that is being perturbed. We use $+$ or $-$ to ascribe an increase ($\epsilon > 0$) or decrease ($\epsilon < 0$) of the amplitude, we use 0 to represent that no perturbation was introduced in that mode ($\epsilon = 0$). In this way, for instance, $M1_{+0-}$ means that $M1$ has been perturbed in the following way: the first scalar field, $\phi_{1,-1}$, has been perturbed with $\epsilon > 0$; the second field $\phi_{1,0}$ has not been perturbed ($\epsilon = 0$), and the third field $\phi_{1,1}$ has been perturbed with $\epsilon < 0$. In summary, we have perturbed $M1, M2, M3$ in the following ways: perturbing all fields with the same amplitude as a test (spher-

Model $M1$ ($\omega/\mu = 0.882$)	ϵ			Collapse
Run	$m=+1$	$m=0$	$m=-1$	
$M1_{000}$	0	0	0	No
$M1_{+++}$	+0.01	+0.01	+0.01	No
$M1_{---}$	−0.01	−0.01	−0.01	No
Model $M2$ ($\omega/\mu = 0.836$)	ϵ			Collapse
$M2_{000}$	0	0	0	No
$M2_{+++}$	+0.01	+0.01	+0.01	Yes
$M2_{---}$	−0.01	−0.01	−0.01	No
Model $M3$ ($\omega/\mu = 0.783$)	ϵ			Collapse
$M3_{000}$	0	0	0	Yes
$M3_{+++}$	+0.01	+0.01	+0.01	Yes
$M3_{---}$	−0.01	−0.01	−0.01	No

Table 8.2: List of simulations performed for the case where all fields are perturbed with the same amplitude (spherical perturbations). These cases are similar to the simulations performed in [101].

ical perturbation), introducing a non-axisymmetric bar-mode perturbation, and finally, we perturbed each constituent field using different amplitudes.

8.4.1 Spherical perturbation test

First, we perform numerical evolutions of the models listed in Table 8.1 with spherical perturbations. We induce perturbations in each field of a ℓ-boson star with all the perturbations having the same amplitude. In this way we guarantee that the spherical symmetry is preserved. This type of perturbations is done in order to compare and validate our results with those found using a spherically symmetric 1D code reported in [101]. While perturbing the initial equilibrium configurations adding perturbations (with a positive or negative value for ϵ) that preserve the spherical symmetry, we find that the configuration that was reported to be stable in Ref. [101] (model $M1$) remains stable in the timescale we reach in the 3D simulations, run $M1_{000}$. The values of the amplitude of the perturbations for these perturbed configurations are reported in Table 8.2 as $M1_{+++}$ and $M1_{---}$, in which we perturb each field adding or subtracting $|\epsilon| = 0.01$ to each mode.

Our results are also consistent with models of ℓ-boson stars that are unstable in spherical symmetry. According to the results in [101], the configuration $M3_{000}$ is unstable in the 1D simulations. When we perturb the amplitudes of the fields adding (run $M3_{+++}$) or subtracting (run $M3_{---}$) the same amount, the configuration collapses or migrates to the stable branch respectively, as described in Table

8.2. We monitor the behaviour of the metric coefficients during the evolution, and, in particular, we use the lapse and the formation of an AH as an indicator of the collapse of the star and the formation of a black hole.

The model $M2$ deserves special mention since it corresponds to

the critical solution: the star with maximum mass. We found that perturbations increasing the amplitude of the field ($\epsilon > 0$, run $M2_{+++}$) make the star collapse whereas perturbations that decrease the amplitude ($\epsilon < 0$, run $M2_{---}$) drive the configuration to a new stable state as described in Table 8.2. These results are consistent with the results reported in [101] for perturbations that increase of decrease the mass of the star.

8.4.2 Non-spherical perturbation: perturbing the energy density

In order to determine whether ℓ-boson stars develop a bar mode instability, we took as initial data a stationary model and modified the energy density in accordance with eq. (8.9). We have performed this analysis for configurations with $\ell = 0$ and $\ell = 1$, both stable against spherical perturbations. In the case $\ell = 0$ we have taken the equilibrium configuration corresponding to $\omega/\mu = 0.937$ and for $\ell = 1$ the configuration with $\omega/\mu = 0.882$, $M1$ in Table. 8.1. By choosing $\kappa = 0.01$, the momenta of inertia I_{xx} and I_{yy} change by less than 0.5% with respect to the equilibrium solution, hence we consider that the induced initial perturbation is small. Then we evolve the perturbed system via the Einstein-N-Klein-Gordon equations and monitor the behaviour of η_z.

In Fig. 8.2 we show η_z as a function of time for perturbed and unperturbed configurations for $\ell = 0$ (top panel) and $\ell = 1$ (bottom panel). For $\ell = 0$, the distortion η_z oscillates around zero for the perturbed case, indicating the star maintains, essentially, the spherical symmetry.

On the other hand, for $\ell = 1$ in the case where the perturbation was included, the initial perturbation induces a small deviation from spherical symmetry therefore η_z acquires a nontrivial value during the evolution. This non-zero value of η_z indicates that the shape of the star deviates from spherical and becomes oblate.

During the evolution time considered ($t \sim 3500$) we did not find any signal of a bar-mode instability for the models considered: no exponential growth in η_z was measured. Most importantly η_z does not grow as it happens for unstable stars [63]. This change in the shape of the $\ell = 1$ configuration, illustrated by $\eta_z \neq 0$, is compared with the case where $M1$ is not perturbed (black solid line). For the unperturbed case, η_z simply oscillates around zero. The conclusion, therefore, is that the perturbed configuration lingers, neither collapsing nor dissipating, thus showing a non-spherical distribution that is either stable or long-lived, without signs of instability. It is worth emphasising the key difference with the $\ell = 0$ case, for which the evolution oscillates around a spherical distribution, in agreement

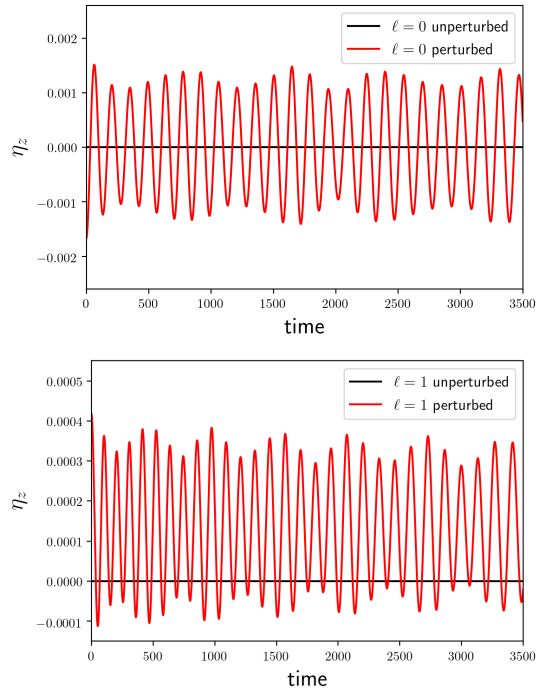

Figure 8.2: Evolution of η_z as a function of time for unperturbed (black solid line) and perturbed density as defined by Eq. (8.9) (red solid line) with $\kappa = 0.01$. Top panel: the unperturbed configuration is a single-field boson star ($\ell = 0$). Bottom panel: the unperturbed configuration is a multi-field boson star ($\ell = 1$). In neither perturbed case has a bar instability been observed. Instead, a long lived departure from spherical symmetry occurs for $\ell = 1$, but not for $\ell = 0$, as long as $\eta_z \neq 0$. In contrast, the unperturbed configurations preserve spherical symmetry as η_z oscillates around zero in both cases.

with the fact that such a distribution is the only equilibrium configuration.

We found that after some time, the stars acquire a small linear momentum due to the numerical error and thus the deviation parameters can not be obtained accurately. Once this becomes noticeable we stop the evolution.

8.4.3 Non-spherical perturbation: perturbing the amplitude of each mode

In this section, we describe the evolutions we have performed implementing non-spherical perturbation by varying the amplitude of each field of the ℓ-boson star.

Model $M1$ ($\omega/\mu = 0.882$)	ϵ			Collapse
Run	$m = +1$	$m = 0$	$m = -1$	
$M1_{+00}$	$+0.01$	0	0	No
$M1_{-00}$	-0.01	0	0	No
$M1_{0+0}$	0	$+0.01$	0	No
$M1_{0-0}$	0	-0.01	0	No
$M1_{00+}$	0	0	$+0.01$	No
$M1_{00-}$	0	0	-0.01	No
$M1_{++0}$	$+0.01$	$+0.01$	0	No
$M1_{+-+}$	$+0.01$	-0.01	$+0.01$	No
$M1_{+0+}$	$+0.01$	0	$+0.01$	No
$M1_{-0+}$	-0.01	0	$+0.01$	No
$M1_{0(-)0}$	0	-0.1	0	No

Table 8.3: List of simulations performed for model $M1$ under the second type of perturbations. The parenthesis indicate a larger amplitude on the perturbations. Notice that gravitational collapse was not observed in any of the simulations.

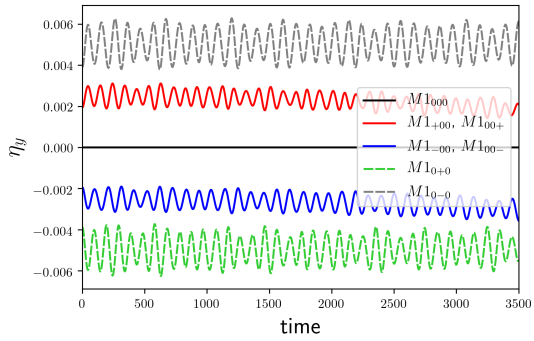

Figure 8.3: Distortion parameter η_y, for model $M1$ for runs shown in Table (8.3) . Departure from spherical symmetry is shown for those configurations that have been perturbed differently in all the three fields $\phi_{1,-1}$, $\phi_{1,0}$ and $\phi_{1,1}$. On the contrary, the configuration $M1_{000}$ has the same perturbation for all the fields (spherical perturbation), and it shows $\eta_y = 0$ at all times.

Non-spherical perturbation of $M1$

In order to illustrate the procedure to perturb the star, let us consider first model $M1$. Different perturbations have been applied to $M1$ and all them are summarised in Table 8.3. Subscripts indicate which fields have been perturbed and if the amplitude is increased by $\epsilon > 0$ (subscript $+$), decreased by $\epsilon < 0$ (subscript $-$) or it has been left without perturbation $\epsilon = 0$ (subscript 0), as described before.

All our evolutions show that $M1$ remains stable without collapsing (none AH was found), independently of the perturbation. Thus, from the results summarised in Table 8.3 we can conclude that the configurations in the stable branch (against spherical perturbations), that is, to the right of configuration $M2$ in Fig. 8.1, are also stable under non-spherical perturbations, against collapse.

Let us now turn to another result that can be extracted by studying the distortion parameters η_z and η_y. For spherical configurations and for those configurations that are spherically perturbed, these are zero. On the other hand, for non-spherical perturbations a small deviation from spherical symmetry is induced. In other words, non-trivial values of η_y are obtained throughout the evolution of $M1$. This behaviour of η_y as a function of time is shown in Fig. 8.3. Indeed, non-zero values of η_y for the evolution of $M1_{+00}, M1_{00,+}, M1_{-00}, M1_{00-}, M1_{0+0}$, and $M1_{0-0}$, are obtained. No instability is observed, but the deformation does not die off either. These long-lived deformed configurations, arising as dynamical solutions of the Einstein-N-Klein-Gordon with three fields with different m are not spherically symmetric. The corresponding perturbations appear to be zero modes, suggesting a larger family of solutions.

As expected, we observe that the equilibrium configuration $M1_{000}$ has $\eta_y = 0$ at all times of the evolution. Besides, we have found that the behaviour of η_y and η_z during the evolution is the same for perturbations in the modes $m = 1$ and $m = -1$ with the same values of ϵ. This suggests that the resulting configurations are axially symmetric.

Finally, we report in Fig. 8.4 the time evolution of the total mass of $M1$ under different spherical and non-spherical perturbations. As expected, the mass of the perturbed configurations decreases or increases when $\epsilon < 0$ or $\epsilon > 0$. Notice, however, the change in mass is the same whether we perturb the $m = -1$ or $m = 1$ modes, for the same the sign of ϵ. This fact supports the assertion that the resulting configurations are axially symmetric.

The total mass of the models decreases with time, showing a small drift, even for the unperturbed solution. We have checked that this drift is due to the numerical error, since it is reduced when the grid resolution is increased (see Appendix A).

Fig. 8.5 displays a series of snapshots of projections in the planes xy and xz of the energy density for the run $M1_{0(-)0}$ (With a large amplitude in the perturbation

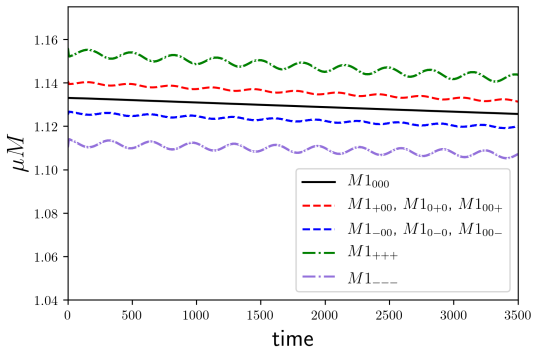

Figure 8.4: Evolution of the mass of the model $M1$ subjected to spherical and non-spherical perturbations listed in Tables 8.2 and 8.3 respectively. The mass, as expected, is increased for those perturbations with $\epsilon > 0$ and decreases when $\epsilon < 0$.

in the mode $m = 0$) . The initial perturbation is introduced in the mode $m = 0$, decreasing the mass of the star and inducing a small deformation. Notice that we have taken the largest perturbation presented in this section (model $M1_{0(-)0}$), so that the deformation can be appreciated in these projections of the energy density. At later times the system evolves and settles down into a configuration without collapsing or exploding. Although the configuration looks almost spherical, the value of η_y at late times is slightly different from zero ($\eta_y \sim 0.05$). We have evolved this configuration for $t \sim 10000$ and remains in the same state not showing any signs of instability, or returning to a ℓ-boson star.

At this point it is important to mention that perturbations in the mode $m = 0$ do not modify the value of the total angular momentum, while perturbations in the modes $m = 1$ or $m = -1$ do. Specifically, $M1_{-00}$ and $M1_{00+}$ ($M1_{+00}$ and $M1_{00-}$) have a positive (negative), non-trivial and constant value of total angular momentum. As we could expect, runs like $M1_{+0+}$ have zero angular momentum. This particular result was also obtained for the perturbations of the models that will be presented below.

Non-spherical perturbation of $M2$ and $M3$

The results of the previous section indicate that those configurations ($M1$) that are stable under spherical perturbations do not show non-spherical growing modes. Furthermore, perturbations to the fields $\phi_{1,-1}$ and $\phi_{1,1}$ applied to those configurations provide evidence for zero modes, producing new equilibrium configurations that are dynamically stable, and have small departures from the spherical configurations.

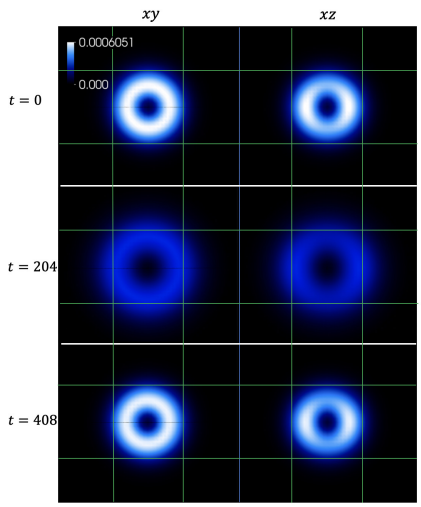

Figure 8.5: Three snapshots of the projection of the rest mass density in two planes. In the second snapshot the star expands and thus the maximum value of the density decreases. In the third snapshot the star returns to its original state. This repetitive behaviour is present during all the evolution time. The mesh represent a box with sides $\frac{1}{2}R_{99}$ of the unperturbed star.

Now we are interested in studying non-spherical perturbations on configurations that might undergo gravitational collapse to a black hole. Those configurations are $M2$ and $M3$. In particular $M2$, as we have mentioned, corresponds to the critical configuration with maximum ADM mass. Configuration $M2$, as is shown in Section 8.4.1 and reported in the literature [101], divides stable from unstable configurations. The latter are those configurations that can collapse into a black hole. We now go one step further and study them under non-spherical perturbations.

The list of perturbation applied to each field of $M2$ is summarised in Table 8.4 and the result of the evolution is reported in the fifth column of the same Table. The results confirm that $M2$ is the configuration that separates stable from unstable configurations. Indeed, as it can be observe in the results of Table 8.4, all those configurations which have perturbations that increased the total mass of the configuration undergo a collapse, while those configurations which have been perturbed and reduced the total mass of the configuration did not collapse to a black hole. In this respect, run $M2_{-0+}$ is of special interest. The perturbation did not change the total mass of the configuration, and the result of their evolution is that it did not collapse.

Finally, we have considered non-spherical perturbations of model $M3$. The results of the evolution of the different models studied are summarised in Table

Model $M2$ ($\omega/\mu = 0.836$)	ϵ			Collapse
Run	$m = +1$	$m = 0$	$m = -1$	
$M2_{+00}$	$+0.01$	0	0	Yes
$M2_{-00}$	-0.01	0	0	No
$M2_{0+0}$	0	$+0.01$	0	Yes
$M2_{0-0}$	0	-0.01	0	No
$M2_{00+}$	0	0	$+0.01$	Yes
$M2_{00-}$	0	0	-0.01	No
$M2_{++0}$	$+0.01$	$+0.01$	0	Yes
$M2_{+-+}$	$+0.01$	-0.01	$+0.01$	Yes
$M2_{+0+}$	$+0.01$	0	$+0.01$	Yes
$M2_{-0+}$	-0.01	0	$+0.01$	No

Table 8.4: List of simulations performed from the model $M2$ under non-spherical perturbations. Those configurations that increased the total mass by the addition of the perturbation did collapse to a black hole. Configurations that did not change the total mass or did not decrease the total mass of the configuration did not collapse.

8.5. This configuration is on the so called unstable branch. The results mimic, to some extent, those observed for $M2$. Perturbations that reduced the total mass of the configuration led to a migration to the stable branch. On the other hand, those that increased the mass of the configuration let to a collapse into a black hole. But a key difference is seen for $M3_{-0+}$. This perturbation did not change the total mass of the configuration, and contrary to $M2_{-0+}$, it did collapse to a black hole. This result, combined with the spherical perturbations mentioned in 8.4.1, further confirms the special status of the maximum mass configuration $M2$: it marks the threshold of unstable configurations of ℓ-boson stars, for both spherical and non-spherical perturbations.

8.5 Discussion and Outlook

In this paper we performed dynamical simulations in the fully non-linear EKG model to investigate the stability of ℓ-boson stars. Unlike previous works we have considered non-spherical perturbations. An expected result is that those configurations known to be unstable under spherical perturbations, are also unstable under more general perturbations. The most interesting question, however, was if the configurations known to be stable under spherical perturbations would remain stable under more general ones. Here, our conclusions are two-fold. Firstly, no growing modes have been measured in our simulations. In this sense ℓ-boson stars are stable against non-spherical perturbations. However, when deformed

Model $M3$ ($\omega/\mu = 0.783$)	ϵ			Collapse
Run	$m=+1$	$m=0$	$m=-1$	
$M3_{+00}$	$+0.01$	0	0	Yes
$M3_{-00}$	-0.01	0	0	No
$M3_{0+0}$	0	$+0.01$	0	Yes
$M3_{0-0}$	0	-0.01	0	No
$M3_{00+}$	0	0	$+0.01$	Yes
$M3_{00-}$	0	0	-0.01	No
$M3_{++0}$	$+0.01$	$+0.01$	0	Yes
$M3_{+-+}$	$+0.01$	-0.01	$+0.01$	Yes
$M3_{+0+}$	$+0.01$	0	$+0.01$	Yes
$M3_{-0+}$	-0.01	0	$+0.01$	Yes

Table 8.5: List of simulations performed form the model $M3$ under non-spherical perturbations. Those configurations that increased the total mass by the addition of the perturbation did collapse to a black hole. Configurations that decreased the total mass of the initial configuration, migrated to the stable branch. The run $M3_{-0+}$ that did not change the total mass did collapse to a black hole.

away from sphericity, ℓ-boson stars do not return to a spherical state. They appear to oscillate around a new (slightly) non spherical state. We take this as evidence that new, multi-field, equilibrium configurations of the Einstein-N-Klein Gordon system exist, which are non-spherical. This conjecture is our second conclusion.

If our conjecture is proven correct, the spherically symmetric ℓ-boson stars are only an enhanced isometry point of a larger family of solutions of the Einstein-N-Klein Gordon. As discussed in the introduction, this is analogous to the Schwarzschild BH being the isometry enhancement point of the Kerr family. It is well known that the Kerr solution brings about qualitatively novel features with respect to the Schwarzschild solution. So it will be quite interesting to understand the novelties brought by the enlarged family of solutions that this work is suggesting.

The conjecture on the existence of these new non-spherical, multi-field configurations can be tested by solving the Einstein-N-Klein Gordon system for static or stationary (*i.e.* spinning) configurations, without assuming spherical symmetry. Research in this direction is already ongoing.

8.6 Appendix of Chap. 8. Code validation

For run $M1_{000}$ we report the time evolution of the mass and violations of the Hamiltonian constraint, with different resolutions, $\{dx,dy,dz\} = 3.2$, $\{dx,dy,dz\} = \sqrt{2}$ 1.6 and $\{dx,dy,dz\} = 1.6$, where dx, dy and dz are the sizes of the coarsest level of refinement

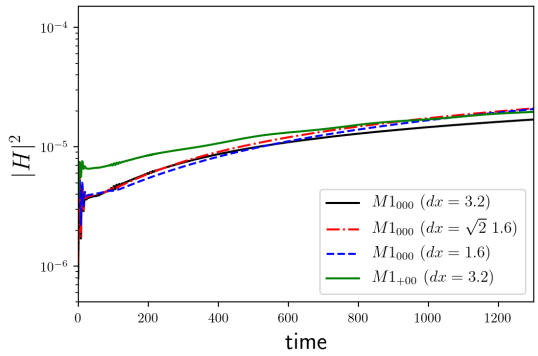

Figure 8.6: Convergence for run $M1_{000}$: Evolution of the L2-norm of the Hamiltonian constraint for three different resolutions rescaled to show fourth order convergence. Green line shows L2-norm of the Hamiltonian constrain for a perturbed run, initially, the violation of the constraint due to the perturbation is evident, as time passes the magnitude of the error is comparable with the error of the unperturbed runs.

The L2-norm of the Hamiltonian constrain, given by $|H|^2 = \sqrt{\frac{\Sigma_{i=1}^{N} H_i^2}{N}}$, where N is the number of points in the grid, is shown in Fig. 8.6. Here we conclude that the constraint equations converge as H reduces when the resolution is increased, the black (solid) and the blue (dashed) line have been multiplied by the factors 4 and 16, showing fourth order convergence. The low resolution (solid line, coarsest grid $dx = 3.2$) corresponds to the one used in all the simulations presented in this work. The L2-norm of H increases with time, however tends to a constant value which approaches zero as $\{dx, dy, dz\} \to 0$.

We plot the mass for run $M1_{000}$. As the resolution is increased the mass converge to a constant value and the overall drift is reduced. In Fig. 8.6 and Fig. 8.7 we have plotted until time equal to 1300, however the ($\{dx, dy, dz\} = 3.2$) simulation extends up to $t \sim 3500$, where the final total mass differs from the initial value by 0.6%.

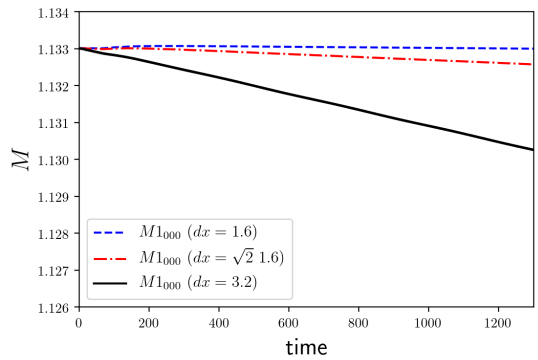

Figure 8.7: Convergence for run $M1_{000}$: Evolution of the mass for three different resolutions.

CHAPTER 9

COLLISIONS[1]

Contents

Fully non-linear numerical evolutions of the Einstein-(multi)–Klein-Gordon equations are performed to study head-on collisions of ℓ-boson stars. Despite being spherically symmetric, ℓ-boson stars have a (hidden) frame of reference, used in defining their individual multipolar fields. To assess the impact of their relative orientation, we perform simulations with different angles between the axes of the two colliding stars. Additionally, two scenarios are considered for the colliding stars: that they are composites of either the same or different scalar fields. Despite some model-specific behaviours, the simulations generically indicate that: 1) the collision of two sufficiently (and equally) massive stars leads to black hole formation; 2) below a certain mass threshold the end

[1]This chapter is extracted with minor revisions from Ref. [212], which was written in collaboration with N. Sanchis-Gual, J. Barranco, A. Bernal, J. C. Degollado, C. Herdeiro, M. Megevand and D. Núñez.

result of the evolution is a bound state of the composite scalar fields, that neither disperses nor collapses into a black hole within the simulation time; 3) this end product (generically) deviates from spherical symmetry and the equipartition of the number of bosonic particles between the different scalar fields composing the initial boson stars is lost, albeit not dramatically. This last observation indicates, albeit without being conclusive, that the end result of these collisions belongs to the previously reported larger family of equilibrium multi-field boson stars, generically non-spherical, and of which ℓ-boson stars are a symmetry enhanced point. We also extract and discuss the waveforms from the collisions studied.

9.1 Introduction

The advent of the gravitational wave (GW) era promises to deliver invaluable information on some of the most prominent challenges in theoretical physics. Amongst these is the nature of the dark Universe. At the time of writing, the LIGO-Virgo and now Kagra (LVK) collaborations released three public catalogues from the first three science runs O1+O2 [213], O3a [214] and O3b [215], reporting 85 events. These events are providing invaluable information about black hole populations [216], constraints on dark energy models [217–220] and even tantalizing hints about the nature of dark matter [95].

LVK searches are performed using “matched filtering”, a data analysis technique to detect characteristic signals in noisy data, which requires a library of theoretical waveform models. In this respect, the issue of degeneracy has been an understated caveat in GW detections. The black hole interpretation seems vindicated within the Kerr black hole paradigm of general relativity. There is, however, a lack of alternative models for which waveforms have been accurately produced, in order to assess whether matched filtering really selects general relativity black holes within a more extensive library of theoretical templates.

Within this empty landscape of alternatives, bosonic stars offer a unique opportunity. First constructed in the late 1960s [44, 45] for massive, complex scalar fields (and more recently for massive complex vector fields [52]) minimally coupled to Einstein’s gravity, these are self-gravitating solitonic solutions that are both compact [54, 221] and dynamically robust in regions of their parameter space [46, 56, 60, 63], forming from fairly generic initial data and reaching the equilibrium state by "gravitational cooling" [47, 61, 63], possibly complemented by GW emission (in non-spherically symmetric evolutions). Thus, they offer an (non-black hole) alternative relativistic two body problem which, unlike neutron stars, need not have electromagnetic counterparts. As a matter of critical importance, the well-posedness/hyperbolicity of the evolutions is under control, and currently available computational infrastructures can be used with fairly minor adaptations,

such as the Einstein Toolkit [14, 204, 222]. This state of affairs contrasts with modified gravity, wherein even promising models may face fundamental issues, such as the breakdown of hyperbolicity, see *e.g* [223]. Thus, one can use bosonic star binaries to produce waveform banks that share features, but also present differences, with respect to those generated by the vanilla black hole binaries of general relativity. In fact, one such recent analysis raised the intriguing possibility that a real GW event [224] could be interpreted as a collision of vector bosonic stars [95], showing, at least as a proof of concept, how such interpretation would lead to the discovery of a fundamental, ultralight dark matter particle.

The simplest bosonic stars arise in single (complex) field models. A realization of the last few years, however, is that there is a wider landscape of bosonic star families when allowing multi-field models. Among these different possibilities, one of the most interesting configurations are the ℓ-boson stars [99], as it has been proved that they are the only stable configuration [104], bestowing them with a central role in the possible scalar field configurations. ℓ-boson stars are spherically symmetric solutions arising in a model with $2\ell+1$ complex scalar fields, wherein the individual fields carry a multipolar structure but the composite object is spherical and static. Note that ℓ-boson stars reduce to standard boson stars in the particular case where $\ell = 0$. Subsequent studies showed these solutions are dynamically robust in regions of the parameter space [101, 102] and also unveiled they can be regarded as part of a wider family of multi-field, multi-frequency bosonic stars [85, 103, 104]. ℓ-boson stars in contrast to $\ell = 0$ regular boson stars have greater compactness and they are hollow in the central region. This empty space becomes larger as ℓ increases as well as their mass and reaches the maximum compactness as $\ell \to \infty$ [85]. The maximum compactness for the ℓ-boson stars almost doubles the maximum compactness pf $\ell = 0$ boson stars. Following this line of thoughts it becomes an interesting problem to evolve ℓ-boson stars in binaries, both to further test their dynamical robustness and to obtain new waveform templates, that enlarge the effort of constructing a vaster library of non-Kerr waveforms. These are precisely the goals of this paper.

In this work we shall study head-on collisions of ℓ-boson stars, as the simplest "binaries" of these objects. Even in this simplest scenario, the multi-field nature of ℓ-boson stars allows more possibilities than when a single field is considered. Firstly, despite being described by a spherically symmetric metric and total energy-momentum tensor, the composite nature of ℓ-boson stars endows the individual fields with a (hidden) frame of reference with respect to which the multipolar structure of the individual fields is defined. Thus, even for head-on collisions starting from rest, there is the additional degree of freedom of misaligning the hidden spin axes of the individual stars. Secondly, since one is entertaining the possibility of many scalar fields, it fits such rationale to allow the ℓ-boson stars

to be composed by the same, or by different, scalar fields. We shall dub the former (latter) scenarios as tackling coherent (incoherent) states. As we shall see, both choices, *i.e.* alignment and coherence, lead to important changes in the dynamics, although some generic trends can also be inferred from the sample of simulations performed.

We have focused on binary ℓ-boson stars with $\ell = 1$, using several initial configurations and evolving them while analysing the spatial distribution of the scalar fields and computing the GW emission. When the individual stars are massive and compact enough, it is found that the remnant is a black hole. However, if the sum of the masses of both stars does not greatly exceed the maximum mass of the corresponding family of solutions, (see Fig. 9.1 below), the collision forms a gravitationally bound scalar field configuration. Whereas in the merger of two standard $\ell = 0$ boson stars some of the final configurations clearly tend towards another $\ell = 0$ boson star [57–59, 62, 195], our results indicate that the merger of two ℓ-boson stars, albeit remaining in a bound state, do not necessarily lead to an ℓ-boson star.

The waveforms generated from the head-on collision of the ℓ-boson stars, like in the usual case of boson stars with $\ell = 0$, present very peculiar features, which make them significantly different from the waveform of a black hole collision, even *nudus oculus*. As we show in the present work, the waveform produced by the head-on collision of ℓ-boson stars has a richer structure depending on the parameters of the initial configuration (such as the relative alignment), which makes a stronger case for the generation of catalogues to be included in the LVK libraries.

This paper is organized as follows. In the next section, we present the main ideas needed to construct ℓ-boson stars, in particular explaining the two different scenarios that shall be considered: when taking two spatially separated lumps composed by the same fields, called coherent states, or when taking two spatially separated lumps composed of different fields, called incoherent states. Next, we describe the numerical implementation of these configurations and in section 9.4 we define the quantities that will be analyzed, together with the GWs during the evolution of the system. We present our results in section 9.5 and conclude with some final remarks. Throughout the paper we use natural units, $c = G = \hbar = 1$.

9.2 Models for ℓ-boson star binaries

A single ℓ-boson star is described by an odd number $\mathcal{N}$ of complex scalar fields, each with a harmonic time dependence, of the form

$$\Phi_{\ell m}(t, r, \vartheta, \varphi) = e^{-i\omega t}\phi_\ell(r)Y_{\ell,m}(\vartheta, \varphi)\,, \tag{9.1}$$

where $Y_{\ell,m}(\vartheta, \varphi)$ are the standard spherical harmonics. Notice that the angular momentum number ℓ for a given solution is fixed and a single star has $\mathcal{N} = 2\ell + 1$

fields, corresponding to each possible value of m within the range $-\ell,\dots 0,\dots,+\ell$. A key ingredient to get a spherically symmetric solution of the Einstein-Klein-Gordon (EKG) system is that the field amplitude $\phi_\ell(r)$ is precisely the same for all m.

We shall be considering models without self-interactions amongst the different scalar fields. These fields, therefore, only see each other via gravity. Still, when considering two stars we may choose that the composing fields of the stars are equal or are different. In this work we shall consider both possibilities. This is reminiscent of the description of coherent and incoherent states in quantum mechanics; for the former case, a macroscopic number of quanta all pile into the same momentum state, being used to describe lasers and superfluids.

Our approach is as follows. The binary system we consider is governed by the EKG theory and the field equations for the metric $g_{\mu\nu}$ are

$$R_{\mu\nu}-\frac{1}{2}g_{\mu\nu}R=8\pi\left(T^{(1)}_{\mu\nu}+T^{(2)}_{\mu\nu}\right):=8\pi T_{\mu\nu}\ , \tag{9.2}$$

where $R_{\mu\nu}$ is the Ricci tensor and $R=g^{\mu\nu}R_{\mu\nu}$. The matter content is given by either one or two sets of $2\ell+1$ complex scalar fields $\Phi_{\ell m}$, each with a stress-energy tensor of the form

$$T^{(i)}_{\mu\nu}=\frac{1}{2}\sum_{m=-\ell}^{\ell}\left[\nabla_\mu\bar{\Phi}^{(i)}_{\ell m}\nabla_\nu\Phi^{(i)}_{\ell m}+\nabla_\mu\Phi^{(i)}_{\ell m}\nabla_\nu\bar{\Phi}^{(i)}_{\ell m}-g_{\mu\nu}\left(\nabla_\alpha\bar{\Phi}^{(i)}_{\ell m}\nabla^\alpha\Phi^{(i)}_{\ell m}+\mu^2\bar{\Phi}^{(i)}_{\ell m}\Phi^{(i)}_{\ell m}\right)\right], \tag{9.3}$$

where $i=1,2$; $\bar{\Phi}_{\ell m}$ denotes the complex conjugate of $\Phi_{\ell m}$ and μ is the mass of the scalar field particle, which we assume is the same for all fields. This assumption amounts to consider that all different scalar fields belong to a larger multiplet.

As expected, each complex scalar field satisfies the Klein-Gordon equation:

$$g^{\mu\nu}\nabla_\mu\nabla_\nu\Phi^{(i)}_{\ell m}-\mu^2\Phi^{(i)}_{\ell m}=0\ . \tag{9.4}$$

9.2.1 Coherent and incoherent states

As mentioned above, in this work we consider two possible systems. We shall refer to the first system as coherent state and to the second as incoherent state. The functional description of both states is as follows.

i) Coherent states. For this case, both ℓ-boson stars are made up of the same set of scalar fields. Such a scenario is modeled with a single set of fields, initially accumulated at two (essentially) disjoint spatial regions, that is:

$$\Phi^{(1)}_{\ell m}\neq 0\ ,\qquad \text{and}\qquad \Phi^{(2)}_{\ell m}=0\ ,\qquad \forall\quad m\ . \tag{9.5}$$

For this system there are $2\ell+1$ independent fields to describe the binary. In this scenario a single set of fields fills up spacetime, which can nonetheless clump at two different locations, forming two ℓ-boson stars centered at different positions.

ii) Incoherent states. Here, each star is composed by a set of $2\ell+1$ fields, being different for each star. This requires to turn on both sets of fields discussed

$$\Phi^{(1)}_{\ell m} \neq 0\,, \qquad \text{and} \qquad \Phi^{(2)}_{\ell m} \neq 0\,, \qquad \forall \quad m\,. \tag{9.6}$$

Consequently, there are $2(2\ell+1)$ independent fields to describe the binary. Notice, however, that in both systems the interaction between any of the fields is only through gravity.

9.3 Numerical implementation

In order to describe the dynamics of the binary it becomes necessary to evolve $2\ell+1$ complex fields for the coherent system and $2(2\ell+1)$ complex fields for the incoherent system. For concreteness, we focus in this work on the simplest non-trivial $\ell=1$ case yielding 3 fields for coherent states and 6 for incoherent states.

9.3.1 Initial data

Initial data for the binary system are obtained using a superposition of two isolated ℓ-boson stars. The construction of single isolated ℓ-boson stars is described in detail in Ref. [99]; here we outline a brief description of the procedure.

The starting point is to consider a static and spherically symmetric spacetime of the form

$$ds^2 = -\alpha^2 dt^2 + \gamma_{jk} dx^j dx^k = -\alpha^2 dt^2 + a^2 dr^2 + r^2 d\Omega^2\,, \tag{9.7}$$

where α and a are functions of r, $d\Omega^2$ is the line element on the unit 2-sphere and the scalar fields that compose the ℓ-boson stars have a harmonic time dependence given by (9.1). According to this assumptions it has been shown in [99] that even though the scalar field oscillates in time the stress-energy tensor is time independent and the EKG equations yield static solutions that are described by the following set of ordinary differential equations:

$$\phi_\ell'' = -\phi_\ell'\left(\frac{2}{r}+\frac{\alpha'}{\alpha}-\frac{a'}{2a}\right)+a\phi_\ell\left(\mu^2+\frac{\ell(\ell+1)}{r^2}-\frac{\omega^2}{\alpha^2}\right), \tag{9.8}$$

$$\frac{a'}{a} = \frac{(1-a)}{r}+4\pi r a\left[\frac{(\phi_\ell')^2}{a}+\phi_\ell^2\left(\mu^2+\frac{\ell(\ell+1)}{r^2}+\frac{\omega^2}{\alpha^2}\right)\right], \tag{9.9}$$

$$\frac{\alpha'}{\alpha} = \frac{(a-1)}{r}+\frac{a'}{2a}-4\pi r a\phi_\ell^2\left(\mu^2+\frac{\ell(\ell+1)}{r^2}\right), \tag{9.10}$$

where a prime denotes derivative with respect to r. By studying the Klein-Gordon equation close the origin $r=0$ one finds that the scalar field behaves as $\phi_\ell \sim \phi_0 r^\ell$.

For a given value of ϕ_0, and demanding that the scalar field has an exponential decay and the metric is Minkowski at infinity, the EKG system becomes a non-linear eigenvalue problem for the frequency ω.

The equilibrium configurations are found by integrating numerically Eqs. (9.8)-(9.10), considering appropriate boundary conditions, by means of a shooting method using the frequency ω as the shooting parameter. The solutions are identified by the value of ω, although for some ranges of ω there may be more than one solution, defining different branches –see Fig. 9.1 (left).

ℓ-boson stars share many features with the single field $\ell = 0$ boson stars. Both exist only for a limited range of frequencies and achieve a maximum Arnowitt-Deser-Misner (ADM) mass. Fig. 9.1 (left) displays the mass of ℓ-boson stars versus ω. The maximum mass solution separates stable from unstable configurations as described in [102]. In this work we shall only consider configurations in the stable branch. More concretely, the stars we shall use as initial data for the evolution below are marked with a box on the existence curve in Fig. 9.1. We define the boundary of the star as the radius of the spherical surface that encloses 99% of the mass; this radius is referred to as R_{99} and it is displayed for the solutions in Fig. 9.1 (right). We define the compactness of the stars as $\mathscr{C} := M/R_{99}$ and it is displayed as an inset in the same panel. In order to use the infrastructure provided by the Einstein Toolkit we transform the solutions to the usual Cartesian coordinates, $x^\mu = (t, r, \vartheta, \varphi) \to x^\mu = (t, x, y, z)$ as

$$x = r\cos\varphi\sin\vartheta\,, \qquad y = r\sin\varphi\sin\vartheta\,, \qquad z = r\cos\vartheta\,. \tag{9.11}$$

In our present investigation we also include configurations that involve an intermediate rotation in the angles to describe a relative misalignment between the stars, as already discussed above and described in detail below. The initial data for the binaries used in this work are obtained by a linear superposition of the isolated solutions of two stars given by the spatial metric and a set of scalar fields $\{\gamma^{(-)}_{jk}, \Phi^{(-)}_{\ell m}\}$ and $\{\gamma^{(+)}_{jk}, \Phi^{(+)}_{\ell m}\}$ for star 1 and star 2, respectively. We shall consider the stars are centered at $(x_c, 0, 0)$ and $(-x_c, 0, 0)$. We also consider the stars to be initially at rest (at $t = 0$).

In this work we restrict our attention to ground state solutions, for which the amplitudes $\Phi_{\ell m}$ have no nodes. These are the solutions exhibited in Fig. 9.1.

We take as initial data for the spatial metric the superposition [57–59, 62, 195, 225]:

$$\gamma_{jk} = \gamma^{(+)}_{jk}(x - x_c, y, z) + \gamma^{(-)}_{jk}(x + x_c, y, z) - \hat{\gamma}_{jk}(x, y, z). \tag{9.12}$$

where $\hat{\gamma}_{\mu\nu}$ is the flat spatial metric. For the scalar fields we need to distinguish between the two systems presented above. For coherent states we construct the field as

$$\Phi^{(1)}_m(t = 0, x, y, z) = \Phi^{(+)}_m(x - x_c, y, z) + \Phi^{(-)}_m(x + x_c, y, z)\,, \tag{9.13}$$

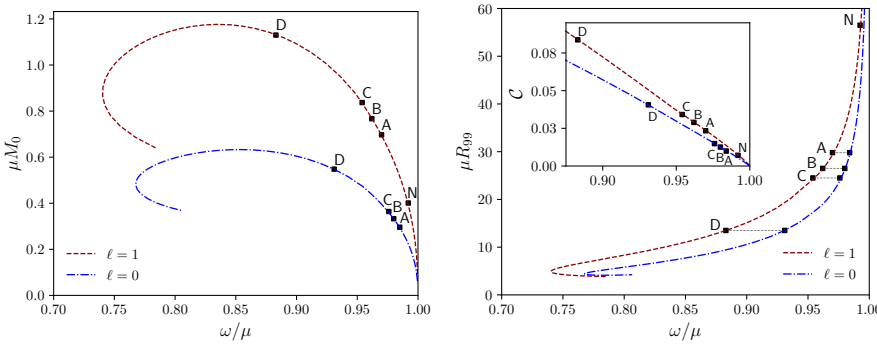

Figure 9.1: ADM mass (left) and radius (right) *vs*. frequency for static ℓ-boson stars with $\ell = 0, 1$. The maximal value of the boson star mass for $\ell = 0$ and $\ell = 1$ is $\mu M_0 = 0.63$ and $\mu M_0 = 1.18$ respectively. The black squares correspond to the solutions used in the head-on collision analysis. In the inset of the right plot the compactness is shown as a function of the frequency.

and $\Phi_m^{(2)}(t,x,y,z) = 0$. Whereas for incoherent states, the field is constructed as

$$\Phi_m^{(1)}(t=0,x,y,z) = \Phi_m^{(+)}(x-x_c,y,z)\,,$$
$$\Phi_m^{(2)}(t=0,x,y,z) = \Phi_m^{(-)}(x+x_c,y,z)\,. \tag{9.14}$$

Due to the nonlinearity of Einstein equations these initial data introduce constraint violations. How this effect has been tracked and controlled throughout the simulations is discussed in Appendix 9.7.

By means of the transformation (9.11), the stress-energy tensor of each star is defined with respect to a Cartesian frame (x,y,z). For the initial data, instead of taking the spherical harmonics of each star defined with respect to the same Cartesian frame, we may consider a relative misalignment of the two corresponding Cartesian frames, by performing a rigid rotation. This allows a more general scenario, in which the stars have arbitrary initial orientations. As we shall see, this has an interesting impact on the dynamics during the merger and in the resulting configuration.

In order to model such non aligned stars we define an intermediate set of coordinates $x' = r\cos\varphi\sin\vartheta$, $y' = r\sin\varphi\sin\vartheta$, $z' = r\cos\vartheta$, and perform a transformation of the form $\mathbf{x} = R_i(\delta)\mathbf{x}'$, where $i = x,y,z$ are the Einstein Toolkit Cartesian coordinates and $R_i(\delta)$ is the rotation matrix for an angle δ around the i-axis. The effect of the rotations $R_z(\pi)$, $R_z(\pi/2)$ and $R_y(\pi)$ can be visualized in Fig. 9.2.

9.3.2 Evolution Scheme

Our numerical simulations are performed using the open source Einstein Toolkit infrastructure [14]. The Einstein equations are integrated in time using the

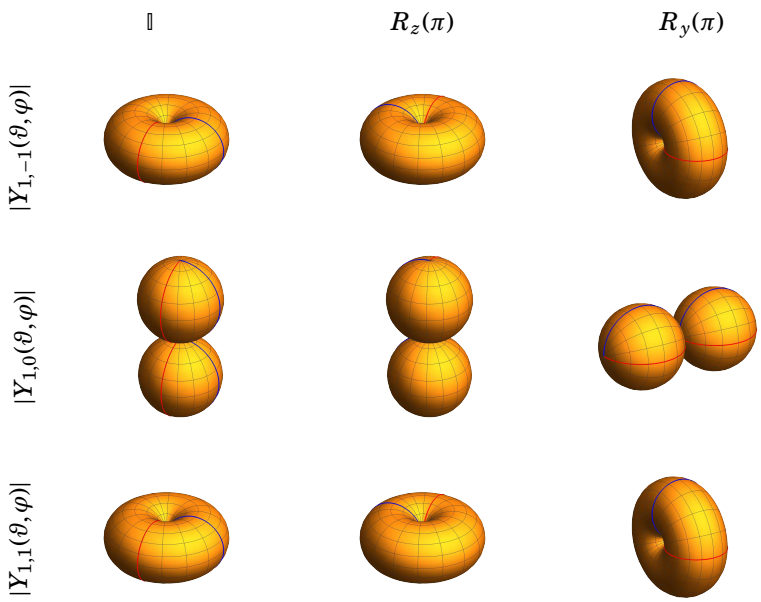

Figure 9.2: Amplitude of spherical harmonics for the modes $m = -1$, $m = 0$, $m = 1$, that compose a boson star with $\ell = 1$. The first column is taken as a reference for the usual alignment; the second column shows the effect of a rotation $R_z(\pi)$; and the third column represents a rotation $R_y(\pi)$. As a reference, we have drawn a a red and a blue line on the surfaces. This is particularly useful when comparing the first two columns, which would otherwise look identical.

Baumgarte-Shapiro-Shibata-Nakamura (BSSN) formulation [210]. We use the Method of Lines of the MoL thorn to solve the equations, via a fourth order Runge-Kutta scheme provided by the McLachlan thorn [211]. The scalar field evolution code has been recently employed to study the stability of ℓ-boson stars [103] and it is described in more detail in that reference.

All the evolutions were made using the 1+log time slicing condition for the lapse α, and the *Gamma-driver* condition for the shift β^i [10]. We have used the thorn AHFinder [209] to follow the formation of an apparent horizon (AH) during the evolution. We have also monitored the Hamiltonian and momentum constraints [13] to check the convergence during the evolution.

The numerical grid consists of nested cubes with six refinement levels and it is handled using the fixed mesh refinement grid hierarchy included in the Carpet arrangements.

In all simulations the stars have their centers placed at $\mu x_c = 25$. The computational domain consists of a box with $\mu x_{\rm max} = 500 = \mu y_{\rm max} = \mu z_{\rm max}$, with a grid structure of six refinement levels. The waveform extraction is made at $\mu r = 100, 120$. The spatial domain of the refinement levels is $\{500, 50, 50, 25, 25, 10\}$. We set the resolution on the finest level to $\mu\{\Delta x, \Delta y, \Delta z\} = 0.3125$. This corresponds to at least 86 points across the initial stars' diameter (defined as $2R_{99}$). The choice of a fixed mesh refinement is mainly motivated by simplicity. The last refinement level that do not contain the stars is included in order to have enough resolution in case a black hole forms. Refinement levels of the grid can produce reflections. However, we do not see any significant impact of the crossing of the mesh boundaries on the dynamics and on the determination of the different quantities (mass, particle number, Hamiltonian constraint). The Cartesian grid can induce a $m = 4$ perturbation (see, for instance, [226, 227]).

9.4 Head-on Collision Dynamics

Once we have constructed the initial data, we allow the systems to evolve freely while monitoring the Hamiltonian and momentum constraints to check the accuracy of the results. As described above, both the evolution and the number of scalar fields are different depending on the system. For the coherent states we evolve 3 complex fields whereas for the incoherent states we evolve 6 fields. We have found that the main differences between the two systems occur near the plunge and this is reflected in the emitted GW signal and in the posterior outcome of the plunge. We quantify the differences using some analysis quantities, such as the mass of the final configuration, the number of particles, and the GW signal.

9.4.1 Analysis Quantities

Starting from the static superposition initial data, the stars approach each other and eventually collide. In some of the scenarios we have established that the final object after the merger is a black hole. To diagnose its appearance in the evolution we use the AHFinder thorn and then compute the mass of the black hole through the apparent horizon area A, using the relation $M_{BH} = \sqrt{A}/16\pi$, which is valid for a Schwarzschild black hole. The use of the Schwarzschild relation relies on no-hair theorems for static spherically symmetric black holes, ruling out final equilibrium configurations with scalar hair, even with a harmonic time dependence. Such no-hair theorems are, however, circumvented for spinning black holes [203].

We focus primarily on the configurations for which the end state has no horizon and the rest mass density is non zero. For the final time reached in our evolution, the final remnant is a localized, perturbed distribution of the different complex scalar fields. However, it is not possible to determine whether that object corresponds to an ℓ-boson star. We describe some of its properties in the next sections.

For the total gravitational mass of localized solutions we use the Komar integral.

$$M = -\int_{\Sigma} \sqrt{\gamma} d^3x \, \alpha (2T^t{}_t - T^{\mu}{}_{\mu}) \,, \tag{9.15}$$

where Σ is a spacelike slice extending up to spatial infinity, γ is the determinant of the 3-metric induced on that slice and α is the lapse function. To describe the end state of the collision we compute the Noether charge associated with the total bosonic number of particles N, which is defined as

$$N = \int_{\Sigma} \sqrt{\gamma} d^3x \, \alpha \, g^{0\mu} j^{(i)}_{\mu} \,, \tag{9.16}$$

where $j^{(i)}_{\mu} = \sum_m \frac{i}{2}(\bar{\Phi}^{(i)}_m \nabla_\mu \Phi^{(i)}_m - \Phi^{(i)}_m \nabla_\mu \bar{\Phi}^{(i)}_m)$. This conserved current is associated with the global invariance of the theory under the action of a $U(1)$ group for each field. We will use this quantity to classify the remnant of the merger. Note that the Noether charge can also be computed for *each* field. The integrals for the Komar mass (9.15) and the number of particles (9.16) are performed in the entire numerical grid on each time step.

We monitor the energy density of matter as $\rho = n^\mu n^\nu T_{\mu\nu}$ during the evolution as a measure of the energy left after the collision, where n^μ is the unitary normal vector to Σ.

Furthermore, in order to determine the deviations from spherical symmetry of the post merger configuration, we compute the moments of inertia I_{xx}, I_{yy} and I_{zz} defined by

$$I_{x^i x^i} = \int_{\Sigma} \sqrt{\gamma} d^3x \, \alpha \, \rho (r^2 - {x^i}^2) \,. \tag{9.17}$$

9.4.2 Gravitational Waves

Gravitational radiation is extracted from the numerical simulations by computing the Newman-Penrose scalar $\Psi_4 = C_{\alpha\beta\gamma\delta}k^\alpha m^\beta k^\delta m^\gamma$, where $C_{\alpha\beta\gamma\delta}$ is the Weyl tensor and k and m are two vectors of the null Kinnersley tetrad [228, 229]. Far from the source Ψ_4 represents an outward propagating wave and has been used as a measure of the gravitational radiation emitted during the merger of compact objects. In order to analyze the structure of the radiated waves it is convenient to decompose the signal in -2 spin weighted spherical harmonics as

$$\Psi_4(t,r,\vartheta,\varphi) = \sum_{l,k} \Psi_4^{l,k}(t,r)\,{}_{-2}Y_{l,k}(\vartheta,\varphi)\,. \tag{9.18}$$

According to the *peeling theorem* the leading order decay of Ψ_4 is $1/r$ [66]. We use this fact to check the accuracy in the computation of the gravitational waveforms. Our description will focus directly on the strongly dominant component $l = 2$, $k = 2$.

9.5 Results

We have investigated five different cases of the ℓ-boson star datasets corresponding to different values of compactness. All the initial configurations correspond to two stars of the same type, localized on the stable branch, and with total mass (sum of the two stars' mass) that is *larger* than the maximal mass of the model. The stars have radii (as defined before) ranging from $\mu R_{99} = 56.5$ (model N), to $\mu R_{99} = 13.5$ (model D), corresponding to a compactness ranging from $\mathscr{C} = 0.0074$ to $\mathscr{C} = 0.0838$, respectively. In this section, we extensively discuss the dynamics for the various cases.

The physical attributes of the initial data and some properties of the end state of the collisions are summarized in Table 9.1 (for coherent states) and Table 9.2 (for incoherent states). Note that the properties of the initial data coincide in both tables, but not the end state. The models CHl1N and INl1N that appear in both tables will appear only on the analyzes related to the study of the final state. Concerning the initial data the tables show the typical size R_{99}, the frequency, the Komar mass of each star M_0, the number of particles in one of the fields of each star (*i.e.* 1/3 of the total number of particles of each star, as described in Appendix 9.7) and the compactness.

We define the time of collision t_c, as the time at which the spheres given by R_{99} of each star intersect. Furthermore, in order to give a simple estimation of the object's size after the merger, we still use the aforementioned definition of R_{99} as the radius of a sphere containing 99% of the total mass, even when the object is not spherically symmetric. The center of such sphere is set at the center of mass, $x = y = z = 0$.

Coh.	$\ell = 1$							
Model	μR_{99}	ω/μ	μM_0	$\mu^2 N_0$	$\mathscr{C}$	Rem.	$\mu R \sim$	μt_c
CHl1N	56.5	0.990	0.418	0.419	0.0074	BS	-	0
CHl1A	31.5	0.970	0.697	0.703	0.0221	BS	24	0
CHl1B	27.5	0.962	0.775	0.784	0.0282	BS	22	70
CHl1C	24.7	0.954	0.837	0.849	0.0391	BH	$\mu r_{\rm AH} = 2.1$	150
CHl1D	13.5	0.883	1.13	1.17	0.0838	BH	$\mu r_{\rm AH} = 3.4$	240

Table 9.1: Coherent cases for $\ell = 1$. R_{99} is the radius that contains 99% of the mass of the star. ω is the frequency, M_0 is the mass of each star, N_0 is the number of particles of each star and $\mathscr{C}$ is the compactness. The end state of the simulation can be a localized boson configuration (BS) or a black hole (BH). R is the radius that encloses 99% of the mass for scalar field remnant at $\mu t = 2500$ while for black holes it labels the radius of the apparent horizon.

Incoh.	$\ell = 1$							
Model	μR_{99}	ω/μ	μM_0	$\mu^2 N_0$	$\mathscr{C}$	Rem.	$\mu R \sim$	μt_c
INl1N	56.5	0.990	0.418	0.419	0.0074	BS	-	0
INl1A	31.5	0.970	0.697	0.703	0.0221	BS	30	0
INl1B	27.5	0.962	0.775	0.784	0.0282	BS	23	0
INl1C	24.7	0.954	0.837	0.849	0.0391	BH	$\mu r_{\rm AH} = 2.2$	0
INl1D	13.5	0.883	1.13	1.17	0.0838	BH	$\mu r_{\rm AH} = 3.6$	230

Table 9.2: Same as Table 9.1 for incoherent states.

9.5.1 Aligned stars

As discussed above, ℓ-boson stars are spherically symmetric at the level of the total energy-momentum tensor but have an internal frame of reference with respect to the different modes. The phrase "aligned stars" refers to both stars having the same orientation. The properties of the remnants are presented in the last columns of Table 9.1 for coherent states and the last columns of Table 9.2 for incoherent states. In particular, the mass of the merger remnant is computed using the Komar integral (9.15). Also, some snapshots of the scalar field energy density ρ, during the coalescence are displayed in Fig. 9.3 and 9.4. Fig. 9.3 exhibits the evolution of a coherent state (model CHl1B) whereas Fig. 9.4 exhibits the evolution of an incoherent state (model INl1B).

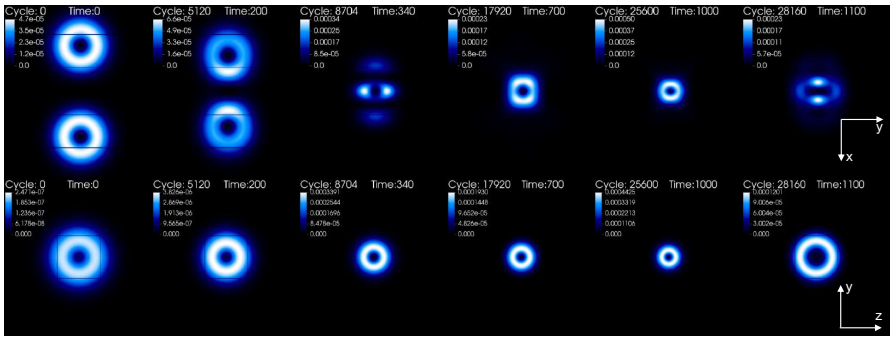

Figure 9.3: Aligned evolutions of a coherent state. Snapshots of the scalar field energy density, ρ/μ^2, for model CHl1B on the $z = 0$ (top) and $x = 0$ (bottom) planes. The maximum density of the final configuration for these models is one order of magnitude larger than the progenitors. Time is given in units of the scalar field mass, μ. Cycle refers to the iteration number.

Despite the fact that in all cases the initial mass of the system is above the maximal mass of the model, we observe two qualitatively distinct behaviours. For the most massive and compact models (C and D) a black hole is formed. But for the less compact models (A and B) neither a black hole forms during the simulation time, nor the field disperses away after the collision. In such cases, a bound scalar field configuration remains after the merger, albeit the system is still evolving at the end of the simulation. Whereas one cannot state with certainty the final outcome of the system, the results suggest that the system does tend to an equilibrium lump of scalar fields. This is an asymptotic process, in which the gravitational cooling mechanism plays a key role to allow relaxation, by slowly decreasing the mass of the system. This slow mass ejection can be observed in Fig. 9.5, where we plot the total mass for models CHl1A, CHl1B, and INl1A, INl1B as a

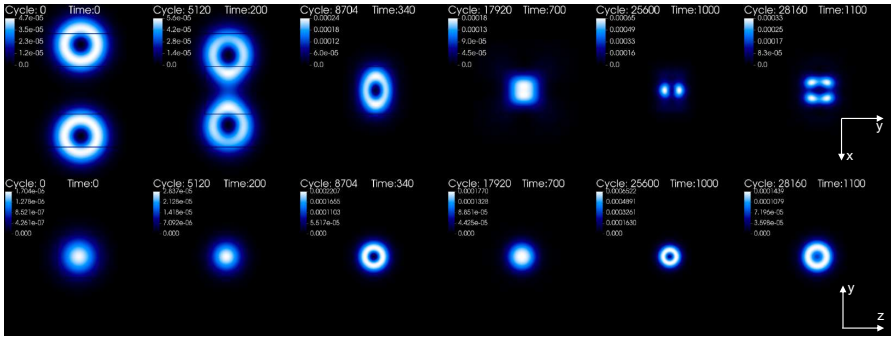

Figure 9.4: Aligned evolutions of an incoherent state. Snapshots of the scalar field energy density, ρ/μ^2, for model INl1B on the $z = 0$ (top) and $x = 0$ (bottom) planes. The maximum density of the final configuration for these models is one order of magnitude larger than the progenitors.

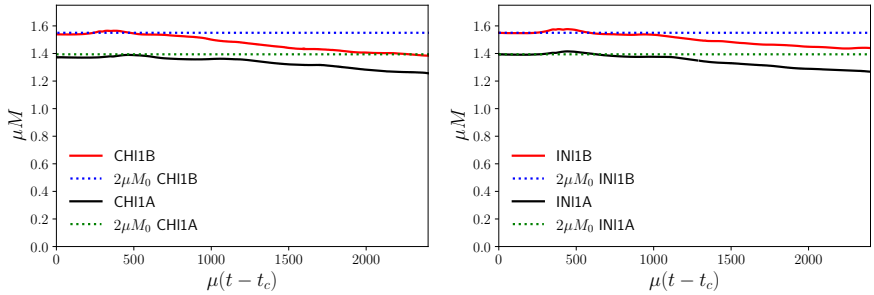

Figure 9.5: Aligned evolutions. Collision remnant mass, for coherent states, models CH1A and CH1B (left) and for incoherent states, models IN1A and IN1B (right).

function of time after the merger. The horizontal dotted lines indicate the value of twice the initial mass of each star. From Figs. 9.3 and 9.4 one can observe that the early phase of the encounter is qualitatively similar for both states; but once the objects make contact, the dynamics becomes complex and model dependent. Nonetheless, we observe the same separation between black hole formation and scalar remnant formation, regardless of the states being coherent or incoherent. The natural question is: what is the system evolving towards, when no black hole forms? In particular, since ℓ-boson stars involve *precisely* equal amplitudes of the scalar fields involved, these collisions test how *fine-tuned* these configurations are, and if such a destructive process readily creates an asymmetry between the different fields.

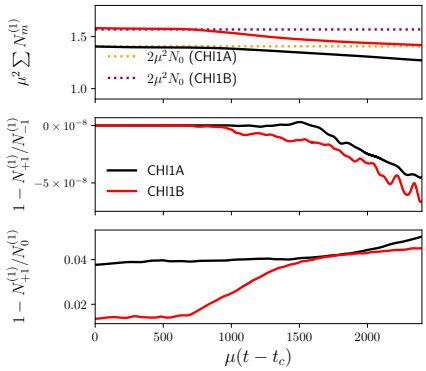

Figure 9.6: Aligned evolutions. (Top) Total number of particles of the remnant of the merger of coherent states CH1A, CH1B. The dotted lines represent twice the initial number of particles present in the binary. (Middle) Ratio between the number of particles associated to the fields $\Phi_m^{(1)}$ with $m = +1$ and $m = -1$. It remains constant at unity. (Bottom) Ratio between the number of particles associated to the fields $\Phi_m^{(1)}$ with $m = +1$ and $m = 0$. At $t = 0$ this quantity is not exactly unity, this is effect of the superposition and appears only in this (coherent) case. During the coalescence a small percentage of their initial value is lost. There is no leaking or exchange of particles of individual fields during the evolution.

To tackle this question one may look at the Noether charge, or particle number, in each field. First, we observe that (as discussed in Appendix 9.7) for a single ℓ-boson star the total number of particles, N, is equally distributed amongst each field. Denoting the Noether charge of each field as N_m, then $N_m = \frac{N}{2\ell+1}$. Thus, we can investigate if such equipartition of the Noether charge remains after the collision. To this end we have computed the time evolution of the number of particles associated to each scalar field. This is displayed for the coherent models CHl1A, CHl1B in Fig. 9.6 and for the incoherent models INl1A, INl1B in Fig. 9.7. One observes that, independently of the state, after the merger there is a monotonic loss of Noether charge, consistent with the gravitational cooling process. Moreover, this scalar field leaking is rather democratic; the equipartition between the $m \pm 1$ modes is kept to high accuracy, and the relative difference between the $m = 0$ and $m = \pm 1$ modes is kept to a few percent. Thus, none of the individual Noether charges (corresponding to the individual fields) suffers dramatic preferential losses, even though there is a slight suppression of the $m = \pm 1$ modes with respect to the $m = 0$ mode.

To gain further insight into the post-merger dynamics, in Fig. 9.8 we have looked at the spatial distribution of the Noether charge during the evolution for model CHl1B. One observes that the $m = 0$ field keeps its morphology throughout the evolution. The dynamics arises from the $m = \pm 1$ modes, which yield a non-

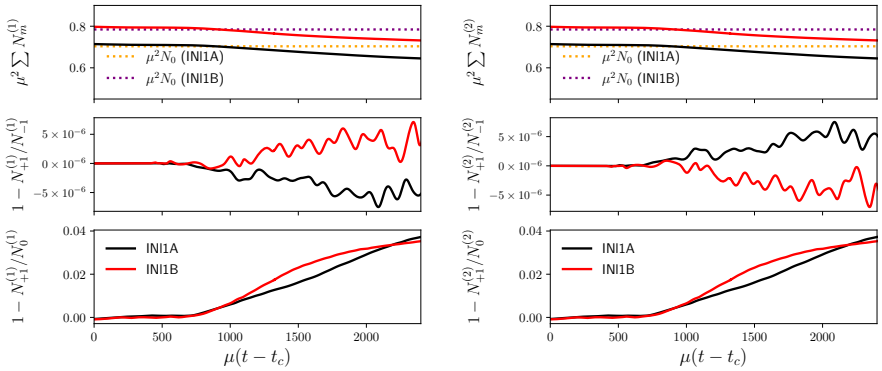

Figure 9.7: Same as Fig. 9.6, but now for incoherent states INI1A and INI1B.

trivial dynamics as the two lumps become superimposed, in particular altering their morphology. This can be corroborated in the left panel of Fig. 9.9, where a difference can be observed between the moments of inertia I_{xx} and $I_{yy} \approx I_{zz}$ after the collision. In the incoherent case, the asymmetry is also evident, as can be seen in the right panel of Fig. 9.9. In both cases a difference between I_{xx} and I_{yy}, I_{zz} remains after $\mu t = 2500$. The above analysis is consistent with the remnants be-

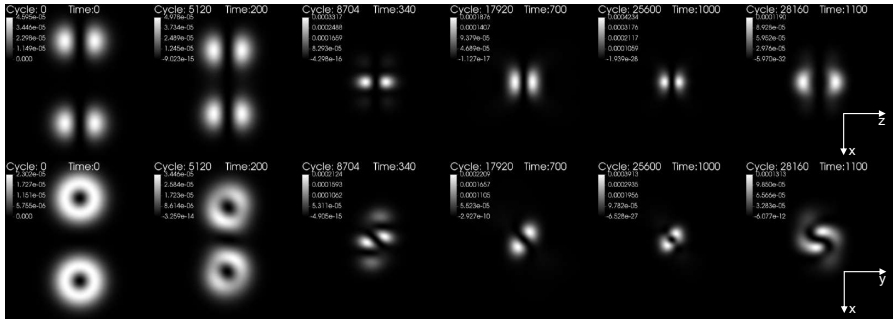

Figure 9.8: Aligned evolutions. Individual currents j_m/μ for model CHl1B. Top panel: $m = 0$ in the $y = 0$ plane. Bottom panel: $m = +1$ in the $z = 0$ plane.

ing undergoing a relaxation process towards an equilibrium configuration which is a multi-field, but not necessarily spherically symmetric, boson star [103, 104]. In particular, for the coherent state, it could be close to an ℓ-boson star, by virtue of the evolution of the moment of inertia, Fig. 9.9 (left panel). See also [59, 113] for the discussion of multistate boson stars in the context of the standard $\ell = 0$ boson stars.

We also look at the evolution of the oscillation frequency of the scalar field(s).

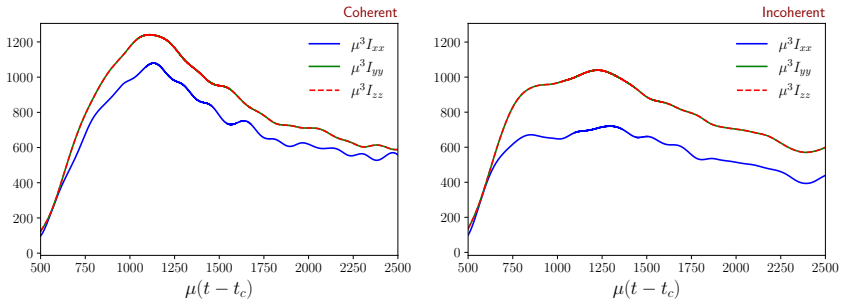

Figure 9.9: Aligned evolutions. Moments of inertia of the post merger configuration as defined in Eq. (9.17) for the models CHl1B (left panel) and INl1B (right panel). Note that the curves of I_{yy} and I_{zz} coincide perfectly in both cases. In the incoherent case, the configuration does not seem to tend to a spherically symmetric distribution of scalar field. Despite the fact that the moments of inertia used in Eq. 4.3 are gauge dependent they represent a good indicator of the presence of nonlinear stability, as has been described in [207].

During the merger process, this frequency changes, which can be investigated by performing a spectral analysis. To this end we have evaluated the discrete Fourier transform (DFT) in time of each scalar field component, $m = -1$, 0 and 1. For more accuracy, we have actually evaluated the DFT at five different points and then calculated the average. Figure 9.10 shows the DFT for the case CHl1B. We notice

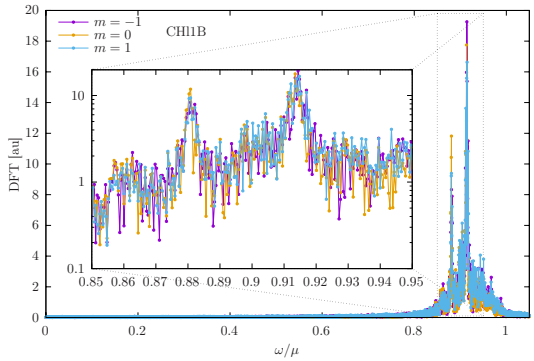

Figure 9.10: DFT in arbitrary units (au) *vs*. frequency. The inner figure shows a zoom-in of he most relevant region in logarithmic scale.

that more than one frequency peak arises, correspond to several bound modes with $\omega < \mu$. Moreover, at least up to the resolution we could achieve, the spectra of the three m components coincide, not only in the peaks locations, but also in

their amplitude. From this viewpoint, therefore, the different modes remain in synchrony, as for the spectrum of the equilibrium states, the ℓ-boson stars. The key difference is, however, that the ℓ-boson stars spectra would only show a single peak.

To better resolve the excited modes, one would have to increase the frequency resolution. This resolution, however, is proportional to the inverse of the evolution time, which implies a high computational cost to improve the frequency resolution. In fact, the case shown here was run up to $\mu t = 14231$, a much longer evolution than for every other model in this work. For this reason we have not considered the spectrum of the other models.

Let us now turn our attention to the GWs emission. In Fig. 9.11 we show the real part of the dominant quadrupolar ($l = 2$, $k = 2$) mode of the Newman-Penrose scalar Ψ_4 as a function of time for both coherent states listed in Table 9.1 and for incoherent sates listed in Table 9.2. The signal is extracted at $\mu r_{\rm ext} = 100$ and we have scaled the amplitude with a factor r to better capture the asymptotic behaviour. The horizontal axis has been shifted as $t \to t - r_{\rm ext}$. For models CHl1A, INl1A with relatively low compactness ($\mathscr{C} = 0.0221$) the GWs signal display some differences between the two. This differences are still visible for models with larger compactness CHl1B and INl1B ($\mathscr{C} = 0.0282$). But for models CHl1C and INl1C the final remnant collapses and the differences in the signal are almost negligible. The waveform indeed resembles the signal of the collision of two black holes. Finally for the most compact binary CHl1D and INl1D, the final product of the merger forms a black hole and the waveforms are identical for both states.

To quantify the differences between waveforms as well as the similarities with the head-on collision of black holes, mentioned in previous statements, we perform the following pair of analyses. First, we calculate the Fourier transform of Ψ_4 to obtain the frequencies of the gravitational signal for the different models. The results are shown in Fig. 9.12, from which it can be confirmed that the main differences in the signal occur in relation to the compactness of the stars; the peak frequency increases by a factor of 4 between model A and C, whether the superposition is coherent or incoherent. Second, we compute the difference between the collapsing models, CHl1C, CHl1D, INl1C and INl1D. To this end, we compare in each case with the gravitational signal from a head-on collision of equal mass black holes hole with the same total mass as the boson star system. In Fig. 9.13 these gravitational waveforms are shown. The more compact model, CHl1D overlaps better with the black hole signal, in particular after the collapse, at the ringdown phase. For the model CHl1C the GW signal differentiates from the black hole signal qualitatively and quantitatively at the first stage, however it matches roughly the frequency and phase of the black hole collision at ringdown. The model CHl1C is close to the BH/BS remnant limit (see Table 9.2), it involves

more complex dynamics before collapse, which is imprinted in the GW at early times.

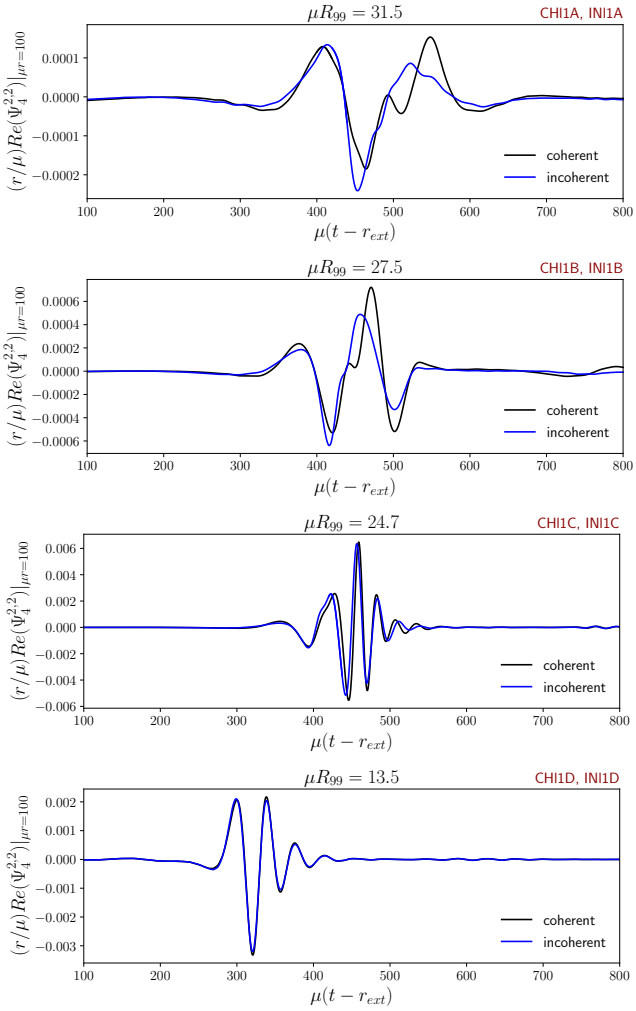

Figure 9.11: Waveforms for $\ell = 1$ binaries described in Table 9.1 and Table 9.2. The extraction radius is $\mu r_{\rm ext} = 100$.

The more compact the binary, the larger the amplitude of the gravitational waveform; for the most compact objects the amplitude is almost one order of magnitude larger than for their less compact counterparts. This result applies for both coherent and incoherent states. This phenomenon is related with the size and geometry of the binary. For ℓ-boson stars the maximum energy density is not located at the geometrical center of the star; the shape of these objects is more like

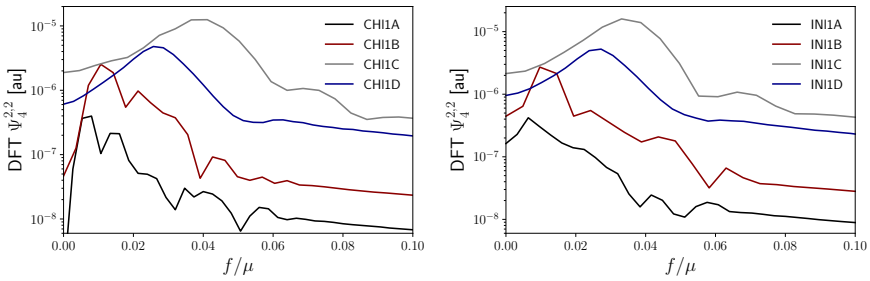

Figure 9.12: Fourier transform of the mode $l = 2$, $k = 2$ of Ψ_4 for coherent (left) and incoherent (right) models.

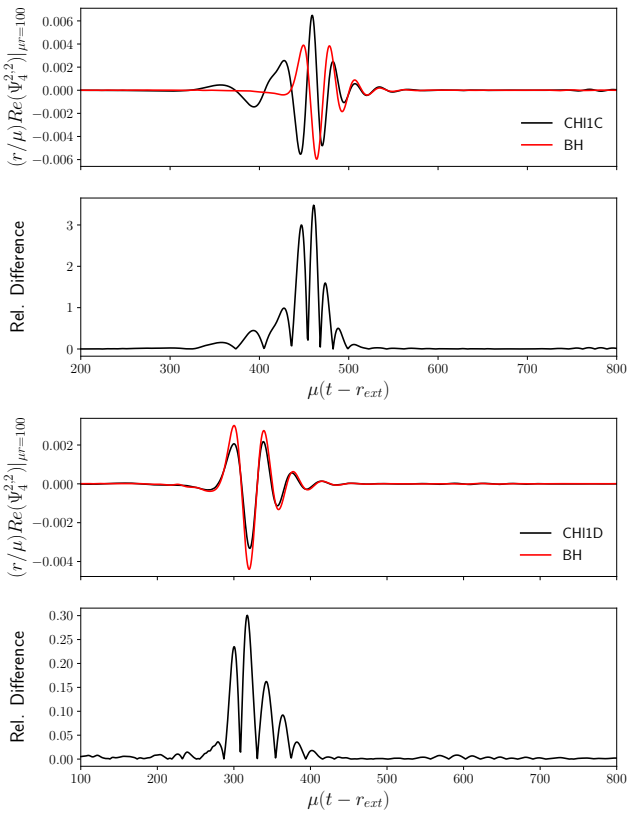

Figure 9.13: Difference between the black hole end state evolutions (CHl1C, CHl1D, INl1C and INl1D) and the corresponding same mass black hole head-on collision. Rel. Difference = $|\Psi_4^{2,2} - \Psi_{4,\mathrm{BH}}^{2,2}|/\max(\Psi_{4,\mathrm{BH}}^{2,2})$.

a spherical shell. As the value of ℓ increases, the maximum of the density tends to the external boundary leaving a region with almost zero density at the geometrical center. For very compact binaries the radius R_{99} is considerably smaller than for the less compact ones and the encounter is more violent producing a stronger gravitational signal.

To further investigate the post-merger behavior, let us compare it for the $\ell = 1$ model B and for the merger of two standard $\ell = 0$ boson stars, with the same radius R_{99} as the $\ell = 1$ model. The $\ell = 0$ corresponding collisions were already discussed in [57], where it was shown that the remnant approaches another $\ell = 0$ boson star. In Fig. 9.15 (left) we can see that the mass decreases in the collision process, reaching below the maximal mass allowed for $\ell = 0$ boson stars. The mass loss can be roughly divided into two phases. There is an initial slower decrease, partly due to GW emission, followed by a larger decrease rate, due to scalar field emission, *i.e.* gravitational cooling, that remains throughout the evolution. The remnant oscillates around a spherical distribution; in fact an equilibrium boson star with $\ell = 0$, with the oscillation amplitude decreasing with time. We stress the main relaxation process to attain the equilibrium state is gravitational cooling. This can be confirmed in Fig. 9.14, where the energy radiated by GW is shown; when compared to the total mass loss, in Fig. 9.5, it is seen that the emitted gravitational radiation is at least one order of magnitude smaller than the the total mass loss, in all the cases.

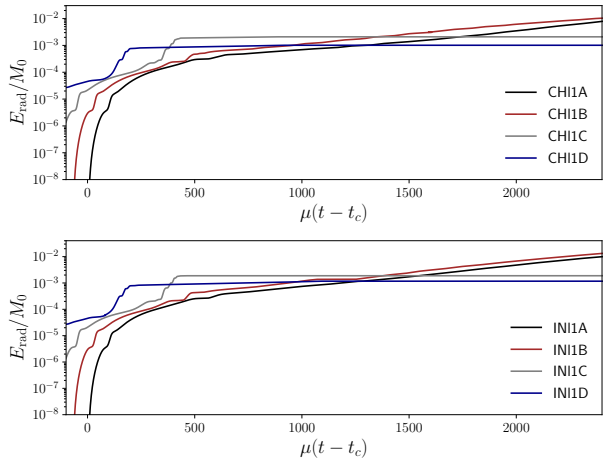

Figure 9.14: Total energy radiated by the gravitational wave.

The right panel of Fig. 9.15 exhibits the analogous behavior for the collision of the stars with $\ell = 1$. Similarities with the previous case are observable: there is a mass loss (together with a decrease in the number of particles), with a GW

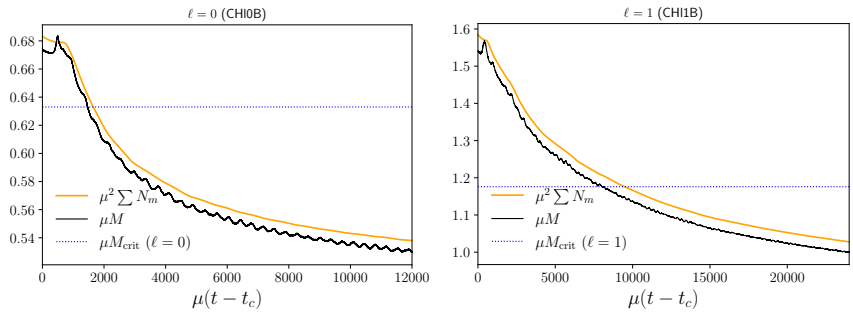

Figure 9.15: Mass and total number of particles for long simulations of the mergers of the $\ell = 0$ CHl0B (Left) and $\ell = 1$ CHl1B (Right).

emission component occurring initially and an expelling of scalar field throughout the entire evolution. In this case, however, it is not clear that the final state oscillates around a spherically symmetric configuration, say an ℓ-boson star. It can be mentioned that the system, as in the previous case, keeps oscillating, but the oscillation amplitudes decrease more slowly in this case. Also binary configurations consisting of boson stars with masses smaller than the CHl1A model have been explored, of particular interest are those cases where the total mass of the system is smaller than the maximum mass of the $\ell = 1$ family of solutions, $M_0^{\rm max} = 1.176$, the results for these cases are very similar to those shown in Fig. 9.15, that is, highly dynamic behavior at late times and a continuous and very slow loss of mass compared to the corresponding $\ell = 0$ models with the same value of R_{99}. For instance, low compactness models CHl1N and INl1N, which can be found in Tables 9.1 and 9.2, are an example of this behaviour since the initial total mass is smaller by half compared to $M_0^{\rm max}$. In Appendix 9.7 we present the wave forms of boson stars mergers with $\ell = 0$ and $\ell = 1$ in order to stress the role of the ℓ parameter in the GW emission.

To establish how spherical the after merger is, one may investigate the evolution of the components of the inertia tensor, described above. For the $\ell = 0$ boson stars merger the difference between the diagonal components averages to zero, confirming the tendency to sphericity. For the ℓ-boson stars with $\ell = 1$ case, on the other hand, this is not so. This supports the conclusion that the end state in the merger of the $\ell = 0$ boson stars tends towards a new $\ell = 0$ boson star, whereas for the ℓ-boson stars with $\ell = 1$ merger, it does not seem to tend towards a new ℓ-boson star with $\ell = 1$, albeit still remaining a bound state of the scalar field. It is possible that the asymptotic end state is a localized configuration with less symmetries; our simulations, however, can only raise this possibility, not establish it.

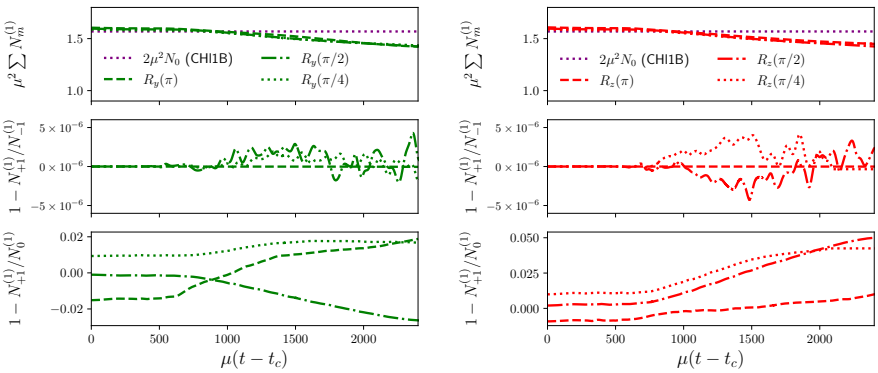

Figure 9.16: Non aligned stars. Total and individual (associated with each field) number of particles. (Left) Rotations around y-axis. (Right) Rotations around z-axis. As in Fig. 9.6, $1 - N_{+1}^{(1)}/N_0^{(1)}$ shows expected deviations from unity at $t = 0$ due to coherent superposition.

9.5.2 Non-aligned stars

As discussed above, a binary system of ℓ-boson stars may be given a relative orientation, despite the sphericity of the individual stars. We shall now discuss the impact of this feature on the head-on collisions. Let us take the orientation of the left (centered at $\mu x = -25$) ℓ-boson star fixed and rotate the right star (centered at $\mu x = +25$) using the R_i matrices presented at the end of section 9.3.1. It turns out that this relative orientation has very noticeable consequences in the outcome of the merger. Specifically we will make rotations around the y and z axes (recall that the collision is along the x axis) for the coherent model B, identifying the cases by the transformation performed, *i.e.*, the $R_y(\delta)$ and $R_z(\delta)$ respectively, where we have chosen the angles of rotation as $\delta = \pi, \frac{\pi}{2}$ and $\frac{\pi}{4}$.

As a general observation before describing specific cases, we do not obtain appreciable differences in the evolution of the mass or of the total number of particles with respect to the aligned case, see the upper panels of Fig. 9.16, despite some particularities that we will address later. Another similarity with the aligned coherent case is that the number of particles in the $m = +1$ mode is equal to that of the $m = -1$ mode throughout the evolution, as indicated by the middle panels of Fig. 9.16.

On the other hand, the relative behaviour of the number of particles in the modes $m = +1$ and $m = 0$ can be different in the non aligned case, although the relative difference is still small, never exceeding 10%. A difference found with respect to the aligned configuration, is that that there are cases where the three momenta of inertia become different.

Let us now discuss the specific cases with $R_y(\pi)$, $R_y(\pi/2)$ and $R_y(\pi/4)$; the last

two cases, however, are qualitatively similar. An $\ell = 1$ boson star is a composite of an $m = 0$ and $m = \pm 1$ modes. The $m = 0$ mode has a dipole-like energy distribution, whereas the $m = \pm 1$ modes are toroidal. In Fig. 9.17a we show snapshots of the energy density for the $z = 0$ (top panels) and $x = 0$ (bottom panels) planes. One observes that the maximum of the density can reach the origin. This behavior is characteristic of this type of merger (rotation $R_y(\pi)$). The bottom panels confirm that the symmetry along the (collision) x-axis is preserved during the merger. Fig. 9.17b shows snapshots for the individual currents for the same collision. The top panels correspond to the mode $m = 0$; one observes that the quadrupolar shape is maintained all along the evolution, presenting a clearly repulsive effect (attributed to the phase difference of π in this mode after the rotation) thus preventing this mode from concentrating at the origin. The bottom panels show the current for the mode $m = +1$ where there is not a well defined shape after the merger.

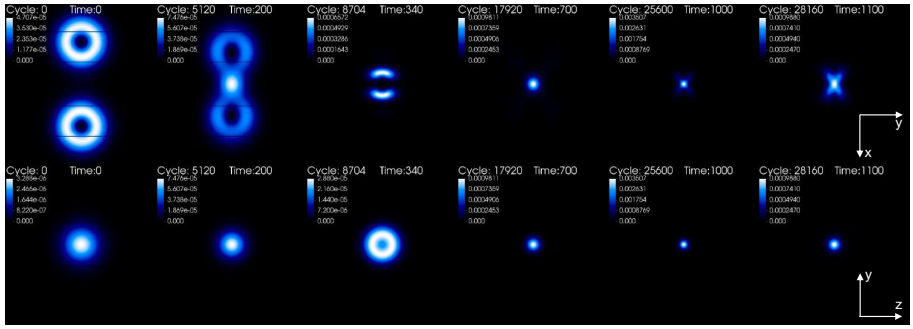

(a) Scalar field energy density, ρ/μ^2, for model CHl1B. Top panel: $z = 0$ plane. Bottom panel: $x = 0$ plane.

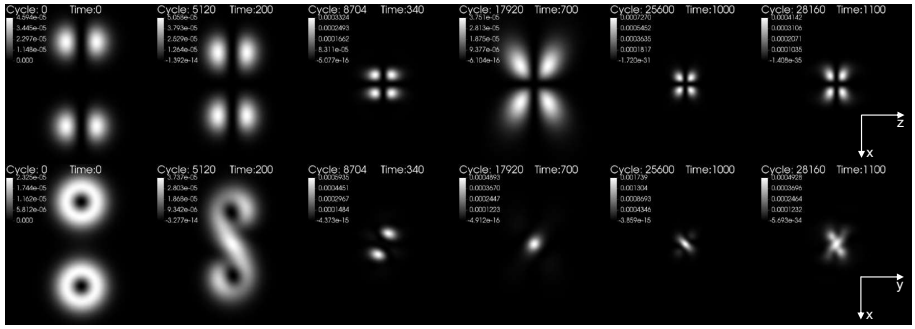

(b) Individual currents j_m/μ for model CHl1B. Top panel: $m = 0$ in the $y = 0$ plane. Bottom panel: $m = +1$ in the $z = 0$ plane.

Figure 9.17: Non aligned stars $R_y(\pi)$.

Regarding the $R_y(\pi/2)$ collision, there is an even more intricate interaction

amongst the modes of each star. In Fig. 9.18a we present snapshots of the energy distribution in the $z = 0$-plane (top panels) and in the $x = 0$-plane (bottom panels). The noticeable feature is that the symmetry of the configuration with respect to the collision axis is lost. Another characteristic is that the maximum density can reach the origin after the merger, despite the hollow shape of each star. Fig. 9.18b shows the individual currents for the $m = 0$ (top panels) and the $m = +1$ (bottom panels) modes. These examples show that the spherical symmetry of the end

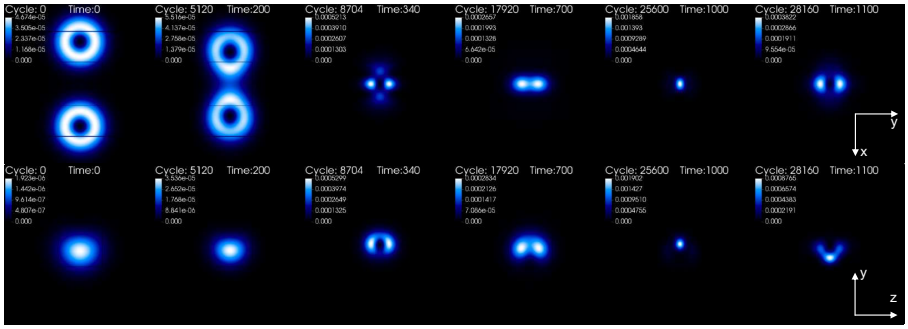

(a) Scalar field energy density, ρ/μ^2, for model CHl1B. Top panel: $z = 0$ plane. Bottom panel: $x = 0$ plane.

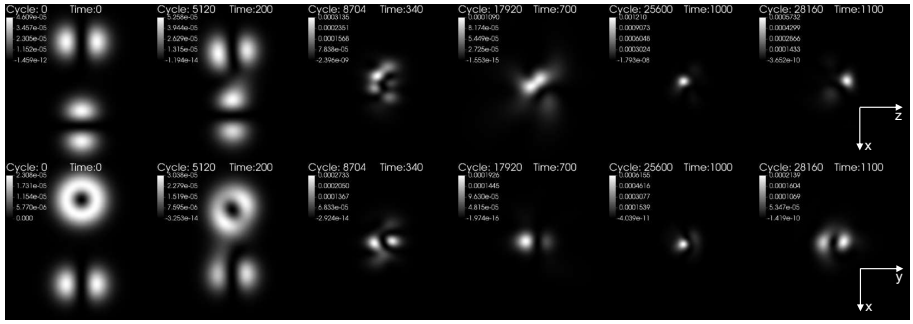

(b) Individual currents j_m/μ for model CHl1B. Top panel: $m = 0$ in the $y = 0$ plane. Bottom panel: $m = +1$ in the $z = 0$ plane.

Figure 9.18: Non aligned stars $R_y(\pi/2)$.

product of the merger is lost. One can further support this statement by looking at the moments of inertia of the final configuration. Fig. 9.19 shows the moments of inertia as a function of time for the rotated case $R_y(\pi)$ and $R_y(\pi/2)$. For the case with CHl1B-$R_y(\pi)$ one of the three moments of inertia is different. For the case with CHl1B-$R_y(\pi/2)$ the three moments of inertia remain all different. We have also studied the evolution of a system where the non alignment is due to a rotation around the z axis. This case shows several effects similar to the previous case, for example, the attraction/repulsion of the modes and a loss of sphericity.

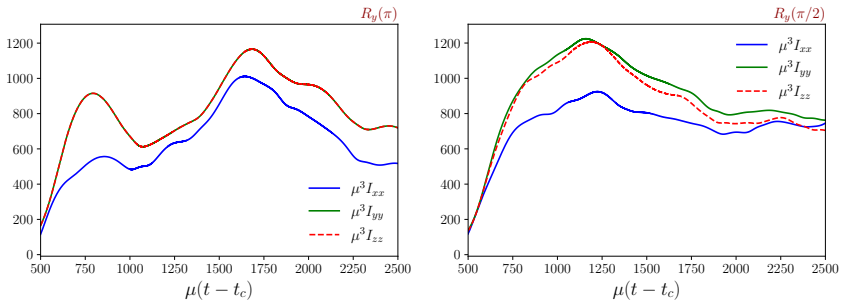

Figure 9.19: Moments of inertia for the non aligned models CHl1B, with $R_y(\pi)$ (left) and $R_y(\pi/2)$ (right). .

In Fig. 9.20a, we present the evolution of the energy density for the $R_z(\pi)$ rotation, and in Fig. 9.20b we present the corresponding evolution of the modes. The energy density diagnosis shows, as in the rest of the cases analyzed, a loss of the original symmetry of each star. As in the aligned case, this kind of rotations keeps unchanged the initial $m = 0$ mode, see Fig. 9.2 (recall that the spherical harmonic $\ell = 1$, $m = 0$ does not depend on the angle φ). During the evolution it can be seen that individually the $m = 0$ mode maintains its morphology, while the $m = \pm 1$ have a drastic change in morphology, yielding the observed change in the energy density. The $R_z(\pi/2)$ rotation case is shown in Fig. 9.21a. We see a twisting effect in the evolution of the energy density distribution in the $z = 0-$plane. Concerning the individual modes, the $m = 0$ mode tends to keep the original morphology, while the $m \pm 1$ modes loose it, a behavior similar to the previous case.

To conclude, we have observed that the rotations around the $y-$axis, R_y, produce more significant changes in the final morphology than the rotations along the $z-$axis, which also modify the final morphology, but keep the shape of the remnant $m = 0$ mode.

Regarding the GW profiles, we looked for any significant difference that could indicate a waveform dependence (particularly in its amplitude) on the angle and direction of rotation. As shown in Fig. 9.22, however, in none of the alignments studied for the model B we have observed significant differences; the amplitude of the seven cases is of the same order, although the first peak appears earlier in the non-aligned cases, with a maximum difference in time with respect to the aligned case of $\mu\Delta t \sim 50$ for the $R_y(\pi)$ case. This is true for all $\Psi_4^{l,k}$ but in particular for the dominant $l = 2$ $k = 0,2$ modes shown in Fig. 9.22.

Rotations R_y of the initial data cause slightly larger differences in the waveforms than the R_z cases. This is consistent with the fact, already pointed out, that

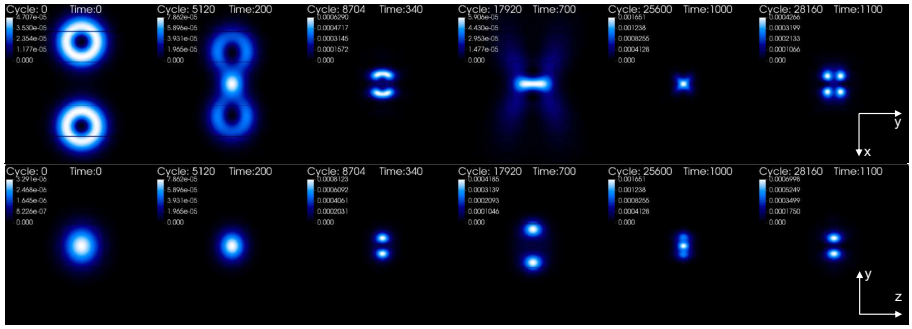

(a) Scalar field energy density, ρ/μ^2, for model CHl1B. Top panel: $z = 0$ plane. Bottom panel: $x = 0$ plane.

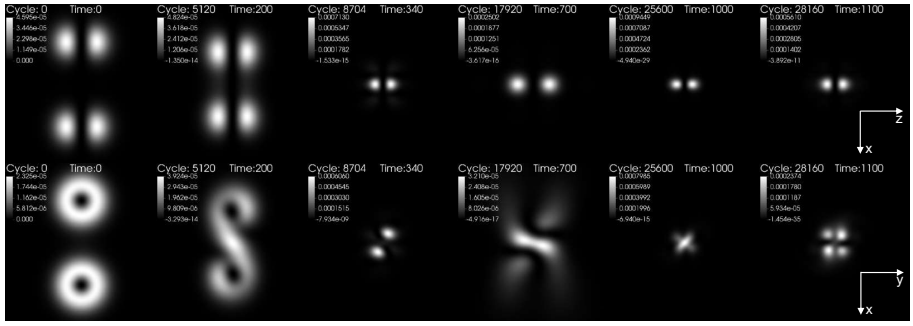

(b) Individual currents j_m/μ for model CHl1B. Top panel: $m = 0$ in the $y = 0$ plane. Bottom panel: $m = +1$ in the $z = 0$ plane.

Figure 9.20: Non aligned stars $R_z(\pi)$.

unexpected dynamics on the $m = 0$ scalar field may occur, essentially because R_y, unlike R_z, modifies the distribution of all the individual fields of the rotated star and not only the $m = \pm 1$ modes.

The GW signals just discussed can be compared with the ones previously presented for coherent (aligned) superposition and the incoherent one. For example, comparing the upper right panel of Fig. 9.11 and 9.22, one observes that at the level of the GWs. We remark that in hypothetical astrophysical scenarios an exact alignment should be accidental, and the generic case should be of misaligned stars. Concerning the end state, however, it is unclear if the coherence could have a greater importance than the relative alignment of the stars.

9.6 Final remarks

In this paper we have studied head-on collisions of ℓ-boson stars, starting from rest. These are *composite* self-gravitating solitons, made up of $2\ell + 1$ complex,

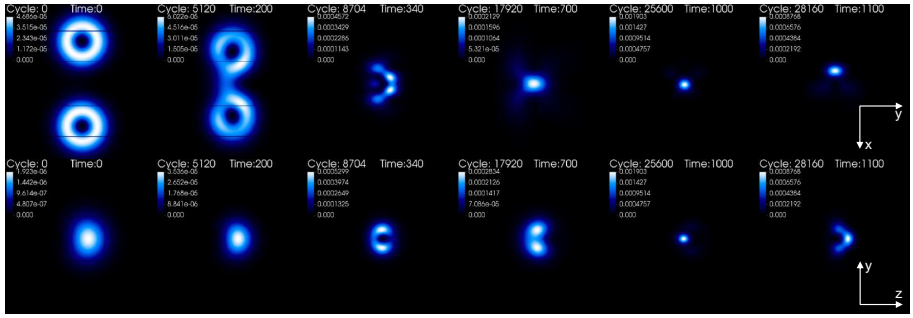

(a) Scalar field energy density, ρ/μ^2, for model CHl1B. Top panel: $z = 0$ plane. Bottom panel: $x = 0$ plane.

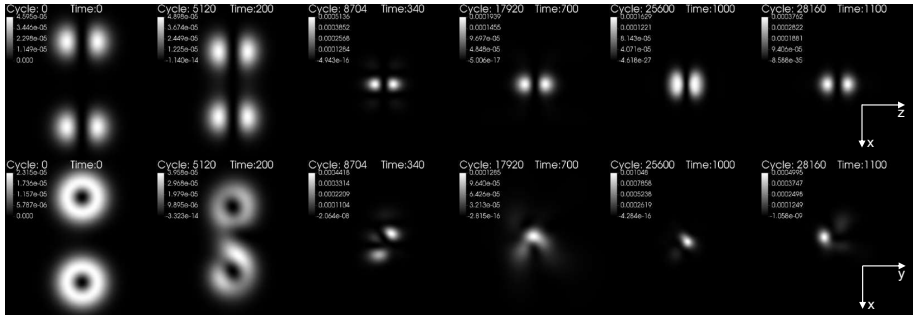

(b) Individual currents j_m/μ for model CHl1B. Top panel: $m = 0$ in the $y = 0$ plane. Bottom panel: $m = +1$ in the $z = 0$ plane.

Figure 9.21: Non aligned stars $R_z(\pi/2)$.

massive scalar fields [99]. In such scalar lumps, the different scalar fields have precisely the same amplitude, which raises the concern of possible self-tuning. Yet, it has been shown that these solutions are dynamically robust in regions of the parameter space [101, 102], at least against small perturbations. Here, we test these solutions against more violent processes: head-on collisions of two such equal stars.

Our simulations consider a variety of cases. As the two main scenarios we consider that the two colliding ℓ-boson stars are made up of the same, or of different, scalar fields. These two cases are dubbed coherent and incoherent, respectively. Additionally, we consider different possible orientations of the colliding stars. It may sound strange that such spherical stars have an "orientation"; yet they do. The point is that the composing fields of each star have a multipolar structure - *cf*. Fig. 9.2 -, defined with respect to a pre-established Cartesian reference frame. We can thus choose that these reference frames coincide, or not, for the two colliding stars. These two cases are dubbed aligned and non aligned, respectively.

Independently of the specific characteristics of each model that we have stud-

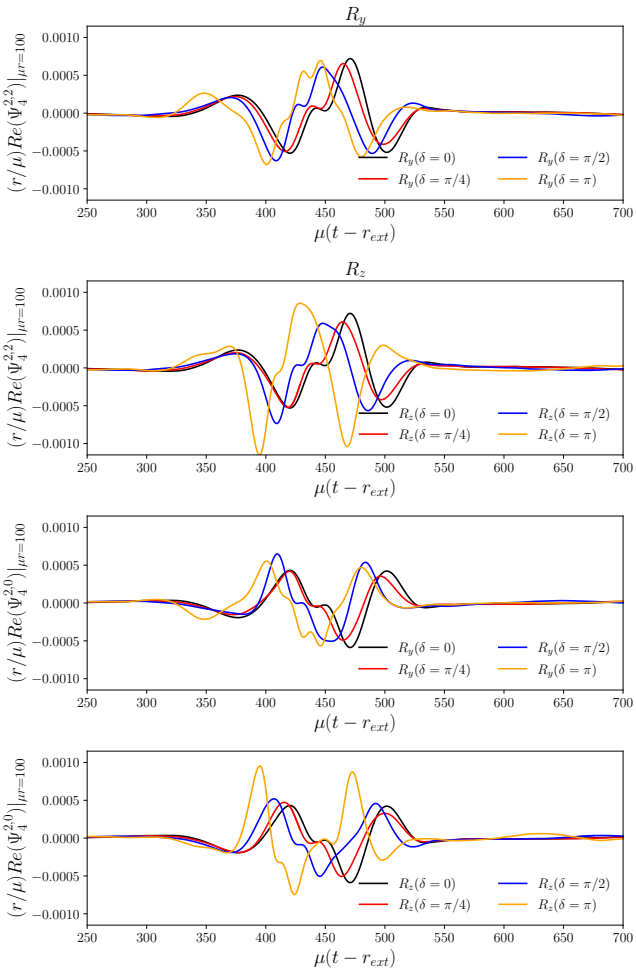

Figure 9.22: Waveforms for non aligned $\ell = 1$ binary. CHl1B model. Top panels show the real part of the $l = 2$, $k = 2$ mode. Bottom panels show the real part of the $l = 2$, $k = 0$ mode. The extraction radius is $\mu r_{\rm ext} = 100$.

ied, a first generic conclusion one can put forward is the following. The collision of sufficiently massive (and therefore compact stars) stars forms a black hole. This is what happens, *e.g.*, for models C and D in Fig. 9.1, corresponding to the collisions CH11C and CH11D in Table 9.1 and IN11C and IN11D in Table 9.2. But below a certain mass threshold, the collisions do not lead to horizon formation; a bound state of the different scalar fields remains, that neither disperses nor collapses. This is seen, for instance, for models A and B in Fig. 9.1, corresponding to the collisions CH11A and CH11B in Table 9.1 and IN11A and IN11B in Table 9.2.

Concerning the end state of collisions that do not form a black hole, the simulations reveal different specificities, depending on the chosen characteristics of the stars and of the collision. Still one sees two generic features. First, the democracy between the different composing fields of each ℓ-boson star is lost, albeit not dramatically. This feature can be diagnosed from the Noether charge in each field - see *e.g.* Fig. 9.6 (for aligned coherent states), Fig. 9.7 (aligned incoherent states) and Fig. 9.16 (for non aligned states). Observe, nonetheless, that the balance of particles in the $m = \pm 1$ modes is kept to high accuracy, and the slight imbalance with the $m = 0$ mode does not exceed a few percent. Second, the collision aftermath deviates from spherical symmetry. This can be quantified by looking at the moments of inertia, see Fig. 9.9 (for aligned collisions) and Fig. 9.19 (for non aligned collisions). Observe that $I_{xx} = I_{yy}$ in all cases, except the non aligned collisions under a rotation $R_y(\pi/2)$; also note that in some cases the three momenta of inertia, I_{xx}, I_{yy}, I_{zz} seem to converge after some time, which may be interpreted as a glimpse of a tendency towards sphericity.

Overall, the above description, albeit not entirely conclusive, allows us to answer the question we have set out to investigate: how dynamically robust are ℓ-boson stars? The answer seems to be two-fold. *Exact*, equilibrium ℓ-boson stars, with precise equipartition of the number of particles amongst the $2\ell+1$ fields are indeed fine tuned, and will not withstand generic perturbations. This is no surprise, and it was already anticipated by considering non-spherical perturbations of equilibrium ℓ-boson stars [103]. Yet, ℓ-boson stars as a particular symmetry enhanced point of a larger family of multi-field bosonic stars, as reported in [104], can be considered to be dynamically robust and long lived. In fact, the violent collisions we have considered, could only produce an imbalance in the Noether charges, of the order of a few percent. Of course, the end states of our simulations remain oscillating and have not yet reached a stationary state. We cannot rule out that gravitational cooling and GW emission will work towards a spherical distribution, getting rid of the non-spherical modes. However, our simulations do not exhibit strong, generic evidence for this possibility. The very slow convergence towards a final state is not a consequence of using models with initial total mass larger than the maximum mass of the final expected state, an $\ell = 1$ boson star, as can be concluded from the CHl1N and INl1N cases presented.

Finally, let us comment that our collisions have generated waveforms which can be quite different from those of BHs. As emphasized in the Introduction, it will be interesting to continue this effort, in order to generate large libraries of alternative waveform templates, to compare with observational data. This effort, of course, will require going towards orbiting binaries.

9.7 Appendices of Chap. 9

Appendix: Code validation

In all binary boson star configurations considered in this paper we have chosen to separate the stars 50 coordinate units ($\mu x_c = 25$). This responds to the fact that this is a distance for which, at least in the solutions studied, the absolute maximum of the violation of the Hamiltonian constraint H at $t = 0$ is approximately of the same order as the floor error of the numerical implementation, estimated from the single isolated star simulations. We verified that the L_∞ norm *i.e.*, the maximum of the absolute value of the Hamiltonian constraint, decreases as the separation of the stars is increased. For example, the value obtained if the binary CHl1B is separated by a distance of 70, 50 and 30 coordinate units, is $L_\infty(H)(t = 0) = 9 \times 10^{-5}, 10^{-4}, 2 \times 10^{-3}$ respectively. Thus, for the chosen separation of 50, the violation induced for the constraint is of the same order of the interpolation error. $L_\infty(H)$ and the L_2 norm of H, defined as $L_2(H) = \sqrt{\sum H_i^2/N_g}$, where N_g is the number of points of the grid, are shown in Fig. 9.23 as functions of t in the case where the separation of the stars is 50 units. The left panel shows that part of the initial data numerical error dissipates until $\mu t = 500$. The right panel indicates that the maximum of $|H|$ remains contained in the same order of magnitude throughout the simulation, in this plot, we show the results using two different computational domains; in the first one, using a blue line we show the case used in the simulations throughout the article, a box of size $\mu x_{\rm max} = 500$, in the second case a box of size $\mu x_{\rm max} = 120$. The maximum of $|H|$ is located (and remains) near the center of the grid.

To evaluate the evolution of the small constraint violations induced by the initial data superposition of the two boson star solutions and test for convergence, we have analyzed the Hamiltonian and momentum constraint together with some of the analysis quantities and GW outputs using three different resolutions. The coarsest level in the low resolution case is set to $\mu\{\Delta x, \Delta y, \Delta z\} = 20$, while for the medium and high resolutions we have $\mu\{\Delta x, \Delta y, \Delta z\} = \sqrt{2}\ 10$, $\mu\{\Delta x, \Delta y, \Delta z\} = 10$, respectively. In the medium and low resolutions we have placed six refinement levels with the same spatial distribution as in the high resolution case (which is the one used in this work) described in section 9.3.2. In Fig. 9.24 we have plotted the gravitational waveform of CHl1A, which converges. The left and the bottom panels of Fig. 9.23 show that the Hamiltonian constraint also converges with resolution. The momentum constrains have been corroborated to be consistent with zero at $t = 0$, and later in the evolution the three components converge with increasing resolution, as expected. At the middle panel of Fig. 9.24 the differences between the gravitational signal at different resolutions are given, this helps to establish convergence of the GW and also gives an estimate of 1×10^{-3}

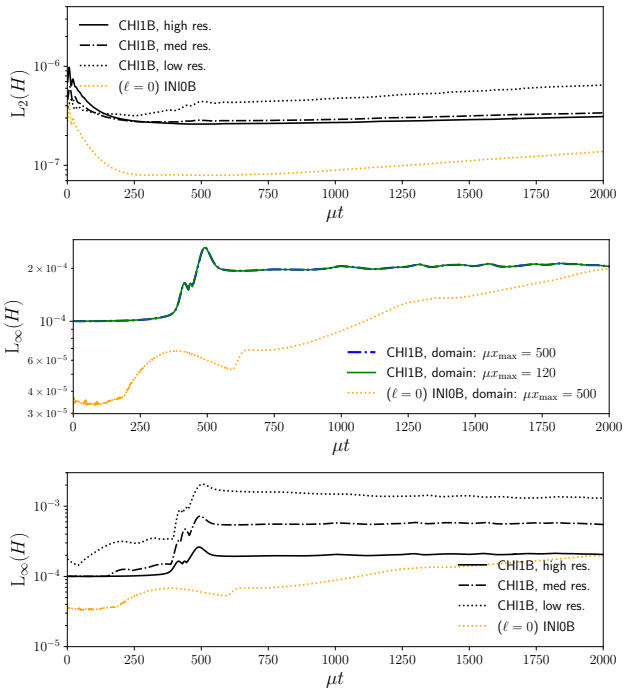

Figure 9.23: L_2 and L_∞ norms of the Hamiltonian constraint for the model CHI1B. In this plot, as in the results presented throughout this article the stars have been separated 50 coordinate units.

for the relative difference when comparing the high and the medium resolutions. Finally, we have generated GW output at different radii in order to check consistency and accuracy of the results; the bottom panels of Fig. 9.24 show that $\Psi_4^{2,2}$ and $\Psi_4^{2,0}$ overlap when properly rescaled by the factor $1/r$. The extraction surfaces are therefore within the "wave-zone".

Appendix: Number of particles

In this appendix we show that the number of boson particles in a single isolated ℓ-boson stars, for a fixed value of ℓ, is equally distributed among the different modes m, that compose the star. There is an *equipartition* of the total Noether charge.

The total conserved (Noether) charge associated to all scalar fields of an ℓ-boson star is given by the zero component of the total current j^0, as

$$N = \int j^0 \alpha\sqrt{\gamma} dx^3 := \int \left(\sum_{m=-\ell}^{\ell} j_m \right) \alpha\sqrt{\gamma} dx^3 \,, \tag{9.19}$$

where j^0 is given by the sum

$$j^0 = \sum_{m=-\ell}^{\ell} \left[\frac{i}{2} g^{0b} (\bar{\Phi}_m \nabla_b \Phi_m - \Phi_m \nabla_b \bar{\Phi}_m) \right] = \sum_{m=-\ell}^{\ell} j_m \ . \tag{9.20}$$

For a single ℓ-boson star the scalar field has a time dependence of the form $\Phi_m = e^{-i\omega t} \phi_\ell(r) Y^{\ell m}(\vartheta, \varphi)$ and the metric is given by (9.7). The individual currents j_m, can be written, after some simplifications, as

$$j_m \quad = \quad -\frac{1}{\alpha^2(r)} \omega \phi_\ell^2(r) \left| Y^{\ell m}(\vartheta, \varphi) \right|^2 \ . \tag{9.21}$$

Integration of Eq. (9.21) over the 3-element of volume gives the number of particles associated to each field

$$N_m = \int \alpha \, j_m \sqrt{\gamma} dx^3 = -\omega \left[\int_0^\infty dr \frac{a(r) r^2}{\alpha(r)} \phi_\ell^2(r) \right] \left[\int_0^\pi \int_0^{2\pi} d\vartheta d\varphi \sin\theta \left| Y^{\ell m}(\vartheta, \varphi) \right|^2 \right] \ ; \tag{9.22}$$

the second integral is equal to 1 due to the normalization of the spherical harmonics. Therefore

$$N_m = -\omega \int_0^\infty dr \frac{a(r) r^2}{\alpha(r)} \phi_\ell^2(r) \ , \tag{9.23}$$

and from Eq. (9.19) one obtains

$$N \quad = \quad \sum_{m=-\ell}^{\ell} \int \alpha \, j_m \sqrt{\gamma} dx^3 = (2\ell + 1) N_m \ . \tag{9.24}$$

Consequently, the total number of particles of a single ℓ-boson star is divided equally into the associated number of particles stored in each field

$$N_m = \frac{1}{2\ell + 1} N \ . \tag{9.25}$$

Appendix: Comparison with $\ell = 0$ boson stars

The purpose of this appendix is to continue the discussion regarding the comparison between boson stars mergers with $\ell = 0$ and $\ell = 1$, presented at the end of section 9.5.1, identifying the effect of the ℓ parameter on the GW signal. The dynamics and GW signatures of the merger of boson star binaries have been discussed extensively in the past, *e.g.* [46, 58]. It has been shown that the gravitational waveform may be very different from that of black holes specially in the early phases. In our numerical experiments, we have obtained similar results to the ones presented in [58, 59] for the standard $\ell = 0$ boson stars merger, in particular that the waveform of the merger of incoherent states is much smaller and occurs after its coherent counterpart.

Coh.	$\ell = 0$							
Model	μR_{99}	ω/μ	μM_0	$\mu^2 N_0$	$\mathscr{C}$	Rem.	$\mu R \sim$	μt_c
CHl0A	31.5	0.985	0.296	0.298	0.009	BS	30	0
CHl0B	27.5	0.980	0.333	0.335	0.012	BS	30	0
CHl0C	24.7	0.976	0.364	0.367	0.015	BS	25	110
CHl0D	13.5	0.931	0.548	0.559	0.041	BH	$\mu r_{AH} = 1.25$	320

Table 9.3: Coherent cases for $\ell = 0$. R_{99} is the radius that contains 99% of the mass of the star. ω is the frequency, M_0 is the mass of each star, N_0 is the number of particles of each star and $\mathscr{C}$ is the compactness. The final remnant can be a localized boson configuration (BS) or a black hole (BH). R is the radius that encloses 99% of the mass for scalar field remnant at $\mu t = 2500$ while for BHs it labels the radius of the apparent horizon.

As discussed above, for the boson stars with $\ell = 1$ mergers, the coherent and incoherent configurations become more similar. Due to this fact, we focus our description of the $\ell = 0$ and $\ell = 1$ comparison, only for the corresponding coherent states. In order to perform such comparison of the gravitational waveforms we select stars with the same R_{99}.

In Table 9.3 we shown some properties of the stars. The radii of the stars are the same as models listed in Table 9.1. In Fig. 9.25 it is shown the waveforms ψ_4^{22}, for models listed in Tables 9.1 and 9.3. For models CHl0A and CHl1A with $\mu R_{99} = 31.5$, the mode ψ_4^{22} for boson stars with $\ell = 0$ has the same order of magnitude despite the fact the compactness is larger for the $\ell = 1$ boson stars. For models with $\mu R_{99} = 27.5$ (CHl0B and CHl1B) the maximum amplitude of the signal is considerably larger for the $\ell = 1$ case. For models with $\mu R_{99} = 24.7$ (CHl0C and CHl1C) the final product of the collision for $\ell = 0$ is a boson star but for $\ell = 1$ the remnant is a black hole. Both signals are clearly distinguishable.

Finally, for models with $\mu R_{99} = 13.5$ (CHl0D and CHl1D) the gravitational imprints for $\ell = 0$ boson stars and $\ell = 1$ boson stars are quite different from each other despite the fact a black hole forms after the merger in both cases. This happens because in the $\ell = 1$ boson star binary, the mass of the BH formed is bigger.

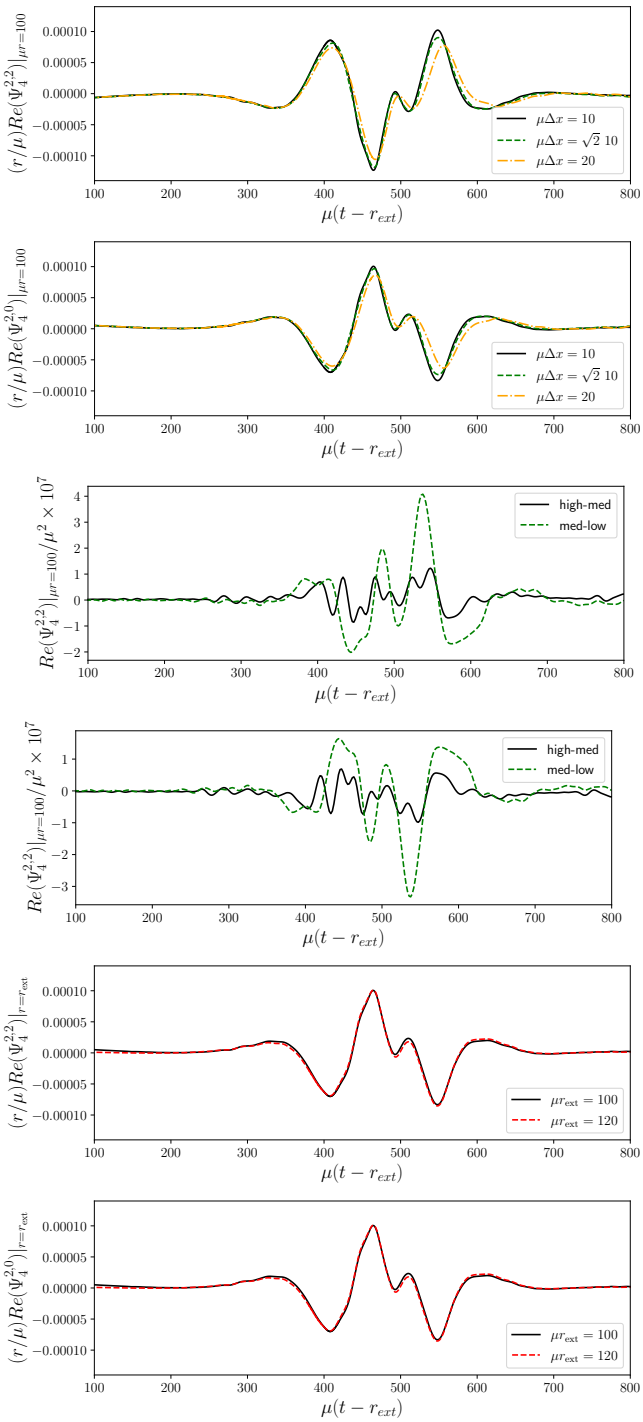

Figure 9.24: Model CHl1A. Top panels show the real part of $r\Psi_4^{2,2}$ and $r\Psi_4^{2,0}$ at $\mu r_{\rm ext} = 100$ using different resolutions. Their differences are displayed in the middle panel. Bottom panels show overlap of waves extracted at different radii when they are appropriately rescaled.

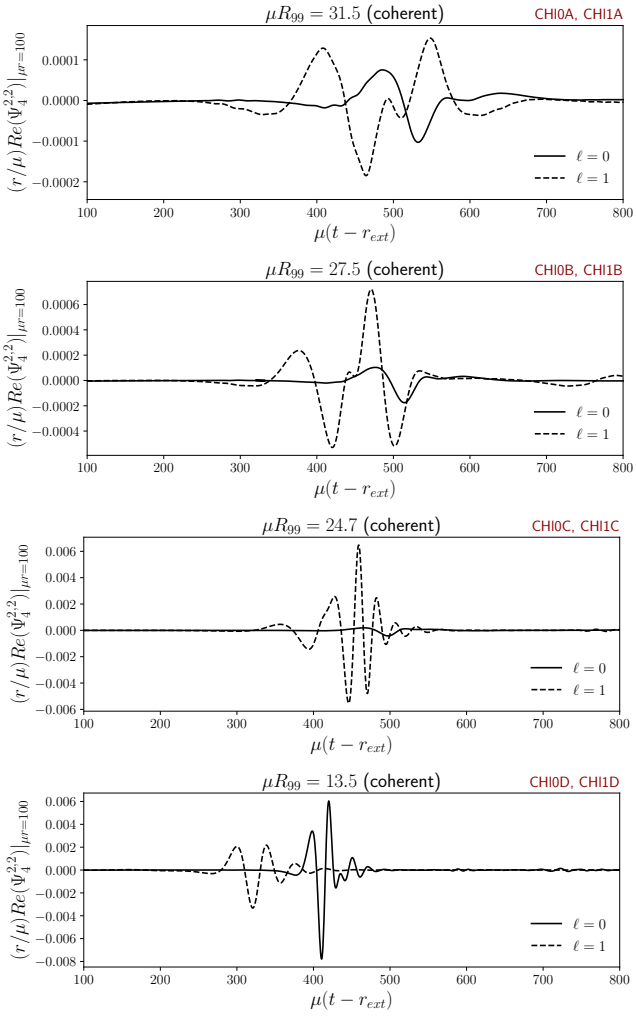

Figure 9.25: GW signal for configurations described in Table 9.3. The extraction radius is $\mu r = 100$.

CONCLUSIONS

Classical scalar fields are multipurpose mathematical objects that, when coupled to gravity serve as excellent and simple models for the cosmological dark matter and dark energy which in turn motivate the exploration of the scalar field physics in astrophysical scales.

There are some examples of compact objects where the source of gravitational field is the scalar field, such as the boson stars, some wormholes, many of the hairy black hole solutions and other canonical-ghost configurations such as the $\mathscr{E}$-boson stars presented here. Emphasis should be placed on the fact that the mentioned solutions, actively studied by the community, do not require any coupling that takes the system out of the description of general relativity although some of these solutions exist, in particular in a group of alternative theories called the scalar-tensor theories. However, as has been argued throughout this manuscript. Einstein's theory of general relativity has passed all tests to date.

In this context, we have developed a kind of mold for stationary solution construction procedures and their subsequent dynamical analysis in full 3+1 General Relativity. This thesis addressed seven solutions among which some are spatially homogeneous and others stationary in different symmetries. In Chap.2, as motivation, we presented a dark matter two-scalar field solution (Sec. 2.2) where the ultralight self-interacting model was combined with Higgs-like and axion fields in the Friedmann cosmological evolution, finding that constrains from big bang nucleosynthesis indicate that the ultralight field must make up at least about 40 percent of the total dark matter. Then in Sec. 2.3 we presented an exact solution for a complex self-interacting model that behaves as quintessence at late times.

Part I was composed by the spherically symmetric compact object solutions. In Chap. 3 ℓ-boson star solutions with $\ell \gg 1$ where constructed by means of a spec-

tral method and rescaling properties. We found that the pressure anisotropy in the configurations as well as their mass and compactness increase with ℓ reaching values close to the Buchdahl limit. Chap. 4 introduced a real self-interacting ghost scalar field and combined the gravitational soliton with a (standard) boson star solution, obtaining composite system of a scalar field star with a phantom nucleus which significantly increases the compactness even to values very close to black hole limit while satisfying the null-energy condition everywhere. Then, using multiple fields, but in this case all ghosts, we presented solutions with wormhole topology in Chap. 5. We should mention with respect to this solution we expected that the rotation parameter ℓ would help the stability of the configuration, however an independent study, outside the scope of this thesis, showed this was not the case.

Part II dealt with axisymmetric solutions as the magnetic boson star, constructed in Chap. 6 and the two-boson star solutions in Chap. 7. Both solutions have interesting applications in the dynamical scenario, which we are currently studying, using them as initial data. Both axially symmetric Einstein-Maxwell-Klein-Gordon and Einstein-Friedberg-Lee-Sirlin systems of Chaps. 6 and 7 respectively, where solved using the library for spectral methods for theoretical physics Kadath.

Then, in Part III, Chaps. 8 and 9 the initial data for ℓ-boson stars was interpolated to the Cartesian grid of Einstein Toolkit in order to analyze the stability of this kind of boson stars and the head-on collisions. Both papers certainly found similarities with the standard $\ell = 0$ boson stars, however a notable difference appeared, as evidence was found for the existence of multifield solutions outside of spherical symmetry, which was confirmed shortly thereafter elsewhere.

Finally, we identify two opportunities in which the results presented in this manuscript give rise to future work. First, we have found (numerical) evidence, that some unstable $\mathscr{E}$-boson stars migrate to a time-dependent periodic solution with a ghost scalar field distribution remaining inside the canonical scalar field, which would be interesting since we are not aware of other phantom field solutions that form bound states in regular spacetimes. And second, the axial data obtained by spectral methods would be very convenient to interpolate directly to the Einstein Toolkit code in order to preserve numerical precision, obtaining more reliable and stable simulations than those that use initial data obtained from finite difference schemes.

Appendices

APPENDIX A

BLACK HOLE SOLUTIONS WITH MAGNETIC DIPOLE MOMENT

The full action of the Einstein-Maxwell system reads

$$S = \frac{c^4}{16\pi G}\int R\sqrt{-g}d^4x - \sum\int m d\tau + \int A_i J^i \sqrt{-g}d^4x - \frac{1}{4\mu_0}\int F_{ab}F^{ab}\sqrt{-g}d^4x \tag{A.1}$$

In this appendix we do not take $c = 1$.

Electrovacuum ($J^i = 0$) imply the following:

$$R_{\mu\nu} - \frac{1}{2}Rg_{\mu\nu} = \frac{8\pi G}{c^4}T_{\mu\nu}; \qquad \nabla^\mu F_{\mu\nu} = 0 \tag{A.2}$$

with

$$T_{\mu\nu} = \frac{1}{\mu_0}\left(F^\lambda_\mu F_{\nu\lambda} - \frac{1}{4}g_{\mu\nu}F_{\alpha\beta}F^{\alpha\beta}\right). \tag{A.3}$$

Kerr-Newman

The Kerr-Newman spacetime is a three-parameter family of solutions to the above equations where the space-time is stationary and axisymmetric.

In Boyer Lindquist coordinates the solution is given by the line element

$$\mathrm{d}s^2 = -\frac{\Delta}{\Sigma}(c\,\mathrm{d}t - a\sin^2\theta\,\mathrm{d}\varphi)^2 + \frac{\sin^2\theta}{\Sigma}\left[(r^2+a^2)\mathrm{d}\varphi - ac\,\mathrm{d}t\right]^2 + \Sigma\left(\frac{\mathrm{d}r^2}{\Delta} + \mathrm{d}\theta^2\right), \tag{A.4}$$

$$A_\mu\,\mathrm{d}x^\mu = -\frac{rQ}{4\pi\epsilon_0 c\Sigma}\left(c\,\mathrm{d}t - a\sin^2\theta\,\mathrm{d}\varphi\right) \tag{A.5}$$

where

$$a = \frac{J}{Mc}, \tag{A.6}$$

$$\Sigma = r^2 + a^2 \cos^2\theta, \tag{A.7}$$

$$\Delta = r^2 - r_s r + a^2 + r_Q^2 \tag{A.8}$$

and

$$r_s = \frac{2GM}{c^2}, \qquad r_Q^2 = \frac{Q^2 G}{4\pi\epsilon_0 c^4} \tag{A.9}$$

The first thing to notice with this solution is that it already has a magnetic dipole moment. In the limit $r \to \infty$ it can be see how the dominant term of the solution is an electric monopole and a magnetic dipole:

$$A_\mu \approx \frac{Q}{4\pi\epsilon_0 cr}\left(-1, 0, 0, a\sin^2\theta\right) \tag{A.10}$$

the 0 component refers to the electric potential produced by a charge Q since in flat space-time, in SI units and in coordinates $(x_0, \mathbf{x})$ it is satisfied that $A^\mu = (\phi/c, \mathbf{A})$ therefore

$$\phi = cg^{00}A_0 = \frac{Q}{4\pi\epsilon_0 r}, \tag{A.11}$$

while the contravariant compontent A^φ is

$$A^\varphi = g^{\varphi\varphi}A_\varphi = \frac{Qa}{4\pi\epsilon_0 cr^3} = \frac{\mu_0 cQa}{4\pi r^3}. \tag{A.12}$$

In order to compare with the three-vector $\mathbf{A} = A^\varphi \mathbf{e}_\varphi$, we place directly the magnitude of the coordinate basis $|\mathbf{e}_\varphi| = r\sin\theta$, we see then that

$$\mathbf{A} = \frac{\mu_0}{4\pi r^3}\mathbf{m} \times \mathbf{x}, \tag{A.13}$$

with $\mathbf{m} = Qca\mathbf{e}_z$. Which is the magnetic moment of a circuit in xy of current $I = \frac{Qc}{\pi a}$ and area πa^2. And it is (like the electron!), twice the magnetic moment of a charge Q spinning in a ring of radius a at speed c: $m_{\text{classical}} = (Q/T)A = (Qc/2\pi a)(\pi a^2) = Qca/2$.

In addition to this identification of the situation in the asymptotic limit, Newman wanted to identify the Kerr-Newman source with a charged rotating ring. Carter then argued that it would not be possible to refer to the sources of this space-time as a rotating charge distribution. However there have been several attempts to give a source for these electromagnetic fields (see [230–232] and others). All these attempts as far as I can see are in the limit $G \to 0$, motivated by the fact that A_μ does not depend on G. This path is the only situation where it seems to be that it makes sense to talk about a source of rotating charges and therefore possible to give an interpretation. There are some references where conductors

are used in vacuum or with infinite magnetic susceptibility that I do not understand, but only for comparison. And others where it is solution, but its source is the disk that generates the singular ring, which generates discontinuities and it seems that infinite energy, etc..

A serious and moreover easy-to-read attempt to give a source to the Kerr-Newman space-time is the one made by [233]. He obtains the source by taking the $G \to 0$ limit directly, but he considers the fact that the topology obtained is non-trivial (though flat) and solves Maxwell equations there, proving that the source is the ring (now spacelike) is unique. Taking the limit $G \to 0$ of (A.4) we obtain that $r_Q = 0 = r_s$, and hence $\Delta = r^2 + a^2$:

$$\begin{aligned} \mathrm{d}s^2 = &- \frac{r^2+a^2}{r^2+a^2\cos^2\theta}(c\,\mathrm{d}t - a\sin^2\theta\,\mathrm{d}\varphi)^2 \\ &+ \frac{\sin^2\theta}{r^2+a^2\cos^2\theta}\left[(r^2+a^2)\mathrm{d}\varphi - ac\,\mathrm{d}t\right]^2 + (r^2+a^2\cos^2\theta)\left(\frac{\mathrm{d}r^2}{r^2+a^2} + \mathrm{d}\theta^2\right) \end{aligned} \tag{A.14}$$

which reduces to

$$\mathrm{d}s^2 = -\mathrm{d}t^2 + (r^2+a^2)\sin^2\theta\,\mathrm{d}\varphi^2 + (r^2+a^2\cos^2\theta)\left(\frac{\mathrm{d}r^2}{r^2+a^2} + \mathrm{d}\theta^2\right) \tag{A.15}$$

and which is Minkowski except for a change of coordinates resulting singular in the ring.

On the other hand A_μ remains identical, and is a solution to Maxwell equations in space-time with such topology with sources located exclusively in the ring.

Ernst

There are magnetized black hole solutions, for example those described in [234, 235] where the homogeneous magnetic field at infinity is a test field. I also understand that there are exact solutions as for example those described in [236] referring to a Black Hole solution found by Ernst using Harrison's method, but as with the Manko-Sibgatulin solutions, are obscure, besides that they have multiple problems; there Aliev and Galtsov indicate which are these problems and how to solve some of them.

Bonnor

If one looks for references to exact solutions (e.g. in the Refs. of Stephani-Kramer, Griffiths-Podolsky, Chandasekhar), they refer (very briefly) to the solutions found by Bonnor and those found by Manko and Sibgatullin. The Bonnor's solution ([237]) is the one that agrees the most with the idea (in vacuum) of giving a

possible description to the exterior of a massive object with a magnetic dipole (a kind of magnet - magnetized sphere), the extension apparently corresponds to a pair of extreme Reissner-Nordstrom black holes with magnetic charge (the magnetic monopole solution) and separated a certain distance by a “strut”. The solution, with its restored units reads,

$$\mathrm{d}s^2 = -\left(\frac{P}{Y}\right)^2 c^2\,\mathrm{d}t^2 + \frac{P^2Y^2}{Q^3Z}(\mathrm{d}r^2 + Z\,\mathrm{d}\theta^2) + \frac{Y^2Z\sin^2\theta}{P^2}\,\mathrm{d}\varphi^2, \tag{A.16}$$

$$A_\mu\,\mathrm{d}x^\mu = \frac{c}{\sqrt{4\pi\epsilon_0 G}}\frac{r_s b r\sin^2\theta}{P}\,\mathrm{d}\varphi, \tag{A.17}$$

where

$$P = r^2 - r_s r - b^2\cos^2\theta, \tag{A.18}$$

$$Q = \left(r - r_s/2\right)^2 - \left(r_s^2/4 + b^2\right)\cos^2\theta, \tag{A.19}$$

$$Y = r^2 - b^2\cos^2\theta, \tag{A.20}$$

$$Z = r^2 - r_s r - b^2 \tag{A.21}$$

with $r_s = 2GM/c^2$. According to Griffiths and Podolsky, this is a naked singularity. However, the solution is asymptotically flat and an identification of its properties can be made since it in $r \to$ and conserving some of the $\mathcal{O}(1/r)$ terms, we obtain

$$\mathrm{d}s^2 \approx -(1 - 2r_s/r)c^2\,\mathrm{d}t^2 + \frac{1}{1 - 2r_s/r}\,\mathrm{d}r^2 + r^2(\mathrm{d}\theta^2 + \sin^2\theta\,\mathrm{d}\varphi^2), \tag{A.22}$$

$$A_\mu\,\mathrm{d}x^\mu \approx \frac{c}{\sqrt{4\pi\epsilon_0 G}}\frac{r_s b\sin^2\theta}{r}\,\mathrm{d}\varphi \tag{A.23}$$

Clearly the spacetime mass is $2M$.

Comparing A_μ with the equation for the Kerr-Newman four-potential, it is clear that this solution has no electric charge, but does have a dipole. We define $A_m u$ through an equation similar to the one that defines Q in the Kerr-Newman solution,

$$b^2 = \frac{\mu^2 G}{4\pi\epsilon_0 r_s^2 c^6} \tag{A.24}$$

In terms of μ we have

$$A_\varphi = \frac{\mu}{4\pi\epsilon_0 c^2}\frac{r\sin^2\theta}{P} \tag{A.25}$$

and in the asymptotic limit,

$$A_\varphi \approx \frac{\mu}{4\pi\epsilon_0 c^2}\frac{\sin^2\theta}{r}. \tag{A.26}$$

Comparing one to one with the equation (A.10) which is the asymptotic analogue of Kerr-Newmann, it is immediately seen that the magnetic moment associated with this solution is

$$\mathbf{m} = \mu\mathbf{e}_z \tag{A.27}$$

In units where $G = c = 1/(4\pi\epsilon_0) = 1$ (Gaussian) one has $A_\mu = 2mb$. Bonnor's paper on the other hand, is in units where $G = c = 1/\mu_0 = 1$, where the four-potential $A_\mu \, \mathrm{d}x^m u \approx \frac{1}{A_\mu} \, \mathrm{d}x^\mu \approx \frac{1}{Mbr\sin^2\theta} P \, \mathrm{d}\varphi$ reported by them is recovered.

The horizon is located at $Z = 0$ however it is a non-regular horizon because $g_{\varphi\varphi} = 0$ there too. It evades the no-hair theorem. This solution does not reduce to Schwarzschild but it does reduce to one of Zipoy's solutions.

Manko-Sibgatullin

The first suerposition of a Kerr black hole with a magnetic dipole was made by Kramer but for the hyperextremal case. Then, Manko, a long time ago, published about 5 articles. His simplest solution was further simplified in the very recent article [238]. These solutions depending on the parameters m, a, q and b, do reduce to Schwarzschild in the limit $a = q = b = 0$. I now switch to units $G = c = 1$, and the simplified, nonrotating, uncharged, case ($a = 0 = q$) has metric,

$$ds^2 = -f(dt - \omega d\varphi)^2 + f^{-1}\left[e^{2\gamma}(d\rho^2 + dz^2) + \rho^2 d\varphi^2\right]. \tag{A.28}$$

with the metric coefficients determined from

$$f = \frac{A^2 - B^2 + C^2}{(A+B)^2}, \quad e^{2\gamma} = \frac{A^2 - B^2 + C^2}{16\kappa_+^4\kappa_-^4 R_+ R_- r_+ r_-}, \quad \omega = -\frac{\mathrm{Im}[G(\bar{A} + \bar{B}) + C\bar{I}]}{A^2 - B^2 + C^2} \tag{A.29}$$

with

$$\begin{aligned}
A =& \kappa_-^2(m^2+b)(R_-r_- + R_+r_+) + \kappa_+^2(m^2-b)(R_-r_+ + R_+r_-) - 4b^2(R_-R_+ + r_-r_+),\\
B =& m\kappa_-\kappa_+[m^2(r_- + r_+ - R_- - R_+) + \kappa_m\kappa_+(r_- + r_+ + R_- + R_+)],\\
C =& b\kappa_-\kappa_+[(\kappa_+ + \kappa_-)(R_- - R_+) + (\kappa_+ - \kappa_-)(r_+ - r_-)],\\
G =& \kappa_+^2\kappa_-(\kappa_-^2 + m^2 + b)(R_-r_+ - R_+r_-)\\
&+ \kappa_-^2\kappa_+(\kappa_-^2 + m^2 - b)(R_-r_- - R_+r_+)\\
&+ mb\kappa_+\kappa_-[(\kappa_+ + \kappa_-)(r_+ - r_-) - (\kappa_+ - \kappa_-)(R_+ - R_-)] - 2zB,\\
I =& m\kappa_+^2[-ib(R_-r_+ + R_+r_-)] + m\kappa_-^2[-ib(R_-r_- + R_+r_+)]\\
&+ 2imb[m^2(R_+R_- + r_+r_-) + 2\kappa_+^2\kappa_-^2]\\
&+ ib\kappa_+\kappa_-[2m(R_+R_- - r_+r_-) + 4m^2(R_+ + R_- - r_+ - r_-)] - ziC + ibB/m.
\end{aligned}$$

where

$$R_\pm = \sqrt{\rho^2 + \left[z \pm \frac{1}{2}(\kappa_+ + \kappa_-)\right]^2}, \quad r_\pm = \sqrt{\rho^2 + \left[z \pm \frac{1}{2}(\kappa_+ - \kappa_-)\right]^2},$$

and

$$\kappa_\pm = \sqrt{m^2 \pm 2b}. \tag{A.30}$$

A,B,C,G are real and I is imaginary. Hence, the solution would be simplified (for the fourth time) to

$$f = \frac{A^2 - B^2 + C^2}{(A+B)^2}, \quad e^{2\gamma} = \frac{A^2 - B^2 + C^2}{16\kappa_+^4 \kappa_-^4 R_+ R_- r_+ r_-}, \quad \omega = -\frac{CI}{A^2 - B^2 + C^2}. \tag{A.31}$$

It is very likely that the equations can be further simplified in order to compare with Bonnor's solution.

BIBLIOGRAPHY

[1] Isaac Newton. *Philosophiæ Naturalis Principia Mathematica*. England, 1687.

[2] A. Einstein. Zur Allgemeinen Relativitätstheorie. *Sitzungsber. Preuss. Akad. Wiss. Berlin (Math. Phys.)*, 1915:778–786, 1915. [Addendum: Sitzungsber.Preuss.Akad.Wiss.Berlin (Math.Phys.) 1915, 799–801 (1915)].

[3] F. W. Dyson, A. S. Eddington, and C. Davidson. A Determination of the Deflection of Light by the Sun's Gravitational Field, from Observations Made at the Total Eclipse of May 29, 1919. *Phil. Trans. Roy. Soc. Lond. A*, 220:291–333, 1920. doi:10.1098/rsta.1920.0009.

[4] B. P. Abbott et al. Observation of Gravitational Waves from a Binary Black Hole Merger. *Phys. Rev. Lett.*, 116(6):061102, 2016. arXiv:1602.03837, doi:10.1103/PhysRevLett.116.061102.

[5] Kazunori Akiyama et al. First Sagittarius A* Event Horizon Telescope Results. I. The Shadow of the Supermassive Black Hole in the Center of the Milky Way. *Astrophys. J. Lett.*, 930(2):L12, 2022. doi:10.3847/2041-8213/ac6674.

[6] Kazunori Akiyama et al. First M87 Event Horizon Telescope Results. I. The Shadow of the Supermassive Black Hole. *Astrophys. J. Lett.*, 875:L1, 2019. arXiv:1906.11238, doi:10.3847/2041-8213/ab0ec7.

[7] Y. Foures-Bruhat. Theoreme d'existence pour certains systemes derivees partielles non lineaires. *Acta Mat.*, 88:141–225, 1952. doi:10.1007/BF02392131.

[8] Y. Choquet-Bruhat and Robert P. Geroch. Global aspects of the Cauchy problem in general relativity. *Commun. Math. Phys.*, 14:329–335, 1969. doi:10.1007/BF01645389.

[9] Olivier Sarbach, Gioel Calabrese, Jorge Pullin, and Manuel Tiglio. Hyperbolicity of the BSSN system of Einstein evolution equations. *Phys. Rev. D*, 66:064002, 2002. arXiv:gr-qc/0205064, doi:10.1103/PhysRevD.66.064002.

[10] Miguel Alcubierre. Introduction to 3+1 numerical relativity. *Introduction to 3+1 Numerical Relativity*, 04 2006. doi:10.1093/acprof:oso/9780199205677.001.0001.

[11] Yvonne Choquet-Bruhat. *General Relativity and the Einstein Equations*. Oxford Mathematical Monographs. Oxford University Press, United Kingdom, 2009.

[12] T. Nakamura, K. Oohara, and Y. Kojima. General Relativistic Collapse to Black Holes and Gravitational Waves from Black Holes. *Prog. Theor. Phys. Suppl.*, 90:1–218, 1987. doi:10.1143/PTPS.90.1.

[13] Eric Gourgoulhon. 3+1 formalism and bases of numerical relativity. 3 2007. arXiv:gr-qc/0703035.

[14] Einstein Toolkit: Open software for relativistic astrophysics. http://einsteintoolkit.org/.

[15] Miguel Zilhão and Frank Löffler. An Introduction to the Einstein Toolkit. *Int. J. Mod. Phys. A*, 28:1340014, 2013. arXiv:1305.5299, doi:10.1142/S0217751X13400149.

[16] Philippe Grandclement. Kadath: A Spectral solver for theoretical physics. *J. Comput. Phys.*, 229:3334–3357, 2010. arXiv:0909.1228, doi:10.1016/j.jcp.2010.01.005.

[17] Philippe Grandclement. Kadath libray, 2009. URL: https://kadath.obspm.fr/.

[18] David H. Weinberg, James S. Bullock, Fabio Governato, Rachel Kuzio de Naray, and Annika H. G. Peter. Cold dark matter: controversies on small scales. *Proc. Nat. Acad. Sci.*, 112:12249–12255, 2015. arXiv:1306.0913, doi:10.1073/pnas.1308716112.

[19] Antonino Del Popolo and Morgan Le Delliou. Small scale problems of the ΛCDM model: a short review. *Galaxies*, 5(1):17, 2017. arXiv:1606.07790, doi:10.3390/galaxies5010017.

[20] Tomohiro Nakama, Jens Chluba, and Marc Kamionkowski. Shedding light on the small-scale crisis with CMB spectral distortions. *Phys. Rev. D*, 95(12):121302, 2017. arXiv:1703.10559, doi:10.1103/PhysRevD.95.121302.

[21] B. Moore, S. Ghigna, F. Governato, G. Lake, Thomas R. Quinn, J. Stadel, and P. Tozzi. Dark matter substructure within galactic halos. *Astrophys. J. Lett.*, 524:L19–L22, 1999. arXiv:astro-ph/9907411, doi:10.1086/312287.

[22] Ben Moore, Thomas R. Quinn, Fabio Governato, Joachim Stadel, and George Lake. Cold collapse and the core catastrophe. *Mon. Not. Roy. Astron. Soc.*, 310:1147–1152, 1999. arXiv:astro-ph/9903164, doi:10.1046/j.1365-8711.1999.03039.x.

[23] Michael Boylan-Kolchin, James S. Bullock, and Manoj Kaplinghat. Too big to fail? The puzzling darkness of massive Milky Way subhaloes. *Mon. Not. Roy. Astron. Soc.*, 415:L40, 2011. arXiv:1103.0007, doi:10.1111/j.1745-3933.2011.01074.x.

[24] Juan Magana and Tonatiuh Matos. A brief Review of the Scalar Field Dark Matter model. *J. Phys. Conf. Ser.*, 378:012012, 2012. arXiv:1201.6107, doi:10.1088/1742-6596/378/1/012012.

[25] Abril Suárez, Victor H. Robles, and Tonatiuh Matos. A Review on the Scalar Field/Bose-Einstein Condensate Dark Matter Model. *Astrophys. Space Sci. Proc.*, 38:107–142, 2014. arXiv:1302.0903, doi:10.1007/978-3-319-02063-1_9.

[26] Lam Hui, Jeremiah P. Ostriker, Scott Tremaine, and Edward Witten. Ultralight scalars as cosmological dark matter. *Phys. Rev. D*, 95(4):043541, 2017. arXiv:1610.08297, doi:10.1103/PhysRevD.95.043541.

[27] L. Arturo Ureña López. Brief Review on Scalar Field Dark Matter Models. *Front. Astron. Space Sci.*, 6:47, 2019. doi:10.3389/fspas.2019.00047.

[28] Adam G. Riess et al. Observational evidence from supernovae for an accelerating universe and a cosmological constant. *Astron. J.*, 116:1009–1038, 1998. arXiv:astro-ph/9805201, doi:10.1086/300499.

[29] N. Aghanim et al. Planck 2018 results. VI. Cosmological parameters. *Astron. Astrophys.*, 641:A6, 2020. [Erratum: Astron.Astrophys. 652, C4 (2021)]. arXiv:1807.06209, doi:10.1051/0004-6361/201833910.

[30] Bharat Ratra and P. J. E. Peebles. Cosmological Consequences of a Rolling Homogeneous Scalar Field. *Phys. Rev. D*, 37:3406, 1988. doi:10.1103/PhysRevD.37.3406.

[31] R. R. Caldwell, Rahul Dave, and Paul J. Steinhardt. Cosmological imprint of an energy component with general equation of state. *Phys. Rev. Lett.*, 80:1582–1585, 1998. arXiv:astro-ph/9708069, doi:10.1103/PhysRevLett.80.1582.

[32] Sean M. Carroll. Quintessence and the rest of the world. *Phys. Rev. Lett.*, 81:3067–3070, 1998. arXiv:astro-ph/9806099, doi:10.1103/PhysRevLett.81.3067.

[33] S.M. Carroll. *Spacetime and Geometry: An Introduction to General Relativity*. Addison Wesley, 2004. URL: https://books.google.com.mx/books?id=1SKFQgAACAAJ.

[34] R. R. Caldwell. A Phantom menace? *Phys. Lett. B*, 545:23–29, 2002. arXiv:astro-ph/9908168, doi:10.1016/S0370-2693(02)02589-3.

[35] S. Westmoreland. ENERGY CONDITIONS AND SCALAR FIELD COSMOLOGY. Master's thesis, Kansas State U., 2013.

[36] Bo Feng, Xiu-Lian Wang, and Xin-Min Zhang. Dark energy constraints from the cosmic age and supernova. *Phys. Lett. B*, 607:35–41, 2005. arXiv:astro-ph/0404224, doi:10.1016/j.physletb.2004.12.071.

[37] Gong-Bo Zhao et al. Dynamical dark energy in light of the latest observations. *Nature Astron.*, 1(9):627–632, 2017. arXiv:1701.08165, doi:10.1038/s41550-017-0216-z.

[38] Jun-Qing Xia, Yi-Fu Cai, Tao-Tao Qiu, Gong-Bo Zhao, and Xinmin Zhang. Constraints on the Sound Speed of Dynamical Dark Energy. *Int. J. Mod. Phys. D*, 17:1229–1243, 2008. arXiv:astro-ph/0703202, doi:10.1142/S0218271808012784.

[39] Yi-Fu Cai, Emmanuel N. Saridakis, Mohammad R. Setare, and Jun-Qing Xia. Quintom Cosmology: Theoretical implications and observations. *Phys. Rept.*, 493:1–60, 2010. arXiv:0909.2776, doi:10.1016/j.physrep.2010.04.001.

[40] Hans Stephani, D. Kramer, Malcolm A. H. MacCallum, Cornelius Hoenselaers, and Eduard Herlt. *Exact solutions of Einstein's field equations*. Cambridge Monographs on Mathematical Physics. Cambridge Univ. Press, Cambridge, 2003. doi:10.1017/CBO9780511535185.

[41] Eloy Ayon-Beato and Alberto Garcia. Regular black hole in general relativity coupled to nonlinear electrodynamics. *Phys. Rev. Lett.*, 80:5056–5059, 1998. arXiv:gr-qc/9911046, doi:10.1103/PhysRevLett.80.5056.

[42] R. Bartnik and J. Mckinnon. Particle - Like Solutions of the Einstein Yang-Mills Equations. *Phys. Rev. Lett.*, 61:141–144, 1988. doi:10.1103/PhysRevLett.61.141.

[43] M. S. Volkov and D. V. Galtsov. NonAbelian Einstein Yang-Mills black holes. *JETP Lett.*, 50:346–350, 1989.

[44] David J. Kaup. Klein-Gordon Geon. *Phys. Rev.*, 172:1331–1342, 1968. doi:10.1103/PhysRev.172.1331.

[45] Remo Ruffini and Silvano Bonazzola. Systems of selfgravitating particles in general relativity and the concept of an equation of state. *Phys. Rev.*, 187:1767–1783, 1969. doi:10.1103/PhysRev.187.1767.

[46] Steven L. Liebling and Carlos Palenzuela. Dynamical Boson Stars. *Living Rev. Rel.*, 15:6, 2012. arXiv:1202.5809, doi:10.12942/lrr-2012-6.

[47] Edward Seidel and Wai-Mo Suen. Formation of solitonic stars through gravitational cooling. *Phys. Rev. Lett.*, 72:2516–2519, 1994. arXiv:gr-qc/9309015, doi:10.1103/PhysRevLett.72.2516.

[48] L. Arturo Urena-Lopez and Argelia Bernal. Bosonic gas as a Galactic Dark Matter Halo. *Phys. Rev. D*, 82:123535, 2010. arXiv:1008.1231, doi:10.1103/PhysRevD.82.123535.

[49] Diego F. Torres, S. Capozziello, and G. Lambiase. A Supermassive scalar star at the galactic center? *Phys. Rev. D*, 62:104012, 2000. arXiv:astro-ph/0004064, doi:10.1103/PhysRevD.62.104012.

[50] Jae-Weon Lee. Is dark matter a BEC or scalar field? *J. Korean Phys. Soc.*, 54:2622, 2009. arXiv:0801.1442, doi:10.3938/jkps.54.2622.

[51] Tanja Rindler-Daller and Paul R. Shapiro. Angular Momentum and Vortex Formation in Bose-Einstein-Condensed Cold Dark Matter Haloes. *Mon. Not. Roy. Astron. Soc.*, 422:135–161, 2012. arXiv:1106.1256, doi:10.1111/j.1365-2966.2012.20588.x.

[52] Richard Brito, Vitor Cardoso, Carlos A. R. Herdeiro, and Eugen Radu. Proca stars: Gravitating Bose–Einstein condensates of massive spin 1 particles. *Phys. Lett. B*, 752:291–295, 2016. arXiv:1508.05395, doi:10.1016/j.physletb.2015.11.051.

[53] Felix Finster, Joel Smoller, and Shing-Tung Yau. Particle - like solutions of the Einstein-Dirac equations. *Phys. Rev. D*, 59:104020, 1999. arXiv:gr-qc/9801079, doi:10.1103/PhysRevD.59.104020.

[54] Carlos A. R. Herdeiro, Alexandre M. Pombo, and Eugen Radu. Asymptotically flat scalar, Dirac and Proca stars: discrete vs. continuous families of solutions. *Phys. Lett. B*, 773:654–662, 2017. arXiv:1708.05674, doi:10.1016/j.physletb.2017.09.036.

[55] Marcelo Gleiser and Richard Watkins. Gravitational Stability of Scalar Matter. *Nucl. Phys. B*, 319:733–746, 1989. doi:10.1016/0550-3213(89)90627-5.

[56] Edward Seidel and Wai-Mo Suen. Dynamical Evolution of Boson Stars. 1. Perturbing the Ground State. *Phys. Rev. D*, 42:384–403, 1990. doi:10.1103/PhysRevD.42.384.

[57] C. Palenzuela, I. Olabarrieta, L. Lehner, and Steven L. Liebling. Head-on collisions of boson stars. *Phys. Rev. D*, 75:064005, 2007. arXiv:gr-qc/0612067, doi:10.1103/PhysRevD.75.064005.

[58] Miguel Bezares, Carlos Palenzuela, and Carles Bona. Final fate of compact boson star mergers. *Phys. Rev. D*, 95(12):124005, 2017. arXiv:1705.01071, doi:10.1103/PhysRevD.95.124005.

[59] Miguel Bezares and Carlos Palenzuela. Gravitational Waves from Dark Boson Star binary mergers. *Class. Quant. Grav.*, 35(23):234002, 2018. arXiv:1808.10732, doi:10.1088/1361-6382/aae87c.

[60] Nicolas Sanchis-Gual, Carlos Herdeiro, Eugen Radu, Juan Carlos Degollado, and José A. Font. Numerical evolutions of spherical Proca stars. *Phys. Rev. D*, 95(10):104028, 2017. arXiv:1702.04532, doi:10.1103/PhysRevD.95.104028.

[61] Fabrizio Di Giovanni, Nicolas Sanchis-Gual, Carlos A. R. Herdeiro, and José A. Font. Dynamical formation of Proca stars and quasistationary solitonic objects. *Phys. Rev. D*, 98(6):064044, 2018. arXiv:1803.04802, doi:10.1103/PhysRevD.98.064044.

[62] Nicolas Sanchis-Gual, Carlos Herdeiro, José A. Font, Eugen Radu, and Fabrizio Di Giovanni. Head-on collisions and orbital mergers of Proca stars. *Phys. Rev. D*, 99(2):024017, 2019. arXiv:1806.07779, doi:10.1103/PhysRevD.99.024017.

[63] N. Sanchis-Gual, F. Di Giovanni, M. Zilhão, C. Herdeiro, P. Cerdá-Durán, J. A. Font, and E. Radu. Nonlinear Dynamics of Spinning Bosonic Stars: Formation and Stability. *Phys. Rev. Lett.*, 123(22):221101, 2019. arXiv:1907.12565, doi:10.1103/PhysRevLett.123.221101.

[64] Bohua Li, Tanja Rindler-Daller, and Paul R. Shapiro. Cosmological Constraints on Bose-Einstein-Condensed Scalar Field Dark Matter. *Phys. Rev. D*, 89(8):083536, 2014. arXiv:1310.6061, doi:10.1103/PhysRevD.89.083536.

[65] Abril Suárez and Pierre-Henri Chavanis. Cosmological evolution of a complex scalar field with repulsive or attractive self-interaction. *Phys. Rev. D*, 95(6):063515, 2017. arXiv:1608.08624, doi:10.1103/PhysRevD.95.063515.

[66] Robert M. Wald. *General Relativity*. Chicago Univ. Pr., Chicago, USA, 1984. doi:10.7208/chicago/9780226870373.001.0001.

[67] A. Friedman. On the Curvature of space. *Z. Phys.*, 10:377–386, 1922. doi:10.1007/BF01332580.

[68] S. Meliujin. *El problema de lo finito y lo infinito*. Grijalbo, México, 1960.

[69] M. Omelianovski. *El Materialismo y la Teoría de la Relatividad*. Colección 70. Grijalbo, México, 1969.

[70] Eréndira Gutiérrez-Luna, Belen Carvente, Víctor Jaramillo, Juan Barranco, Celia Escamilla-Rivera, Catalina Espinoza, Myriam Mondragón, and Darío Núñez. Scalar field dark matter with two components: Combined approach from particle physics and cosmology. *Phys. Rev. D*, 105(8):083533, 2022. arXiv:2110.10258, doi:10.1103/PhysRevD.105.083533.

[71] Bohua Li, Paul R. Shapiro, and Tanja Rindler-Daller. Bose-Einstein-condensed scalar field dark matter and the gravitational wave background from inflation: new cosmological constraints and its detectability by LIGO. *Phys. Rev. D*, 96(6):063505, 2017. arXiv:1611.07961, doi:10.1103/PhysRevD.96.063505.

[72] Saikat Chakraborty, Esteban González, Genly Leon, and Bin Wang. Time-averaging axion-like interacting scalar fields models. *Eur. Phys. J. C*, 81(11):1039, 2021. arXiv:2107.04651, doi:10.1140/epjc/s10052-021-09802-5.

[73] L. O. Téllez-Tovar, Tonatiuh Matos, and J. Alberto Vázquez. Cosmological constraints on the multiscalar field dark matter model. *Phys. Rev. D*,

106(12):123501, 2022. arXiv:2112.09337, doi:10.1103/PhysRevD.106.123501.

[74] Mateja Gosenca, Andrew Eberhardt, Yourong Wang, Benedikt Eggemeier, Emily Kendall, J. Luna Zagorac, and Richard Easther. Multifield Ultralight Dark Matter. 1 2023. arXiv:2301.07114.

[75] Gianpiero Mangano, Gennaro Miele, Sergio Pastor, Teguayco Pinto, Ofelia Pisanti, and Pasquale D. Serpico. Relic neutrino decoupling including flavor oscillations. *Nucl. Phys. B*, 729:221–234, 2005. arXiv:hep-ph/0506164, doi:10.1016/j.nuclphysb.2005.09.041.

[76] Max Pettini and Ryan Cooke. A new, precise measurement of the primordial abundance of Deuterium. *Mon. Not. Roy. Astron. Soc.*, 425:2477–2486, 2012. arXiv:1205.3785, doi:10.1111/j.1365-2966.2012.21665.x.

[77] Y. I. Izotov, G. Stasinska, and N. G. Guseva. Primordial 4He abundance: a determination based on the largest sample of HII regions with a methodology tested on model HII regions. *Astron. Astrophys.*, 558:A57, 2013. arXiv:1308.2100, doi:10.1051/0004-6361/201220782.

[78] Gary Steigman. Neutrinos And Big Bang Nucleosynthesis. *Adv. High Energy Phys.*, 2012:268321, 2012. arXiv:1208.0032, doi:10.1155/2012/268321.

[79] Kenneth M. Nollett and Gary Steigman. BBN And The CMB Constrain Neutrino Coupled Light WIMPs. *Phys. Rev. D*, 91(8):083505, 2015. arXiv:1411.6005, doi:10.1103/PhysRevD.91.083505.

[80] Belen Carvente, Víctor Jaramillo, Celia Escamilla-Rivera, and Darío Núñez. Observational constraints on complex quintessence with attractive self-interaction. *Mon. Not. Roy. Astron. Soc.*, 503(3):4008–4015, 2021. arXiv:2008.11211, doi:10.1093/mnras/stab650.

[81] E. A. Cornell and C. E. Wieman. Nobel Lecture: Bose-Einstein condensation in a dilute gas, the first 70 years and some recent experiments. *Rev. Mod. Phys.*, 74:875–893, 2002. doi:10.1103/RevModPhys.74.875.

[82] Juan Barranco, Argelia Bernal, Juan Carlos Degollado, Alberto Diez-Tejedor, Miguel Megevand, Miguel Alcubierre, Dario Nunez, and Olivier Sarbach. Are black holes a serious threat to scalar field dark matter models? *Phys. Rev. D*, 84:083008, 2011. arXiv:1108.0931, doi:10.1103/PhysRevD.84.083008.

[83] J. Barranco and A. Bernal. Self-gravitating system made of axions. *Phys. Rev. D*, 83:043525, 2011. arXiv:1001.1769, doi:10.1103/PhysRevD.83.043525.

[84] Latham A. Boyle, Robert R. Caldwell, and Marc Kamionkowski. Spintessence! New models for dark matter and dark energy. *Phys. Lett. B*, 545:17–22, 2002. arXiv:astro-ph/0105318, doi:10.1016/S0370-2693(02)02590-X.

[85] Miguel Alcubierre, Juan Barranco, Argelia Bernal, Juan Carlos Degollado, Alberto Diez-Tejedor, Víctor Jaramillo, Miguel Megevand, Darío Núñez, and Olivier Sarbach. Extreme ℓ-boson stars. *Class. Quant. Grav.*, 39(9):094001, 2022. arXiv:2112.04529, doi:10.1088/1361-6382/ac5fc2.

[86] P. A. Zyla et al. Review of Particle Physics. *PTEP*, 2020(8):083C01, 2020. doi:10.1093/ptep/ptaa104.

[87] David J. E. Marsh. Axion Cosmology. *Phys. Rept.*, 643:1–79, 2016. arXiv:1510.07633, doi:10.1016/j.physrep.2016.06.005.

[88] Jens C. Niemeyer. Small-scale structure of fuzzy and axion-like dark matter. 12 2019. arXiv:1912.07064, doi:10.1016/j.ppnp.2020.103787.

[89] Wayne Hu, Rennan Barkana, and Andrei Gruzinov. Fuzzy Cold Dark Matter: The wave properties of ultralight particles. *Phys. Rev. Lett.*, 85:1158–1161, 2000. arXiv:astro-ph/0003365, doi:10.1103/PhysRevLett.85.1158.

[90] Tonatiuh Matos, Francisco Siddhartha Guzman, and L. Arturo Ureña López. Scalar field as dark matter in the universe. *Class. Quantum Grav.*, 17:1707–1712, 2000. arXiv:astro-ph/9908152, doi:10.1088/0264-9381/17/7/309.

[91] Tonatiuh Matos and L. Arturo Ureña López. A further analysis of a cosmological model of quintessence and scalar dark matter. *Phys. Rev.*, D63:063506, 2001. arXiv:astro-ph/0006024, doi:10.1103/PhysRevD.63.063506.

[92] Hans A. Buchdahl. General Relativistic Fluid Spheres. *Phys. Rev.*, 116:1027, 1959. doi:10.1103/PhysRev.116.1027.

[93] Vitor Cardoso and Paolo Pani. Testing the nature of dark compact objects: a status report. *Living Rev. Rel.*, 22(1):4, 2019. arXiv:1904.05363, doi:10.1007/s41114-019-0020-4.

[94] Carlos Palenzuela, Paolo Pani, Miguel Bezares, Vitor Cardoso, Luis Lehner, and Steven Liebling. Gravitational Wave Signatures of Highly Compact Boson Star Binaries. *Phys. Rev. D*, 96(10):104058, 2017. arXiv:1710.09432, doi:10.1103/PhysRevD.96.104058.

[95] Juan Calderón Bustillo, Nicolas Sanchis-Gual, Alejandro Torres-Forné, José A. Font, Avi Vajpeyi, Rory Smith, Carlos Herdeiro, Eugen Radu, and Samson H. W. Leong. GW190521 as a Merger of Proca Stars: A Potential New Vector Boson of 8.7×10^{-13} eV. *Phys. Rev. Lett.*, 126(8):081101, 2021. arXiv:2009.05376, doi:10.1103/PhysRevLett.126.081101.

[96] Alma X. Gonzalez-Morales, David J. E. Marsh, Jorge Penarrubia, and Luis Ureña López. Unbiased constraints on ultralight axion mass from dwarf spheroidal galaxies. [arXiv:1609.05856], 2016. arXiv:1609.05856.

[97] Victor H. Robles, James S. Bullock, and Michael Boylan-Kolchin. Scalar Field Dark Matter: Helping or Hurting Small-Scale Problems in Cosmology? *Mon. Not. Roy. Astron. Soc.*, 483(1):289–298, 2019. arXiv:1807.06018, doi:10.1093/mnras/sty3190.

[98] Hsi-Yu Schive, Tzihong Chiueh, and Tom Broadhurst. Cosmic Structure as the Quantum Interference of a Coherent Dark Wave. *Nature Phys.*, 10:496–499, 2014. arXiv:1406.6586, doi:10.1038/nphys2996.

[99] Miguel Alcubierre, Juan Barranco, Argelia Bernal, Juan Carlos Degollado, Alberto Diez-Tejedor, Miguel Megevand, Darío Núñez, and Olivier Sarbach. ℓ-Boson stars. *Class. Quant. Grav.*, 35(19):19LT01, 2018. arXiv:1805.11488, doi:10.1088/1361-6382/aadcb6.

[100] Ignacio Olabarrieta, Jason F. Ventrella, Matthew W. Choptuik, and William G. Unruh. Critical Behavior in the Gravitational Collapse of a Scalar Field with Angular Momentum in Spherical Symmetry. *Phys. Rev.*, D76:124014, 2007. arXiv:0708.0513, doi:10.1103/PhysRevD.76.124014.

[101] Miguel Alcubierre, Juan Barranco, Argelia Bernal, Juan Carlos Degollado, Alberto Diez-Tejedor, Miguel Megevand, Darío Núñez, and Olivier Sarbach. Dynamical evolutions of ℓ-boson stars in spherical symmetry. *Class. Quant. Grav.*, 36(21):215013, 2019. arXiv:1906.08959, doi:10.1088/1361-6382/ab4726.

[102] Miguel Alcubierre, Juan Barranco, Argelia Bernal, Juan Carlos Degollado, Alberto Diez-Tejedor, Miguel Megevand, Darío Núñez, and Olivier Sarbach. On the linear stability of ℓ-boson stars with respect to radial perturbations.

Class. Quant. Grav., 38(17):174001, 2021. arXiv:2103.15012, doi:10.1088/1361-6382/ac0160.

[103] Víctor Jaramillo, Nicolas Sanchis-Gual, Juan Barranco, Argelia Bernal, Juan Carlos Degollado, Carlos Herdeiro, and Darío Núñez. Dynamical ℓ -boson stars: Generic stability and evidence for nonspherical solutions. *Phys. Rev. D*, 101(12):124020, 2020. arXiv:2004.08459, doi:10.1103/PhysRevD.101.124020.

[104] Nicolas Sanchis-Gual, Fabrizio Di Giovanni, Carlos Herdeiro, Eugen Radu, and José A. Font. Multifield, Multifrequency Bosonic Stars and a Stabilization Mechanism. *Phys. Rev. Lett.*, 126(24):241105, 2021. arXiv:2103.12136, doi:10.1103/PhysRevLett.126.241105.

[105] F. S. Guzmán and L. Arturo Ureña López. Gravitational atoms: General framework for the construction of multistate axially symmetric solutions of the Schrödinger-Poisson system. *Phys. Rev. D*, 101(8):081302, 2020. arXiv:1912.10585, doi:10.1103/PhysRevD.101.081302.

[106] Marcelo Gleiser. Stability of Boson Stars. *Phys. Rev.*, D38:2376, 1988. [Erratum: Phys. Rev.D39,no.4,1257(1989)]. doi:10.1103/PhysRevD.38.2376,10.1103/PhysRevD.39.1257.

[107] Krsna Dev and Marcelo Gleiser. Anisotropic stars: Exact solutions. *Gen. Rel. Grav.*, 34:1793–1818, 2002. arXiv:astro-ph/0012265, doi:10.1023/A:1020707906543.

[108] Juan Barranco, Javier Chagoya, Alberto Diez-Tejedor, Gustavo Niz, and Armando A. Roque. Horndeski stars. *JCAP*, 10:022, 8 2021. arXiv:2108.01679, doi:10.1088/1475-7516/2021/10/022.

[109] Pedro V. P. Cunha, Emanuele Berti, and Carlos A. R. Herdeiro. Light-Ring Stability for Ultracompact Objects. *Phys. Rev. Lett.*, 119(25):251102, 2017. arXiv:1708.04211, doi:10.1103/PhysRevLett.119.251102.

[110] Hakan Andreasson and Gerhard Rein. On the steady states of the spherically symmetric Einstein-Vlasov system. *Class. Quant. Grav.*, 24:1809–1832, 2007. arXiv:gr-qc/0611053, doi:10.1088/0264-9381/24/7/008.

[111] Hakan Andreasson. On static shells and the Buchdahl inequality for the spherically symmetric Einstein-Vlasov system. *Commun. Math. Phys.*, 274:409–425, 2007. arXiv:gr-qc/0605151, doi:10.1007/s00220-007-0285-4.

[112] Jayashree Balakrishna, Edward Seidel, and Wai-Mo Suen. Dynamical evolution of boson stars. 2. Excited states and selfinteracting fields. *Phys. Rev. D*, 58:104004, 1998. arXiv:gr-qc/9712064, doi:10.1103/PhysRevD.58.104004.

[113] Argelia Bernal, Juan Barranco, Daniela Alic, and Carlos Palenzuela. Multistate Boson Stars. *Phys. Rev. D*, 81:044031, 2010. arXiv:0908.2435, doi:10.1103/PhysRevD.81.044031.

[114] W. H. Press, B. P. Flannery, S. A. Teukolsky, and W. T. Vetterling. *Numerical Recipes*. Cambridge University Press, Cambridge, England, 1986.

[115] Miguel Megevand, Ignacio Olabarrieta, and Luis Lehner. Scalar field confinement as a model for accreting systems. *Class. Quantum Grav.*, 24:3235–3258, 2007. arXiv:0705.0644, doi:10.1088/0264-9381/24/13/007.

[116] Philippe Grandclément and Jerome Novak. Spectral methods for numerical relativity. *Living Rev. Rel.*, 12:1, 2009. arXiv:0706.2286, doi:10.12942/lrr-2009-1.

[117] Philippe Grandclément, Claire Somé, and Eric Gourgoulhon. Models of rotating boson stars and geodesics around them: new type of orbits. *Phys. Rev. D*, 90(2):024068, 2014. arXiv:1405.4837, doi:10.1103/PhysRevD.90.024068.

[118] Víctor Jaramillo, Erik Jiménez-Vázquez, and Darío Núñez. Confinement of exotic matter: Static solutions. *Phys. Rev. D*, 107(6):064061, 2023. arXiv:2302.07889, doi:10.1103/PhysRevD.107.064061.

[119] K. A. Bronnikov. Scalar-tensor theory and scalar charge. *Acta Phys. Polon. B*, 4:251–266, 1973.

[120] Tonatiuh Matos and Dario Nunez. Rotating scalar field wormhole. *Class. Quant. Grav.*, 23:4485–4496, 2006. arXiv:gr-qc/0508117, doi:10.1088/0264-9381/23/13/012.

[121] Vladimir Dzhunushaliev, Vladimir Folomeev, Burkhard Kleihaus, and Jutta Kunz. Wormhole solutions with a complex ghost scalar field and their instability. *Phys. Rev. D*, 97(2):024002, 2018. arXiv:1710.01884, doi:10.1103/PhysRevD.97.024002.

[122] Belen Carvente, Víctor Jaramillo, Juan Carlos Degollado, Darío Núñez, and Olivier Sarbach. Traversable ℓ-wormholes supported by ghost scalar fields. *Class. Quant. Grav.*, 36(23):235005, 2019. arXiv:1906.08295, doi:10.1088/1361-6382/ab4dfb.

[123] Xiao Yan Chew, Vladimir Dzhunushaliev, Vladimir Folomeev, Burkhard Kleihaus, and Jutta Kunz. Rotating wormhole solutions with a complex phantom scalar field. *Phys. Rev. D*, 100(4):044019, 2019. arXiv:1906.08742, doi:10.1103/PhysRevD.100.044019.

[124] Vladimir Dzhunushaliev, Vladimir Folomeev, Ratbay Myrzakulov, and Douglas Singleton. Non-singular solutions to Einstein-Klein-Gordon equations with a phantom scalar field. *JHEP*, 07:094, 2008. arXiv:0805.3211, doi:10.1088/1126-6708/2008/07/094.

[125] Darío Núñez. Discussion on dark matter nature. *AIP Conf. Proc.*, 1577(1):208–212, 2015. doi:10.1063/1.4861956.

[126] Pedro V. P. Cunha, Carlos Herdeiro, Eugen Radu, and Nicolas Sanchis-Gual. The fate of the light-ring instability. 7 2022. arXiv:2207.13713.

[127] Pedro V. P. Cunha, Carlos Herdeiro, Eugen Radu, and Nicolas Sanchis-Gual. Exotic Compact Objects and the Fate of the Light-Ring Instability. *Phys. Rev. Lett.*, 130(6):061401, 2023. doi:10.1103/PhysRevLett.130.061401.

[128] Víctor Jaramillo and Darío Núñez. Magnetostatic boson stars. *Phys. Rev. D*, 106(10):104023, 2022. arXiv:2209.07549, doi:10.1103/PhysRevD.106.104023.

[129] J. Kunz, I. Perapechka, and Ya Shnir. Kerr black holes with synchronised scalar hair and boson stars in the Einstein-Friedberg-Lee-Sirlin model. *JHEP*, 07:109, 2019. arXiv:1904.13379, doi:10.1007/JHEP07(2019)109.

[130] Vladimir Dzhunushaliev, Vladimir Folomeev, Christian Hoffmann, Burkhard Kleihaus, and Jutta Kunz. Boson Stars with Nontrivial Topology. *Phys. Rev. D*, 90(12):124038, 2014. arXiv:1409.6978, doi:10.1103/PhysRevD.90.124038.

[131] Eric Poisson. *A Relativist's Toolkit: The Mathematics of Black-Hole Mechanics*. Cambridge University Press, 12 2009. doi:10.1017/CBO9780511606601.

[132] M. Colpi, S. L. Shapiro, and I. Wasserman. Boson Stars: Gravitational Equilibria of Selfinteracting Scalar Fields. *Phys. Rev. Lett.*, 57:2485–2488, 1986. doi:10.1103/PhysRevLett.57.2485.

[133] Guilherme Raposo, Paolo Pani, Miguel Bezares, Carlos Palenzuela, and Vitor Cardoso. Anisotropic stars as ultracompact objects in General Relativity. *Phys. Rev. D*, 99(10):104072, 2019. arXiv:1811.07917, doi:10.1103/PhysRevD.99.104072.

[134] Paolo Pani. I-Love-Q relations for gravastars and the approach to the black-hole limit. *Phys. Rev. D*, 92(12):124030, 2015. [Erratum: Phys.Rev.D 95, 049902 (2017)]. arXiv:1506.06050, doi:10.1103/PhysRevD.95.049902.

[135] Hakan Andreasson. Sharp bounds on 2m/r of general spherically symmetric static objects. *J. Diff. Eq.*, 245:2243–2266, 2008. arXiv:gr-qc/0702137, doi:10.1016/j.jde.2008.05.010.

[136] Artur Alho, José Natário, Paolo Pani, and Guilherme Raposo. Compactness bounds in general relativity. *Phys. Rev. D*, 106(4):L041502, 2022. arXiv:2202.00043, doi:10.1103/PhysRevD.106.L041502.

[137] Vitor Cardoso, Caio F. B. Macedo, Kei-ichi Maeda, and Hirotada Okawa. ECO-spotting: looking for extremely compact objects with bosonic fields. *Class. Quant. Grav.*, 39(3):034001, 2022. arXiv:2112.05750, doi:10.1088/1361-6382/ac41e7.

[138] S. Krasnikov. A Traversable wormhole. *Phys. Rev.*, D62:084028, 2000. [Erratum: Phys. Rev.D76,109902(2007)]. arXiv:gr-qc/9909016, doi:10.1103/PhysRevD.62.084028,10.1103/PhysRevD.76.109902.

[139] Matt Visser, Sayan Kar, and Naresh Dadhich. Traversable wormholes with arbitrarily small energy condition violations. *Phys. Rev. Lett.*, 90:201102, 2003. arXiv:gr-qc/0301003, doi:10.1103/PhysRevLett.90.201102.

[140] Francisco S. N. Lobo. Energy conditions, traversable wormholes and dust shells. *Gen. Rel. Grav.*, 37:2023–2038, 2005. arXiv:gr-qc/0410087, doi:10.1007/s10714-005-0177-x.

[141] Francisco S. N. Lobo. Phantom energy traversable wormholes. *Phys. Rev.*, D71:084011, 2005. arXiv:gr-qc/0502099, doi:10.1103/PhysRevD.71.084011.

[142] Francisco S. N. Lobo. Stability of phantom wormholes. *Phys. Rev.*, D71:124022, 2005. arXiv:gr-qc/0506001, doi:10.1103/PhysRevD.71.124022.

[143] John L. Friedman, Kristin Schleich, and Donald M. Witt. Topological censorship. *Phys. Rev. Lett.*, 71:1486–1489, 1993. [Erratum:

Phys. Rev. Lett.75,1872(1995)]. arXiv:gr-qc/9305017, doi:10.1103/PhysRevLett.75.1872,10.1103/PhysRevLett.71.1486.

[144] C. Armendariz-Picon, Viatcheslav F. Mukhanov, and Paul J. Steinhardt. A Dynamical solution to the problem of a small cosmological constant and late time cosmic acceleration. *Phys. Rev. Lett.*, 85:4438–4441, 2000. arXiv:astro-ph/0004134, doi:10.1103/PhysRevLett.85.4438.

[145] J. Garriga and A. Vilenkin. Solutions to the cosmological constant problems. *Phys. Rev.*, D64:023517, 2001. arXiv:hep-th/0011262, doi:10.1103/PhysRevD.64.023517.

[146] Dragan Huterer and Michael S. Turner. Probing the dark energy: Methods and strategies. *Phys. Rev.*, D64:123527, 2001. arXiv:astro-ph/0012510, doi:10.1103/PhysRevD.64.123527.

[147] Edmund J. Copeland, M. Sami, and Shinji Tsujikawa. Dynamics of dark energy. *Int. J. Mod. Phys.*, D15:1753–1936, 2006. arXiv:hep-th/0603057, doi:10.1142/S021827180600942X.

[148] Celia Escamilla-Rivera, Ruth Lazkoz, Vincenzo Salzano, and Irene Sendra. Tension between SN and BAO: current status and future forecasts. *JCAP*, 1109:003, 2011. arXiv:1103.2386, doi:10.1088/1475-7516/2011/09/003.

[149] Eyal A. Kazin et al. The WiggleZ Dark Energy Survey: improved distance measurements to z = 1 with reconstruction of the baryonic acoustic feature. *Mon. Not. Roy. Astron. Soc.*, 441(4):3524–3542, 2014. arXiv:1401.0358, doi:10.1093/mnras/stu778.

[150] H. G. Ellis. Ether flow through a drainhole - a particle model in general relativity. *J. Math. Phys.*, 14:104–118, 1973. doi:10.1063/1.1666161.

[151] M. S. Morris and K. S. Thorne. Wormholes in space-time and their use for interstellar travel: A tool for teaching general relativity. *Am. J. Phys.*, 56:395–412, 1988. doi:10.1119/1.15620.

[152] Francisco S. N. Lobo. Exotic solutions in General Relativity: Traversable wormholes and 'warp drive' spacetimes. In *Classical and Quantum Gravity Research, 1-78, (2008), Nova Sci. Pub. ISBN 978-1-60456-366-5*. 2007. arXiv:0710.4474.

[153] Matt Visser. *Lorentzian wormholes: From Einstein to Hawking*. 1995.

[154] Panagiota Kanti, Burkhard Kleihaus, and Jutta Kunz. Wormholes in Dilatonic Einstein-Gauss-Bonnet Theory. *Phys. Rev. Lett.*, 107:271101, 2011. doi:10.1103/PhysRevLett.107.271101.

[155] Eloy Ayon-Beato, Fabrizio Canfora, and Jorge Zanelli. Analytic self-gravitating Skyrmions, cosmological bounces and AdS wormholes. *Phys. Lett.*, B752:201–205, 2016. doi:10.1016/j.physletb.2015.11.065.

[156] Elisabetta Majerotto, Domenico Sapone, and Luca Amendola. Supernovae Type Ia data favour negatively coupled phantom energy. *Submitted to: Phys. Rev. D*, 2004. arXiv:astro-ph/0410543.

[157] J. A. Gonzalez, F. S. Guzman, and O. Sarbach. Instability of wormholes supported by a ghost scalar field. I. Linear stability analysis. *Class. Quant. Grav.*, 26:015010, 2009. arXiv:0806.0608, doi:10.1088/0264-9381/26/1/015010.

[158] J. A. Gonzalez, F. S. Guzman, and O. Sarbach. Instability of wormholes supported by a ghost scalar field. II. Nonlinear evolution. *Class. Quant. Grav.*, 26:015011, 2009. arXiv:0806.1370, doi:10.1088/0264-9381/26/1/015011.

[159] F. S. Guzman and J. M. Rueda-Becerril. Spherical boson stars as black hole mimickers. *Phys. Rev. D*, 80:084023, 2009. arXiv:1009.1250, doi:10.1103/PhysRevD.80.084023.

[160] Carlos A. R. Herdeiro, Alexandre M. Pombo, Eugen Radu, Pedro V. P. Cunha, and Nicolas Sanchis-Gual. The imitation game: Proca stars that can mimic the Schwarzschild shadow. *JCAP*, 04:051, 2021. arXiv:2102.01703, doi:10.1088/1475-7516/2021/04/051.

[161] Shinji Tsujikawa. Quintessence: A Review. *Class. Quant. Grav.*, 30:214003, 2013. arXiv:1304.1961, doi:10.1088/0264-9381/30/21/214003.

[162] Alan H. Guth. The Inflationary Universe: A Possible Solution to the Horizon and Flatness Problems. *Phys. Rev. D*, 23:347–356, 1981. doi:10.1103/PhysRevD.23.347.

[163] P. Jetzer and J. J. van der Bij. CHARGED BOSON STARS. *Phys. Lett. B*, 227:341–346, 1989. doi:10.1016/0370-2693(89)90941-6.

[164] Shijun Yoshida and Yoshiharu Eriguchi. Rotating boson stars in general relativity. *Phys. Rev. D*, 56:762–771, 1997. doi:10.1103/PhysRevD.56.762.

[165] Lucas G. Collodel, Burkhard Kleihaus, and Jutta Kunz. Structure of rotating charged boson stars. *Phys. Rev. D*, 99(10):104076, 2019. arXiv:1901.11522, doi:10.1103/PhysRevD.99.104076.

[166] C. A. R. Herdeiro, J. Kunz, I. Perapechka, E. Radu, and Ya. Shnir. Multipolar boson stars: macroscopic Bose-Einstein condensates akin to hydrogen orbitals. *Phys. Lett. B*, 812:136027, 2021. arXiv:2008.10608, doi:10.1016/j.physletb.2020.136027.

[167] M. Bocquet, S. Bonazzola, E. Gourgoulhon, and J. Novak. Rotating neutron star models with magnetic field. *Astron. Astrophys.*, 301:757, 1995. arXiv:gr-qc/9503044.

[168] Christian Y. Cardall, Madappa Prakash, and James M. Lattimer. Effects of strong magnetic fields on neutron star structure. *Astrophys. J.*, 554:322–339, 2001. arXiv:astro-ph/0011148, doi:10.1086/321370.

[169] Debarati Chatterjee, Thomas Elghozi, Jerome Novak, and Micaela Oertel. Consistent neutron star models with magnetic field dependent equations of state. *Mon. Not. Roy. Astron. Soc.*, 447:3785, 2015. arXiv:1410.6332, doi:10.1093/mnras/stu2706.

[170] Asaf Oron. Relativistic magnetized star with poloidal and toroidal fields. *Phys. Rev. D*, 66:023006, 2002. doi:10.1103/PhysRevD.66.023006.

[171] Kenta Kiuchi and Shijun Yoshida. Relativistic stars with purely toroidal magnetic fields. *Phys. Rev. D*, 78:044045, 2008. arXiv:0802.2983, doi:10.1103/PhysRevD.78.044045.

[172] Joachim Frieben and Luciano Rezzolla. Equilibrium models of relativistic stars with a toroidal magnetic field. *Mon. Not. Roy. Astron. Soc.*, 427:3406–3426, 2012. arXiv:1207.4035, doi:10.1111/j.1365-2966.2012.22027.x.

[173] S. W. Hawking and G. F. R. Ellis. *The Large Scale Structure of Space-Time*. Cambridge Monographs on Mathematical Physics. Cambridge University Press, 2 2011. doi:10.1017/CBO9780511524646.

[174] Santiago Ontanon and Miguel Alcubierre. Rotating boson stars using finite differences and global Newton methods. *Class. Quant. Grav.*, 38(15):154003, 2021. arXiv:2103.13993, doi:10.1088/1361-6382/ac0b53.

[175] Eric Gourgoulhon. An Introduction to the theory of rotating relativistic stars. In *CompStar 2010: School and Workshop on Computational Tools for Compact Star Astrophysics*, 3 2010. arXiv:1003.5015.

[176] C. A. R. Herdeiro, J. Kunz, I. Perapechka, E. Radu, and Y. Shnir. Chains of Boson Stars. *Phys. Rev. D*, 103(6):065009, 2021. arXiv:2101.06442, doi:10.1103/PhysRevD.103.065009.

[177] G. Quintero Angulo, A. Pérez Martínez, H. Pérez Rojas, and D. Manreza Paret. (Self-)Magnetized Bose–Einstein condensate stars. *Int. J. Mod. Phys. D*, 28(10):1950135, 2019. arXiv:1812.07657, doi:10.1142/S0218271819501359.

[178] Daniela Pugliese, Hernando Quevedo, Jorge A. Rueda H., and Remo Ruffini. On charged boson stars. *Phys. Rev. D*, 88:024053, 2013. arXiv:1305.4241, doi:10.1103/PhysRevD.88.024053.

[179] Ts.I. Gutsunaev and V.S. Manko. On the gravitational field of a mass possessing a magnetic dipole moment. *Physics Letters A*, 123(5):215–216, 1987. doi:https://doi.org/10.1016/0375-9601(87)90063-6.

[180] William B. Bonnor. An exact solution of the einstein-maxwell equations referring to a magnetic dipole. *Zeitschrift für Physik*, 190:444–445, 1966.

[181] Victoria M. Kaspi and Andrei Beloborodov. Magnetars. *Ann. Rev. Astron. Astrophys.*, 55:261–301, 2017. arXiv:1703.00068, doi:10.1146/annurev-astro-081915-023329.

[182] S. Bonazzola, E. Gourgoulhon, M. Salgado, and J. A. Marck. Axisymmetric rotating relativistic bodies: A new numerical approach for 'exact' solutions. *Astron. Astrophys.*, 278:421–443, 1993.

[183] Shijun Yoshida and Yoshiharu Eriguchi. New static axisymmetric and nonvacuum solutions in general relativity: Equilibrium solutions of boson stars. *Phys. Rev. D*, 55:1994–2001, 1997. doi:10.1103/PhysRevD.55.1994.

[184] R. Friedberg, T. D. Lee, and A. Sirlin. A Class of Scalar-Field Soliton Solutions in Three Space Dimensions. *Phys. Rev. D*, 13:2739–2761, 1976. doi:10.1103/PhysRevD.13.2739.

[185] A. Levin and V. Rubakov. Q-balls with scalar charges. *Mod. Phys. Lett. A*, 26:409–413, 2011. arXiv:1010.0030, doi:10.1142/S0217732311034992.

[186] J. Kunz, V. Loiko, and Ya. Shnir. U(1) gauged boson stars in the Einstein-Friedberg-Lee-Sirlin model. *Phys. Rev. D*, 105(8):085013, 2022. arXiv:2112.06626, doi:10.1103/PhysRevD.105.085013.

[187] Viktor Loiko, Ilya Perapechka, and Yakov Shnir. Q-chains in the $U(1)$ gauged Friedberg-Lee-Sirlin model. *EPL*, 133(4):41001, 2021. arXiv:2012.01052, doi:10.1209/0295-5075/133/41001.

[188] P. Cunha, C. Herdeiro, E. Radu, and Ya. Shnir. Two boson stars in equilibrium. *Phys. Rev. D*, 106(12):124039, 2022. arXiv:2210.01833, doi:10.1103/PhysRevD.106.124039.

[189] V. Loiko, I. Perapechka, and Ya. Shnir. Q-balls without a potential. *Phys. Rev. D*, 98(4):045018, 2018. arXiv:1805.11929, doi:10.1103/PhysRevD.98.045018.

[190] T. D. Lee and Yang Pang. Stability of Mini - Boson Stars. *Nucl. Phys. B*, 315:477, 1989. doi:10.1016/0550-3213(89)90365-9.

[191] M. Gleiser and R. Watkins. Gravitational stability of scalar matter. *Nucl. Phys.*, B319:733, 1989. arXiv:gr-qc/9905067.

[192] Fyodor V. Kusmartsev, Eckehard W. Mielke, and Franz E. Schunck. Stability of neutron and boson stars: A New approach based on catastrophe theory. 1991.

[193] S.H. Hawley and M.W. Choptuik. Boson stars driven to the brink of black hole formation. *Phys. Rev.*, D62:104024, 2000. arXiv:gr-qc/0007039, doi:10.1103/Phys.Rev.D.62.104024.

[194] Hector Olivares, Ziri Younsi, Christian M. Fromm, Mariafelicia De Laurentis, Oliver Porth, Yosuke Mizuno, Heino Falcke, Michael Kramer, and Luciano Rezzolla. How to tell an accreting boson star from a black hole. 2018. arXiv:1809.08682.

[195] C. Palenzuela, L. Lehner, and Steven L. Liebling. Orbital Dynamics of Binary Boson Star Systems. *Phys. Rev.*, D77:044036, 2008. arXiv:0706.2435, doi:10.1103/PhysRevD.77.044036.

[196] B. P. Abbott et al. Observation of Gravitational Waves from a Binary Black Hole Merger. *Phys. Rev. Lett.*, 116(6):061102, 2016. arXiv:1602.03837, doi:10.1103/PhysRevLett.116.061102.

[197] B. P. Abbott et al. GW150914: First results from the search for binary black hole coalescence with Advanced LIGO. *Phys. Rev.*, D93(12):122003, 2016. arXiv:1602.03839, doi:10.1103/PhysRevD.93.122003.

[198] Jae-weon Lee and In-gyu Koh. Galactic halos as boson stars. *Phys. Rev.*, D53:2236–2239, 1996. arXiv:hep-ph/9507385, doi:10.1103/PhysRevD.53.2236.

[199] L.Arturo Urena-Lopez and Argelia Bernal. Bosonic gas as a Galactic Dark Matter Halo. *Phys.Rev.*, D82:123535, 2010. arXiv:1008.1231, doi:10.1103/Phys.Rev.D.82.123535.

[200] Hong-Bo Li, Shuo Sun, Tong-Tong Hu, Yan Song, and Yong-Qiang Wang. Rotating multistate boson stars. *Phys. Rev.*, D101(4):044017, 2020. arXiv:1906.00420, doi:10.1103/PhysRevD.101.044017.

[201] T. Regge and J. Wheeler. Stability of a Schwarzschild singularity. *Phys. Rev.*, 108:1063–1069, 1957.

[202] F. J. Zerilli. Effective potential for even parity Regge-Wheeler gravitational perturbation equations. *Phys. Rev. Lett.*, 24:737, 1970.

[203] Carlos A. R. Herdeiro and Eugen Radu. Kerr black holes with scalar hair. *Phys. Rev. Lett.*, 112:221101, 2014. arXiv:1403.2757, doi:10.1103/PhysRevLett.112.221101.

[204] Frank Loffler et al. The Einstein Toolkit: A Community Computational Infrastructure for Relativistic Astrophysics. *Class. Quant. Grav.*, 29:115001, 2012. arXiv:1111.3344, doi:10.1088/0264-9381/29/11/115001.

[205] Erik Schnetter, Scott H. Hawley, and Ian Hawke. Evolutions in 3D numerical relativity using fixed mesh refinement. *Class. Quant. Grav.*, 21:1465–1488, 2004. arXiv:gr-qc/0310042, doi:10.1088/0264-9381/21/6/014.

[206] http://www.carpetcode.org/. Carpet: Adaptive Mesh Refinement for the Cactus Framework.

[207] Motoyuki Saijo, Masaru Shibata, Thomas W. Baumgarte, and Stuart L. Shapiro. Dynamical bar instability in rotating stars: Effect of general relativity. *Astrophys. J.*, 548:919–931, 2001. arXiv:astro-ph/0010201, doi:10.1086/319016.

[208] Masaru Shibata and Hirotaka Yoshino. Bar-mode instability of rapidly spinning black hole in higher dimensions: Numerical simulation in general relativity. *Phys. Rev.*, D81:104035, 2010. arXiv:1004.4970, doi:10.1103/PhysRevD.81.104035.

[209] Peter Diener. A New general purpose event horizon finder for 3-D numerical space-times. *Class. Quant. Grav.*, 20:4901–4918, 2003. arXiv:gr-qc/0305039, doi:10.1088/0264-9381/20/22/014.

[210] Thomas W. Baumgarte and Stuart L. Shapiro. On the numerical integration of Einstein's field equations. *Phys. Rev.*, D59:024007, 1998. arXiv:gr-qc/9810065.

[211] J. David Brown, Peter Diener, Olivier Sarbach, Erik Schnetter, and Manuel Tiglio. Turduckening black holes: An Analytical and computational study. *Phys. Rev. D*, 79:044023, 2009. arXiv:0809.3533, doi:10.1103/PhysRevD.79.044023.

[212] Víctor Jaramillo, Nicolas Sanchis-Gual, Juan Barranco, Argelia Bernal, Juan Carlos Degollado, Carlos Herdeiro, Miguel Megevand, and Darío Núñez. Head-on collisions of ℓ-boson stars. *Phys. Rev. D*, 105(10):104057, 2022. arXiv:2202.00696, doi:10.1103/PhysRevD.105.104057.

[213] B. P. Abbott et al. GWTC-1: A Gravitational-Wave Transient Catalog of Compact Binary Mergers Observed by LIGO and Virgo during the First and Second Observing Runs. *Phys. Rev. X*, 9(3):031040, 2019. arXiv:1811.12907, doi:10.1103/PhysRevX.9.031040.

[214] R. Abbott et al. GWTC-2: Compact Binary Coalescences Observed by LIGO and Virgo During the First Half of the Third Observing Run. *Phys. Rev. X*, 11:021053, 2021. arXiv:2010.14527, doi:10.1103/PhysRevX.11.021053.

[215] R. Abbott et al. GWTC-3: Compact Binary Coalescences Observed by LIGO and Virgo During the Second Part of the Third Observing Run. 11 2021. arXiv:2111.03606.

[216] B. P. Abbott et al. Binary Black Hole Population Properties Inferred from the First and Second Observing Runs of Advanced LIGO and Advanced Virgo. *Astrophys. J. Lett.*, 882(2):L24, 2019. arXiv:1811.12940, doi:10.3847/2041-8213/ab3800.

[217] B. P. Abbott et al. GW170817: Observation of Gravitational Waves from a Binary Neutron Star Inspiral. *Phys. Rev. Lett.*, 119(16):161101, 2017. arXiv:1710.05832, doi:10.1103/PhysRevLett.119.161101.

[218] Paolo Creminelli and Filippo Vernizzi. Dark Energy after GW170817 and GRB170817A. *Phys. Rev. Lett.*, 119(25):251302, 2017. arXiv:1710.05877, doi:10.1103/PhysRevLett.119.251302.

[219] T. Baker, E. Bellini, P. G. Ferreira, M. Lagos, J. Noller, and I. Sawicki. Strong constraints on cosmological gravity from GW170817 and GRB 170817A. *Phys. Rev. Lett.*, 119(25):251301, 2017. arXiv:1710.06394, doi:10.1103/PhysRevLett.119.251301.

[220] Jose María Ezquiaga and Miguel Zumalacárregui. Dark Energy After GW170817: Dead Ends and the Road Ahead. *Phys. Rev. Lett.*, 119(25):251304, 2017. arXiv:1710.05901, doi:10.1103/PhysRevLett.119.251304.

[221] C. Herdeiro, I. Perapechka, E. Radu, and Ya. Shnir. Asymptotically flat spinning scalar, Dirac and Proca stars. *Phys. Lett. B*, 797:134845, 2019. arXiv:1906.05386, doi:10.1016/j.physletb.2019.134845.

[222] Helvi Witek and Miguel Zilhão. CANUDA. https://bitbucket.org/canuda/.

[223] Justin L. Ripley and Frans Pretorius. Scalarized Black Hole dynamics in Einstein dilaton Gauss-Bonnet Gravity. *Phys. Rev. D*, 101(4):044015, 2020. arXiv:1911.11027, doi:10.1103/PhysRevD.101.044015.

[224] R. Abbott et al. GW190521: A Binary Black Hole Merger with a Total Mass of $150M_{\odot}$. *Phys. Rev. Lett.*, 125(10):101102, 2020. arXiv:2009.01075, doi:10.1103/PhysRevLett.125.101102.

[225] Miguel Bezares, Mateja Bošković, Steven Liebling, Carlos Palenzuela, Paolo Pani, and Enrico Barausse. Gravitational waves and kicks from the merger of unequal mass, highly compact boson stars. *Phys. Rev. D*, 105(6):064067, 2022. arXiv:2201.06113, doi:10.1103/PhysRevD.105.064067.

[226] Pedro L Espino, Vasileios Paschalidis, Thomas W Baumgarte, and Stuart L Shapiro. Dynamical stability of quasitoroidal differentially rotating neutron stars. *Physical Review D*, 100(4):043014, 2019.

[227] Fabrizio Di Giovanni, Nicolas Sanchis-Gual, Pablo Cerdá-Durán, Miguel Zilhão, Carlos Herdeiro, José A Font, and Eugen Radu. Dynamical bar-mode instability in spinning bosonic stars. *Physical Review D*, 102(12):124009, 2020.

[228] Christopher Beetle, Marco Bruni, Lior M. Burko, and Andrea Nerozzi. Towards wave extraction in numerical relativity: Foundations and initial value formulation. *Phys. Rev. D*, 72:024013, 2005. arXiv:gr-qc/0407012, doi:10.1103/PhysRevD.72.024013.

[229] Manuela Campanelli, Bernard J. Kelly, and Carlos O. Lousto. The Lazarus project. II. Space-like extraction with the quasi-Kinnersley tetrad. *Phys. Rev. D*, 73:064005, 2006. arXiv:gr-qc/0510122, doi:10.1103/PhysRevD.73.064005.

[230] W. Israel. Source of the kerr metric. *Phys. Rev. D*, 2:641–646, 1970. doi:10.1103/PhysRevD.2.641.

[231] J. Tiomno. Electromagnetic field of rotating charged bodies. *Phys. Rev. D*, 7:992–997, 1973. doi:10.1103/PhysRevD.7.992.

[232] D. Lynden-Bell. Electromagnetic magic: The Relativistically rotating disk. *Phys. Rev. D*, 70:105017, 2004. arXiv:gr-qc/0410109, doi:10.1103/PhysRevD.70.105017.

[233] A. Shadi Tahvildar-Zadeh. On a zero-gravity limit of the Kerr–Newman spacetimes and their electromagnetic fields. *J. Math. Phys.*, 56(4):042501, 2015. arXiv:1410.0416, doi:10.1063/1.4915290.

[234] Robert M. Wald. Black hole in a uniform magnetic field. *Phys. Rev. D*, 10:1680–1685, 1974. doi:10.1103/PhysRevD.10.1680.

[235] A. N. Aliev and D. V. Galtsov. Magnetized Black Holes. *Sov. Phys. Usp.*, 32:75, 1989. doi:10.1070/PU1989v032n01ABEH002677.

[236] A. N. Aliev and D. V. Galtsov. Exact Solutions For Magnetized Black Holes. *Astrophys. Space Sci.*, 155:181, 1989. doi:10.1007/BF00643854.

[237] W. Bonnor. An exact solution of the Einstein-Maxwell equations referring to a magnetic dipole. *Zeitschrift für Physik*, 190:444–445, 1966. doi:10.1007/BF01327262.

[238] V. S. Manko. A note on magnetic generalizations of the Kerr and Kerr–Newman solutions. *Class. Quant. Grav.*, 34(17):177002, 2017. doi:10.1088/1361-6382/aa80bb.